Discovery strategies for dark matter and Higgsinos at the LHC

Jesse Liu

St Catherine's College

University of Oxford

A thesis submitted for the degree of

Doctor of Philosophy

Hilary Term 2019

Abstract

New dynamics beyond the Standard Model is expected at scales probed by the Large Hadron Collider. In particular, weak scale supersymmetry can provide a dark matter candidate and stabilise the electroweak hierarchy. This thesis presents two studies investigating new strategies to discover such phenomena. First, a theoretical assessment uses six search strategies based on 3.2 fb^{-1} of 13 TeV data to constrain a 19-parameter framework of supersymmetry. This identified the fermionic partners of Higgs bosons, called Higgsinos, as a key target for dark matter searches. Such scenarios are very difficult to discover at colliders in electroweak production, as produced states are one to tens of GeV heavier than the dark matter and leave little detector activity. The second part of this thesis presents a new experimental strategy targeting these so-called compressed scenarios, exploiting electrons and muons down to the lowest transverse momenta detectable by the ATLAS Experiment. Using 36.1 fb^{-1} of 13 TeV data, this strategy opens hadron collider sensitivity to Higgsino dark matter down to mass splittings of 3 GeV, and coannihilation scenarios involving winos and sleptons down to mass splittings of 2.5 and 1 GeV respectively. While no statistically significant excesses are observed, this landmark LHC sensitivity surpasses lepton collider limits for the first time in nearly two decades.

Dedicated to the memory of my mother.

Acknowledgements

This thesis and doctorate is only possible with the invaluable support I received throughout my education. I would like to thank the institutions from which I benefited, before turning my gratitude to specific individuals.

It is a privilege to be in a society that recognises the importance of fundamental research, generously supports education, and enables peaceful international collaborations.

Specifically, I thank the Science and Technology Facilities Council, St Catherine's College, Sub-department of Particle Physics at the University of Oxford, ICHEP Travel Grant, and Santander Academic Travel Award for funding. In particular, they enabled my two year visit to the European Organisation for Nuclear Research (CERN) in Geneva, together with two-week summer programmes at the University of Manchester and Institute for Advanced Studies in Princeton.

For research visits and conferences, I am grateful to the generous hospitality at Barcelona, Berkeley, Birmingham, Bristol, Bucharest, Cambridge, Canterbury, CERN, Durham, Heidelberg, Imperial, Liverpool, MIT, Perimeter Institute, Rome, Santa Cruz, Sheffield, Stanford, Seoul, and Sussex.

The experimental work would not be possible without the successful operation of the Large Hadron Collider (LHC) at CERN, and the ATLAS Collaboration for coordinating the physics and operations programme. I thank the Perimeter Institute for Theoretical Physics and University of Waterloo for supporting my pre-doctoral year in Canada, where my graduate interest in fundamental physics began.

Turning my gratitude to the many extraordinary individuals, it is humbling to reflect on just how wide-ranging the expertise and supportive friendships I am lucky to have.

First, I am indebted to Alan Barr and John March-Russell for their supervision. I thank Alan for welcoming me to the Oxford supersymmetry group, his exemplary organisational efficiency, encouraging me to be creative while striving for high standards, introducing me to excellent international collaborators, and entrusting me with intellectual freedom early on. I thank John for welcoming me to the theory group, filled with interesting conversations and willingness to teach me theoretical aspects of new physics searches.

I thank Moritz Backes for his expertise and patient guidance throughout my trigger and analysis work, without which the principal subject of this thesis would not have realised so soon or to such high quality.

I am deeply grateful to Lydia Beresford for her invaluable support and enduring friendship. While we only started working together recently, her insights and intellect have made this among the most enjoyable and creative collaborations.

Within Oxford, I have enjoyed discussions with Giles Barr, Kathrin Becker, Daniela Bortoletto, Fady Bishara, James Frost, Claire Gwenlan, Lucian Harland-Lang, Todd Huffman, Çiğdem İşsever, Jaya John John, Kashif Mohammad, Koichi Nagai, Subir Sarkar, Elisabeth Schopf, Ian Shipsey, Mika Vesterinen, and Tony Weidberg. In addition, I thank Jeff Tseng for patiently introducing me to particle physics as a summer student. I also thank my examiners Monica D'Onofrio and Dave Wark for feedback on this thesis.

I thank fellow Oxford ATLAS students for teaching me about their subjects: Luca Ambroz, Gabriel Gallardo, Luigi Marchese, Nurfikri Norjoharuddeen, Aaron O'Neill, Santiago Paredes, Mariyan Petrov, Gavin Pownall, Abhishek Sharma, Hayden Smith, Beojan Stanislaus, Cecilia Tosciri, Luigi Vigani, Jonas Würzinger, Gabija Žemaitytė and Miha Zgubič. Special thanks to Jon Burr, Will Fawcett and Will Kalderon for patiently teaching me python, ROOT, SCT, trigger and physics in my nascent supersymmetry group years. I am particularly grateful to Mike Nelson for providing enthusiastic company and discussions throughout this degree.

This gratitude is extended to fellow theorists Callum Brodie, Fran Day, George Johnson, Jack Kemp, Olivier Lennon, Ben Meiring, James Scargill, James Scoville, and Hannah Tillim for enjoyable conversations in their community. Furthermore, I am grateful to Mikkel Bjørn, Tom Hadavizadeh, Thomas Hancock, Colm Murphy, Anita Nandi, Hannah Pullen, Alex Rollings for welcoming me to Oxford LHCb offices, together with Theresa Fruth, Charles Simpson, Esther Turner for educating me beyond colliders. I especially thank Barak Gruberg for all the ice cream breaks during our time at CERN.

For helping me navigate departmental administration, I owe my thanks to Sue Geddes, Jennifer Matthews, Francesca Oliver, and Kim Proudfoot.

Outside the Oxford group, I am grateful to Ben Allanach, Stanley Brodsky, Jon Butterworth, Lance Dixon, Val Gibson, Howard Haber, Chris Lester, Jason Nielsen, Christoph Paus, Andy Pilkington, Brian Petersen, Tina Potter, Tom Rizzo, Dave Robinson, Josh Ruderman, Brian Shuve, Jesse Thaler, Hendrik Vogel, Haichen Wang for stimulating discussions and hospitality in their respective groups. I remain grateful to my master's supervisor Natalia Toro for her encouragement during and since my research project with her, and educating me about searches for dark sectors.

My analysis work is indebted to the leadership of Mike Hance, Joana Machado Miguéns and later Stefano Zambito, who fostered an efficient, pragmatic and welcoming group. I am moreover grateful to my collaborators Sara Alderweireldt, Matthew Gignac,

Julia Gonski, Ben Hooberman, Tommaso Lari, Judita Mamuzic, Masahiro Morii, Joey Reichert, Lorenzo Rossini, Sheena Schier, Yu-Ting Shen, Sarah Williams, and Keisuke Yoshihara. Gratitude is also expressed to the numerous conveners Alex Mann, Andreas Petridis, Till Eifert, Zach Marshall and Iacopo Vivarelli, together with Jamie Boyd and Stephane Wilocq for many helpful comments. Special thanks to Elodie Resseguie for teamwork and tea breaks throughout this project.

At CERN, I profited from discussions with Cameron Bravo, Savannah Clawson, James Cowley, Anna Duncan, Michael Fenton, Oliver Lantwin, Chiao-Ying Lin, Holly Pacey, Rebecca Pickles, Baptiste Ravina, Leigh Schaefer, Matt Tilley, Alison Tully, Amal Vaidya, and David Yallup. I also thank fellow theorists Mariana Carrillo Gonzalez, Andrew Cheek, Joe Davighi, Nicolas Fernandez, Simon King, Euan Mclean, Sonali Mohapatra, Alex Pozas, Jack Setford and Patrick Tunney welcome me into their community. I am particularly indebted to Ricky Nathvani for his infectious enthusiasm since school.

For their pre-doctoral pedagogy, I especially thank Tibra Ali, Dan Wohns and Gang Xu at the Perimeter Institute, along with my undergraduate tutors at Exeter College: Frank Close, Jo Dunkley, Richard Roberts and Andrew Steane. I thank my high school science teachers Ala El-Hendi, Jon Bradford, Mike Singer and the late William Quaye for their inspiration, and extend this gratitude to Davy Adriaens and Richard Yuan for arranging a school trip to CERN where it was delightful to host. I am grateful to Paul Bartlett, Chris Pickard and Hilary Wigmore for giving me previews of physics research at University College London.

I thank my friends who have generously hosted or visited me during the DPhil across the world: Amany Amin, Heidi Barnett, Kale Colville, Chrislyn D'lima, Iain Frenkiel, Matt Garrod, Qi Hu, Ruoyu Li, Kevin McEwan, Karina Moy, Nathan Musoke, Nicole Nagy, Saagar Patel, Sam Perkins, Bijan Rafraf, Andrea Rialas, Rob Rockwood, Luke Smith, Maia Srebernik, Mae Hwee Teo, Mikesh Udani, Olivia Wigmore, and Natasha Wood. I especially thank Lydia Heinrichs, Jingyi Liu, and Nitza Solis for regularly welcoming me so warmly to Cambridge, Boston, and Chicago over these years.

Finally, I am eternally grateful to my brother and father for their unwavering support in my endeavours.

This thesis is dedicated to the memory of my mother. She taught me to be curious, conscientious and compassionate, but was never able to witness my past ten years in further education. I hope she would have been proud of who I have become had she still been with us. Her timeless inspiration carried this doctorate to its timely completion.

Preface

Contemporary research in fundamental physics is typically conducted in large international collaborations comprising thousands of scientists. Chapters 2 and 3 review the experimental and theoretical foundations of this enterprise before subsequent chapters present my original research based on published work. My contributions during the DPhil are summarised in what follows, a subset of which is presented in this thesis.

Supersymmetry and dark matter phenomenology

Chapter 4 is based on work published in the *European Physical Journal C* [1, 2], where I led the entire intellectual effort and was corresponding lead author. I performed all aspects of the Monte Carlo simulation, implementation of six early 13 TeV searches, production of all figures and tables, and the editorial process.

Physics analysis search for supersymmetry

Chapter 5 is based on the article published in *Physical Review D* [3], where I was lead analyser and editor. All figures not produced by me in this chapter are explicitly labelled in the figure captions. As a new analysis in ATLAS, I played a central role designing the search strategy and steering the technical implementation from inception through to the final results, paper editorial process, and wider scholarly dissemination. Specific personal contributions are detailed in what follows:

- I proposed the slepton analysis and designed the slepton signal Monte Carlo samples. I devised the sampling of points from the slepton and neutralino mass grid, and ensured sufficient statistics based on expected acceptances. Further, I implemented a selection after the showering step of Monte Carlo generation called a filter. This retains events satisfying a missing transverse momentum threshold to reduce computational resources at simulation, reconstruction, and analysis. I studied how the cross-sections of Higgsino-like states behaved as electroweakino composition changed in more 'realistic' MSSM scenarios.

- I optimised signal regions and ensured a coherent analysis strategy targeting both Higgsinos and sleptons. I expanded an existing SUSYSKIMHIGGSINO analysis framework, where I implemented high-level $m_{\tau\tau}$ and m_{T2}^{100} variables. This

framework is used to process data and Monte Carlo samples produced centrally by the ATLAS Collaboration into analysis ntuples. The improved code is used by collaborators to produce samples for the analysis team to use.

- I led the background estimation strategy, namely proposing and designing all the control and validation regions. I studied their process purity and potential signal contamination to define the final kinematic selections. I conducted early composition studies of fake/nonprompt lepton backgrounds and used a same-sign selection to validate these estimates subsequently produced by collaborators.

- I initiated and led the statistical analysis, where I was the principal coordinator of the HIGGSINOFITTER code, based on the HISTFITTER package. I implemented the 'cut-and-count' and 'shape fit' analyses, and the detector systematic uncertainties. I produced kinematic distributions, statistical fits, the final figures and tables of results, and interpretation in 3 simplified models for the paper.

- I implemented analysis selections in the SIMPLEANALYSIS package to calculate signal acceptances. I prepared this code, its results and digitisation, cutflows, model parameter files, and kinematic distributions for the public auxiliary HEPDATA material [4] of this publication to facilitate external reinterpretation.

- I produced and maintained the first ATLAS SUSY summary plots for both Higgsino dark matter and direct slepton scenarios [5], combining limits from multiple searches by overlaying each exclusion contour, primarily for presentation at conferences.

- I co-authored the companion internal documentation [6], where I led extensive supplementary studies crucial for the detailed scrutiny of this work during its development and internal review. This material and accompanying discussions are beyond the scope of this thesis.

- I developed new multi-object hardware topological triggers called 'L1 Topo' to increase signal acceptance while maintaining tolerable trigger rates. This work is documented in Ref. [6] and is commissioned for data-taking in 2017 and 2018, but not considered in this thesis.

- I led the detailed physics scrutiny during migration to 'Release 21' software, featuring substantial changes to ATLAS-wide object reconstruction algorithms used to analyse the full 2015–2018 dataset. I devised and implemented significant revisions to the slepton signals in Release 21, including those not in the compressed

region used in a separate lepton trigger analysis [7]. I performed validation studies of an updated release of Monte Carlo generators MADGRAPH+PYTHIA that impact ATLAS-wide production. This work comprises the technical foundations crucial for the improved analysis [8, 9], but is not presented in this thesis.

Detector operations of silicon tracker

I led radiation damage studies during operations of the ATLAS SemiConductor Tracker (SCT). This work is accepted in the *Journal of Instrumentation* [10], but is not presented in this thesis. Preliminary results were documented in the internal note [11], and I prepared public results presented in September 2016 [12] and November 2017 [13]. Part of this work qualified me as an ATLAS author.

Specifically, I maintained the software for monitoring the optical power of fibres connecting the on-detector SCT modules to the data acquisition over a period of 2 years (2015–2017). I presented the first quantitative correlation between LHC luminosity and optical power, evidencing radiation degradation. I quantified the decrease in optical power of on-detector p-i-n photodiodes (transmission 'Tx' cables) with luminosity. I also studied the optical power received by the back-of-crate photodiodes ('Rx' cables) across 1 year, as well as depletion voltage studies.

Proposal for photon collider new physics search

I proposed a novel way of using the LHC as a photon collider and completed a feasibility study to search for new physics [14]. This work targets a challenging blind spot in LHC slepton searches for moderate mass splittings. A strategy is proposed that measures initial state kinematics from proton tagging, allowing missing momentum 4-vector reconstruction and powerful discrimination against neutrino backgrounds. I performed the MC simulation, devised the analysis, and edited the paper. As first steps for experimental realisation, I recently joined commissioning efforts of the ATLAS Forward Proton detectors, study and calibration of proton reconstruction performance, and the Standard Model exclusive dilepton measurement. This work is not presented in this thesis.

Contents

1

Introduction

Scattering experiments govern our study of natural phenomena. Our eyes make observations via the scattering of light. Understanding its behaviour allowed microscopes and telescopes to be built, which Hooke and Galileo used to unveil then hidden structures of cellular biology and extraterrestrial moons. This set the basis of empirical enquiry: making measurements to probe known phenomena allows the construction of instruments to reveal unknown sectors of nature. The science at the Large Hadron Collider (LHC) is no exception. This modern incarnation of the microscope is the most sophisticated scattering experiment in human history. Situated at CERN on the Swiss–French border, its discoveries could profoundly deepen our understanding of space and time to the matter and forces in our universe.

The LHC scatters protons at the world's highest centre-of-momentum energy of 13 TeV. The ATLAS detector measures the resulting debris using tracking, calorimetry and muon systems based on a variety of solid, liquid and gaseous phase technologies, enabling a rich physics programme. This class of scattering experiment exploits two striking features of relativity and quantum mechanics: 1) matter–energy equivalence enables production of new distinct particles, and 2) particle–wave duality opens non-optical probes of subatomic structures. Decades of experimental and theoretical work reconciled these pictures, culminating in the *Standard Model* (SM) of particle physics. This principled and predictive theory continues to describe observed phenomena at colliders with remarkable success.

However, among the most startling realisations in contemporary physics arise from striking shortcomings of the SM. This thesis addresses two of the most pressing problems. First, there is no viable particle to account for the dark matter observed across vast astrophysical scales, and second, electroweak symmetry breaking is dynamically unstable to

the mass hierarchy between the gravitational and electroweak sectors. A well-motivated class of solutions is *supersymmetry*, which is the theoretical framework underpinning this thesis. This extension of spacetime symmetries predicts partners of SM particles that differ by half a unit of spin and may be accessible at the LHC. To seek evidence for such new phenomena, precision measurements indirectly probing deviations from the SM are complemented by direct searches for production of new states.

This thesis focuses on the second approach, where Chapter 2 introduces the principles of scattering experiments before summarising its contemporary realisation as the LHC and ATLAS. The theoretical motivations for new physics at the weak scale and strategies to discover supersymmetry and dark matter are reviewed in Chapter 3. Two published pieces of original work are then presented: the first is a theoretical survey of supersymmetry searches in strong production, while the second is an experimental search for supersymmetry with compressed mass spectra in electroweak production.

Chapter 4 presents the theoretical survey exploring constraints of six early 13 TeV searches for the supersymmetric partners of the gluon and quarks (gluinos and squarks) beyond simplified models. A 19-dimensional parameter space is used, which ascribes dark matter interpretations to these searches and comparisons with non-collider direct detection experiments. Notably, a promising scenario that is not constrained by these searches involves the partners of the Higgs boson, namely Higgsino dark matter.

Chapter 5 presents a new search motivated by Higgsino dark matter using 36.1 fb^{-1} of 13 TeV proton–proton collision data recorded by ATLAS. This targets very challenging but phenomenologically favoured compressed scenarios in electroweak production. Here, mass differences between produced states and dark matter are of order one to tens of GeV, where no hadron collider sensitivity existed before this work. New strategies are devised to overcome obstructions of conventional LHC approaches. Events are selected with initial state radiation in signals and among the lowest transverse momentum leptons detectable in ATLAS. This strategy opens LHC sensitivity to dark matter scenarios involving Higgsinos and scalar partners of charged leptons known as sleptons, surpassing limits set by LEP experiments for the first time in nearly two decades.

Conclusions and outlook are summarised in Chapter 6.

2

High energy scattering experiments

Scattering experiments are the heart of fundamental physics. It is underpinned by two concepts: *preparation* and *measurement*. Accelerators prepare initial states $|i\rangle$ and detectors measure final states $|f\rangle$. Studying how the final states change with respect to the initial allows the underlying interactions to be probed. Historically, the seminal Geiger–Marsden–Rutherford experiments [15–17] measured the elastic scattering of alpha particles to reveal atomic substructure. A century later, the nuclear constituents of this very discovery are used at the Large Hadron Collider (LHC) [18]. The scientific goals remain unchanged: empirically testing theories and probing the structure of matter in uncharted regimes. The theories tested by this thesis using these experiments are discussed in Chapter 3. Protons accelerated to several TeV energies are the initial states that collide after which the ATLAS Experiment [19] measures the final states:

$$\text{LHC prepares } |i\rangle, \quad \text{ATLAS measures } |f\rangle.$$

The total beam energy in the centre-of-momentum frame $\sqrt{s}$ is a key design metric of particle accelerators. Raising $\sqrt{s}$ allows smaller length scales to be probed and production of previously inaccessible heavy states. Recent realisations of such efforts as ring accelerators at the energy frontier include:

- **Large Electron–Positron Collider (LEP)** [20]. Electrons e^- and positrons e^+ underwent collisions at $\sqrt{s}$ of up to 208 GeV. Highlights include measuring the Z boson invisible width [21] and searches for supersymmetry [22–24]. LEP constraints on supersymmetric states with only electroweak interactions are particularly relevant for this thesis and discussed in Chapter 5.

- **Tevatron** [25]. This accelerator collided protons p with anti-protons $\bar{p}$ at $\sqrt{s}$ of up to 1.92 TeV. Highlights include the top quark discovery [26, 27] and searches

for supersymmetry [28, 29], the sensitivity to which is now surpassed by the LHC.

- **LHC**. This facility collides protons at $\sqrt{s}$ of up to 13 TeV at the time of writing, and is further discussed in Section 2.1. Highlights include the Higgs boson discovery [30, 31] and searches for supersymmetry, the latter being the focus of this thesis.

Modern particle detectors that measure properties of final states $|f\rangle$ at these colliders have three main components. First, a tracking system enables precision position–momentum measurements of electrically charged particles. Surrounding this are calorimeters, which measure the energy deposited by electrons, photons, and hadrons. Finally, muon chambers measure the trajectories of muons escaping the calorimeter. Section 2.2 discusses these subsystems in the ATLAS detector.

2.1 Large Hadron Collider

The LHC [18] is the culminating 27 km circumference two-ring synchrotron of the CERN accelerator complex. It straddles the French–Swiss border near Geneva roughly 100 m underground. Protons obtained from ionised hydrogen gas enter the linear accelerator LINAC2 and undergo several further stages of acceleration illustrated in Figure 2.1 before LHC injection. The beams are arranged with up to 2544 bunches in 25 ns intervals, each containing $\sim 10^{11}$ protons. Dipole bending magnets and quadrupole focusing magnets steer the proton beams into collision at four interaction points at the ATLAS, ALICE [32], CMS [33], and LHCb [34] experiments. This thesis focuses on the LHC proton–proton (pp) physics programme at ATLAS.

Protons are comprised of quarks and gluons, referred to as partons. In a pp collision event, hard-scatter processes involve high momentum transfer between partons. The remaining interactions are known as the underlying event. A principal observable that experimentalists measure is the interaction cross-section σ of hard processes, where heavy states may be produced in collisions. Another key beam parameter is the instantaneous luminosity $\mathscr{L}_{\text{inst}}$ delivered to the interaction point, which reaches 2×10^{34} cm^{-2} s^{-1} at the LHC. The rate of hard-scatter events is then given by

$$\frac{\mathrm{d}N}{\mathrm{d}t} = \mathscr{L}_{\text{inst}}\sigma. \tag{2.1}$$

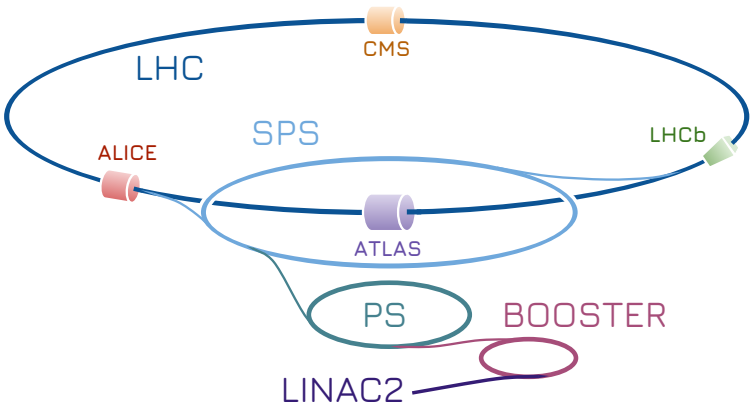

Figure 2.1: Schematic of the CERN accelerator complex delivering proton beams to the LHC experiments, adapted from [35].

Integrating the instantaneous luminosity over time gives the integrated luminosity $L = \int \mathscr{L}_{\text{inst}}\,\mathrm{d}t$, also referred to as luminosity. This is related to the total number of hard-scatter events N by $N = L\sigma$. Increasing the luminosity allows low cross-section processes to be probed, which is characteristic of the signals considered in this thesis.

The LHC delivered pp collisions up to $\sqrt{s} = 8$ TeV until 2012 (referred to as Run 1). After upgrades during 2013–2015, pp collisions took place at $\sqrt{s} = 13$ TeV with 25 ns bunch spacings. The data-collecting period in 2015–2018 is referred to as Run 2, and the cumulative luminosity over the 2015–2017 period is displayed in Figure 2.2a. The 13 TeV data analysed in this thesis corresponds to 3.2 fb^{-1} and 36.1 fb^{-1}, accumulated by the end of 2015 and 2016 respectively. Adding the data collected during 2017 and 2018 results in 140 fb^{-1} available for analysis.

Increasing instantaneous luminosity, such as augmenting the number of protons per bunch, results in further pp interactions known as pileup. Pileup is considered background, as its kinematics are stochastic and have lower momentum than hard-scatter interactions of interest. *In-time pileup* arises when these extra interactions occur in the same bunch, which is parametrised by the number of reconstructed primary vertices N_{PV}. Meanwhile, *out-of-time pileup* refers to events misidentified with those from different bunch crossings due to detector readout rate being lower than the bunch crossing frequency; this is parametrised by the mean number of interactions per bunch crossing $\langle\mu\rangle$. This distribution separated by year is shown in Figure 2.2b.

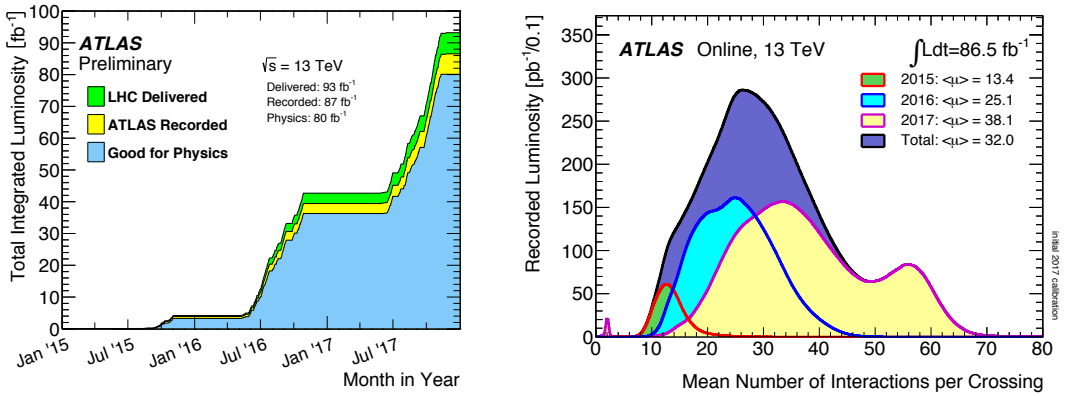

(a) Luminosity collected by ATLAS (b) Pileup distributions

Figure 2.2: Displayed are: (a) Total integrated luminosity delivered by the LHC during Run 2 in 2015–2017 data-taking (green) and recorded by ATLAS (yellow), and the subset that is good for physics analysis (blue); (b) the luminosity weighted distribution of the mean number of interactions per bunch crossings for the different years of data-taking. Reproduced from [36].

2.2 ATLAS Experiment

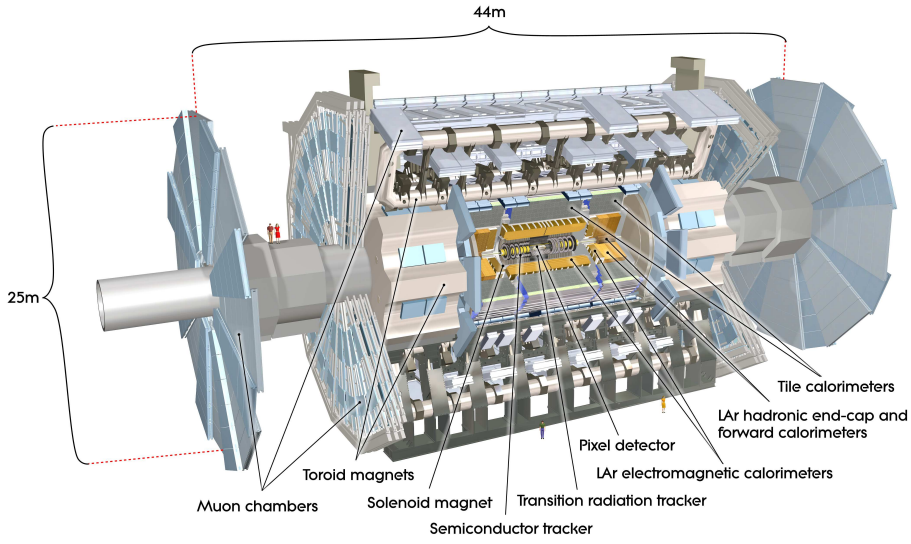

Figure 2.3: Cutaway render of the ATLAS detector, reproduced from Ref. [19].

The ATLAS (A Toroidal LHC ApparatuS) Experiment [19] is a general-purpose particle detector of cylindrical geometry (Figure 2.3). Its design facilitates a broad physics programme, which demands robust triggering, identification and reconstruction of particles amidst challenging radiation conditions [37].

ATLAS uses a right-handed coordinate system with the origin defined at the interaction point. The x axis points toward the centre of the LHC and y upwards. Cylindrical coordinates (r, ϕ) are used and the pseudorapidity is defined by $\eta = \ln\cot(\theta/2)$, where θ is the polar angle relative to the beam axis z. Angular distances are measured by $\Delta R \equiv \sqrt{(\Delta\eta)^2 + (\Delta\phi)^2}$. Rapidity is defined as $y = \frac{1}{2}\ln[(E + p_z)/(E - p_z)]$, where E is the energy and p_z is the longitudinal component of the momentum of the particle. The rapidity equals the pseudorapidity for massless particles.

The design of ATLAS is influenced by the physics expected to be probed by the LHC. Detection of the Higgs boson and new physics searches are principal targets. These heavy states are produced close to threshold, whose decay products tend to have lower values of $|\eta|$ than those from background processes. ATLAS is hermetic in ϕ and has good forward–backward coverage up to $|\eta| < 4.9$. This favours reconstruction of nearly every energetic particle in an event, allowing determination of missing momentum from neutrinos or dark matter.

Table 2.1 summarises the various subsystems of the ATLAS detector, where brief overviews of each are henceforth discussed. The information recorded by the wide-ranging detector technologies underpins triggering and objects reconstructed for analysis. Table 2.2 summarises the particles produced in high energy LHC collisions and their resulting signature in the ATLAS detector. Multiple subsystems minimise ambiguous identification of objects. For example, a muon relies on both inner detector and muon spectrometer information. States that are unstable on detector timescales, such as the Z boson, are reconstructed from its decays to objects sufficiently stable to be detected by ATLAS e.g. muons. Electrons, muons, jets (collimated streams of hadrons) and missing transverse momentum are the objects used in the search for supersymmetry presented in Chapter 5, which require information from all the ATLAS subsystems of Table 2.1. Details on the definitions of these objects are deferred to Section 5.3.

2.2.1 Inner detector

The inner detector [39] (Figure 2.4) is situated nearest the beam pipe, employing silicon sensor [40] and transition radiation technologies [41]. Traversing charged particles leave signals, referred to as hits, in the sensors of these subsystems. These are used for

Subsystem	$\lvert\eta\rvert$ coverage	Active material	Hardware trigger	Object reconstruction
Inner detector				
Pixel	< 2.5	Silicon	Not used	Vertex, Q, $\mathbf{p}$
SCT	< 2.5	Silicon	Not used	
TRT	< 2.0	Argon, xenon gas	Not used	Vertex, Q, $\mathbf{p}$, e PID
Calorimetry				
ECal Barrel	< 3.2	Liquid argon	$E_{\mathrm{T}}^{\mathrm{miss}}$, jet, e	EM energy, e/γ PID
HCal Endcap	$[1.5, 3.2]$	Liquid argon		Hadronic energy
FCal	$[3.1, 4.9]$	Liquid argon		EM & hadronic energy
HCal Barrel	< 1.7	Tile scintillator		Hadronic energy
Muon spectrometry				
RPC	< 1.05	$C_2H_2F_4$ gas	Muon	$Q, \mathbf{p}$ of μ
TGC	$[1.05, 2.4]$	CO_2, n-C_5H_{12} gas	Muon	
MDT	< 2.7	Ar, CO_2 gas	Not used	
CSC	$[2.0, 2.7]$	Ar, CO_2 gas	Not used	

Table 2.1: Summary of the ATLAS detector subsystems [19] used in this thesis. For each, the pseudorapidity $|\eta|$ coverage, its active material, and use in the Level 1 (L1) hardware trigger for this thesis are indicated. Brief remarks on the primary roles each subsystem plays in object reconstruction are also displayed, such as charge Q and momentum $\mathbf{p}$ determination, particle identification (PID), and electromagnetic (EM) or hadronic energy measurements. Electrically neutral states, such as photons and neutrons do not leave a signature in the inner detector. Particles that interact only via the weak force, such as neutrinos and dark matter candidates, are not detected by any subsystem.

precision reconstruction of tracks and their associated vertices. These subsystems are immersed in a uniform 2 T magnetic field aligned parallel to the beam pipe, generated by the enclosing superconducting solenoid. This enables measurement of track curvature and thus determination of particle charge and momentum.

Pixel detector Located closest to the interaction point, the pixel detector [42, 43] comprises 80 million channels distributed across 1744 silicon modules, with fine spatial granularity of 8 μm in r–ϕ and 115 μm in z. The modules are arranged across three concentric barrel layers at r of 50.5, 88.5 and 122.5 mm and two endcaps, each with three disks at $|z| = 495, 580$ and 650 mm from the interaction point. A fourth layer, referred to as the insertable B-layer [44], was installed for Run 2 at $r = 33$ mm, $|z| < 332$ mm to provide an extra hit near the beam pipe, enhancing impact parameter resolution. This improves primary vertex reconstruction, secondary vertex finding, with flavour tagging

Particle	Mass [GeV]	Stability	Detector signature
Quarks			
Up u	2×10^{-3}	Unstable	ECal, HCal (jets)
Down d	5×10^{-3}	Unstable	ECal, HCal (jets)
Strange s	0.1	Unstable	ECal, HCal (jets)
Charm c	1.3	Metastable	ECal, HCal (jets), displaced vertex
Bottom b	4.2	Metastable	ECal, HCal (jets), displaced vertex
Top t	173	Unstable	m_t from e.g. $t \to bW \to$ jets
Leptons			
Neutrinos $\nu_{e,\mu,\tau}$	$< 10^{-9}$	Stable	Invisible (missing momentum)
Electron e	5×10^{-4}	Stable	Silicon, TRT hits, transition radiation, ECal
Muon μ	0.106	Stable	Silicon, TRT hits, muon spectrometer
Tau τ	1.78	Metastable	Jets, displaced vertex
Bosons			
Gluon g	0	Unstable	ECal, HCal (jets)
Photon γ	0	Stable	No tracks, ECal deposit
$W^{\pm}$ boson	80.3	Unstable	m_W from e.g. $W \to \mu\nu_\mu$
Z boson	90.1	Unstable	m_Z from e.g. $Z \to \mu\mu$
Higgs boson h	125.1	Unstable	m_h from e.g. $h \to \gamma\gamma$

Table 2.2: Summary of particles produced in LHC collisions, their mass, stability on timescales resolved by ATLAS, and their typical signature in the various ATLAS subsystems. Further details of particle properties and their field theoretic formalism are presented in Section 3.1. Jets are collimated streams of hadrons, formed from the fragmentation of quarks and gluons. Additional details of object reconstruction as used in this thesis are discussed in Section 5.3. Masses are from the Particle Data Group [38].

performance seeing a four-fold increase in light flavour jet rejection for 80% efficiency of identifying jets with b-quarks from benchmark simulation studies [45].

Semiconductor tracker (SCT) The SCT [46, 47] surrounds the pixels and comprises over 6 million silicon strips across 4088 independent modules, each mounted with 768 active silicon strip sensors. The modules are arranged on four concentric barrel layers at r ranging from 299 to 514 mm, covering the region $|\eta| < 1.5$, while nine disks on each endcap spread over a $|z|$ of 853.8 to 2720.2 mm extend the tracking range to $|\eta| < 2.5$. Each layer has transverse $r - \phi$ plane resolution of 17 μm and a z-resolution of 580 μm.

Transition radiation tracker (TRT) Surrounding the SCT is the TRT, consisting of $\sim$ 350,000 straw drift tubes, each with 4 mm diameter. These are oriented parallel to

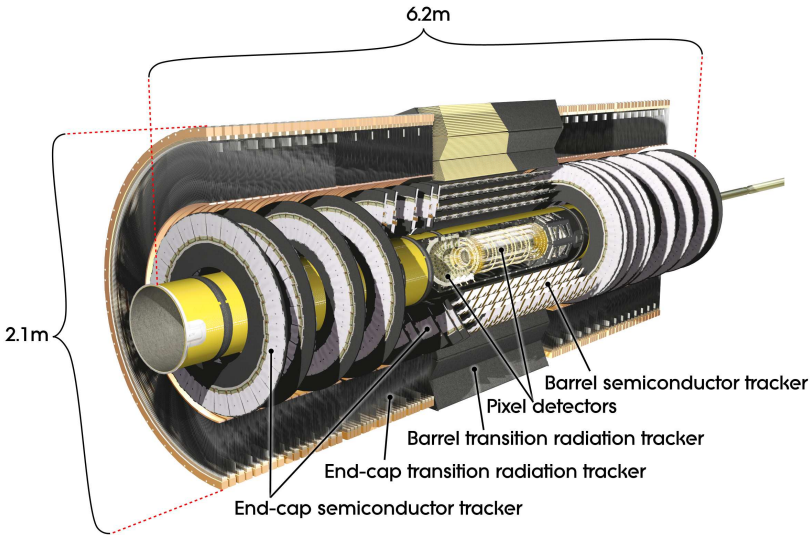

Figure 2.4: Cutaway render of the inner detector, reproduced from Ref. [19].

the beam pipe for the 73 layers between r of 563 and 1066 mm in the barrel region. Meanwhile, 160 layers of straws are oriented radially on the endcaps between $|z|$ of 848 and 2710 mm. Together, these provide $r-\phi$ measurements of charged particles up to $|\eta| \lesssim 2$ with a spatial resolution of 130 μm [41]. The straws are filled with a mixture of gases comprising primarily of xenon or argon gas, and electron identification is possible through the detection of X-ray photons known as transition radiation [48].

2.2.2 Calorimetry

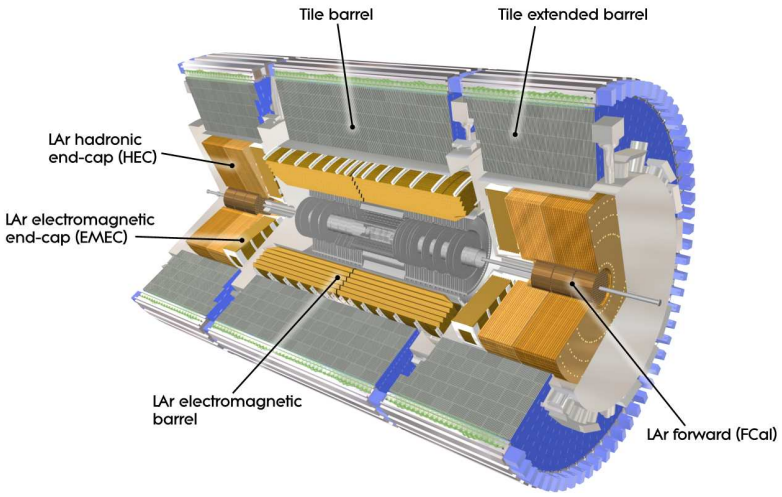

Figure 2.5: Cutaway render of the calorimetry system, reproduced from Ref. [19].

The ATLAS calorimeters (Figure 2.5) uses sampling calorimetry for particle energy measurement, ensuring a compact design with excellent shower containment [49]. These measurements underpin reconstruction of electrons, jets, and missing transverse energy used in this thesis. Alternating layers of passive absorbing and active recording material induce showering and measure cascade energies respectively. Two active materials are employed: liquid argon [50], and plastic scintillator tiles [51] for the calorimetry of electromagnetic and hadronic processes as follows.

Liquid argon Liquid Argon (LAr) technology is used for calorimetry of both electromagnetic and hadronic processes [50, 52, 53]. The LAr electromagnetic calorimeter (ECal) has a barrel part covering $|\eta| < 1.475$. It is made of 1024 pairs of lead absorbers arranged in an accordion geometry. The remaining cavities are filled with liquid argon for fine granularity energy measurement of photons and electrons.

The barrel consists of three distinct sections of increasing radius. First, strip cells provide fine η granularity, enabling discrimination of electromagnetic photons from $\pi^0 \to \gamma\gamma$, while the following two layers measure the bulk and tail of the shower and have coarser granularity. LAr presamplers are placed in front of the ECal for $|\eta| < 1.8$ to recover lost energy from premature showering of particles traversing through the inner detector. Particles typically traverse $\gtrsim 22$ radiation lengths through the ECal.

Two coaxial disks form the ECal endcap, covering $1.375 < |\eta| < 3.2$ and also have an accordion structure. In the range $1.5 < |\eta| < 3.2$, the endcap has modules for hadronic calorimetry (HCal), whose showers are broader than electromagnetic ones, and uses copper absorbers for faster heat dissipation.

Forward calorimeter (FCal) modules [54] extend coverage up to $|\eta| < 4.9$. The module closest to the interaction point uses copper as the absorbing material for electromagnetic showers. Two further modules are used for hadronic calorimetry, using tungsten absorbers for better hadronic shower containment.

Tile scintillator Hadronic calorimetry in the barrel region $|\eta| < 1.7$ uses tile scintillators [51, 55–57]. Steel absorbers have an nuclear interaction length of 16.8 cm, while the active material comprises plastic scintillation tiles. Scintillation photons proportional to deposition energy are collected by wavelength-shifting fibres at the end of cells.

Photomultiplier tubes at the end of each row of cells measure these signals.

2.2.3 Muon spectrometry

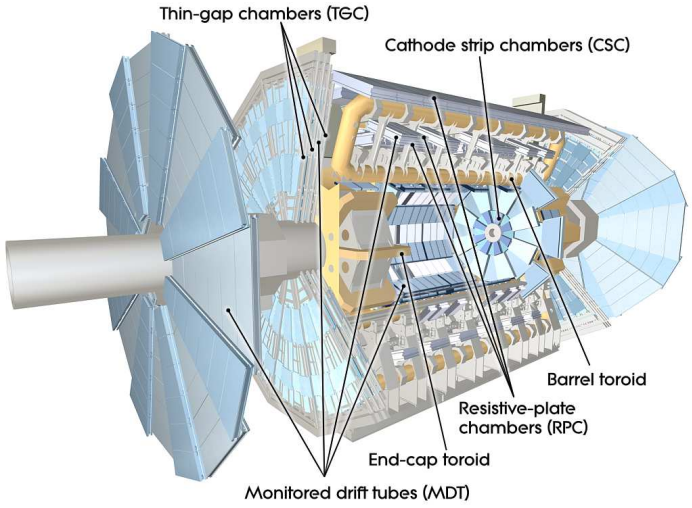

Figure 2.6: Schematic diagram of the muon spectrometer, reproduced from Ref. [19].

The muon spectrometer [58, 59] (Figure 2.6) comprises a system of fast but coarse detectors for triggering, complemented by slower but higher precision tracking chambers. These are surrounded by three $0.5-1$ T superconducting toroidal magnets, which curve muons in the $r-\eta$ plane for momentum measurement.

Triggering Resistive plate chambers (RPCs) [60] and thin gap chambers (TGCs) [61] provide triggering in the region $|\eta| < 2.4$. These feature two parallel plates with a gas gap and release an avalanche of ionised electrons upon muon traversal. The position resolutions are relatively coarse, ranging between 2 to 10 mm for the TGC (RPC). Together, they have a particle hit-to-signal response time of less than 25 ns enabling robust association with bunch crossings.

Tracking The monitored drift tubes (MDTs) [62] perform precision tracking and momentum measurements of the muons in the region $|\eta| < 2.7$. The tubes are gas filled and ionised electrons drift towards the central anode wire. The fine position resolution is as good as 35 μm while charge collection times are as high as 700 ns. Complementing the MDTs in the forward region $2 < |\eta| < 2.7$ are cathode strip chambers (CSCs) [63]. To-

gether, these can measure muons with energies as low as 3 GeV (restricted by calorimetry losses), which limits reconstruction of low momentum muons relevant for this thesis.

2.2.4 Trigger and data processing

Bandwidth and storage limitations make recording every event produced at the LHC collision rate of 40 MHz unfeasible. A subset of these events, typically those with energetic objects, are therefore selected using a two-stage trigger system [64]. The Level 1 (L1) triggers are implemented in hardware processors that reduce event rates from 40 MHz to 100 kHz. Only relatively coarse signatures reconstructed from calorimeter or muon chamber information in regions of interest are used to ensure decision times remain within 2.5×10^{-6} s. The software-based High Level Trigger (HLT) then selects a subset of these events to further reduce the recording rate to 1 kHz. The HLT has processing times of order 0.2 s, allowing use of more information from other subsystems. To reduce bandwidth, some triggers record a random subset of events selected (typically those with low thresholds); these are referred to as *prescaled* triggers.

The search presented in Chapter 5 uses triggers that select events with large magnitudes of missing transverse momentum ($E_{\mathrm{T}}^{\mathrm{miss}}$), which is a typical signature of dark matter production. Specifically, `HLT_xe110_mht_L1XE50` is the lowest unprescaled $E_{\mathrm{T}}^{\mathrm{miss}}$ trigger with the highest threshold considered in 2015–16 data analysed in Chapter 5. Here, the `L1XE50` indicates a $E_{\mathrm{T}}^{\mathrm{miss}} > 50$ GeV threshold is applied by the L1 trigger, which makes use of calorimeter measurements. The `HLT_xe110_mht` denotes $E_{\mathrm{T}}^{\mathrm{miss}} > 110$ GeV, calculated from the negative of the transverse momentum vector sum of all jets reconstructed by the HLT. Figure 2.7 shows the performance of this trigger as a function of the analysis-level (offline) $E_{\mathrm{T}}^{\mathrm{miss}}$ measured during 2017 data-taking, where full efficiency is reached for $E_{\mathrm{T}}^{\mathrm{miss}} > 200$ GeV. As part of the estimation of reducible backgrounds presented in Section 5.5, prescaled single electron (HLT thresholds between $p_{\mathrm{T}} > 5$ and 20 GeV) or muon triggers (HLT thresholds between $p_{\mathrm{T}} > 4$ and 18 GeV) are also used. For further details on triggers, see Ref. [64].

Even retaining 1 in $\sim 10^5$ events, ATLAS records $\sim 10^{16}$ bytes of data per year. A multi-tier computing system called the Worldwide LHC Computing Grid distributes this data across the world for processing [66]. All ATLAS data and Monte Carlo simulations

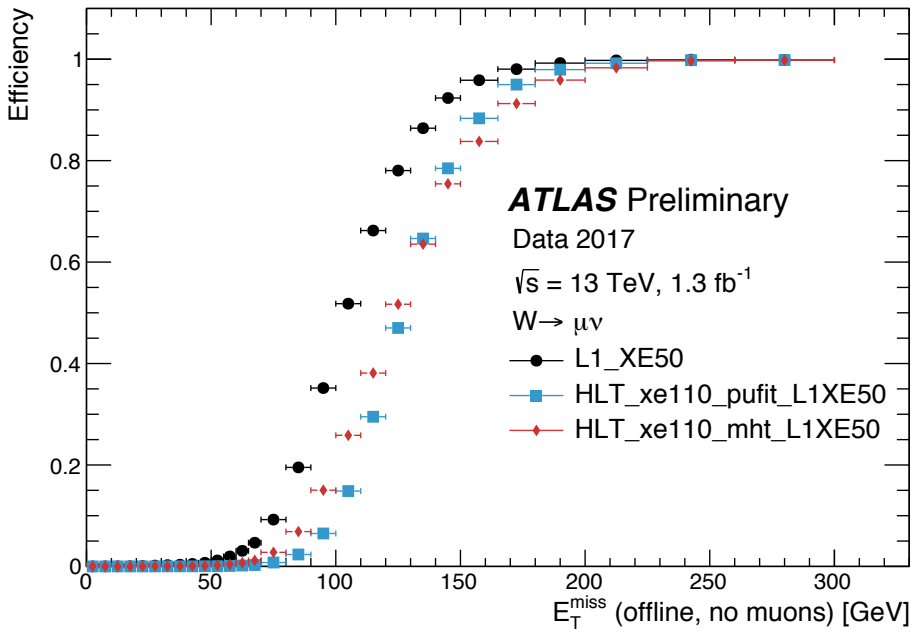

Figure 2.7: Efficiency of various missing transverse momentum triggers as a function of analysis-level $E_{\mathrm{T}}^{\mathrm{miss}}$ (before correcting for muons). These are measured in events selected using single muon triggers. The `HLT_xe110_mht_L1XE50` trigger is the one with highest threshold considered for data analysed in Chapter 5. The `mht` algorithm defines $E_{\mathrm{T}}^{\mathrm{miss}}$ as the transverse component of the negative vectorial sum of jets reconstructed at the HLT. This differs from analysis-level $E_{\mathrm{T}}^{\mathrm{miss}}$, which considers the negative sum of all visible reconstructed objects. The `HLT_xe110_pufit_L1XE50` trigger is the nominal $E_{\mathrm{T}}^{\mathrm{miss}}$ trigger used to record data in 2017, but is not considered in this thesis. Reproduced from Ref. [65].

are stored at the CERN Tier 0 (T0) data centre, and are distributed to regional Tier 1 nodes. The initial processing is done in the ATHENA computing infrastructure, while subsequent data analysis is typically performed using ROOT [67].

Figure 2.8 visualises the result of this particle detection and data processing, displaying an event with large $E_{\mathrm{T}}^{\mathrm{miss}}$ and an energetic jet recorded using the $E_{\mathrm{T}}^{\mathrm{miss}}$ trigger. The observation and calculation of $E_{\mathrm{T}}^{\mathrm{miss}}$ is possible due to the hermetic nature and excellent reconstruction capabilities of the detector. Figure 2.9 shows a Higgs boson candidate event in the final state with two electrons and two muons. The 25 additional vertices demonstrate the importance of the tracker and the robustness of lepton reconstruction in harsh pileup conditions. Large $E_{\mathrm{T}}^{\mathrm{miss}}$, an energetic jet, electron and muon pairs are objects used in the supersymmetry search presented in Chapter 5.

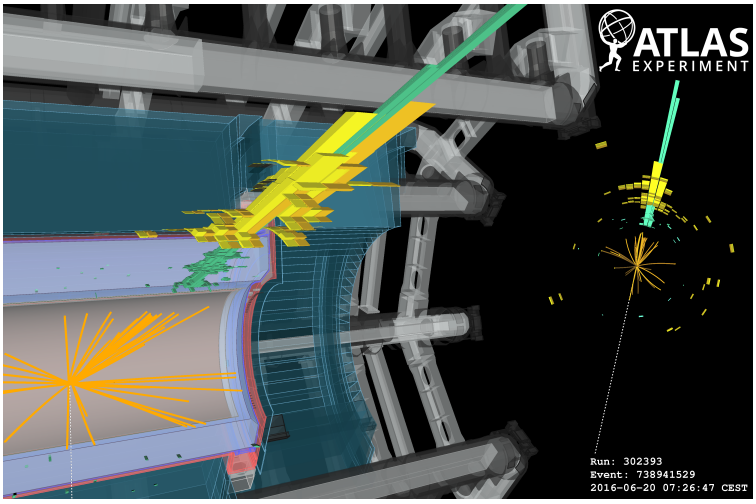

Figure 2.8: Event from 2016 ATLAS data taking showing a jet with $p_{\mathrm{T}} = 1.71$ TeV indicated by the green and yellow bars corresponding to the energy deposited in the electromagnetic and hadronic calorimeters respectively. The $E_{\mathrm{T}}^{\mathrm{miss}} = 1.74$ TeV is shown as the white dashed line. The left-hand side shows a three-dimensional cutaway render of the calorimeters (light blue) and toroidal magnets (grey). The right-hand side shows a transverse projection of the detector. Reproduced from Ref. [68].

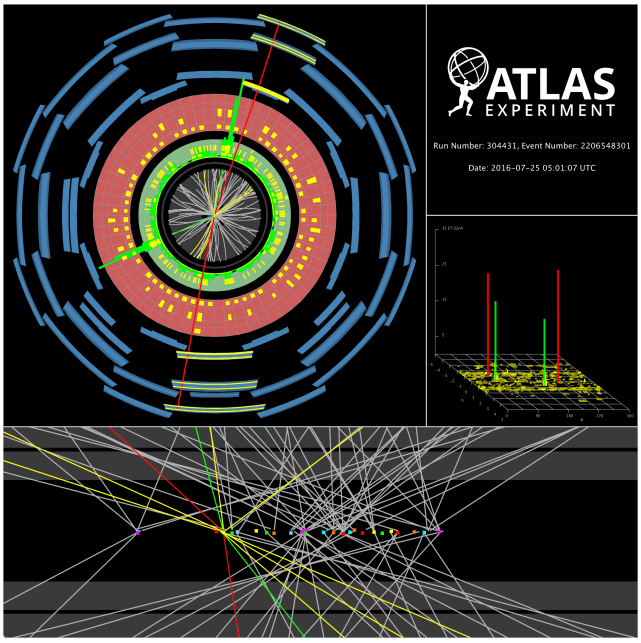

Figure 2.9: A Higgs boson candidate event from 2016 ATLAS data-taking. Displayed are the trajectories of 2 electrons and their energy deposition in the electromagnetic calorimeter (green bars) together with 2 reconstructed muons and hits in the muon spectrometer (red lines). The electrons have $p_{\mathrm{T}}(e) = 23, 19$ GeV, while the muons have $p_{\mathrm{T}}(\mu) = 31, 29$ GeV. The invariant mass of the electrons and muons is 119 GeV. Grey lines indicate reconstructed tracks with $p_{\mathrm{T}} > 1$ GeV arising from 25 additional pp collisions due to pileup. Reproduced from Ref. [69].

3

Theory for fundamental physics

The remarkable capabilities of the LHC and ATLAS experiment (Chapter 2) enable precision measurement of event rates and cross-sections σ, specified by Eq. 2.1, across wide-ranging final states and kinematic regimes. Equally remarkable is the ability to describe and predict these phenomena using principled theoretical understanding. Two concepts in quantum field theory connect the observables of scattering experiments with the underlying theory. First is the principal equation of scattering physics [70]

$$\sigma = \frac{1}{I} \int |\langle f | \mathscr{M} | i \rangle|^2 \, \mathrm{d}\Pi_f . \tag{3.1}$$

Here, I is the flux of the initial state $|i\rangle$ protons delivered by the LHC, and $\mathrm{d}\Pi_f$ is the differential kinematic phase space of the final states $|f\rangle$ measured by ATLAS. The probability of a process $P(|i\rangle \to |f\rangle)$ is given by the modulus square of the quantum amplitude $\langle f | \mathscr{M} | i \rangle$. Second, particles are excitations of fields and the particle scattering matrix $\mathscr{M}$ is related to a path integral $\int \mathscr{D}[\Phi]$ over field configurations [70]

$$\langle f | \mathscr{M} | i \rangle \sim \int \mathscr{D}[\Phi] \, \mathrm{e}^{\mathrm{i}S[\Phi]}. \tag{3.2}$$

The action S is a functional of the set of fields $\Phi(x)$ and this chapter discusses the forms of $S[\Phi]$ tested in this thesis. Section 3.1 summarises the conceptual structure of the *Standard Model* (SM) that governs the properties and interactions of the particles detected by ATLAS (Table 2.2). Striking phenomenological shortcomings reviewed in Section 3.2 motivate physics beyond the SM, emphasising why new states are expected near the weak scale and merit dedicated searches at the LHC. Section 3.3 then highlights supersymmetry and how certain mass spectra explored in this thesis are phenomenologically favoured.

3.1 The structure of matter and forces

Particles observed in detectors (Table 2.2) are quantum states $|m,s\rangle$ labelled by mass m and spin s, which can be massive or massless, while s can be integer or half-integer units of spin [71]. These quantum numbers are associated with spacetime symmetries; further quantum numbers, such as charge or flavour, are labels associated with internal symmetries. These physical degrees of freedom are embedded into *field representations* of the Poincaré group of spacetime symmetries: scalar $\phi(x)$, Weyl spinor $\psi^\alpha(x), \psi_{\dot\alpha}(x)$, and vector $A_\mu(x)$. These fields are assembled into an action, S in Eq. 3.2, to define the SM. Our description will be concise; the reader is referred to Refs. [70–75] for details.

Sector	Spin	Field	Representation
Higgs ϕ	0	$\begin{pmatrix} H^+ & H^0 \end{pmatrix}$	$(\mathbf{1},\mathbf{2},1)$
Quarks q	$\frac{1}{2}$	$(u\ d)_L$	$\left(\mathbf{3},\mathbf{2},\frac{1}{3}\right)$
		u^c_R	$\left(\bar{\mathbf{3}},\mathbf{1},-\frac{4}{3}\right)$
		d^c_R	$\left(\bar{\mathbf{3}},\mathbf{1},\frac{2}{3}\right)$
Leptons ℓ	$\frac{1}{2}$	$(\nu_e\ e)_L$	$(\mathbf{1},\mathbf{2},-1)$
		e^c_R	$(\mathbf{1},\mathbf{1},2)$
Gauge A	1	g^a Gluon	$(\mathbf{8},\mathbf{1},0)$
		W^a Weak bosons	$(\mathbf{1},\mathbf{3},0)$
		B Hypercharge boson	$(\mathbf{1},\mathbf{1},0)$

Table 3.1: Field content of the Standard Model and their representations under $(\mathrm{SU(3)_C}, \mathrm{SU(2)_L}, \mathrm{U(1)_Y})$. The electric charge Q (in units of electric charge e) is related to the $\mathrm{SU(2)_L}$ isospin eigenvalue I_3 and hypercharge Y by $Q = I_3 + \frac{1}{2}Y$. The c superscript q^c denotes complex conjugation. The quarks and leptons run over 3 generations, while L and R subscripts denote left and right chirality respectively.

Table 3.1 displays the field content of the SM, defined by their representations under the *SM gauge group*: $\mathrm{SU(3)_C} \times \mathrm{SU(2)_L} \times \mathrm{U(1)_Y}$. The three generations of quarks and leptons (Table 2.2) are spinor fields. The bosonic content comprises a scalar Higgs field ϕ and vector fields, namely eight gluons g^a mediating the strong force while four bosons W^a, B govern the electroweak force, where a is the group index. Their dynamics are governed by terms in the action $S = \int \mathrm{d}^4x\, \mathscr{L}_{\mathrm{SM}}$ consistent with global Poincaré symmetry, invariance under the SM gauge group, energetic stability, and renormalisability [75]. Just

six non-trivial classes of terms[1] in the Lagrangian density $\mathscr{L}_{\text{SM}}$ satisfy these conditions:

$$\mathscr{L}_{\text{SM}} = -\frac{1}{4}F^2 + \mathrm{i}\overline{\psi}\gamma \cdot D\psi + |D\phi|^2 + \mu^2\phi^2 + \lambda\phi^4 - y\phi\overline{\psi}\psi. \tag{3.3}$$

Sums over Lorentz, spinor, gauge group and fermion generation indices are suppressed for clarity. We summarise the conceptual features of each term:

- **Yang–Mills** $-\frac{1}{4}F^2$. This term governs the dynamics of the gauge fields $A(x)$, which are adjoint representations of the respective gauge groups. The field strength $F(x)$ is formed by the commutator of the covariant derivatives $D = \partial - \mathrm{i}gA$ by $\mathrm{i}F = [D, D]$, with one dimensionless coupling g for each of the three gauge groups.

- **Dirac** $\mathrm{i}\overline{\psi}\gamma \cdot D\psi$. This term is the kinetic term for the Weyl fields $\psi(x)$ (quarks q and leptons ℓ) and defines their coupling to the gauge fields, as implied by the covariant derivative and representations (Table 3.1). The gamma matrices γ ensure Lorentz invariance of this term, defined by the anticommutator $\{\gamma^\mu, \gamma^\nu\} = 2\eta^{\mu\nu}$, where $\eta^{\mu\nu}$ is the spacetime metric.

- **Higgs sector** $|D\phi|^2 + \mu^2\phi^2 + \lambda\phi^4$. These terms comprise a kinetic term $|D\phi|^2$ for the complex scalar $\phi(x)$. The two potential terms feature the only dimensionful parameter here, μ, which sets the scale of electroweak symmetry breaking, while the dimensionless coupling λ parametrises the quartic term.

- **Yukawa** $y\phi\overline{\psi}\psi$. This term couples quarks and leptons to the Higgs field. The dimensionless couplings y parametrise the fermion masses and flavour mixing angles, namely the Cabbibo–Kobayashi–Maskawa (CKM) matrix in the quark sector.

The experimentally determined parameters are three gauge couplings g, two Higgs potential parameters μ, λ, nine Yukawa couplings for fermion masses (six quarks, three charged leptons), with three angles and one phase of the CKM matrix. Once these are measured at a particular scale, Eq. 3.3 and Tab. 3.1 completely specify the SM. Fig. 3.1 shows the empirical consistency in the theoretical predictions of cross-sections for various SM processes with those measured by ATLAS.

[1] One more non-trivial term actually satisfies these requirements, namely $-\theta F * F$, where $*$ denotes a totally antisymmetric Lorentz contraction and θ is a dimensionless parameter. However, this 'topological term' does not contribute to perturbation theory or collider observables within the scope of this thesis.

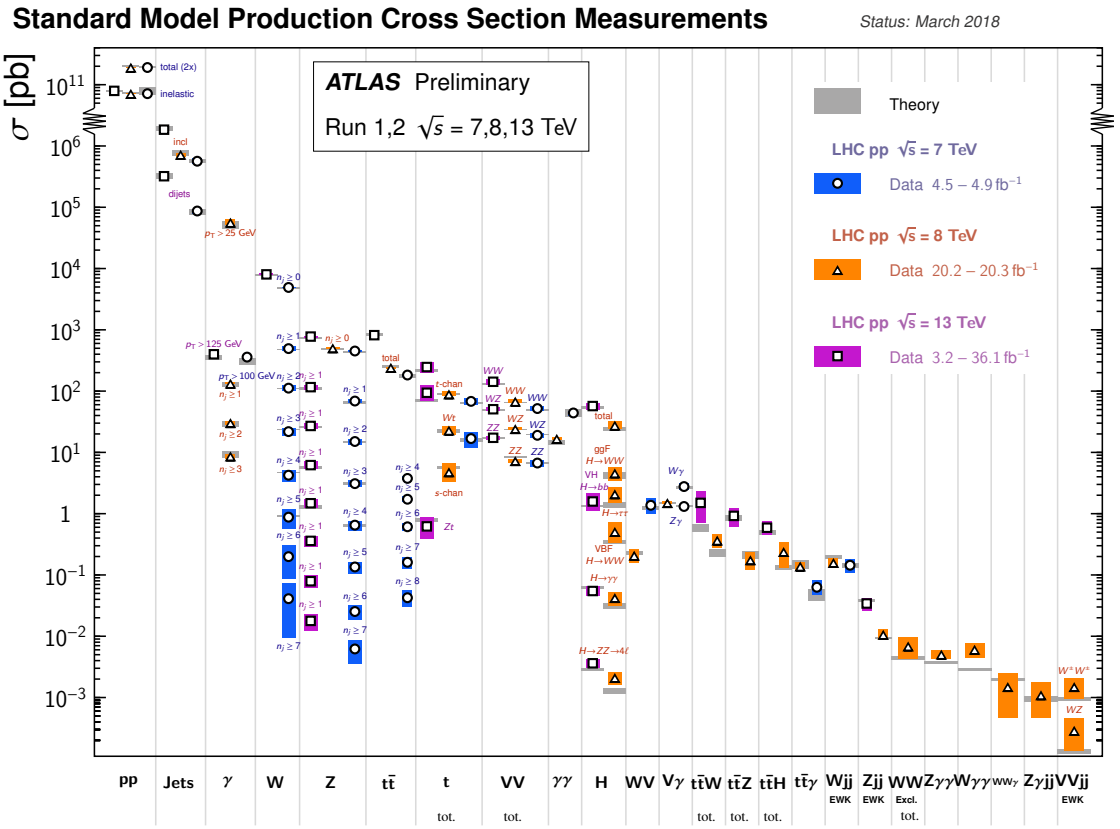

Figure 3.1: Summary of several total and fiducial cross-section measurements by ATLAS and comparisons to their theoretical SM predictions, where fiducial means within the acceptance of the detector volume. The theoretical predictions are calculated at next-to-leading order or higher. Certain processes assume SM branching ratios, namely Higgs boson production. Not all processes have statistically significant observations. Reproduced from Ref. [76].

3.2 Physics beyond the Standard Model

The SM has numerous shortcomings that motivate broad searches for new physics beyond the Standard Model (BSM). We elaborate on the dark matter and hierarchy problems due to their relevance in motivating BSM dynamics near the weak scale studied in this thesis. Other observational motivations include tension in tests of lepton flavour universality [77–80], tension in the muon anomalous magnetic moment [81, 82], the nature of neutrino masses [83, 84], anomalies in short baseline and reactor neutrino experiments [85–87], insufficient CP violation to explain the $\sim 10^{-9}$ matter–antimatter asymmetry [88, 89], absence of strong CP violation motivating axions [90, 91], dark

energy accelerating cosmic expansion [92–98], and new dynamics driving cosmological inflation [99–101]. Meanwhile, unexplained representations of the SM gauge group, relative strength of gauge couplings, chiral structure of weak interactions, tri-generational fermions, and hierarchy of Yukawa couplings all motivate deeper theoretical explanation, such as grand unification [102–104].

3.2.1 Particle dark matter

One of the most startling realisations of contemporary physics is that the SM cannot account for particle dark matter (DM) [105–109]. This is motivated by a multitude of independent astrophysical phenomena. Evidence for the existence and particle nature of DM arises from the gravitational sector, spanning a wide range of scales from galactic to cosmological. At smaller scales, galactic rotation curves [110,111], galaxy cluster motion [112,113], through to weak and strong gravitational lensing [114,115] require additional non-baryonic matter content for empirical consistency. Galaxy cluster collisions, notably the Bullet Cluster [116], and a recently observed galaxy without measurable DM [117] are difficult to reconcile with modifications to gravity alone, further evidencing the particle nature of DM. At intergalactic scales, DM is necessary for simulations of large scale structure formation to be consistent with cosmological surveys [94]. Cosmic microwave background measurements by the WMAP and Planck collaborations [95,96] show DM to be about five times as abundant as SM matter.

Elucidating the identity and elementary properties of DM is one of the most pressing questions in fundamental physics. Astrophysical constraints motivate canonical assumptions about particle DM: candidates interact via gravity, have suppressed electromagnetic interactions, cosmological lifetime, lower thermal dissipation than baryons, small self-interactions, are cold i.e. non-relativistic at early universe decoupling [105].

One favoured class of candidates is the *weakly interacting massive particle* (WIMP). WIMPs χ are thermal relics, assumed to have been in thermal equilibrium with SM states during the early universe. The cosmological relic abundance[2] $\Omega_\chi h^2$ is set by the thermally-averaged self-annihilation $\chi + \chi \to \text{SM} + \text{SM}$ cross-section $\langle \sigma v \rangle$ such

[2]When appearing with the present-day dimensionless energy density parameter Ω, $h = H_0/(100\ \text{km s}^{-1}\ \text{megaparsec}^{-1})$ is the reduced Hubble constant [118] rather than the Higgs boson also denoted by h.

that [119]

$$\Omega_\chi h^2 \simeq \frac{0.1\,\text{pb}}{\langle\sigma v\rangle} \simeq 0.1\left(\frac{0.01}{\alpha}\right)^2\left(\frac{m_\chi}{100\,\text{GeV}}\right)^2. \tag{3.4}$$

If WIMPs have weak scale masses m_χ and couplings α, the observed abundance $\Omega_\chi h^2 \simeq 0.120 \pm 0.001$ [95, 96, 120] is naturally obtained. This use of cosmological arguments to motivate DM near the weak scale provides a key target to search for their production at the LHC. Due to its weak interaction, DM escapes detection in ATLAS. One therefore relies on measurement of other visible objects produced in association with DM to infer its production via excesses in E_T^miss. The class of WIMP DM studied in this thesis is the neutralino $\widetilde{\chi}_1^0$ predicted by supersymmetric theories, which is introduced in Section 3.3.

3.2.2 Mass hierarchies and radiative instability

The hierarchy problem in the Higgs sector [121, 122] is an issue of dynamical stability. To underscore its severity, let us recount the generation of fermion masses in the SM. Upon electroweak symmetry breaking [123–127], the Higgs field gains a vacuum expectation value (vev) $\langle\phi\rangle = \begin{pmatrix} 0 \\ v/\sqrt{2} \end{pmatrix}$, where $v \equiv \sqrt{2\mu^2/\lambda} \simeq 246\,\text{GeV}$. Fluctuations $h(x)$ about v are identified as the Higgs boson with tree-level mass $m_h = \mu$ while fermion masses m_i are proportional to the Yukawa couplings $m_i = y_i v/\sqrt{2}$.

A mass hierarchy exists between the Higgs boson and electron $m_h/m_e \sim 10^6$. While unexplained in the SM, this hierarchy is radiatively stable because small fermion masses are *technically natural* [128]. This means an enhanced symmetry (chiral symmetry for fermions) exists in the limit $m_e \to 0$. Radiative corrections to fermion masses are proportional to the fermion mass itself $\delta m_e \sim m_e \log(m_h/m_e)$.

By contrast, fundamental scalars have no symmetry to protect their masses from radiative instability induced by heavy states e.g. those expected near the Planck scale $M_\text{Pl} \sim 10^{18}$ GeV. Radiative corrections to the Higgs mass parameter μ are quadratically sensitive to ultraviolet scales $\delta\mu \sim M_\text{Pl}^2$, leading to severe dynamical fine-tuning $\sim 10^{30}$. This runs contrary to conventional intuition from effective field theory [129], where ultraviolet physics is decoupled from infrared dynamics e.g. planetary motion is insensitive to molecular fluctuations.

To stabilise this hierarchy, canonical solutions propose novel dynamics near the weak

scale that are accessible to the LHC. Examples include extra spatial dimensions [130,131] or composite Higgs scenarios [132]. This thesis explores the supersymmetric solution, which ties the Higgs mass to that of a new fermion (Higgsino) by supersymmetry. The Higgs–Higgsino supermultiplet is then technically natural due to the chiral symmetry of the fermion [133]. If realised in nature, this solution is complicated by the fact supersymmetry is broken, discussed in the next section. A search for Higgsinos is presented in Chapter 5.

3.3 Weak scale supersymmetry

The previous section detailed two independent arguments—one astrophysical (dark matter), the other field theoretic (radiative instability)—that favour BSM physics near the weak scale. Supersymmetry (SUSY) [134–140] realised near the weak scale would address both issues, while providing a consistent theoretical framework for BSM phenomenology at the LHC. SUSY extends the Poincaré spacetime symmetry with fermionic generators and predicts new states that differ by half a unit of spin from SM particles. The formalism of SUSY is not reviewed but results stated, following Refs. [141, 142].

3.3.1 The minimal supersymmetric Standard Model

This thesis focuses on the *minimal supersymmetric Standard Model* (MSSM) [143–145], which extends the SM to contain two Higgs doublets. These Higgs bosons and their spin $\frac{1}{2}$ partners called Higgsinos $\widetilde{H}$ are embedded in *chiral supermultiplets*. The SM fermions and their spin 0 partners (referred to as sfermions, namely squarks $\tilde{q}$ and sleptons $\tilde{\ell}$) are also embedded in chiral supermultiplets. The SM gauge bosons and their spin $\frac{1}{2}$ partners (referred to as gauginos, namely the bino $\widetilde{B}$, winos $\widetilde{W}$ and gluino $\tilde{g}$) are embedded in *vector supermultiplets*. This field content of the MSSM is displayed in Table 3.2.

A global, multiplicative $\mathbb{Z}_2$ symmetry referred to as *R-parity* [146] is assumed throughout this thesis, with quantum numbers assigned by

$$R \equiv (-1)^{3(B-L)+2S} = \begin{cases} +1 & \text{for Higgs bosons, gauge bosons, fermions,} \\ -1 & \text{for Higgsinos, gauginos, sfermions.} \end{cases} \tag{3.5}$$

Here, S denotes the spin, B and L are the baryon and lepton number respectively. Imposing this symmetry gives phenomenologically favourable features: baryon-number

Chiral supermultiplet	Spin 0	Spin $\frac{1}{2}$	Representation
	Higgs	Higgsinos	
H_u	$\left(H_u^+ \; H_u^0\right)$	$\left(\widetilde{H}_u^+ \; \widetilde{H}_u^0\right)$	$(\mathbf{1},\mathbf{2},1)$
H_d	$\left(H_d^0 \; H_d^-\right)$	$\left(\widetilde{H}_d^0 \; \widetilde{H}_d^-\right)$	$(\mathbf{1},\mathbf{2},-1)$
	Squarks $\tilde{q}$	Quarks q	
Q	$\left(\tilde{u} \; \tilde{d}\right)_L$	$(u \; d)_L$	$\left(\mathbf{3},\mathbf{2},\frac{1}{3}\right)$
U^c	$\tilde{u}_R^c$	u_R^c	$\left(\bar{\mathbf{3}},\mathbf{1},-\frac{4}{3}\right)$
D^c	$\tilde{d}_R^c$	d_R^c	$\left(\bar{\mathbf{3}},\mathbf{1},\frac{2}{3}\right)$
	Sleptons $\tilde{\ell}$	Leptons ℓ	
L	$(\tilde{\nu}_e \; \tilde{e})_L$	$(\nu_e \; e)_L$	$(\mathbf{1},\mathbf{2},-1)$
E^c	$\tilde{e}_R^c$	e_R^c	$(\mathbf{1},\mathbf{1},2)$
Vector supermultiplet	Spin $\frac{1}{2}$	Spin 1	Representation
$\mathscr{G}$	$\widetilde{g}^a$ Gluino	g^a	$(\mathbf{8},\mathbf{1},0)$
$\mathscr{W}$	$\widetilde{W}^a$ Wino	W^a	$(\mathbf{1},\mathbf{3},0)$
$\mathscr{B}$	$\widetilde{B}$ Bino	B	$(\mathbf{1},\mathbf{1},0)$

Table 3.2: Field content of the minimal supersymmetric extension to the Standard Model (MSSM), with notation as that in Table 3.1.

violating interactions such as unobserved proton decay $p \to \pi^0 e^+$ are forbidden, while the lightest supersymmetric particle (LSP) is stable such that neutral massive states are DM candidates. Another consequence is that SUSY states are pair-produced at colliders.

Masses of supersymmetric states If realised near the weak scale, SUSY must be broken for new states to have evaded detection. Specific SUSY breaking mechanisms are discussed in Refs. [141, 142]. The MSSM parametrises the unknown masses using *soft SUSY breaking* terms

$$\begin{aligned}
-\mathscr{L}_{\text{soft}} = {} & m_{H_d}^2 |H_d|^2 + m_{H_u}^2 |H_u|^2 - \mu (H_u \cdot H_d + \text{h.c.}) && \text{Higgs sector} \\
& + m_{\widetilde{Q}}^2 \left|\widetilde{Q}\right|^2 + m_{\widetilde{U}}^2 \left|\widetilde{U}^c\right|^2 + m_{\widetilde{D}}^2 \left|\widetilde{D}^c\right|^2 + m_{\widetilde{L}}^2 \left|\widetilde{L}\right|^2 + m_{\widetilde{E}}^2 \left|\widetilde{E}\right|^2 && \text{sfermion masses} \\
& + \frac{1}{2}\left(M_1 \widetilde{B}\widetilde{B} + M_2 \widetilde{W}\widetilde{W} + M_3 \widetilde{g}\widetilde{g}\right) && \text{gaugino masses} \\
& + \left(y_u A_u \widetilde{Q} \cdot H_u U^c - y_d A_d \widetilde{Q} \cdot H_d D^c - y_e A_e \widetilde{L} \cdot H_d \widetilde{E}^c + \text{h.c.}\right) && \text{trilinear } A \text{ terms.}
\end{aligned} \tag{3.6}$$

Electroweak symmetry breaking occurs when the two Higgs fields obtain a vev $\langle H_u \rangle = v s_\beta$, $\langle H_d \rangle = v c_\beta$, where $v \simeq 174$ GeV and $s_\beta \equiv \sin\beta, c_\beta \equiv \cos\beta$. The resulting

Higgs bosons states are two CP-even neutral states h and H, where $m_h < m_H$, one CP-odd neutral state A, and a charged scalar $H^\pm$.

The scalar partners of the left- and right- handed fermions (denoted $\tilde{f}_L$ and $\tilde{f}_R$ respectively) mix to form mass eigenstates, typically to an extent proportional to the Yukawa coupling. Thus, we refer to the selectron and smuon mass eigenstates by the chirality of their SM partner ($\tilde{\ell}_L, \tilde{\ell}_R$), while significant mixing is expected in the third generation such that the masses of the stau are denoted $\tilde{\tau}_{1,2}$ with $m_{\tilde{\tau}_1} < m_{\tilde{\tau}_2}$. The squark sector also follows this pattern of mixing. Throughout this thesis, no additional CP violation is assumed beyond that of the CKM matrix.

Particularly relevant to this thesis is the mass spectrum of the fermionic partners of the electroweak gauge bosons and Higgs bosons, referred to as electroweakinos. Their mass spectrum is largely controlled by the values of the Higgsino μ, bino M_1, and wino M_2 mass parameters. The neutral bino and wino ($\widetilde{B}, \widetilde{W}^0$) mix with the neutral Higgsinos ($\widetilde{H}_d^0, \widetilde{H}_u^0$) to form four neutralino mass eigenstates $\widetilde{\chi}^0_{i=1,2,3,4}$ (subscripts ordered by increasing mass). Denoting the gauge eigenbasis of 2-component spinors as $\widetilde{\psi}^0 = (\widetilde{B}, \widetilde{W}, \widetilde{H}_d^0, \widetilde{H}_u^0)^{\mathrm{T}}$, the mass Lagrangian takes the Majorana form [147]

$$\mathscr{L}^{\mathrm{mass}}_{\widetilde{\psi}^0} = -\frac{1}{2}\widetilde{\psi}_0^{\mathrm{T}} M_{\widetilde{\psi}^0} \widetilde{\psi}_0 + \mathrm{h.c.}\,, \tag{3.7}$$

where the mass matrix $M_{\widetilde{\psi}^0}$ is parametrised at tree-level by

$$M_{\widetilde{\psi}^0} = \begin{pmatrix} M_1 & 0 & -m_W t_{\theta_W} c_\beta & m_W t_{\theta_W} s_\beta \\ 0 & M_2 & m_W c_\beta & -m_W s_\beta \\ -m_W t_{\theta_W} c_\beta & m_W c_\beta & 0 & -\mu \\ m_W t_{\theta_W} s_\beta & -m_W s_\beta & -\mu & 0 \end{pmatrix}. \tag{3.8}$$

This is diagonalised into the neutralino mass eigenbasis $\widetilde{\chi}_i^0$ by a unitary transformation $\widetilde{\chi}_i^0 = N_{ij}\widetilde{\psi}_j^0$, where N_{ij} are the components of the neutralino mixing matrix, such that $(M_{\widetilde{\chi}^0})_{ij} = m(\widetilde{\chi}_i^0)\delta_{ij}$ are the neutralino mass eigenvalues. These eigenmasses are taken to be real because no additional CP violation is assumed, but can be negative as described in Ref. [147]. The lightest neutralino $\widetilde{\chi}_1^0$ is assumed to be the LSP throughout and is a DM candidate [148, 149]. Similarly, the electrically charged winos $\widetilde{W}^\pm = (\widetilde{W}^1 \pm \mathrm{i}\widetilde{W}^2)/\sqrt{2}$ mix with the charged Higgsinos $\widetilde{H}_u^+, \widetilde{H}_d^-$ to form chargino mass eigenstates $\widetilde{\chi}^\pm_{i=1,2}$, as detailed in Ref. [147].

Guiding principles for mass spectra The MSSM mass spectrum is not uniquely predicted, but various scenarios favour certain mass hierarchies featured in this thesis:

- **Natural SUSY with low fine-tuning**. In the MSSM, the Z boson mass m_Z is related to the Higgsino mass parameter μ and Higgs boson mass m_{H_u} by $-m_Z^2/2 = |\mu|^2 + m_{H_u}^2$ at tree-level [150, 151]. In particular, the masses of the third-generation squarks (stops) and gluino contribute to the value of $m_{H_u}^2$ at one-loop and two-loop, respectively. Naturalness arguments [152, 153] motivate the terms $|\mu|^2 + m_{H_u}^2$ to be near m_Z^2, ensuring low fine-tuning. This suggests that the Higgsinos, stops and gluinos are accessible at the LHC. LHC constraints on gluinos are further discussed in Chapter 4 while a search for Higgsinos is presented in Chapter 5.

- **Split SUSY with high fine-tuning**. Highly fine-tuned scenarios where SUSY is broken far above the weak scale, e.g. the unification scale $M_{\mathrm{U}} \sim 10^{16}$ GeV, are known as split SUSY [154, 155]. Fermions remain near the weak scale, protected by chiral symmetry, which facilitate gauge coupling unification and provide a DM candidate. Meanwhile, all scalars are decoupled near M_{U} except for the observed light Higgs boson. This exemplifies that even highly fine-tuned scenarios can motivate Higgsino dark matter at the weak scale, pursued in Chapter 5.

- **Compressed spectra in DM coannihilation**. DM coannihilation arguments [156, 157] motivate small mass splittings between the DM and next-to-lightest SUSY state, referred to as compressed mass spectra. The relic abundance of bino $\widetilde{\chi}_1^0$ DM is typically larger than that observed by Planck, but can be depleted by a coannihilator C nearby in mass $m_{\widetilde{\chi}_1^0} \simeq m_C$, via $\widetilde{\chi}_1^0 + \mathrm{C} \to \mathrm{SM} + \mathrm{SM}$. Chapter 4 considers gluino or squark coannihilators, while Chapter 5 details scenarios where C is the wino or slepton, together with their LHC search strategy and results.

3.3.2 Simplified models for experimental searches

Direct searches for BSM phenomena involve extracting statistically significant excesses of events above the background prediction in regimes sensitive to production of new particles. Model-agnostic strategies seek, for example, localised peaks above a smoothly falling dijet invariant mass spectrum m_{jj} [158]. However, such inclusive searches may not

have sufficient sensitivity to specific BSM scenarios with richer kinematic correlations, such as gluino decays. Furthermore, mass and spin determination of SUSY states—spectroscopy—is non-trivial due to invisible particles in the final state. Several strategies exist in the literature that can also act as powerful signal discriminants, such as those in Refs. [159–164].

A separate problem is what theoretical framework best facilitates the design of searches. Ideally, search strategies maximise the parameter space they are sensitive to, while facilitating post-discovery model discrimination. *Simplified models* [165–171] were conceived to address this problem as the first step in connecting excesses across numerous search channels to the structure of the underlying theory. A small number of free parameters characterise the most salient kinematic features of new on-shell states X targeted by an experimental search, such as mass, spin, decay tree, and cross-sections of X. Masses of other states are set to kinematically inaccessible values, while decay branching fractions are fixed by hand. Figure 3.2 displays simplified model cross-sections for various processes, showing the hierarchy of strong to electroweak production.

To reduce model-dependence, no explicit requirement is imposed on the structure of the full theory nor the details of SUSY breaking or unification scheme. The key insight advocated by Ref. [166] is that these simplified models can be used even if the structure of the underlying theory were significantly more complex. For example, Figure 3.3a shows a gluino simplified model characterised by two free parameters: $m(\tilde{g})$ and $m(\widetilde{\chi}_1^0)$. For comparison, Figure 3.3b shows the so-called 2-step model that captures the kinematics of longer cascades often found in MSSM scenarios.

The sensitivity of these simplified models for gluino to neutralino DM cascades are typically presented as Figure 3.4a, with exclusion limits reaching 2 TeV for neutralinos near 100 GeV in mass. Similar plots are presented for a stop $\tilde{t}$ to bino DM with sensitivity reaching 1 TeV for weak-scale neutralinos (Figure 3.4b). However, these simplified model limits should only be viewed as benchmarks. Chapter 4 examines how search sensitivity optimised for simplified models maps to more realistic spectra in the so-called phenomenological MSSM with 19 parameters. Searches for electroweak production of SUSY also use simplified models, which are further discussed in Chapter 5.

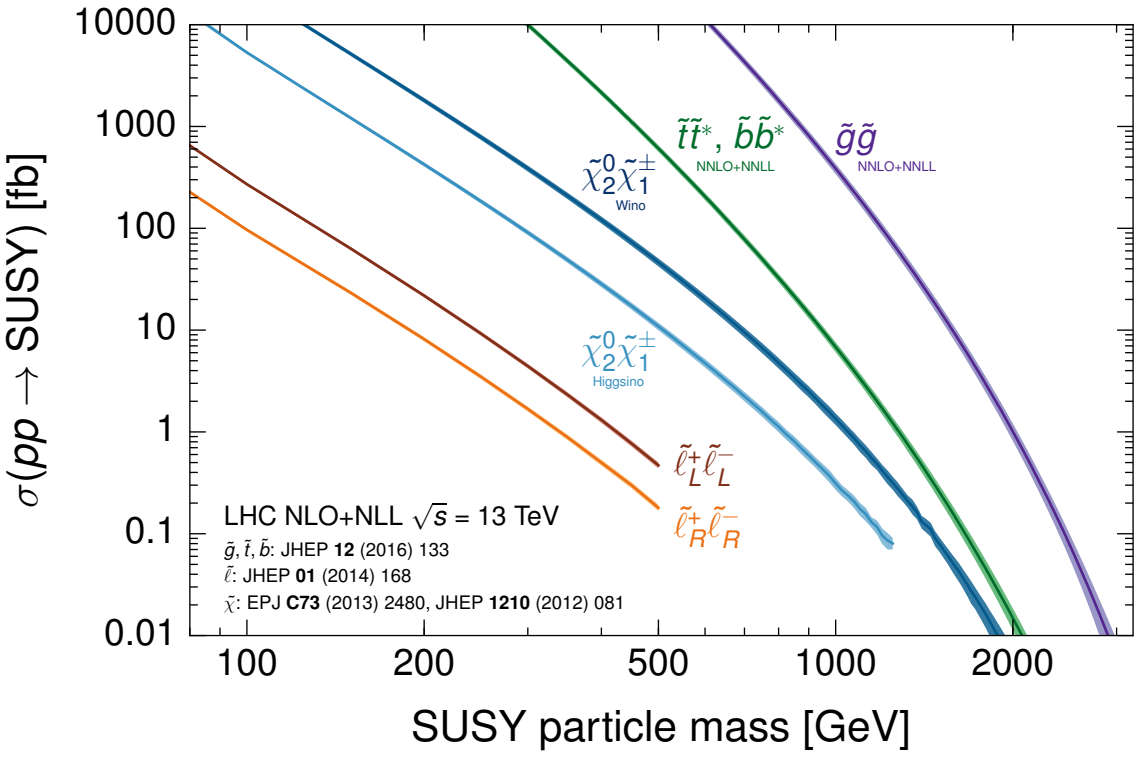

Figure 3.2: Simplified model cross-sections for gluino $\tilde{g}\tilde{g}$, stop/sbottom $\tilde{t}\tilde{t}^*, \tilde{b}\tilde{b}^*$, neutralino–chargino $\tilde{\chi}_2^0\tilde{\chi}_1^\pm$, and slepton $\tilde{\ell}\tilde{\ell}$ production for pp collisions at $\sqrt{s} = 13$ TeV. This plot is made by interpolating values computed in Refs. [172–176]. Neutralino–chargino production is displayed for pure wino and Higgsino scenarios, and sleptons by the chirality for the partner lepton. The width of lines indicates the uncertainty.

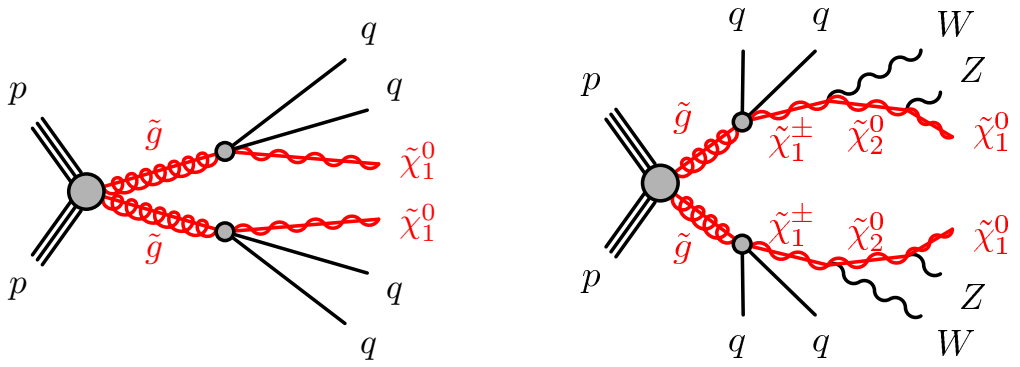

(a) Gluino direct decay to neutralino DM

(b) Gluino '2-step' decay to neutralino DM

Figure 3.3: Example diagrams illustrating simplified models of gluino pair production and example decays. The grey blobs indicate effective couplings mediated by some off-shell state (such as a squark) but the simplified model is agnostic to the structure of this ultraviolet physics. The branching fraction of the $\tilde{g} \to qq\tilde{\chi}_1^0$ direct decay, along with each of the $\tilde{g} \to qq\tilde{\chi}_1^\pm$, $\tilde{\chi}_1^\pm \to W^\pm\tilde{\chi}_2^0$, $\tilde{\chi}_2^0 \to Z\tilde{\chi}_1^0$ decays in the 2-step cascade are set to 100%. Reproduced from Refs. [177, 178].

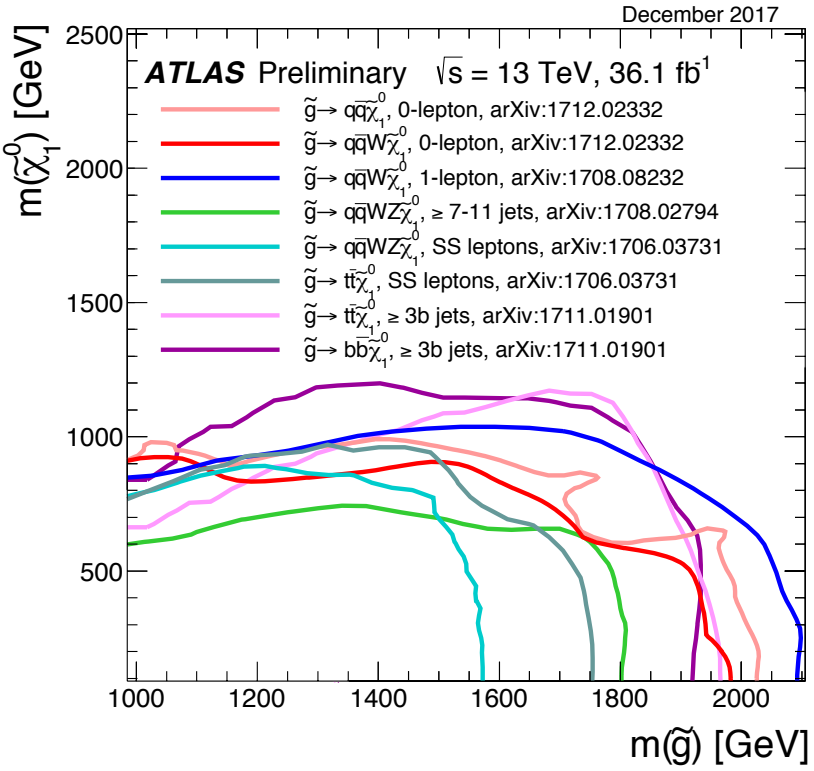

(a) Gluino to neutralino DM searches

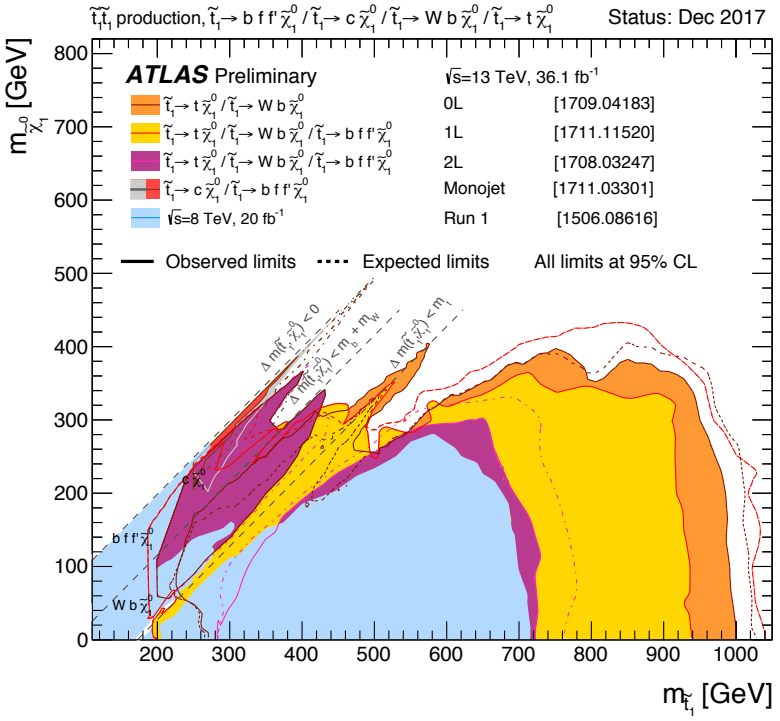

(b) Stop to neutralino DM searches

Figure 3.4: Summary of simplified model interpretations for gluino to DM and stop to DM searches. Regions enclosed by the contours and axes are excluded at 95% confidence level, as of December 2017. Care must be taken when interpreting different limits, as each assumes different decay modes in the simplified model. Reproduced from Ref. [5].

4

Dark matter and strong SUSY searches

In 2015, the LHC commenced Run 2 operations at the new energy frontier of $\sqrt{s} = 13$ TeV, prompting a broad search programme for SUSY [179–199]. These primarily focused on promising scenarios with largest cross-sections, such as strongly interacting states. However, no statistically significant excesses were reported. This chapter explores how the sensitivity of these searches optimised using simplified models map to more complete models, based on work published in the *European Physical Journal C* [1,2]. The theoretical framework of a 19-dimensional phenomenological MSSM (pMSSM) [200–209] is used, which facilitates dark matter interpretations [210–217].

4.1 Overview of issues addressed

The ATLAS Collaboration previously examined the sensitivity of 22 Run 1 analyses within the context of a 19-parameter pMSSM [218], while CMS undertook a similar survey using different assumptions [219]. Our analysis extends such studies by including constraints from six early 13 TeV ATLAS searches based on 3.2 fb^{-1} of integrated luminosity, and reveals previously unexamined correlations in the pMSSM space. These strategies target production of the gluino and light flavour squark sector. We organise our discussion around the following questions that address various limitations in the literature:

1. *How distinct are the regions of parameter space being probed by individual analyses?* Interpretations using the pMSSM often present combined constraints from multiple searches as fractions of models excluded [204, 213, 218–220]. However, this marginalisation obscures which analyses had greatest sensitivity to different parameter subspaces, and also depends on the prior distribution of the parameter scan and non-LHC constraints. Overlap matrices used in the literature [218] to quantify the fraction of points jointly excluded by two analyses also face this issue.

2. *To what extent are analyses over-optimising to a set of simplified models, which may preclude sensitivity to a wider class of scenarios?* The pMSSM offers a greater variety of decay chains, such as those with more intermediate on-shell sparticles, which alter kinematics and branching fractions. How well these simplified model focused searches are capturing the wider classes of signatures remains relatively unexplored.

3. *What neutralino DM scenarios can be probed competitively by 13 TeV collider searches for coloured sparticles?* Simplified dark matter models are stimulating the collider frontier for DM searches [221–231]. ATLAS uses these to perform an explicit DM interpretation for the Monojet search [184]. However, in the richer dark sector of the pMSSM, the Monojet analysis can have substantially different reach, beyond just the electroweakino sector [217, 232–234].

Section 4.3 addresses the first question by directly correlating the most sensitive of the six analyses considered with the masses of the gluino, LSP and lightest squark. We examine the individual searches that provide sensitivity to distinct regions within these mass plane projections. The regions identified are both prior-independent and reveal significantly richer information than the overlap matrices previously used in literature.

Subsection 4.4.2 explores the second question by considering the analyses that select leptonic events as a case study. By mapping simplified models onto pMSSM sensitivity targeted by the 1-lepton analysis [181] and the same-sign or 3-lepton (SS/3L) search [183], we identify scenarios beyond those considered for analysis optimisation.

Section 4.5 examines the third question by ascribing DM interpretations to each 13 TeV search considered, allowing comparisons to the Monojet search and non-collider direct detection experiments [235, 236]. Striking correlations are exhibited, and we discuss how distinct decay cascades are influenced by the bino, Higgsino or wino content of the LSP, together with the coannihilation roles of coloured sparticles.

4.2 Theoretical framework and experimental constraints

This section reviews the assumptions and constraints applied to the pMSSM points considered in this chapter. The points were produced by ATLAS in collaboration with

external expertise [201–204], which we review in 4.2.1; for full details, see Ref. [218]. Section 4.2.2 summarises the method used for exclusion after interpreting six early 13 TeV ATLAS searches, with results summarised in 4.2.3. Finally, 4.2.4 displays the prior distributions after Run 1 constraints before any 13 TeV constraints.

4.2.1 Review of the ATLAS pMSSM19

The 19 parameters of the R-parity conserving MSSM were scanned using flat priors with sparticle mass scales capped at 4 TeV [218]. Starting with this MSSM, minimal flavour violation was imposed and CP violation was restricted to the CKM phase in the quark sector[1] The neutralino was required to be the lightest supersymmetric particle (LSP). Table 4.1 displays the three categories of LSP composition, as defined in Ref. [218]. Due to their different phenomenology, ATLAS employed importance sampling [218] to ensure approximately equal proportions of each LSP type are selected. The relative gauge eigenstate fractions for each of the three categories are displayed in Fig. 4.1.

The resulting model points were subjected to the following non-LHC constraints. Lower mass bounds from LEP [22] were imposed together with precision measurements from the electroweak isospin splitting parameter $\Delta\rho$ [238], $g-2$ of the muon [81,82,239–244], Z boson invisible width [21], branching fractions of heavy flavour states [245–252] and Higgs boson mass [30] at the time of pMSSM points generation were applied [218]. Dark matter constraints were subsequently considered. To account for uncertainties in nuclear form factors, ATLAS quadrupled[2] the upper limit on the spin-independent cross-section for LSP–nucleon interaction from LUX 2013 [253] before applying this to the points. Similar constraints for the spin-dependent cross-section of LSP–proton interactions were applied from COUPP [254], and XENON100 [255] for the LSP–neutron cross-section. The LSP was not assumed to be the sole constituent of dark matter so only an upper limit[3] was set for the LSP relic abundance $\Omega_{\tilde{\chi}_1^0}h^2$, taken as $\Omega_{\text{CDM}}h^2 = 0.1208$, which is the central value plus twice the reported uncertainty from Planck [95].

[1] For investigations of the pMSSM with additional CP violating phases, see Ref. [237].

[2] This factor of four is based on varying low energy input parameters for various benchmark points as discussed in Ref. [201].

[3] An independent study [220] considered ATLAS constraints with up to 14.8 fb^{-1}, but on the subset of points whose neutralino relic abundance was within 10% of Planck. We instead take the Planck measurement as an upper bound, allowing for non-SUSY contributions to DM.

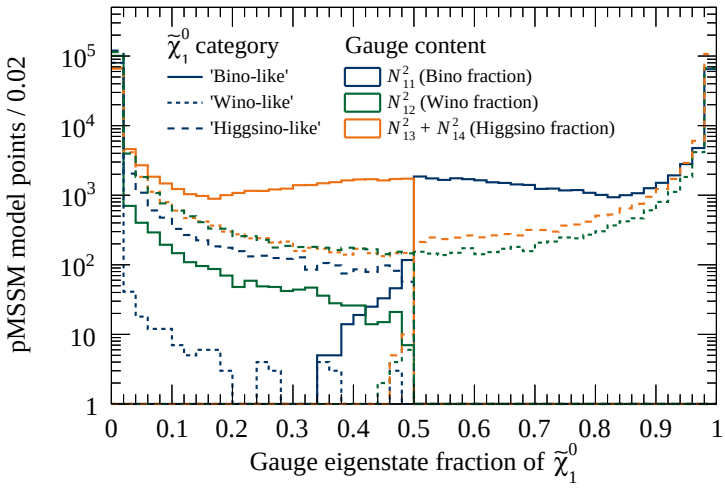

Figure 4.1: Each lightest neutralino $\tilde{\chi}_1^0$ category 'Bino-like' (solid), 'Wino-like' (dotted), 'Higgsino-like' (dashed) defined in Table 4.1, the gauge eigenstate fraction is displayed for N_{11}^2 (Bino fraction), N_{12}^2 (Wino fraction), and $N_{13}^2 + N_{14}^2$ (Higgsino fraction).

The 310.3k pMSSM points surviving all non-LHC constraints underwent evaluation against 22 relevant Run 1 ATLAS searches using Run 1 data; for full details, see Ref. [218]. A total of 40.9% of points were excluded at 95% confidence level, and the numbers that survive by LSP type are displayed in Table 4.2.

LSP type	Definition
Bino-like $\tilde{B}$	$N_{11}^2 > \max\left(N_{12}^2, N_{13}^2 + N_{14}^2\right)$
Wino-like $\tilde{W}$	$N_{12}^2 > \max\left(N_{11}^2, N_{13}^2 + N_{14}^2\right)$
Higgsino-like $\tilde{H}$	$\left(N_{13}^2 + N_{14}^2\right) > \max\left(N_{11}^2, N_{12}^2\right)$

Table 4.1: Definition of neutralino $\tilde{\chi}_1^0$ LSP categories from Ref. [218]. In the neutralino mixing parameter N_{ij}, the first index denotes the neutralino mass eigenstate $\tilde{\chi}_i^0$ while the second indicates its dominant composition in the order $\left(\tilde{B}, \tilde{W}, \tilde{H}_d, \tilde{H}_u\right)$.

4.2.2 Interpretation of early 13 TeV searches

We apply constraints from six 13 TeV ATLAS searches to the 183.8k pMSSM points that survived Run 1. Long-lived squarks, gluinos and sleptons ($c\tau > 1$ mm as defined in Ref. [218]) make up 1.9k of these points. These require dedicated Monte Carlo simulation and are beyond the scope of this chapter. Of the remaining 181.8k points, we use MadGraph5 2.3.3 [256, 257] to calculate the total leading order production

Models	Bino	Wino	Higgsino
Viable after ATLAS Run 1	61.6k	43.8k	78.4k
Without long-lived	59.9k	43.6k	78.3k
Without LL, with $\sigma_{\text{tot}} \geq 5$ fb	48.7k	29.7k	52.8k

Table 4.2: Viable model points before Run 2 constraints. These are classified by the dominant contribution to the LSP being bino, wino or Higgsino. Long-lived (LL) gluinos, squarks and sleptons with $c\tau > 1$ mm require dedicated Monte-Carlo simulation and are omitted from this study. Event simulation was performed on non-LL models with total strong sparticle production cross-section $\sigma_{\text{tot}} \geq 5$ fb.

cross-section for any pair of coloured sparticles σ_{tot}. As indicated at the bottom of Table 4.2, 28.6% of the points had cross-section below 5 fb and are deemed not to have sensitivity with 3.2 fb^{-1} of luminosity. The remaining 71.4% underwent event simulation for evaluation of sensitivity as follows.

We use MADGRAPH5 for event generation involving production of any two coloured sparticles, interfaced with PYTHIA 6.428 [258] for hadronisation and showering, using the CTEQ6L parton distribution functions [259]. Up to one additional parton in the matrix element and the MLM prescription [260] is used to match jets, setting the MADGRAPH minimum parton k_T parameter to 100 GeV and PYTHIA jet measure cutoff at 120 GeV, in accord with Ref. [218]. The DELPHES 3.3.2 [261] fast detector simulator was employed with FASTJET 3.1.3 [262, 263], using the anti-k_T clustering algorithm with cone parameter $R = 0.4$, to parametrise the performance of the ATLAS detector.

We implement the six analyses in Table 4.3 using MADANALYSIS5 1.3 [264, 265], for which an overview is given below. We adapt codes from the Public Analysis Database [266–268] where available, and authored our own otherwise. The RECASTINGTOOLS package was used for limit setting using the CLs prescription [269], where a point is deemed excluded if the CLs value is below 0.05. To validate our code, we ensured at least one benchmark point had signal rates after each kinematic requirement (cutflows) agreeing to better than 30% and reproduced the simplified model limits to within the uncertainties published by ATLAS (see Refs. [1, 2] for further details).

Overview of analyses implemented We now summarise the key features of the analyses listed in Table 4.3. For full details of the event selection, see the references in Table 4.3.

Analysis	Reference	$N_{\text{Lowest CLs}}/N^{\text{Excluded}}_{\text{13 TeV 3.2 fb}^{-1}}$	$N^{\text{Excluded}}_{\text{13 TeV 3.2 fb}^{-1}}/N^{\text{Survived}}_{\text{ATLAS Run 1}}$	$N^{\text{Excluded Uniquely}}_{\text{13 TeV 3.2 fb}^{-1}}/N^{\text{Survived}}_{\text{ATLAS Run 1}}$
2–6 jets	[179]	72%	12.6%	11%
7–10 jets	[180]	0.3%	0.6%	0.02%
1-lepton	[181]	1.5%	1.0%	0.2%
Multi-b	[182]	23%	4.2%	3.5%
SS/3L	[183]	2.7%	0.5%	0.4%
Monojet	[184]	1.1%	3.3%	0.01%
All analyses	–	100%	15.7%	15.1%

Table 4.3: Searches used to constrain the 181.8k model points surviving Run 1. The column $N_{\text{Lowest CLs}}/N^{\text{Excluded}}_{\text{13 TeV 3.2 fb}^{-1}}$ denotes the fraction of the 28.5k excluded models for which the analysis is most sensitive, i.e. had the lowest CLs value $N_{\text{Lowest CLs}}$ (Section 4.3.1); these figures may not sum to 100% due to rounding. The column $N^{\text{Excluded}}_{\text{13 TeV 3.2 fb}^{-1}}/\text{N}^{\text{Survived}}_{\text{ATLAS Run 1}}$ is the fraction of points excluded by each analysis $N^{\text{Excluded}}_{\text{13 TeV 3.2 fb}^{-1}}$ divided by those surviving Run 1 $N^{\text{Survived}}_{\text{ATLAS Run 1}}$. The right-most column quantifies the subset of points uniquely excluded by each analysis and not by the other five considered $N^{\text{Excluded Uniquely}}_{\text{13 TeV 3.2 fb}^{-1}}$. Models with long-lived gluinos, squarks and sleptons are not considered.

2–6 jets [179]. This analysis requires $E_{\text{T}}^{\text{miss}} > 200$ GeV and varied minimum jet multiplicities $N_{\text{jets}}^{\text{min}}$ from 2 to 6, which target a range of squark and gluino decays. A key discriminating variable is the effective mass $m_{\text{eff}} = \sum_{\text{jets}} p_{\text{T}} + E_{\text{T}}^{\text{miss}}$, where minimum requirements range from 1200 GeV to 2200 GeV, which provides a proxy for the high mass scales of the produced SUSY signals. A lepton veto suppresses W boson backgrounds.

7–10 jets [180]. Requiring no leptons, $N_{\text{jets}}^{\text{min}}$ of 7 to 10 allows this analysis to probe hadronic decays of long decay cascades of gluinos. No explicit $E_{\text{T}}^{\text{miss}}$ selection is made, instead a $E_{\text{T}}^{\text{miss}}/\sqrt{H_{\text{T}}} > 4$ GeV$^{1/2}$ requirement suppresses the SM multijet background.

1-lepton [181]. Exactly 1 isolated electron or muon is required along with large $E_{\text{T}}^{\text{miss}}$ of at least 200 GeV. One class of signal regions requires soft leptons where $p_{\text{T}}(e/\mu) > 7/6$ to 35 GeV to target compressed mass spectra, while a second class requires hard leptons $p_{\text{T}}^{\ell} > 35$ GeV to target cascades with large mass splittings.

Multi-b [182]. Targeting scenarios where gluinos decay to multiple top $\tilde{g} \to t\bar{t}\tilde{\chi}_1^0$ or bottom quarks $\tilde{g} \to b\bar{b}\tilde{\chi}_1^0$, events are required to have large $E_{\text{T}}^{\text{miss}}$ and at least 3 b-tagged jets. The regions selecting signals enriched in top quarks are categorised by 0-lepton and 1-lepton categories.

SS/3L [183]. The SS/3L search targets gluino production decaying via cascades that result in multiple isolated electrons or muons. Events are required to have at least two

leptons, and if there are exactly two, they must have the same electric charge. Modest $E_{\mathrm{T}}^{\mathrm{miss}}$ is imposed, whose minimum ranges from 125 to 200 GeV.

Monojet [184]. This selects events with an energetic jet $p_{\mathrm{T}} > 250$ GeV, large $E_{\mathrm{T}}^{\mathrm{miss}} > 250$ GeV, up to three additional jets, and a lepton veto. This probes signals in which the energetic jet originates from initial state radiation, probing compressed mass spectra where no final state particles are reconstructed.

4.2.3 Summary of sparticle masses excluded by early 13 TeV searches

	2–6 jets	7–10 jets	1-lepton	Multi-b	SS/3L	Monojet
2–6 jets	100%	3%	5%	13%	0%	10%
7–10 jets	76%	100%	59%	91%	4%	6%
1-lepton	65%	34%	100%	55%	8%	7%
Multi-b	39%	12%	13%	100%	1%	1%
SS/3L	10%	5%	17%	6%	100%	3%
Monojet	99%	3%	6%	5%	1%	100%

Table 4.4: Exclusion overlap: percentage of models excluded by a Run 2 analysis on each row that is also excluded by another in the columns. 100% is reserved for complete overlap of models excluded.

Overall, the six 13 TeV searches considered excluded 15.7% of the 181.8k pMSSM points that survived Run 1. Figure 4.2 displays the fraction of these points surviving Run 1. These are projected into the 2-dimensional planes in the masses of the gluino $\tilde{g}$, $\tilde{\chi}_1^0$ and lightest light flavour squark $\tilde{q}$. For gluinos $\tilde{g}$, the new sensitivity from increasing centre-of-mass energy to 13 TeV is unambiguous, even with an order of magnitude less luminosity than 8 TeV searches. The sensitivity reduces when gluino–LSP mass splitting are less than 200 GeV, as the emitted jets have softer momentum spectra and do not pass the analysis requirements. Overall, good corroboration with the simplified models is observed.

Meanwhile, the lightest squark $\tilde{q}$ shows a smaller but noticeable extension of sensitivity beyond Run 1. This is due to the less advantageous scaling of cross-sections between 8 and 13 TeV compared with gluino production from LHC parton distribution functions. Note that the simplified model limit of Figure 4.2 assumes all eight squarks of the first two generations are mass-degenerate, leading to optimistic exclusion.

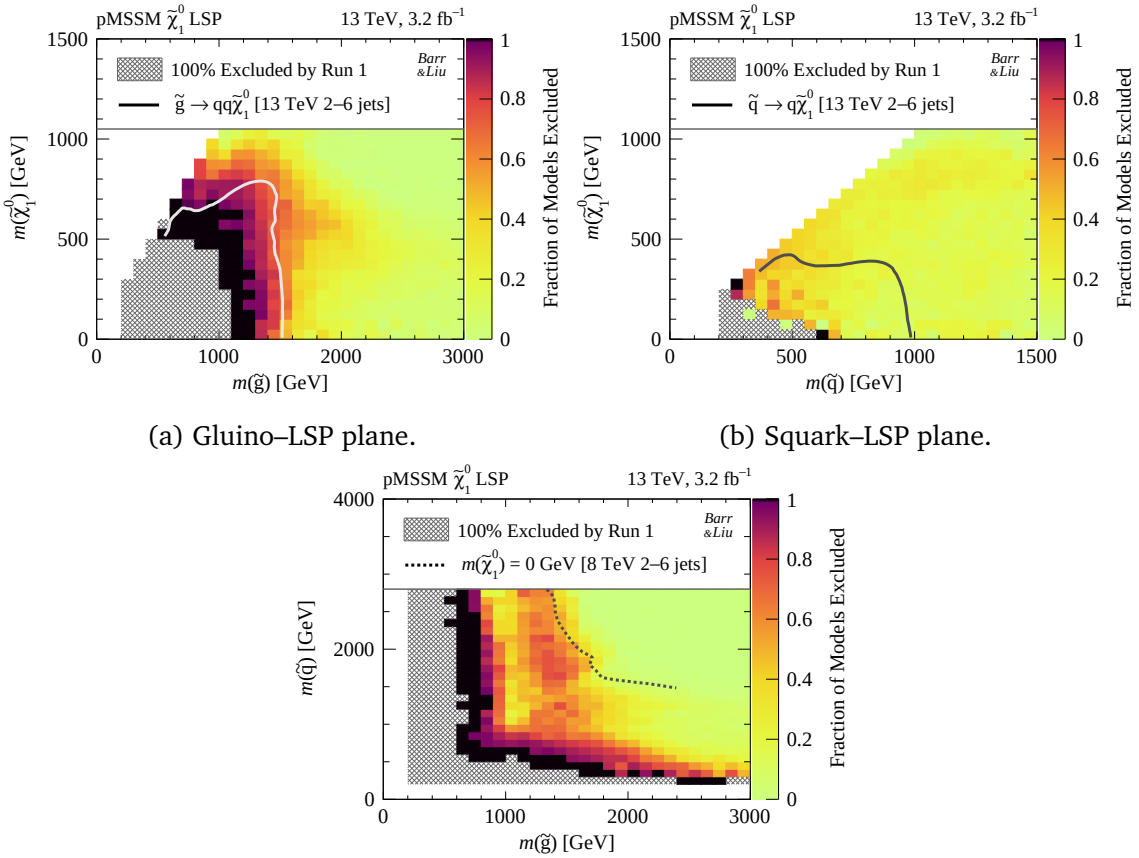

(a) Gluino–LSP plane.

(b) Squark–LSP plane.

(c) Gluino–squark plane.

Figure 4.2: Fraction of points excluded by the six early 13 TeV searches considered in Table 4.3, out of the points that survived Run 1 constraints. The colour scale denotes the per bin fraction of points excluded at 95% CL divided by the number of points satisfying 'Without long-lived' in Table 4.2, where black indicates 100% exclusion. Here, $\tilde{q}$ is the lightest squark among the first two generations. White regions show no points being produced while hatched grey indicates all points being excluded by Run 1 [218]. Overlayed grey solid lines are the simplified model limits from the 13 TeV 2–6 jets search [179] for (a) gluinos $\tilde{g} \to qq\tilde{\chi}_1^0$; for (b) squarks $\tilde{q} \to q\tilde{\chi}_1^0$ (upper right), all eight squarks are assumed to be mass-degenerate. For (c) gluino–squark plane, the overlayed grey dashed line is taken from the 'gluino–squark–LSP simplified pMSSM' scenario from the 8 TeV 2–6 jets search [193].

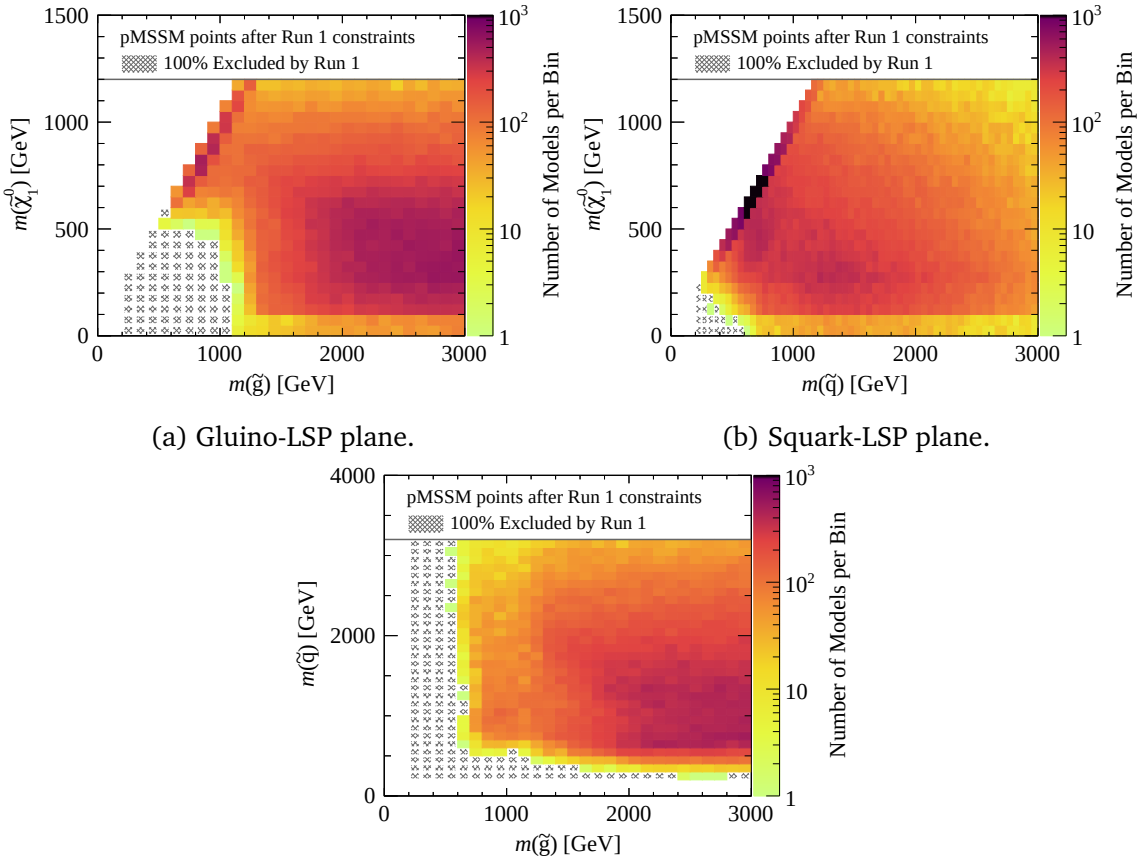

(a) Gluino-LSP plane.

(b) Squark-LSP plane.

(c) Gluino-squark plane.

Figure 4.3: Number of points surviving Run 1 but before Run 2 constraints applied. White regions indicate no points, while grey hatched show 100% exclusion by Run 1 [218]. The colour scale has a maximum of 1000 models per bin, indicated by black. Models with long-lived gluinos, squarks or sleptons are not considered.

Table 4.4 shows the overlap matrix between the six searches we considered. This quantifies the fraction of points excluded by one analysis are also excluded by another. For example, of the points excluded by the 7–10 jets search, 76% of them were also excluded by the 2–6 jets analysis. Overall, the sensitivity is complementary, with no analysis completely excluding the points probed by another search.

4.2.4 Distributions prior to 13 TeV interpretation

To aid interpreting Figures 4.2, the prior distributions of the 181.8k points before 13 TeV constraints are displayed in Figure 4.3. The density of points along the diagonal with small $\Delta m(\tilde{q} \text{ or } \tilde{g}, \tilde{\chi}_1^0) \lesssim 50$ GeV were enhanced by importance sampling used by

ATLAS [218] to preferentially select bino LSP scenarios that satisfy relic density bounds via coannihilation with the squark or gluino.

Further, the region $m(\tilde{\chi}_1^0) \lesssim 100$ GeV has substantially fewer models and are also mainly bino-like LSP models. These correspond to where the dark matter abundance is reduced by resonant annihilation through a Z or h^0 boson in so-called 'funnel' mechanisms. Models with Higgsino- or wino-like $\tilde{\chi}_1^0$ have near-degenerate charginos $\tilde{\chi}_1^\pm$ which are constrained by LEP bounds, hence reducing the density of these class of models here. There are also very few (less than 10) models in the mass bins coloured green close to the region where 100% of models were excluded in Run 1.

4.3 Complementarity between early 13 TeV searches

This section presents the distinct regions of sensitivity for each analysis. Section 4.2.3 presents results using existing practices in the literature, based on fractions of models excluded (marginalised distributions) and overlap matrices. This section addresses their limitations as discussed in the Introduction. Subsection 4.3.1 defines the 'most sensitive analysis' before Subsection 4.3.2 projects this information into 2-dimensional subspaces of the pMSSM involving gluinos, squarks and the neutralino dark matter. Finally, we examine the complementary sensitivity of each analysis to distinct regions of parameter space in Subsection 4.4, partitioning our discussion between analyses that veto events with leptons from those that select them.

Henceforth in this chapter, 'squark' $\tilde{q}$ refers to only the lightest superpartner of the left- or right-handed quark of the first or second generations $\tilde{q} \in \{\tilde{u}, \tilde{d}, \tilde{c}, \tilde{s}\}_{L,R}$. Similarly, 'slepton' $\tilde{\ell}$ refers to the lightest superpartner of the left- or right-handed lepton of the first or second generation $\tilde{\ell} \in \{\tilde{e}_L, \tilde{\nu}_{eL}, \tilde{\mu}_L, \tilde{\nu}_{\mu L}, \tilde{e}_R, \tilde{\mu}_R\}$.

4.3.1 Most sensitive analyses used for exclusion

In this study, a point is deemed excluded at 95% confidence level if at least one analysis returned a CLs value less than 0.05. Of the 181.8k points surviving Run 1 [218], a total of $N^{\text{Excluded}}_{\text{13 TeV 3.2 fb}^{-1}} = 28.5$k are excluded by the six 13 TeV searches. We deem the analysis with the smallest CLs value as the 'most sensitive analysis' used to exclude the point. In Table 4.3, we normalise the number of points satisfying this for each analysis $N_{\text{Lowest CLs}}$

to the total excluded $N^{\text{Excluded}}_{\text{13 TeV 3.2 fb}^{-1}}$. For example, the Multi-b search was the analysis with the lowest CLs value for 23% of the 28.5k excluded points. Indeed, almost 95% of the excluded points have either the 2–6 jets or Multi-b searches being the most sensitive. Care should be taken when interpreting these fractions, as they are prior dependent and correlated with non-LHC constraints.

Less than 4% of the excluded points have two or more analyses associated with the same smallest CLs value. In such cases, the 'most sensitive analysis' is randomly chosen from this subset of analyses with smallest CLs value to minimise systematic selection bias. The majority of these cases occurs from analyses sharing a CLs value of 0.0.

Also displayed in Table 4.3 is the total number of excluded points by each analysis $N^{\text{Excluded}}_{\text{13 TeV 3.2 fb}^{-1}}$ out of those that survived Run 1 $N^{\text{Survived}}_{\text{ATLAS Run 1}}$. The overlap between analyses is quantified in Table 4.4. Importantly in Table 4.3, all analyses retain non-zero percentages in the total fraction of points uniquely excluded by each analysis and none of the other five $N^{\text{Excluded Uniquely}}_{\text{13 TeV 3.2 fb}^{-1}}$. This underscores the importance of a broad programme of searches. While most of the searches optimise for gluino production, and some have dedicated signal regions for squarks, each search maintains unique sensitivity to particular classes of signatures within the MSSM, featuring distinct final states and kinematic regimes.

We note that at the time this work was completed, no 13 TeV searches for electroweak production of SUSY states were public, as their small production cross-sections require greater luminosity than 3.2 fb^{-1} for sensitivity beyond Run 1. Nonetheless, from the Run 1 study [218], we expect these to play an important role in constraining scenarios with light electroweakinos and sleptons where gluinos and squarks are beyond LHC reach.

4.3.2 Features in mass plane projections

The distinct regions of sensitivity for each of the six searches become unambiguous when we project into various two-dimensional subspaces of the pMSSM. Figures 4.4 and 4.6 display each excluded point styled and coloured according to the analysis that returned the lowest CLs value, projected into the mass planes of gluino vs LSP, gluino vs squark and squark vs LSP respectively. Due to their large numbers, the 2–6 jets and Multi-b analyses are allocated smaller markers to improve clarity of other points.

Before discussing the sensitivity of each analysis in turn (Section 4.4), we note that

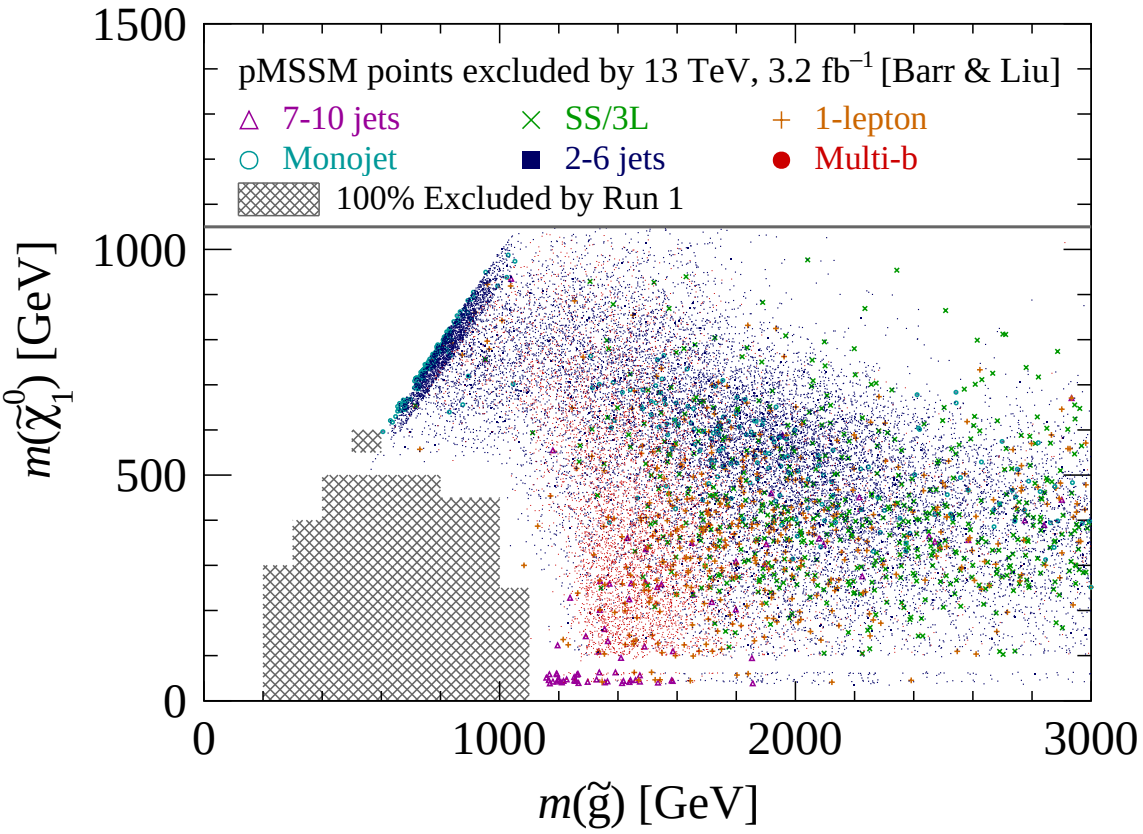

Figure 4.4: Most sensitive analysis for the 28.5k points excluded at 95% CL by the six searches in Table 4.3. Here, $\tilde{q}$ denotes the lightest squark of the first or second generations. Markers are styled according to the analysis with the lowest CLs value: 7–10 jets (magenta triangle), 1-lepton (orange plus), SS/3L (green cross), Monojet (cyan ring), 2–6 jets (blue filled square), and Multi-b (red filled circle). Markers for 2–6 jets and Multi-b are smaller for clarity. Hatched grey regions indicate mass bins with all model points excluded by Run 1 searches [218]. Models with long-lived gluinos, squarks or sleptons are not considered.

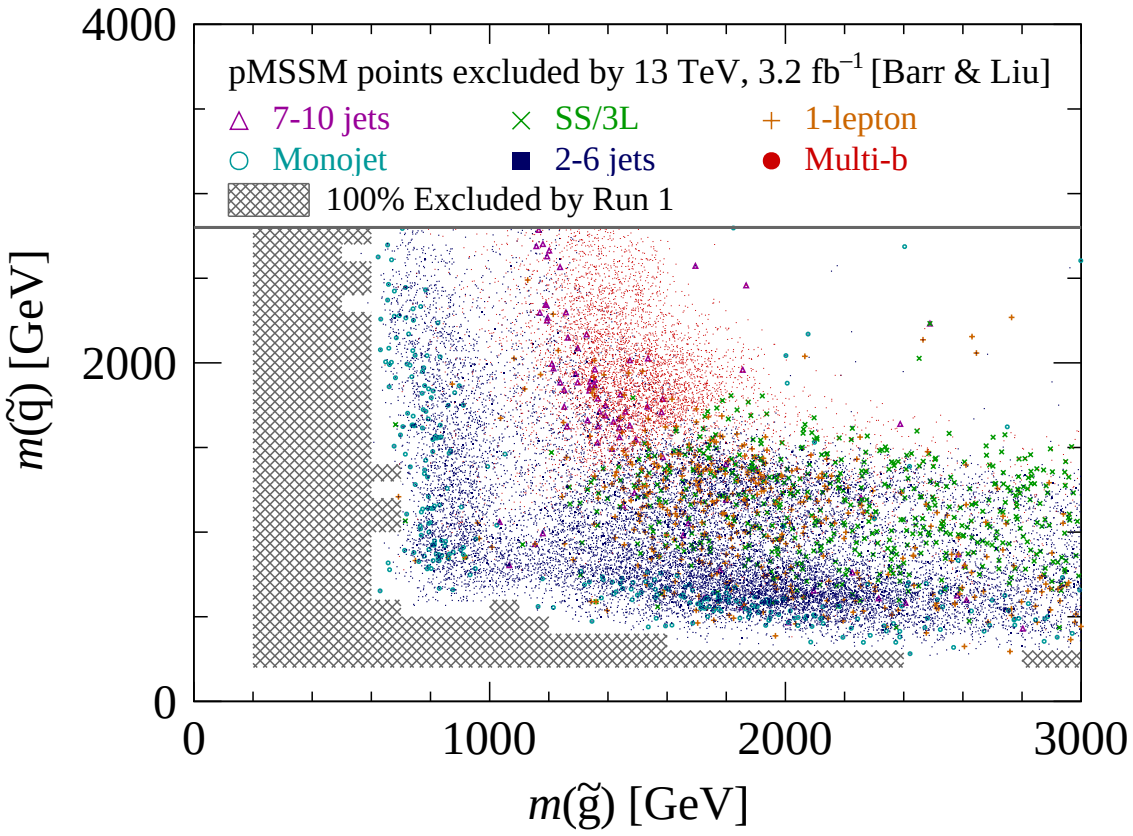

Figure 4.5: Same plot as Figure 4.4 but projected into the squark–LSP plane Here, $\tilde{q}$ denotes the lightest squark of the first or second generations.

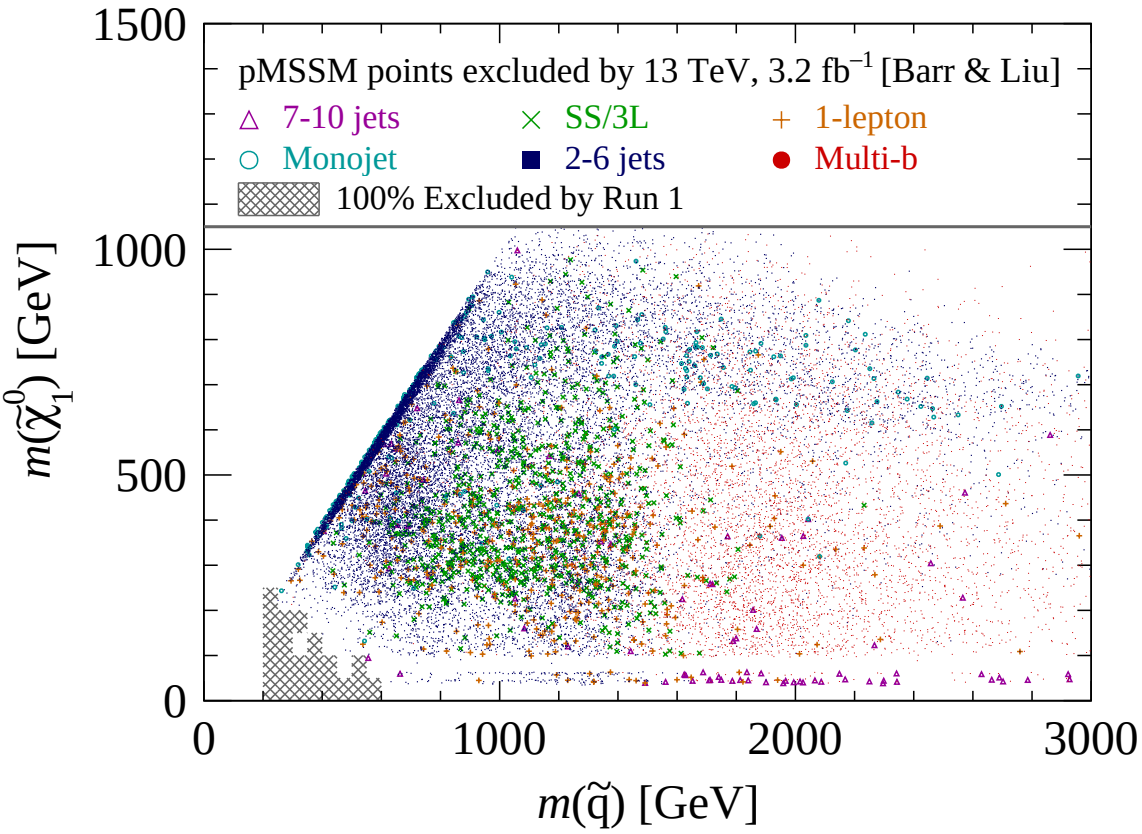

Figure 4.6: Same plot as Figure 4.4 but projected into the squark–LSP plane.

the two-dimensional *distributions* (but not the *regions* to be discussed in Sections 4.4 and 4.5.1) of excluded points do depend on the prior distributions due to sampling effects in addition to non-LHC constraints. This is especially apparent in the mass planes involving $m(\tilde{\chi}_1^0)$ (Figures 4.4 and 4.6), and we comment on features to aid interpretation:

- Within around 100 GeV of the grey hatched regions, very few points are present. The number of models close to this boundary is often less than ten (Figure 4.3), which correspond to those that marginally survived Run 1 constraints.
- There is a visible break in points at $m(\tilde{\chi}_1^0) \sim 100$ GeV. Below this mass, there are few models with Higgsino- or wino-like $\tilde{\chi}_1^0$ as these have a near-degenerate chargino, which are excluded by LEP searches.
- Points below $m(\tilde{\chi}_1^0) \sim 100$ GeV have predominantly bino-like $\tilde{\chi}_1^0$. These bino states lie in funnel regions, close to half the mass of the Z or Higgs boson h to enable resonant annihilation and satisfy dark matter abundance constraints.
- A large density of points is visible along the diagonals for $\Delta m(\tilde{g} \text{ or } \tilde{q}, \tilde{\chi}_1^0) \lesssim 50$ GeV and is an artefact of importance sampling used to ensure the number of bino-like LSP models is similar to that of the other types [218], as mentioned in Section 4.2.4.

4.4 Mass plane correlations of searches for squarks and gluinos

This subsection examines the parameter space where each analysis has most sensitivity, discussing those with and without a lepton veto.

4.4.1 Searches with a lepton veto

First, we investigate the excluded points where each of the 2–6 jets, Multi-b, 7–10 jets, and Monojet searches are most sensitive. These analyses all veto leptons, and exhibit the most unambiguous correlations in the mass planes of the gluino, squark and LSP (Figures 4.4 and 4.6).

2–6 jets Figure 4.4 reveals the points in the gluino–LSP plane where the 2–6 jets is the most sensitive analysis (blue points). The 2–6 jets search uses the effective mass

m_{eff} discriminant, with varying degrees of minimum jet multiplicity to target squark or gluino production directly decaying to the LSP. The larger jet multiplicity regions target scenarios where a chargino mediates the decay of the gluino to the LSP.

This analysis has almost unique sensitivity to points with gluino $\tilde{g}$ masses below 1 TeV for $25 \lesssim m(\tilde{g}, \tilde{\chi}_1^0) \lesssim 500$ GeV. Larger mass splitting scenarios for sub-TeV mass gluinos are excluded by Run 1 searches (hatched grey mass regions). For regions with gluinos above 1 TeV and large gluino–LSP mass splittings, we find the 2–6 jets has reduced sensitivity compared with other analyses, especially for $m(\tilde{\chi}_1^0) \lesssim 500$ GeV. For masses $m(\tilde{g}) \gtrsim 2$ TeV, we expect reduced sensitivity to gluino production, but points in this region are correlated with excluded points involving low mass squarks. This is confirmed by comparing with the gluino–squark plane (Figure 4.5). Indeed, the 2–6 jets search is also predominantly the most sensitive analysis for light squarks in regions not far beyond Run 1 sensitivity. High mass gluinos in such scenarios can nevertheless contribute to production cross-sections of the squarks as a mediator via t-channel diagrams.

The gluino–squark plane (Figure 4.5) also reveals a vertical strip with a lower density of points around gluino mass between about 1 TeV and 1.2 TeV. This corresponds to a region where a lower fraction of models is excluded per mass interval (see also Figures 4.2c and 4.3c in 4.2). This reduced sensitivity corresponds to smaller gluino–LSP splittings between around 25 and 200 GeV. Such scenarios are challenging for traditional 'missing energy plus jets' searches due to reduced acceptance of lower momentum final states, where novel techniques may bring improved sensitivity [270].

In the squark–LSP plane (Figure 4.6), the 2–6 jets search has sensitivity to a wide variety of squark mass scenarios, gradually reducing above $m(\tilde{q}) \sim 1$ TeV. The strip of blue points for $m(\tilde{q}) \gtrsim 1.5$ TeV and $600 \lesssim m\left(\tilde{\chi}_1^0\right) \lesssim 900$ GeV where we would expect reduced squark sensitivity are correlated with low mass gluinos. These points largely have sub-TeV gluinos, as seen in the squark–gluino plane (Figure 4.5).

Multi-b The Multi-b analysis (red points) is most sensitive in a more localised region complementary to the 2–6 jets analysis. In the gluino–LSP plane (Figure 4.4), the region is enclosed by gluino masses of $1.2 \lesssim m(\tilde{g}) \lesssim 1.7$ TeV and LSP masses of $100 \lesssim m\left(\tilde{\chi}_1^0\right) \lesssim 500$ GeV. This sensitivity also extends to smaller gluino–LSP mass

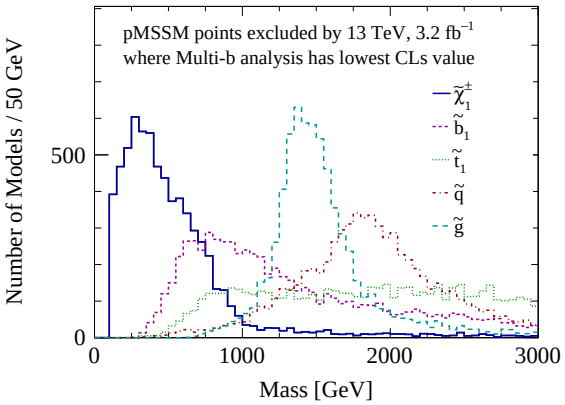

Figure 4.7: Distribution of sparticle masses for the excluded points where the Multi-b analysis is most sensitive. The lines correspond to the chargino $\tilde{\chi}_1^{\pm}$ (blue solid), lightest sbottom $\tilde{b}_1$ (magenta short-dashed), lightest stop $\tilde{t}_1$ (green dotted), lightest squark $\tilde{q}$ (red dot-dashed) and gluino $\tilde{g}$ (light-blue long-dashed).

splittings, though to a lesser extent.

The distinctiveness of this region of sensitivity remains in the gluino–squark plane (Figure 4.5). Here, points where the Multi-b analysis is most sensitive are correlated with squarks of the 1st or 2nd generation having masses above 1.5 TeV, largely unprobed by other analyses, being strikingly separated from 2–6 jets and to some extent the 7–10 jets analysis. Figure 4.6 also confirms such correlations of the Multi-b in the squark–LSP plane. These correlations arise from the Multi-b search targeting $\tilde{g} \to b\bar{b}\tilde{\chi}_1^0$ and $\tilde{g} \to t\bar{t}\tilde{\chi}_1^0$ scenarios.

Figure 4.7 takes the points where the Multi-b is most sensitive and illuminates the mass distributions of various pertinent sparticles. The light flavour squarks $\tilde{q}$ are centred around 2 TeV with gluinos around 1.4 TeV, where Figure 4.5 indicates that squarks are predominantly heavier than gluinos. This fact suppresses gluino decays to light flavour quarks (1st and 2nd generations), which proceed via the three body $\tilde{g} \to q\bar{q}\tilde{\chi}_1^0$ process. By contrast, the mass distribution of sbottoms $\tilde{b}_1$ peaks around 800 GeV in Figure 4.7 and have a preference to be lighter than the gluinos, allowing on-shell $\tilde{g} \to \tilde{b}b$ decays to be favoured. Meanwhile, the distribution of stop masses is relatively uniform for $m(\tilde{t}_1) \gtrsim 900$ GeV. The requirement of three or more jets originating from bottom quarks therefore favours such scenarios. We furthermore note that out of the models excluded where the Multi-b is most sensitive, 56% models have a Higgsino-like LSP

while 22% are wino-like, which have light charginos consistent with the corresponding mass distribution in Figure 4.7. This preference of the Multi-b analysis for Higgsino-like LSP models can be understood by the higher Yukawa couplings to heavy flavour quarks, which also enhance decays of the gluino to bottom and/or top quarks.

From the region in Figure 4.5 where the density of red points is greatest, we show a representative point with model number 148229034 (Figure 4.8a). This contains an LSP with a bino–Higgsino mixture at a mass of 175 GeV, a relatively low mass 1.2 TeV gluino and a 1.3 TeV sbottom enabling $\tilde{g} \to b\bar{b}\tilde{\chi}_1^0$ branching ratios to be preferred.

We note that with recent 13 TeV searches for direct stop and sbottom production are not considered at the time of publication likely have sensitivity to these scenarios. These typically search for fewer jets, and have dedicated optimisation to third generation quarks, allowing greater sensitivity than the inclusive searches considered in this chapter. Detailed evaluation of this will be interesting, but is deferred for future work.

7–10 jets The concentration of magenta triangles in Figure 4.4 shows that the 7–10 jets search is the most sensitive analysis when $\Delta m(\tilde{g}, \tilde{\chi}_1^0)$ is large. Most of these LSPs have masses below 100 GeV, which are bino-like as discussed in Section 4.3.2, and undergo early universe annihilation via the Z or h 'funnels'. Since this annihilation mechanism requires Higgsino or wino admixtures to proceed, such scenarios typically have light charginos $\tilde{\chi}_1^\pm$ and next-to-lightest neutralinos $\tilde{\chi}_2^0$ nearby.

These types of decays are consistent with the simplified models containing long decay chains that this analysis optimises for. The observed missing transverse energy $E_{\mathrm{T}}^{\mathrm{miss}}$ therefore tends to be smaller than that required by the 2–6 jets or Multi-b searches. Indeed no explicit requirement on $E_{\mathrm{T}}^{\mathrm{miss}}$ is made by the search (instead the main discriminant is a ratio $E_{\mathrm{T}}^{\mathrm{miss}}/\sqrt{\sum p_{\mathrm{T}}^{\mathrm{jet}}}$ involving the missing energy and scalar sum of transverse jet momentum). The 7–10 jet search also has a looser requirement on jets originating from bottom quarks compared with the Multi-b analysis. Together, this allows the 7–10 jets analysis to maintain a unique coverage of models. In the gluino–squark plane (Figure 4.5), the 7–10 jets points occupy a similar space as Multi-b, but the longer cascade chains mean the gluino mass reach is lower. The remainder of the spectrum can be relatively decoupled. Figure 4.8b displays model number 227558023, which is

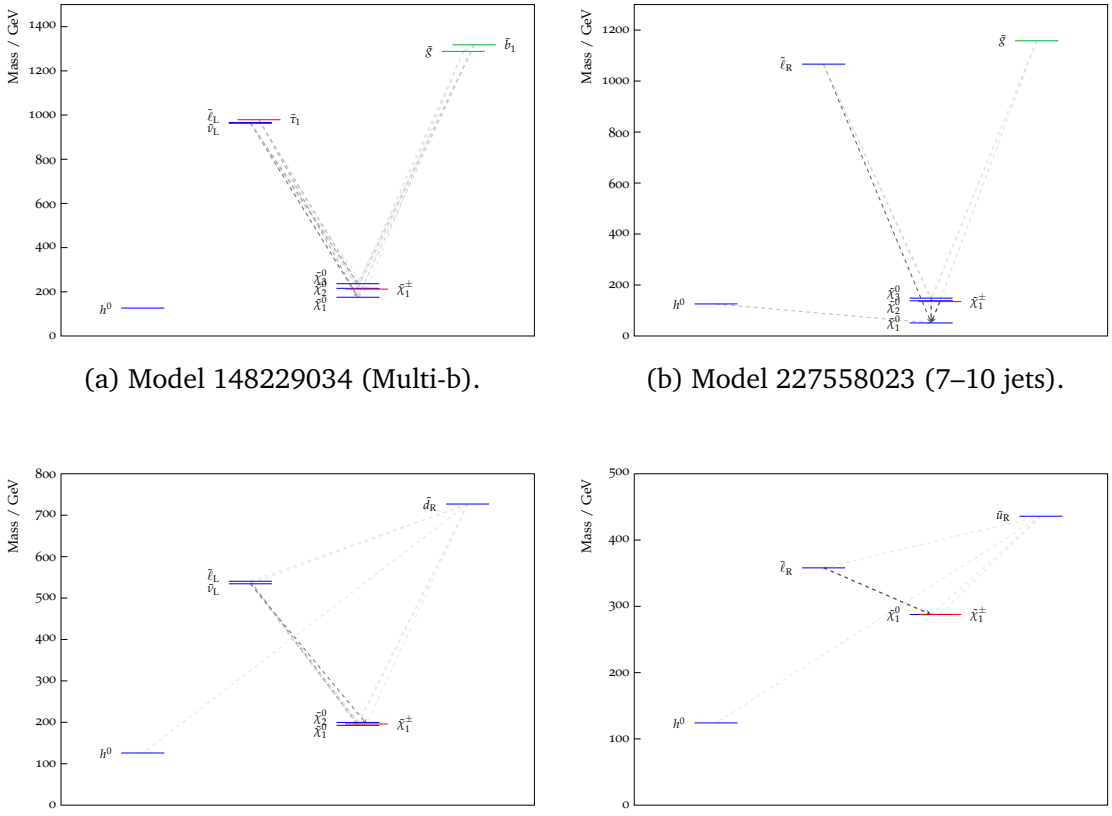

(a) Model 148229034 (Multi-b).

(b) Model 227558023 (7–10 jets).

(c) Model 13382371 (1-lepton).

(d) Model 11733067 (SS/3L).

Figure 4.8: Representative mass spectra produced using PySLHA [271] with model number in the captions for excluded points where the corresponding analysis in parentheses had greatest sensitivity. These show the most relevant low-mass sparticles and their decays. The grey arrows show the branching ratios between two sparticles and proportional to its brightness. The model displayed for the 7–10 jets analysis is the one with the lightest gluino with an LSP mass below 100 GeV, while for the SS/3L search, we selected the model with the lightest squark. For the Multi-b analysis, displayed is a model selected from the region in Figures 4.4 where the density of red points is greatest. The model for the 1-lepton search is chosen based on one that is representative from the mass distributions in Figure 4.9a.

representative of the models where the 7–10 jets analysis is most sensitive, where we selected the one with lowest gluino mass which had an LSP below 100 GeV.

Monojet In terms of SUSY models, this is optimised for scenarios where the mass of the squark is almost equal to that of the LSP, so-called 'compressed scenarios'.

In Figures 4.4 and 4.6, the excluded points (cyan rings) where this analysis is most sensitive involve very small mass splittings. Though there is significant overlap in regions of sensitivity for the Monojet and 2–6 jets analyses, the former is exclusively the most sensitive analysis involving squark–LSP splittings below 30 GeV. We note that the 2–6 jets search includes a similar signal region but requires a minimum of two jets called '2jm'. The different jet multiplicity requirements ensure the dedicated Monojet maintains a unique sensitivity to the smallest squark–LSP mass splittings, again demonstrating the complementarity of searches. We find a small number (fewer than 10) of scenarios involving small mass splittings between the lightest 3rd generation squark and the LSP in the models for which the Monojet is most sensitive.

4.4.2 Searches selecting one or more leptons

Turning to leptonic searches, Figures 4.4 and 4.6 show less distinct regions where the 1-lepton (orange plus) or SS/3L (green cross) analyses were most sensitive. These points tend to cluster around $m(\tilde{q}) \lesssim 1.5$ TeV with fewer points present for $m(\tilde{g}) \lesssim 1.2$ TeV. Further investigation reveals other correlations driven by slepton and gaugino masses not apparent in these figures, which we discuss below. We also identify scenarios where these searches had most sensitivity beyond what ATLAS optimised for.

1-lepton Figure 4.9a shows the distribution of masses for various sparticles from the excluded points where the 1-lepton analysis had the lowest CLs value. Though optimised for gluino production, there is also a prevalence of light squarks, whose distribution peaks around $m(\tilde{q}) \sim 1$ TeV. The distributions of the $\tilde{\chi}_1^\pm$ and also $\tilde{\chi}_2^0$ are skewed towards low masses, peaking around 300 GeV, with a tail that extends above 1 TeV. The tendency for the $\tilde{\chi}_1^\pm$ and $\tilde{\chi}_2^0$ to be light is characteristic of Higgsino content in the LSP, or a bino-like LSP with a wino near in mass.

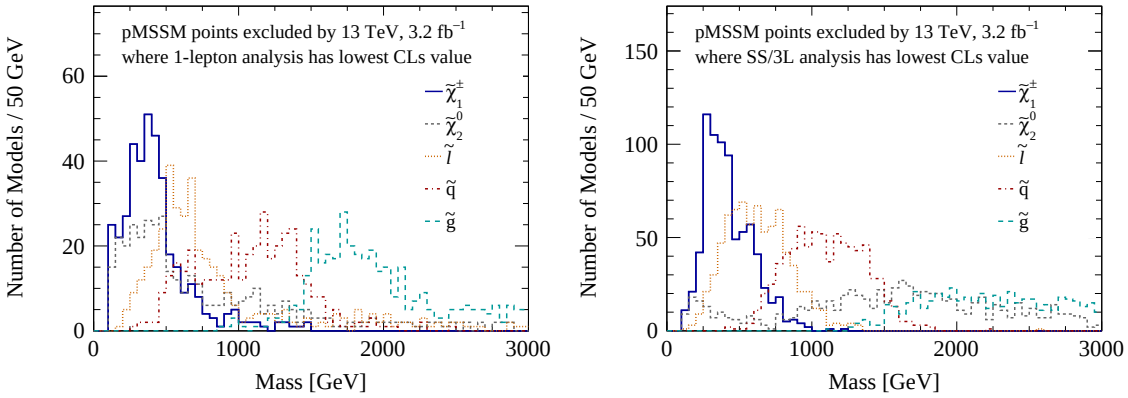

(a) 1-lepton analysis. (b) SS/3L analysis.

Figure 4.9: Distribution of sparticle masses for the excluded points where the 1-lepton (left) and SS/3L (right) analyses are most sensitive. Presented sparticles are the chargino $\tilde{\chi}_1^{\pm}$ (blue solid), next-to-lighest neutralino $\tilde{\chi}_2^0$ (grey short-dashed), lightest slepton $\tilde{\ell}$ (orange dotted), lightest squark $\tilde{q}$ (red dot-dashed) and gluino $\tilde{g}$ (light-blue long-dashed).

The mass distribution also reveals a preponderance of light sleptons, peaking around $m(\tilde{\ell}) \sim 600$ GeV. We find these typically reside between the coloured sparticle and the $\tilde{\chi}_1^{\pm}, \tilde{\chi}_1^0$ states. To demonstrate this, we define the splitting parameter

$$x \equiv \frac{m\left(\tilde{\ell}\right) - m\left(\tilde{\chi}_1^{\pm}\right)}{m\left(\tilde{q}\right) - m\left(\tilde{\chi}_1^{\pm}\right)}, \tag{4.1}$$

where $m\left(\tilde{\ell}\right)$ and $m\left(\tilde{q}\right)$ are respectively the masses of the lightest slepton and squark among the first or second generations. The red dashed line in Figure 4.10 then shows the distribution in x of models where 1-lepton was most sensitive in x, and indeed the majority of models in the histogram have $0 < x < 1$.

The 1-lepton analysis considers a single simplified model with a gluino–chargino–LSP $\tilde{g} \to qq\tilde{\chi}_1^{\pm}, \tilde{\chi}_1^{\pm} \to W\tilde{\chi}_1^0$ decay chain and optimises for various mass splittings between these three sparticles. This is noteworthy given we find the 1-lepton search is most sensitive to richer mass spectra, where squarks and intermediate sleptons feature prominently. Given the mass distributions in Figure 4.9a, we display model number 13382371 (Figure 4.8c) to illustrate the wider sensitivity of the 1-lepton analysis. This point features a 727 GeV squark that can cascade to a slepton doublet and a 173 GeV Higgsino-like LSP. We also note that all the signal regions were involved in the exclusion of these models, indicating sensitivity to a wide variety of splittings. This addresses the question

of over-optimisation raised in the Introduction (Section 4.1). Despite optimising robustly for the gluino–chargino–LSP model, this analysis was sensitive to wider classes of models.

We note that with recent 13 TeV searches for direct electroweak production not considered at the time of publication likely have sensitivity to these scenarios with light chargino–slepton scenarios, but detailed evaluation is deferred for future work.

SS/3L The SS/3L is the most sensitive analysis almost exclusively to wino-like LSPs. This is consistent with the mass distributions of these models in Figure 4.9b: compared with the 1-lepton case (Figure 4.9a), the SS/3L has a smaller tail of high chargino mass while the next-to-lightest neutralino $\tilde{\chi}_2^0$ distribution is no longer skewed to lower masses. We note that a Run 2 version of the 'Disappearing Track' analysis [194], not considered in this work, could be sensitive to these models, since the compressed chargino–LSP splitting means that the chargino is typically long-lived on collider time scales. For these points, the gluino is relatively heavy and not strongly correlated with a particular mass scale, being fairly uniformly distributed for $m(\tilde{g}) \gtrsim 1.5$ TeV, in contrast to the 1-lepton discussion. This suggests that the SS/3L is consistently not as sensitive to light gluinos as other analyses such as the 2–6 jets. By contrast, squarks retain a peaked distribution centred around 1 TeV.

Figure 4.10 demonstrates that the slepton mass is almost always between the chargino and the lightest squark for SS/3L. We find a negligible number of models (a single entry) has $x > 1$, corresponding to a slepton mass being above that of the lightest squark. Thus, we reveal that points where the SS/3L has best sensitivity are strongly correlated with one common feature: a squark–slepton–chargino–LSP $\tilde{q}$–$\tilde{\ell}$–$\tilde{\chi}_1^\pm$–$\tilde{\chi}_1^0$ ordered mass spectrum. The squark can undergo a three-body decay to a quark, lepton and a slepton $\tilde{q} \to q\ell\tilde{\ell}$ if the intermediate neutralino is off-shell $m(\tilde{\chi}_2^0) > m(\tilde{q})$. This hierarchical structure is displayed in model number 11733067 (Figure 4.8d). Among the models where SS/3L is most sensitive, this has the lightest squark mass at 436 GeV.

Moreover, we find one signal region 'SR0b3j' was used to exclude 98% of these models where the analysis was most sensitive. This suggests other analyses had better sensitivity to models targeted by the other three signal regions, for example the Multi-b analysis is particularly sensitive to $\tilde{g} \to t\bar{t}\tilde{\chi}_1^0$ scenarios. The 'SR0b3j' signal region

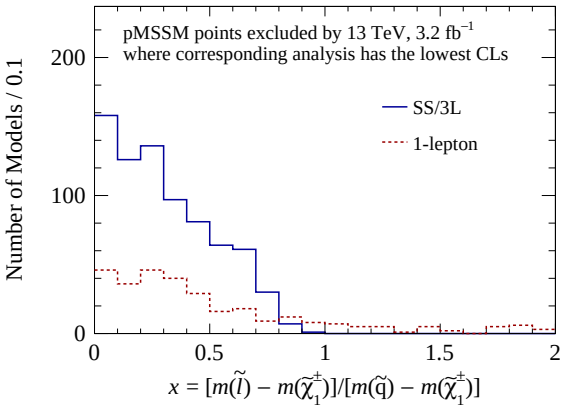

Figure 4.10: Distribution of mass splitting for the chargino–slepton–squark $\tilde{\chi}_1^{\pm}$–$\tilde{\ell}$–$\tilde{q}$ system, parametrised by x as defined in Eq. 4.1. These are presented for the excluded points where the 1-lepton (dashed red) and SS/3L (solid blue) analyses are most sensitive.

requires at least three leptons and was optimised to capture a $\tilde{g}$–$\tilde{\chi}_2^0$–$\tilde{\ell}$–$\tilde{\chi}_1^0$ decay chain, distinct from the $\tilde{q}$–$\tilde{\ell}$–$\tilde{\chi}_1^{\pm}$–$\tilde{\chi}_1^0$ scenario we just identified.

4.5 Probing dark matter with strong SUSY searches

Dark matter phenomenology in the pMSSM is strongly influenced by the gaugino and Higgsino composition of the LSP. While the Monojet search is considered the flagship DM search, other collider searches are needed to fully cover the DM space in the pMSSM. This section demonstrates that searches for coloured SUSY states indirectly probe different DM scenarios in the pMSSM. Subsection 4.5.1 ascribes DM interpretations to each of the six 13 TeV searches. Subsection 4.5.2 also considers the impact of recent direct detection PandaX-II/LUX experiments [235, 236] on gluino and squark masses. Present constraints from indirect detection searching for DM annihilation in galactic halos are expected to have little sensitivity on the pMSSM space considered[4].

4.5.1 Impact of 13 TeV constraints on dark matter observables

Relic density Figure 4.11a shows each of the 28.5k points excluded by six searches, styled according to the analysis with the lowest CLs value, projected into the plane of

[4]Indirect detection was examined in Ref. [213], which finds Fermi-LAT constraints are not expected to impact the pMSSM but the future Cherenkov Telescope Array (CTA) [272] is projected to have sensitivity to high mass LSPs scenarios $\sim$ 1 TeV.

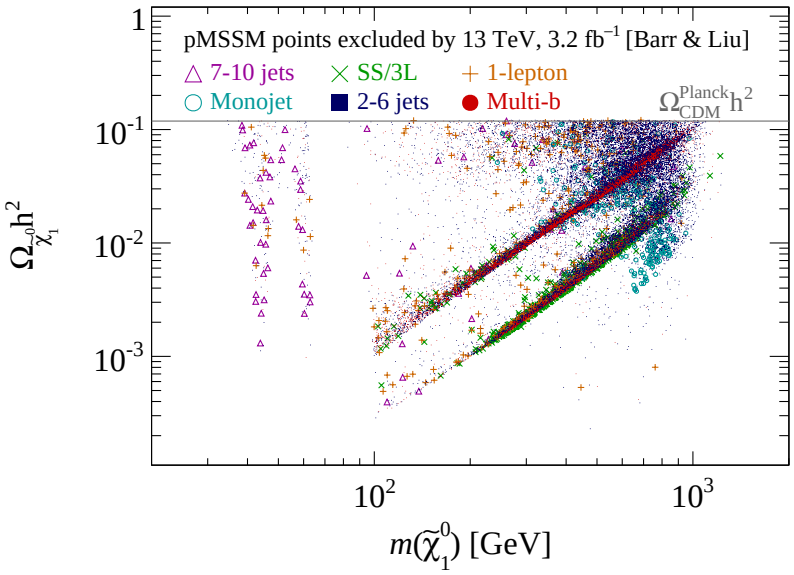

(a) Relic density.

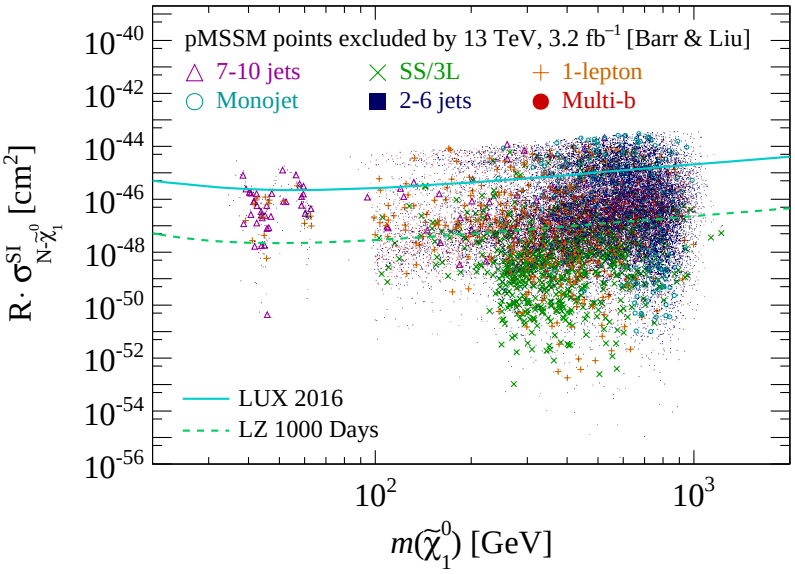

(b) Spin independent cross-section.

Figure 4.11: Same as Figure 4.4 but projected into planes involving (a) relic density and (b) spin-independent neutralino–nucleon cross-section $\sigma^{\text{SI}}_{N\text{-}\tilde{\chi}^0_1}$. The grey line in Figure 4.11a indicates the relic density $\Omega^{\text{Planck}}_{\text{CDM}}h^2$ measured by Planck [95]. In Figure 4.11b, the cross-section is scaled by the ratio $R = \Omega_{\chi^0_1}h^2/\Omega^{\text{Planck}}_{\text{CDM}}h^2$ of the neutralino relic density $\Omega_{\chi^0_1}h^2$ to that observed $\Omega^{\text{Planck}}_{\text{CDM}}h^2$. Overlayed on Figure 4.11b are upper limits at 90% CL on the cross-section observed by LUX 2016 [236] (solid light blue), together with the projected limit from 1000 days of data taking by LZ [273] (dashed green). The central value of the limit from LUX 2016 is twice as strong as that recently reported by PandaX-II [235].

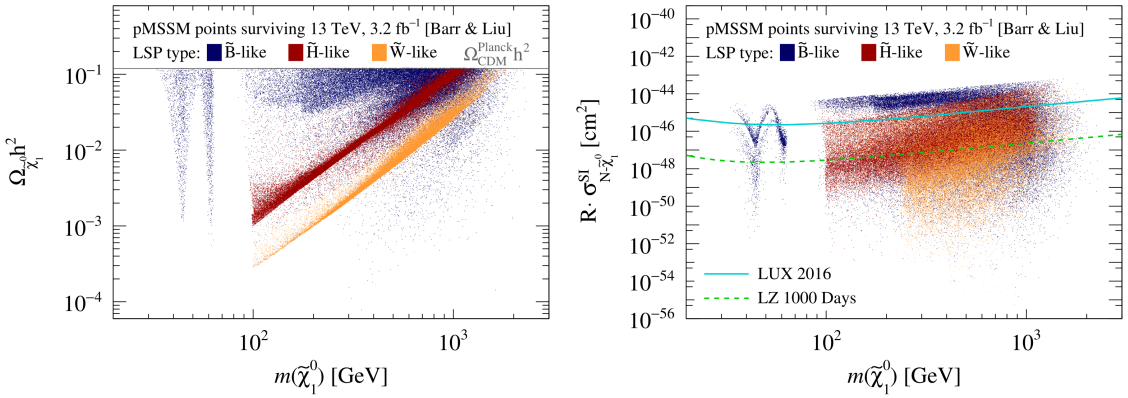

(a) Relic density.

(b) Spin independent cross-section.

Figure 4.12: Points surviving constraints from the six 13 TeV ATLAS searches, projected into (a) relic density and (b) LSP-nucleon cross-section vs LSP mass $m(\tilde{\chi}^0_1)$. The points are coloured by the composition of the neutralino LSP being dominantly bino (blue), Higgsino (red) or wino (orange) as defined in Table 4.1.

$\tilde{\chi}^0_1$ dark matter mass vs relic density. To facilitate interpretation, we discuss the salient underlying processes for several features:

- The $\tilde{\chi}^0_1$ neutralino is not required to be the sole constituent of dark matter, as other candidates such as axions can contribute [105], making the points considered more general than Ref. [220]. The Planck measurement of the cold dark matter (CDM) abundance [218] only serves as an upper bound $\Omega_{\chi^0_1}h^2 \leq \Omega_{\text{CDM}}h^2$.

- The composition of $\tilde{\chi}^0_1$ influences the value of its relic density $\Omega_{\chi^0_1}h^2$. Figure 4.12a illustrates the relic density against the mass of the LSP that survived the constraints from six 13 TeV analyses, coloured by the dominant composition to the LSP, as defined in Table 4.1. Notably, the Higgsino- and wino-like LSP models are concentrated along a straight diagonal line in the plot. This is because the thermally averaged cross-section is set by $\langle\sigma v\rangle \propto m^{-2}_{\tilde{\chi}^0_1}$ [274], and the relic density $\Omega_{\tilde{\chi}^0_1}h^2$ is therefore nearly proportional to the neutralino mass squared, the hallmark of the weakly interacting massive particle (WIMP) paradigm. There are also no Higgsino- or wino-like LSPs below around 100 GeV due to LEP bounds.

- By contrast, bino dark matter has suppressed annihilation cross-sections[5], leading to larger relic abundance, as generally seen in Figure 4.12a. To satisfy the

[5]Pure binos do not couple to any gauge or Higgs bosons. This is seen from the couplings $g_{Z\tilde{\chi}^0_1\tilde{\chi}^0_1}$ ($g_{h\tilde{\chi}_1\tilde{\chi}_1}$)

Planck bound, bino dark matter must either have non-negligible mixing with winos and/or Higgsinos, or there is another mechanism to deplete the relic density, such as coannihilation. In Ref. [218], the type of coannihilators were discussed but no distinction was made between light flavour squarks and gluinos. Their phenomenological consequences are different, which we elucidate in Figure 4.13. We observe that light gluino coannihilators (light orange) are more stringently excluded, with few points $m(\tilde{g}) \lesssim 800$ GeV than for squarks due to powerful Run 1 constraints.

- Focusing now on electroweak particles ('Other' in Figure 4.13a), for LSP masses $m\left(\tilde{\chi}_1^0\right) \lesssim 250$ GeV, the coannihilation mechanism is predominantly via uncoloured sparticles due to stringent LHC constraints on squarks and gluinos. The two dips in $\Omega_{\tilde{\chi}_1^0}h^2$ centred around $m\left(\tilde{\chi}_1^0\right) \approx 45$ and 63 GeV involve resonant annihilation through a Z or Higgs boson. Meanwhile, for $90 \lesssim m\left(\tilde{\chi}_1^0\right) \lesssim 250$ GeV, the coannihilators are predominantly slepton or gauginos, which are bounded by LEP limits.

Returning to the discussion of points excluded by individual analyses in Figure 4.11a, the strong SUSY searches considered are sensitive to models with a wide variety of $\Omega_{\tilde{\chi}_1^0}h^2$. As previously discussed in Section 4.4, the 7–10 jets search is particularly sensitive to models with $m\left(\tilde{\chi}_1^0\right) \lesssim 100$ GeV, where bino-like LSPs are associated with the Z and h^0 funnel region. Meanwhile, the SS/3L analysis is most sensitive to wino-like LSPs models while the Multi-b analysis had preferential sensitivity to Higgsino dark matter scenarios, as indicated by the clustering of green crosses and red dots along the wino and Higgsino respective diagonal bands (compare with Figure 4.12a).

The 1-lepton analysis has sensitivity away from the Higgsino and wino diagonal bands, for dark matter masses below about 300 GeV, where slepton and gaugino coannihilators are prevalent. The extensive presence of blue dots and cyan rings away from these bands

of the neutralino to the Z and (Higgs) bosons are given at tree-level by [275]

$$g_{Z\tilde{\chi}_1^0\tilde{\chi}_1^0} = \frac{g_2}{2\cos_W}\left(|N_{13}|^2 - \left|N_{14}\right|^2\right), \tag{4.2}$$

$$g_{h\tilde{\chi}_1^0\tilde{\chi}_1^0} = g_2 \cos\alpha\,(N_{11} - N_{12}\tan\theta_W)\left(N_{13}\tan\alpha + N_{14}\right). \tag{4.3}$$

Here we have the neutralino mixing matrix elements N_{ij} defined in Table 4.1, the SU(2) gauge coupling g_2, Weinberg angle θ_W and the Higgs mixing parameter α. Pure binos have $N_{12} = N_{13} = N_{14} = 0$.

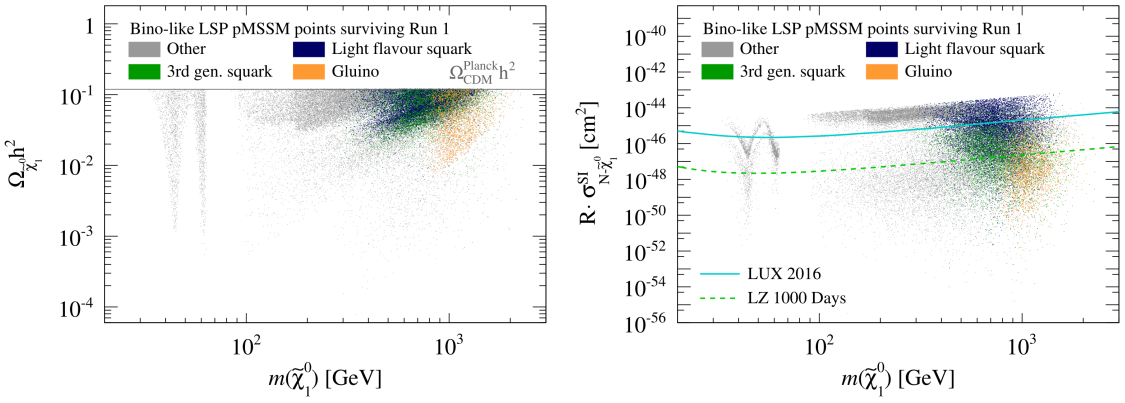

(a) Relic density.

(b) Spin independent cross-section.

Figure 4.13: Coannihilators for points with bino-like LSP surviving Run 1 constraints, projected into (a) relic density (left) and (b) LSP-nucleon cross-section vs LSP mass $m(\tilde{\chi}_1^0)$. The points are coloured according to dominant coannihilator: gluino (light orange), light flavour squarks (dark blue), 3rd generation squarks (green). 'Other' refers to (co)annihilation mechanisms involving the electroweak sector.

shows respectively that the 2–6 jets and Monojet searches are particularly sensitive to gluinos and squarks that have small mass splitting with the bino dark matter. Crucially, these impact scenarios where such coloured sparticles are the coannihilators (compare with Figure 4.13) and therefore indirectly probe dark matter masses higher than those currently accessible by direct electroweakino searches at the LHC. Nevertheless, the 2–6 jets analysis also has sensitivity covering Higgsino- and wino-like LSP points, with clusters along the Higgsino and wino bands.

Direct detection The neutralino $\tilde{\chi}_1^0$ contributes to the local dark matter density and can induce nuclei recoils in direct detection experiments. Figure 4.11b illustrates the points excluded by the most sensitive of the six ATLAS searches, allowing us to compare with direct detection sensitivity for each analysis. This projects into the plane defined by the spin-independent[6] cross-section $\sigma^{\text{SI}}_{N\text{-}\tilde{\chi}_1^0}$ of the LSP interacting with a Xenon nucleus, normalised per nucleon, and dark matter mass $m(\tilde{\chi}_1^0)$. We discuss several features, with reference to other projections where appropriate, to aid interpretation:

- Direct detection experiments typically interpret results assuming the neutralino

[6] It is found in Ref. [218] that recent upper limits on spin-dependent cross-sections lack sensitivity to this set of pMSSM points, although future sensitivity can provide complementary probes to spin-independent limits [213].

$\tilde{\chi}_1^0$ fully saturates the relic abundance measured by Planck. As $\tilde{\chi}_1^0$ need not be the sole constituent of dark matter, we rescale the direct detection interaction cross-sections $\sigma^{\text{SI}}_{N\text{-}\tilde{\chi}_1^0}$ by a factor

$$R \equiv \Omega_{\tilde{\chi}_1^0} h^2 / \Omega^{\text{Planck}}_{\text{CDM}} h^2 \tag{4.4}$$

to account for reduced direct detection sensitivity from lower $\tilde{\chi}_1^0$ abundance.

- Recently, the PandaX-II [235] and LUX [236] collaborations presented results that extend sensitivity for WIMP masses $m\left(\tilde{\chi}_1^0\right) \gtrsim 20$ GeV by a factor of 2 and 4 respectively beyond the LUX 2015 result [276]. As a guide to the sensitivity of direct detection, the observed limits from LUX 2016 [236] and the projected sensitivity of LZ [273] are overlayed in Figure 4.11b.

- Constraints from spin-independent cross-section $R \cdot \sigma^{\text{SI}}_{N\text{-}\tilde{\chi}_1^0}$ results of LUX 2013 [253] carves out points at the highest $R \cdot \sigma^{\text{SI}}_{N\text{-}\tilde{\chi}_1^0} \sim 10^{-44}$ cm^2. In Ref. [218], ATLAS conservatively increased by a factor of four the upper limit on $R \cdot \sigma^{\text{SI}}_{N\text{-}\tilde{\chi}_1^0}$ to account for uncertainties in nuclear form factors, before rejecting points.

- Figure 4.12b reveals points that survived constraints from the six 13 TeV searches in the plane of spin-independent cross-section against dark matter mass. The points are coloured according to the $\tilde{\chi}_1^0$ composition, which has a significant impact on $R \cdot \sigma^{\text{SI}}_{N\text{-}\tilde{\chi}_1^0}$. This is due both to the couplings of the $\tilde{\chi}_1^0$ to nucleons and the relic density suppression (Eq. 4.4 and Figure 4.12a). Notably, wino-like $\tilde{\chi}_1^0$ have suppressed direct detection cross-sections given the small coupling to the Higgs boson.

Returning to the discussion of the regions of sensitivity from the ATLAS searches (Figure 4.11b), points above the blue solid line are independently excluded by both LUX 2016 and the 13 TeV ATLAS searches considered. Collider searches are free from astrophysical uncertainties, and therefore provide powerful cross-checks should either approach report tentative signals. On the other hand, the cosmological lifetime of the $\tilde{\chi}_1^0$ dark matter candidate can only be verified by non-collider means. For $m\left(\tilde{\chi}_1^0\right) \gtrsim 1$ TeV, the number of models excluded by the ATLAS searches decreases rapidly. There remain many points surviving in this regime (Figure 4.12b), and those with high $R \cdot \sigma^{\text{SI}}_{N\text{-}\tilde{\chi}_1^0}$ are within direct detection sensitivity.

The 2–6 jets analysis (blue points) is sensitive to a large class of models, particularly those with gluino or squark coannihilators. As this difference has important phenomenological consequences, we display the strong sector coannihilators in Figure 4.13b for bino-like LSPs of points that survived Run 1 constraints. In this projection, it is evident that coannihilation points involving light flavour squarks have enhanced cross-section $R \cdot \sigma^{\mathrm{SI}}_{N\text{-}\tilde{\chi}^0_1}$ compared with gluinos. This is due to the s-channel diagram involving the quarks and LSP scattering via an intermediate squark, a point we will elaborate further in Section 4.5.2. Thus, the 2–6 jets and Monojet analyses share sensitivity to many squark coannihilator scenarios with LUX 2016.

As discussed in previous sections, the 7–10 jets is most sensitive to $m(\tilde{\chi}^0_1) \lesssim 100$ GeV with significant bino content. Many of the points excluded by this search are below the LUX 2016 sensitivity. Meanwhile, the Multi-b analysis tends to favour Higgsino-like LSP scenarios where squark masses are above 2 TeV. There is particular sensitivity to a region centred around cross-section from 10^{-46} cm^2 to 10^{-49} cm^2 and LSP mass of 300 to 700 GeV (Figure 4.11b). Many Higgsino-like LSP models inhabit this region and are beginning to be probed by LUX 2016, but the majority of points where the Multi-b analysis is most sensitive are below the LUX limit.

Notably, ATLAS strong SUSY searches are sensitive to scenarios with direct detection cross-section $R \cdot \sigma^{\mathrm{SI}}_{N\text{-}\tilde{\chi}^0_1}$ well below even the projected sensitivity of LZ based on 1000 days of data taking [273]. The SS/3L reach into this regime is especially prominent, being most sensitive to wino-like LSP models with highly suppressed cross-sections $R \cdot \sigma^{\mathrm{SI}}_{N\text{-}\tilde{\chi}^0_1}$. Many gluino coannihilator scenarios occupy this region (Figure 4.13b) and are dominantly probed by the 2–6 jets analysis. The projected LZ sensitivity is within an order of magnitude of the irreducible neutrino background 'floor', which is a challenging regime for Xenon-target direct detection experiments.

Concluding this subsection, we demonstrated the important complementarity of strong SUSY searches for probing pMSSM points beyond Monojet alone and direct detection experiments. This enables colliders to indirectly constrain bino-like DM with coloured coannihilators, in addition to Higgsino DM scenarios before electroweak SUSY searches gain sensitivity.

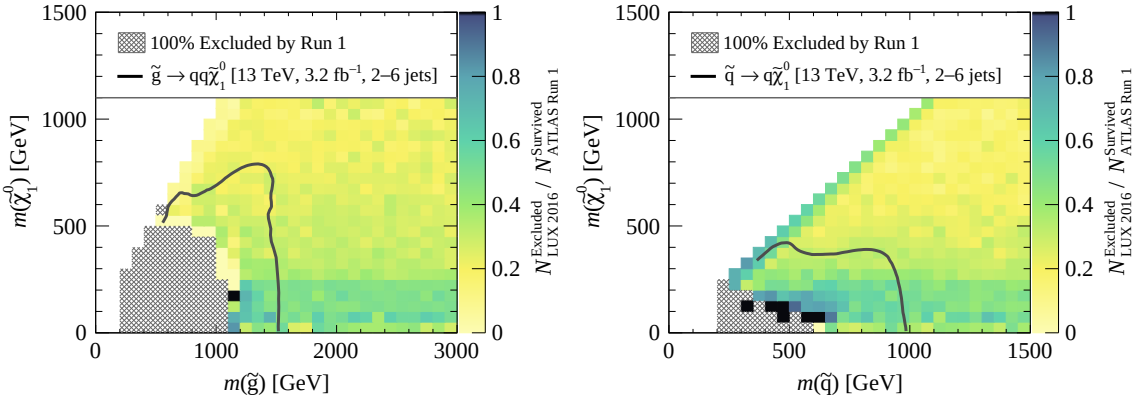

(a) Gluino vs LSP. (b) Lightest squark vs LSP.

Figure 4.14: Fraction of points excluded at 90% CL on the spin-independent result from LUX 2016 [276], projected into the LSP vs (a) gluino and (b) lightest squark planes. Here, $\tilde{q}$ is the lightest squark of the first or second generations. The colour scale indicates the per bin number of points excluded by LUX 2016 [236] $N^{\text{Excluded}}_{\text{LUX 2016}}$ divided by the number of points surviving Run 1 $N^{\text{Survived}}_{\text{ATLAS Run 1}}$; black denotes 100% exclusion. Hatched grey indicate all the points excluded by Run 1 searches. Points with long-lived gluinos, squarks and sleptons are not considered. Overlayed grey solid lines correspond to the simplified models shown in Figure 4.2 from the 2–6 jets search [179].

4.5.2 Impact of direct detection constraints on squarks and gluinos

Finally, turning the question around, we explore the impact of LUX 2016 constraints on the parameter space relevant to LHC gluino and squark searches. Considering the set of points that survived Run 1 [218], we now deem any point with scaled cross-section $R \cdot \sigma^{\text{SI}}_{N\text{-}\tilde{\chi}_1^0}$ above the 90% CL limit observed by LUX 2016 to be excluded. We take the observed central value of the upper limit [236] without rescaling to account for the nuclear form factor uncertainties[7]. We find that LUX 2016 excludes 30.3% of such pMSSM points constraints (with long-lived gluinos, squarks and sleptons removed). Figure 4.12b shows that LUX is particularly sensitive to pMSSM points with bino-like LSP, due in part to the relic density suppression of Higgsino and wino-like models.

Figure 4.14a projects the fractional exclusion[8] by LUX 2016 into the gluino vs LSP plane. There is a band of modest exclusion for LSP masses $m(\tilde{\chi}_1^0) \lesssim 250$ GeV, which is relatively uncorrelated with gluino masses. This apparent enhancement of sensitivity

[7] Had we weakened this constraint by a factor of four [218], the key qualitative features in the discussion are unaffected; only the numerical fraction of models excluded is reduced to 18.0%.

[8] Although $N^{\text{Excluded}}_{\text{LUX 2016}}/N^{\text{Survived}}_{\text{ATLAS Run 1}}$ is prior-dependent, we will momentarily discuss this, while the forthcoming comparison of gluino and squark coannihilation regions has minimal prior dependence.

is partly an artefact due to the systematic oversampling of coannihilators for bino-like LSPs in Ref. [218]. This region is rich in gaugino and slepton coannihilators due to their weak LHC constraints compared with strongly interacting sparticles. Due to smaller annihilation cross-sections of this electroweak process in the early universe, the relic abundance $\Omega_{\tilde{\chi}_1^0}h^2$ for a given bino-like LSP mass is larger. These models are thus not scaled down as far by the $R = \Omega_{\tilde{\chi}_1^0}h^2/\Omega_{\text{CDM}}^{\text{Planck}}h^2$ factor.

A prominent feature of the points excluded by LUX appears when projecting into the squark vs LSP plane (Figure 4.14b). The diagonal region where the mass splitting between the LSP and squark is small $m(\tilde{q}) - m(\tilde{\chi}_1^0) \lesssim 50$ GeV shows a distinctly higher exclusion fraction; this feature is absent in the gluino vs LSP plane. Furthermore, mass bins with higher exclusion fraction are correlated with lower squark masses. This is particular salient along the diagonal, where points are predominantly squark coannihilators. The band of modest exclusion fraction for LSPs with $m(\tilde{\chi}_1^0) \lesssim 250$ GeV remains, as with the gluino vs LSP plane.

Such contrasting features between gluinos and squarks highlight the importance of the s-channel squark exchange diagram in direct detection $\tilde{\chi}_1^0 + q \to \tilde{q} \to \tilde{\chi}_1^0 + q$. Here, a squark $\tilde{q}$ mediates the LSP $\tilde{\chi}_1^0$ scattering off light flavour quarks q inside the nucleons. Resonant scattering occurs when the LSP and squarks are nearly mass degenerate, enhancing the sensitivity of LUX along the squark–LSP diagonal of Figure 4.14b. Thus, direct detection experiments are particularly sensitive to bino-like LSP scenarios with a squark coannihilator. The cross-section $\sigma^{\text{SI}}_{N\text{-}\tilde{\chi}_1^0}$ decreases with heavier squarks due to the $\sim 1/\left(m_{\tilde{q}}^2 - m_{\tilde{\chi}_1^0}^2\right)$ suppression in the propagator.

These observations are consistent with the LSP–nucleon cross-section vs LSP mass plane with coannihilation mechanism identified (Figure 4.13b). Squarks of the first or second generation (dark blue) have particularly enhanced direct detection cross-sections. The points with gluino coannihilators (light orange) feature $R \cdot \sigma^{\text{SI}}_{N\text{-}\tilde{\chi}_1^0}$ primarily below 10^{-46} cm^2 and will only begin to be probed at the direct detection frontier by future experiments such as LZ. Coannihilation points involving third generation squarks (light blue) also tend to have suppressed direct detection cross-sections compared with squarks, due to the negligible 3rd generation quark content in nucleons.

Taken together, this highlights the important implications of LHC searches for squarks

in the context of direct detection experiments, especially when the squark–LSP mass splitting is small. Yet these squark coannihilation scenarios are challenging for colliders, where direct detection experiments can provide a complementary probe.

4.6 Conclusions

This chapter examined how six ATLAS discovery strategies using 3.2 fb^{-1} of $\sqrt{s} = 13$ TeV data optimised for simplified models impact the 19-parameter phenomenological MSSM. First, we examined these correlations in collider parameter spaces, and found Multi-b was the most sensitive analysis for models with larger gluino–LSP mass splittings, where the 2–6 jets search began to lose sensitivity. Second, we identified classes of models beyond those ATLAS used for optimisation. The SS/3L search had one signal region being most sensitive to a different scenario in the pMSSM not considered by the ATLAS search. It involved a squark cascading to a slepton and wino-like LSP. Finally, we showed the prominent role searches for new coloured states have in DM phenomenology. Bino-like LSPs can rely on coloured coannihilators to satisfy relic density constraints, which are probed by the 2–6 jets and Monojet analyses, but also cascades down to the DM.

After these early Run 2 searches, it was evident from Figure 4.12 that many scenarios of neutralino DM remained viable. The electroweak sector plays a non-trivial role in both dark matter and collider phenomenology. Searches for direct electroweak production therefore provide an important probe of neutralino DM that are complementary to the strong production searches considered in this chapter. One notable scenario is Higgsino DM where neutralino masses are near 100 GeV, which are poorly constrained both from non-collider and LHC based searches. A hallmark of Higgsino DM is the compressed mass spectrum of states near the neutralino DM. This makes Higgsino DM particularly difficult to probe, which is not simply resolved by adding more luminosity to previous strategies. Overcoming these challenges in a new dedicated ATLAS search strategy sensitive to these compressed scenarios is the principal subject of the next chapter.

5

Search for compressed electroweak SUSY

Electroweak production of supersymmetric states—charginos, neutralinos and sleptons—is central to the LHC discovery programme. This is important not only because it probes the electroweak sector independent of strongly interacting states, but also because it may be the *only* discovery window if coloured states are too heavy to be accessible at the LHC. In particular, the conclusions of Chapter 4 highlighted the Higgsino as a promising dark matter candidate, motivating new strategies to open LHC sensitivity.

Direct searches of electroweakinos and sleptons are sensitive to masses as high as 500 GeV, but only if mass differences with the neutralino DM are larger than 60 GeV [197, 217, 277–279]. Remarkably, for mass differences below 60 GeV, the mass reach can be as low as around 100 GeV, with no LHC sensitivity prior to the work of this thesis. Higgsino dark matter inhabits this blind spot and the most stringent direct constraints are from LEP searches [22–24, 280–288]. Such scenarios are known as *compressed mass spectra* and are very difficult to discover at the LHC. This is in part due to small cross-sections and low momenta of the visible decay products.

This chapter presents the first LHC publication to overcome these challenges and open sensitivity to several key compressed scenarios in electroweak production, based on work published in *Physical Review D* [3]. Section 5.1 presents the phenomenological motivations and existing constraints for the scenarios explored. Section 5.2 outlines the data and simulated samples. The object definitions used in analysis are discussed in Section 5.3 before Section 5.4 details the discriminating variables used for optimising signal sensitivity. The estimation of background rates and systematic uncertainties are described in Sections 5.5 and 5.6 respectively. Results are presented in Section 5.7 and sensitivity is compared with other ATLAS results using summary plots in Section 5.8, before conclusions are summarised in Section 5.9.

5.1 Motivation to search for compressed mass spectra

Three scenarios involving compressed mass spectra in electroweak SUSY production are considered in this chapter, whose phenomenological motivations are now discussed.

Scenario one: light Higgsino dark matter Naturalness arguments [152,153] suggest that the absolute value of the Higgsino mass parameter μ is near the weak scale, not far from the Z boson mass [150,151]. Meanwhile, the magnitude of the bino and wino mass parameters, M_1 and M_2, can be significantly larger (such as 1 TeV), i.e. $|\mu| \ll |M_1|, |M_2|$. The Higgsino component consequently dominates the composition of the four lightest electroweakino states, $\widetilde{\chi}_1^0$, $\widetilde{\chi}_1^\pm$, and $\widetilde{\chi}_2^0$.

As the Higgsino states are the partners of two doublet representations of $\mathrm{SU(2)_L}$, this symmetry requires these mass eigenstates to be degenerate. In the pure Higgsino limit, M_1 and M_2 are decoupled relative to μ (such as magnitudes above tens of TeV). The masses of the charged states receive loop corrections involving electroweak bosons and are separated by hundreds of MeV relative to the neutral states [289]. An analogous example of this mechanism in the SM are the pions, where the three states π^0, π^+, π^- are a triplet representation of SU(2) (approximate flavour symmetry). The charged–neutral mass difference is generated radiatively, resulting in a compressed mass spectrum $\Delta m(\pi^\pm, \pi^0)/\sqrt{m_{\pi^\pm} m_{\pi^0}} \sim 3\%$.

Nonetheless, the mass splittings of the Higgsino states can be as large as tens of GeV. This occurs when there is some bino and/or wino mixing, which is determined by the values of M_1 and M_2 [290]. Heuristically, the mass splitting between the neutralinos is parametrised approximately by [291]

$$\Delta m(\widetilde{\chi}_2^0, \widetilde{\chi}_1^0) \approx \frac{m_W^2}{g_2^2}\left(\frac{g_1^2}{M_1} + \frac{g_2^2}{M_2}\right), \quad |\mu| \ll |M_1|, |M_2|. \tag{5.1}$$

Therefore when either or both M_1, M_2 are around 1 TeV, there is a dynamical mechanism of electroweak mixing that induces the compressed spectra to be of order one to tens of GeV. For the scenarios considered by this analysis, the chargino $\widetilde{\chi}_1^\pm$ mass is between those of the two neutralinos. The analogous mechanism in the SM is realised by the $W^\pm$ and Z boson masses. Here, mixing of electroweak parameters result in mass splittings of $\Delta m(Z, W)/\sqrt{m_Z m_W} \sim 10\%$.

Scenario two: bino dark matter with wino coannihilator The complement of the light Higgsino scenario considers absolute values of the M_1 and M_2 parameters being near the weak scale. Meanwhile, the magnitude of μ is significantly larger, such that $|M_1| < |M_2| \ll |\mu|$. The $\widetilde{\chi}_1^{\pm}$ and $\widetilde{\chi}_2^0$ states are wino-dominated, which are nearly mass degenerate as they are a triplet of SU(2) [292], similar to the pion masses in the SM. The $\widetilde{\chi}_1^0$ is bino-dominated, and this is collectively referred to as the wino–bino scenario.

Dark matter coannihilation arguments [156, 157] motivate a next-to-lightest SUSY particle (NLSP), the wino in this case, to have masses of one to tens of GeV above that of the bino $\widetilde{\chi}_1^0$, as considered by this chapter. This ensures that the relic density of the $\widetilde{\chi}_1^0$ satisfies constraints from Planck measurements. Further, recent global fits to the phenomenological MSSM using a wide range of collider and non-collider data also favour such compressed wino–bino scenarios [209, 293, 294].

In contrast to the light Higgsino scenario, there is no dynamical mechanism linking the M_1 and M_2 mass parameters to give the $\sim 10\%$ mass splitting matching the relic abundance. Nonetheless, a compressed wino–bino mass spectrum may be expected circumstantially as such accidents of dynamically unrelated parameters also arise in the SM. One notable example is the charm quark and tau lepton masses being similar $\Delta m(c,\tau)/\sqrt{m_c m_\tau} \sim 30\%$, despite the absence of any known dynamical mechanism relating these two SM parameters. In these cases, one can hypothesise an undiscovered mechanism at high mass scales that induces such mass configurations.

Scenario three: bino dark matter with slepton coannihilator Dark matter coannihilation of the bino $\widetilde{\chi}_1^0$ may also proceed via sleptons rather than a wino. The sleptons masses are just above the mass of a pure bino $\widetilde{\chi}_1^0$, resulting in a compressed spectrum. Resolutions to the tension between the measurements of the muon anomalous magnetic moment $(g-2)_\mu$ from predictions [81, 82] motivate smuons and neutralinos near the weak scale [295, 296]. The μ and M_2 parameters (and all other SUSY states) are decoupled, and this is therefore a complement to the first two scenarios.

Furthermore, the principle of minimal lepton flavour violation is assumed, suggested by observational constraints on e.g. $\mathcal{B}(\mu \to e\gamma)$ processes [297], motivate the selectrons and smuons to be mass degenerate. In this thesis, only pair production of the first two

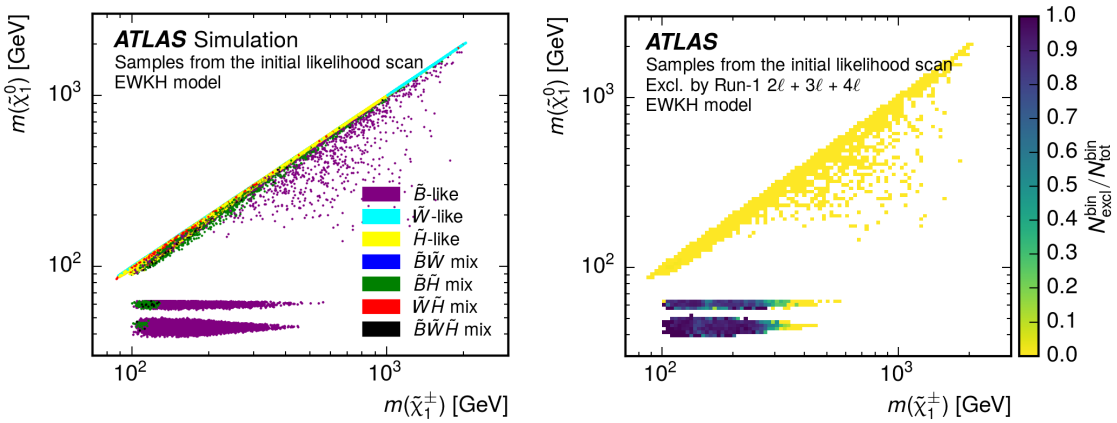

(a) Composition of lightest neutralino $\tilde{\chi}_1^0$ (b) Fraction excluded by multilepton searches

Figure 5.1: Constraints from multilepton searches on the electroweakino sector of a 5-dimensional pMSSM scan by ATLAS, reproduced from Ref. [217]. Fig. (a) shows the composition of the lightest neutralino DM candidate denoted by the different colours in the plane of $m(\tilde{\chi}_1^0)$ vs $m(\tilde{\chi}_1^\pm)$. Fig. (b) shows the per-bin fraction of excluded points $N_{\text{excl}}^{\text{bin}}$ out of those scanned $N_{\text{tot}}^{\text{bin}}$ from ATLAS 8 TeV multilepton searches. Note the absence of sensitivity to points in the compressed region where $\Delta m(\tilde{\chi}_1^\pm, \tilde{\chi}_1^0) \lesssim 30$ GeV, which is the region targeted by this chapter.

generations of sleptons are considered, since staus have sufficiently different collider phenomenology to be beyond the scope of this thesis. Indeed, searches for direct stau production at the LHC saw little to no sensitivity in Run 1 [298].

5.1.1 Existing experimental constraints

Experimental constraints prior to the work of this chapter are summarised in Figures 5.1 and 5.2, which illustrate striking gaps in LHC sensitivity for compressed scenarios.

For the Higgsino dark matter scenario, Figure 5.1 shows the absence of sensitivity from a 5-dimensional pMSSM scan of the electroweakino sector. Only the multilepton searches [277, 278, 298, 300] were considered. Higgsino $\tilde{H}$ dominated $\tilde{\chi}_1^0$ (yellow points) are confined exclusively to the diagonal region (Figure 5.1a), where the ATLAS 8 TeV multilepton searches had no sensitivity (Figure 5.1b). The disappearing track analysis [194] was not considered in this scan, unlike the 19-dimensional pMSSM study [218], which showed this to have powerful sensitivity to the wino-like $\tilde{\chi}_1^0$ but not Higgsino-like $\tilde{\chi}_1^0$ scenarios.

For the wino–bino scenario, Figure 5.2a illustrates the simplified model constraints.

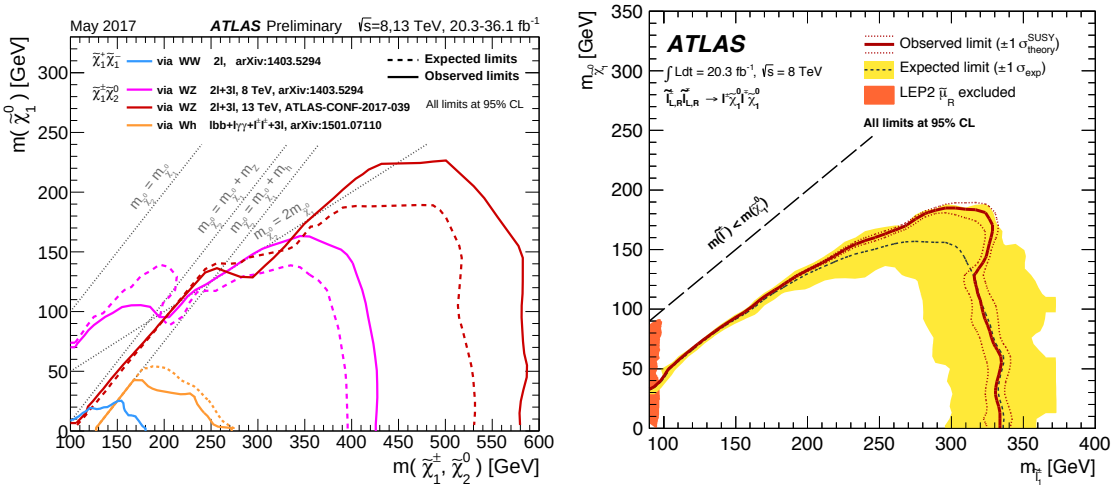

(a) Electroweakino via bosons limits

(b) Slepton Run 1 limit

Figure 5.2: Simplified model limits prior to this work reproduced from Refs. [197, 217, 277, 278, 299] on (5.2a) electroweakinos (assuming pure wino production) decaying via bosons and (5.2b) slepton (assuming four-fold degeneracy of the first two generations). Scenarios along the so-called 'coannihilation corridor' where $\Delta m(\widetilde{\chi}_1^{\pm}, \widetilde{\chi}_1^0) \lesssim 35$ GeV or $\Delta m(\tilde{\ell}, \widetilde{\chi}_1^0) \lesssim 55$ GeV had no sensitivity, which is the subject of this work.

Specifically, 8 TeV [197, 217, 277, 278] and 13 TeV multilepton searches [279] are considered for wino decaying via gauge bosons to a bino $\widetilde{\chi}_1^0$. Despite the mass reach exceeding 500 GeV for massless $\widetilde{\chi}_1^0$, there was strikingly no sensitivity for scenarios with mass splittings of $\Delta m(\widetilde{\chi}_1^{\pm}, \widetilde{\chi}_1^0) \lesssim 35$ GeV. CMS also have similar multilepton searches for charginos and neutralinos at $\sqrt{s} = 8$ TeV [301, 302] and $\sqrt{s} = 13$ TeV [303], which had no sensitivity to wino-production for $\Delta m(\widetilde{\chi}_1^{\pm}, \widetilde{\chi}_1^0) \lesssim 23$ GeV. After the article on which this chapter is based was published, CMS also published a search [304] targeting these Higgsino dark matter and compressed wino–bino scenarios.

For direct slepton production, the 8 TeV ATLAS search [277] (Figure 5.2b) shows no LHC sensitivity existed for the coannihilation corridor $\Delta m(\tilde{\ell}, \widetilde{\chi}_1^0) \lesssim 55$ GeV. The 13 TeV ATLAS slepton search [279] and the CMS counterpart [305] published after this work has no sensitivity to this compressed region.

The lack of sensitivity in these regions is partly due to lack of optimisation for compressed scenarios, but also that the high p_{T} thresholds of the multilepton triggers used in these searches inhibit signal acceptance in compressed scenarios. The strongest constraints in these compressed mass spectra regimes are from a combination of LEP

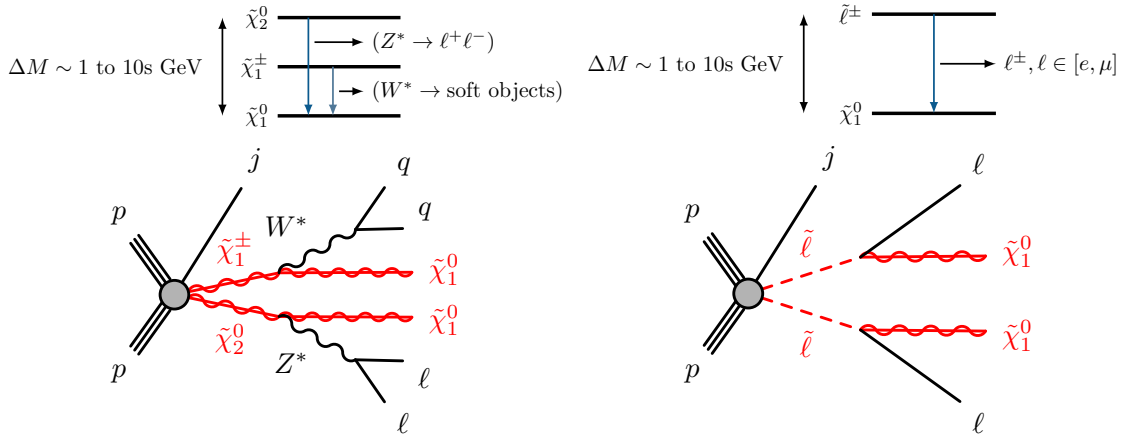

(a) Higgsino simplified model (b) Slepton simplified model

Figure 5.3: The mass spectrum and decays (upper) assumed in the schematic diagrams (lower) of the simplified models representing the two lepton final state of (a) associated neutralino–chargino $\widetilde{\chi}_2^0\widetilde{\chi}_1^\pm$ and (b) slepton pair $\widetilde{\ell\ell}$ production in association with an initial state radiation jet.

results [22–24, 280–288]. The lower bounds on direct chargino production from these results correspond to $m(\widetilde{\chi}_1^\pm) > 103.5$ GeV for $\Delta m(\widetilde{\chi}_1^\pm, \widetilde{\chi}_1^0) \gtrsim 3$ GeV [23] and $m(\widetilde{\chi}_1^\pm) > 92.4$ GeV for smaller mass differences [22].

For sleptons, conservative lower limits on the mass of the scalar partner of the right-handed muon are $m(\widetilde{\mu}_R) > 94.6$ GeV for mass splittings down to $\Delta m(\widetilde{\mu}_R, \widetilde{\chi}_1^0) \gtrsim 2$ GeV [24]. For right-handed selectrons, there is a universal lower bound of $m(\widetilde{e}_R) > 73$ GeV, which is independent of mass splitting $\Delta m(\widetilde{e}_R, \widetilde{\chi}_1^0)$; this constraint relies on the $e^+e^- \to \widetilde{e}_R^+\widetilde{e}_R^-$ process via t-channel neutralino $\widetilde{\chi}_1^0$ exchange [282]. The scalar partners of the left-handed charged leptons $\widetilde{e}_L, \widetilde{\mu}_L$ have larger cross-sections and therefore stronger limits than the corresponding partners of the right-handed leptons [24, 282].

5.1.2 Overview of analysis strategy

Recent phenomenological studies propose probing compressed scenarios using leptons with small transverse momentum, p_{T}, referred to as soft leptons [290, 306–312]. This chapter develops these proposals by analysing 36.1 fb^{-1} of $\sqrt{s} = 13$ TeV pp collected by the ATLAS experiment in 2015 and 2016. Events are selected if they contain large missing transverse momentum, along with two same-flavour soft leptons (electrons e or muons μ) with opposite electric charge. The leptons provide leverage for background

discrimination, while the final state topology is selected such that the produced SUSY states and neutralino $\widetilde{\chi}_1^0$ recoil against initial state radiation. This aligns the neutralinos to produce sufficient $E_{\mathrm{T}}^{\mathrm{miss}}$ to pass the $E_{\mathrm{T}}^{\mathrm{miss}}$ triggers.

Schematic diagrams of processes targeted by this search are shown in Figure 5.3. Figure 5.3a considers the two leptons arising from the same leg, as realised in electroweakino production, where the $\widetilde{\chi}_2^0$ decays via an off-shell Z boson. Such decays have a kinematic endpoint in the dileptonic invariant mass $m_{\ell\ell}$ related to $\Delta m(\widetilde{\chi}_2^0, \widetilde{\chi}_1^0)$, which is exploited for background discrimination. The second case is where the two leptons arise from different legs, which is realised by the slepton model (Figure 5.3b). Each slepton decays directly to the bino $\widetilde{\chi}_1^0$ and corresponding lepton, where a similar kinematic endpoint is realised in the stransverse mass m_{T2} variable [159, 160]. The stransverse mass generalises the transverse mass (used to reconstruct the W boson mass in $W \to \ell\nu$ decays) to a pair of semi-invisible decays, discussed further in Section 5.4.

5.2 Data and simulated samples

Data events from pp collisions are selected for this analysis using the $E_{\mathrm{T}}^{\mathrm{miss}}$ trigger, with high level trigger thresholds ranging from 70 to 110 GeV depending on the run period. The triggers are more than 95% efficient for events with an offline $E_{\mathrm{T}}^{\mathrm{miss}}$ greater than 200 GeV. This data sample corresponds to a luminosity of 36.1 fb^{-1} with a relative uncertainty of 2.1%, derived using methods similar to those described in Ref. [313].

5.2.1 Simplified model signals

For the SUSY signals, simplified models [166, 170, 314] are used to guide analysis design and interpretation. The models considered are motivated by the scenarios described in Section 5.1, but make several simplifying assumptions detailed below. One simplified model is inspired by the light Higgsino dark matter scenario, referred to as the Higgsino model. Another is a model of slepton pair production decaying to bino $\widetilde{\chi}_1^0$. These two models are considered for both signal region optimisation and interpretation of results. For the interpretation of analysis results, an additional simplified model based on the wino–bino scenario assumes wino production decaying to a bino $\widetilde{\chi}_1^0$, referred to as the wino–bino model. All coloured SUSY states are kinematically inaccessible with masses

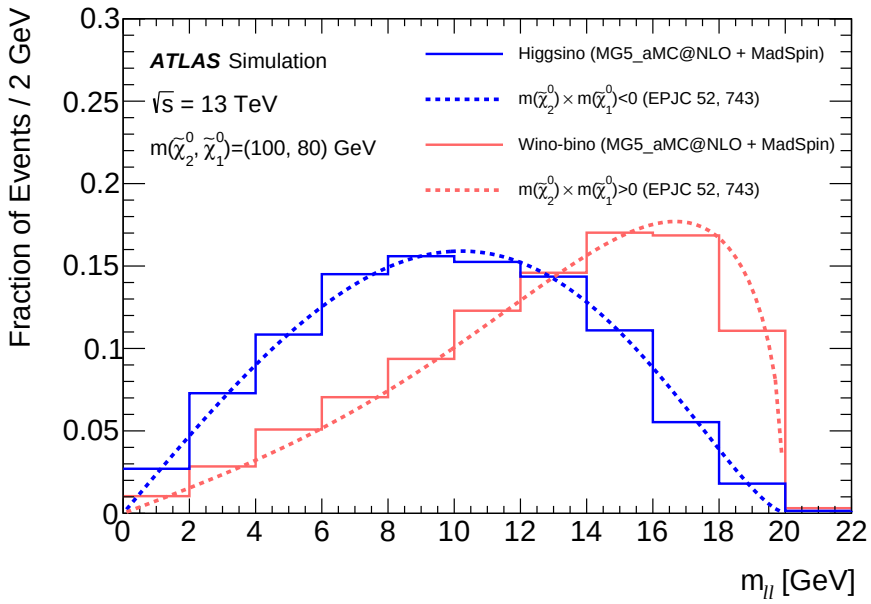

Figure 5.4: Dilepton invariant mass for Higgsino (blue) vs wino–bino model (red) predicted by theory [315] (dashed lines) and the result of the simulation (solid lines) used for this analysis. This figure was produced by a collaborator.

set to multi-TeV scales.

Higgsino model The Higgsino simplified model includes the production of $\widetilde{\chi}_2^0\widetilde{\chi}_1^\pm$, $\widetilde{\chi}_2^0\widetilde{\chi}_1^0$, and $\widetilde{\chi}_1^+\widetilde{\chi}_1^-$, which has the following features:

- The cross-sections assume the electroweakino mixing matrices are such that the $\widetilde{\chi}_1^0, \widetilde{\chi}_1^\pm, \widetilde{\chi}_2^0$ states are pure Higgsinos.
- The $\widetilde{\chi}_1^0$ and $\widetilde{\chi}_2^0$ masses are free parameters, while the chargino masses are set to $m(\widetilde{\chi}_1^\pm) = \frac{1}{2}[m(\widetilde{\chi}_1^0) + m(\widetilde{\chi}_2^0)]$.
- The branching ratios for $\widetilde{\chi}_2^0 \to Z^*\widetilde{\chi}_1^0$ and $\widetilde{\chi}_1^\pm \to W^*\widetilde{\chi}_1^0$ are fixed to 100%. The $Z^* \to \ell^+\ell^-$ branching ratios (and similarly for the W^*) are computed using SUSY-HIT v1.5b [316], which accounts for finite b-quark and τ-lepton masses.

Wino–bino model For the wino–bino simplified model, only the production of $\widetilde{\chi}_2^0\widetilde{\chi}_1^\pm$ is considered as the $\widetilde{\chi}_2^0\widetilde{\chi}_1^0$ process is suppressed and $\widetilde{\chi}_1^+\widetilde{\chi}_1^-$ is found to have low acceptance (Section 5.4). This chapter only uses the wino–bino model for interpretation of the final

results (Section 5.7) in order to allow direct comparison with existing ATLAS simplified models in Section 5.8. This model has the following assumptions:

- The mass of the $\widetilde{\chi}_2^0$ is equal to the mass of the $\widetilde{\chi}_1^\pm$.
- The electroweakino mixing matrices are such that the $\widetilde{\chi}_2^0\widetilde{\chi}_1^\pm$ is pure wino and $\widetilde{\chi}_1^0$ is pure bino, and the decays are the same as that of the Higgsino model.

The $m_{\ell\ell}$ spectra of the wino–bino model from the $Z^* \to \ell^+\ell^-$ boson in the $\widetilde{\chi}_2^0$ to $\widetilde{\chi}_1^0$ decay differs from that of the Higgsino model. To accurately model this, the leptonic decays of the electroweakinos are modelled using MADSPIN [317]. Figure 5.4 illustrates the $m_{\ell\ell}$ shape differences between the Higgsino and wino–bino model for $m(\widetilde{\chi}_2^0, \widetilde{\chi}_1^0) = (100, 80)$ GeV. This is due to a relative sign difference in the underlying neutralino mass parameters [315]. While our strategy does not optimise for these differences, the analysis performs a binned shape analysis of the $m_{\ell\ell}$ variable (Section 5.4). Therefore, there is sensitivity to distinguish between the two cases in case of discovery.

Slepton model For the slepton simplified model, the direct pair production of the selectron and smuons are generated. This model assumes the following:

- Only selectrons $\widetilde{e}_{L,R}$ and smuons $\widetilde{\mu}_{L,R}$ are generated. The subscripts L, R denote the left- or right-handed chirality of the partner electron or muon.
- The four slepton masses are degenerate $m(\widetilde{e}_L) = m(\widetilde{e}_R) = m(\widetilde{\mu}_L) = m(\widetilde{\mu}_R)$.
- The sleptons decay with a 100% branching ratio as $\tilde{\ell} \to \ell\widetilde{\chi}_1^0$.

The signals are generated using MG5_aMC@NLO [257] with up to two extra partons in the matrix element (ME) using version 2.4.2 for the Higgsino and wino–bino models, while the slepton model uses version 2.3.3. The resulting events are interfaced with PYTHIA 8.186 [318] using the A14 tune [319] to model the parton shower (PS), hadronisation and underlying event. The ME-PS matching is performed using the CKKW-L [320] scheme and the NNPDF23LO PDF set [321] is used. Heuristically, ME-PS matching defines the scale above which the matrix element models jets, while the parton shower is used below the scale. Following standard recommendations in the ATLAS SUSY

group, this is set to one quarter of the slepton mass. For the Higgsino and wino–bino models, this scale was revisited and studies suggest that a lower 15 GeV scale allows the matrix element to more accurately model initial state radiation.

Signal cross-sections are calculated at next-to-leading order (NLO) in the strong coupling, and next-to-leading logarithm (NLL) accuracy for soft gluon resummation using RESUMMINO v1.0.7 [173–175]. Figure 3.2 illustrates the production cross-sections for electroweakinos and sleptons. As all coloured SUSY states are decoupled, contributions from diagrams involving squark exchange are negligible.

In general, production cross-sections for electroweakinos are around an order of magnitude larger than those for sleptons. These cross-sections for mass-degenerate $\widetilde{\chi}_2^0$, $\widetilde{\chi}_1^\pm$, $\widetilde{\chi}_1^0$ assume either pure Higgsino $\widetilde{H}$ and wino $\widetilde{W}$ mixing matrices. The Higgsino cross sections are recalculated for the samples used in this analysis assuming non-degenerate $\widetilde{\chi}_2^0$, $\widetilde{\chi}_1^\pm$, $\widetilde{\chi}_1^0$. Note that production cross-sections for wino states are around four times larger than Higgsino states, while that for partners of left-handed leptons $\tilde{\ell}_L$ are approximately three times larger than partners of right-handed leptons $\tilde{\ell}_R$.

5.2.2 Simulation of Standard Model processes

Table 5.1 summarises the MC generator configurations considered for the Standard Model background processes. Displayed are the matrix element and parton shower programs, the PDF sets, and the cross-section calculations used for normalisation. Further details about the simulation of these SM processes can be found in Refs. [322–325].

Processes involving vector bosons, namely $Z^{(*)}/\gamma^*(\rightarrow \tau\tau)$ + jets, diboson, and triboson, are generated using SHERPA versions 2.1.1, 2.2.1, and 2.2.2 [326–330]. Simulation of the single top and $t\bar{t}$ processes employ POWHEG-BOX v1 and v2 [331–333] interfaced to PYTHIA 6.428 using the PERUGIA2012 [334] tune. Events involving Higgs bosons production use the POWHEG-BOX v2 generator with PYTHIA 8.186. Meanwhile, MG5_aMC@NLO 2.2.2 with PYTHIA 8.186 are used to simulate production of a Higgs boson in association with a W or Z boson, in addition to processes containing $t\bar{t}$ in association with at least one electroweak boson. The production of Higgs bosons in association with a W or Z boson, in addition to $t\bar{t}$ plus one or more electroweak bosons use MG5_aMC@NLO v2.2.2 with PYTHIA versions 6.428 or 8.186 and the ATLAS

A14 tune. These processes were generated at NLO in the matrix element except for $t\bar{t}+WW/t\bar{t}$, $t+t\bar{t}$, and $t+Z$, which were generated at LO.

Process	Matrix element	Parton shower	PDF set	Cross-section
$Z^{(*)}/\gamma^*$ + jets	SHERPA 2.2.1		NNPDF 3.0 NNLO [335]	NNLO [336]
Diboson	SHERPA 2.1.1 / 2.2.1 / 2.2.2		NNPDF 3.0 NNLO	Generator NLO
Triboson	SHERPA 2.2.1		NNPDF 3.0 NNLO	Generator LO, NLO
$t\bar{t}$	POWHEG-BOX v2	PYTHIA 6.428	NLO CT10 [337]	NNLO+NNLL [338–341]
t (s-channel)	POWHEG-BOX v1	PYTHIA 6.428	NLO CT10	NNLO+NNLL [342]
t (t-channel)	POWHEG-BOX v1	PYTHIA 6.428	NLO CT10f4	NNLO+NNLL [343, 344]
$t+W$	POWHEG-BOX v1	PYTHIA 6.428	NLO CT10	NNLO+NNLL [345]
$h(\to \ell\ell, WW)$	POWHEG-BOX v2	PYTHIA 8.186	NLO CTEQ6L1 [259]	NLO [346]
$h+W/Z$	MG5_aMC@NLO 2.2.2	PYTHIA 8.186	NNPDF 2.3 LO	NLO [346]
$t\bar{t}+W/Z/\gamma^*$	MG5_aMC@NLO 2.3.3	PYTHIA 8.186	NNPDF 3.0 LO	NLO [257]
$t\bar{t}+WW/t\bar{t}$	MG5_aMC@NLO 2.2.2	PYTHIA 8.186	NNPDF 2.3 LO	NLO [257]
$t+Z$	MG5_aMC@NLO 2.2.1	PYTHIA 6.428	NNPDF 2.3 LO	LO [257]
$t+WZ$	MG5_aMC@NLO 2.3.2	PYTHIA 8.186	NNPDF 2.3 LO	NLO [257]
$t+t\bar{t}$	MG5_aMC@NLO 2.2.2	PYTHIA 8.186	NNPDF 2.3 LO	LO [257]

Table 5.1: Summary of simulated samples for the Standard Model background processes.

Simulation of experimental effects Pileup is modelled by generating additional interactions using the soft QCD processes of PYTHIA 8.186 with the A2 tune [347] and the MSTW2008LO PDF set [348]. These samples are overlaid onto each simulated hard-scatter event. As these are usually generated before the conditions in data are known, the average number of interactions per bunch crossing in the MC samples is reweighted to match the observed pileup distribution.

The ATLAS detector simulation [349] is applied to all MC samples, which is based on GEANT4 [350]. A fast simulation that parametrises the response of the calorimeter [351] is used for the SUSY signal samples, while the SM background samples used the full GEANT4 simulation. To improve the modelling of decays of bottom and charm hadron, the EVTGEN v1.2.0 [352] package is used in all samples except those generated by SHERPA, which has its own detailed internal modelling.

5.3 Object definitions

Candidate events for this analysis must have a minimum of one pp interaction vertex. Vertices have at least two tracks satisfying $p_{\mathrm{T}} > 0.4$ GeV, $|\eta| < 2.5$, which are reconstructed from inner detector information. The primary vertex of an event is defined as the

Property	Signal	Preselected
Electrons		
Kinematic	$p_{\mathrm{T}} > 4.5$ GeV, $\lvert\eta\rvert < 2.47$	$p_{\mathrm{T}} > 4.5$ GeV, $\lvert\eta\rvert < 2.47$
Identification	Tight Likelihood	VeryLoose Likelihood
Isolation	GradientLoose	–
Impact parameter	$\lvert d_0/\sigma(d_0)\rvert < 5$, $\lvert z_0 \sin\theta\rvert < 0.5$ mm	$\lvert z_0 \sin\theta\rvert < 0.5$ mm
Muons		
Kinematic	$p_{\mathrm{T}} > 4$ GeV, $\lvert\eta\rvert < 2.5$	$p_{\mathrm{T}} > 4$ GeV, $\lvert\eta\rvert < 2.5$
Identification	Medium	Medium
Isolation	FixedCutTightTrackOnly	–
Impact parameter	$\lvert d_0/\sigma(d_0)\rvert < 3$, $\lvert z_0 \sin\theta\rvert < 0.5$ mm	$\lvert z_0 \sin\theta\rvert < 0.5$ mm
Jets		
Kinematic	$p_{\mathrm{T}} > 30$ GeV, $\lvert\eta\rvert < 2.8$	$p_{\mathrm{T}} > 20$ GeV, $\lvert\eta\rvert < 4.5$
Clustering	Anti-k_t $R = 0.4$ EMTopo	Anti-k_t $R = 0.4$ EMTopo
Pileup mitigation	JVT Medium for $p_{\mathrm{T}} < 60$ GeV, $\lvert\eta\rvert < 2.4$	–
b-tagging	$p_{\mathrm{T}} > 20$ GeV, $\lvert\eta\rvert < 2.5$, MV2c10 FixedCutBeff 85%	–

Table 5.2: Summary of object definitions. Signal objects are used in the final analysis selection, which are a subset of preselected objects. References and definitions for specific properties of each object can be found in the main text.

one with the largest $\sum p_{\mathrm{T}}^2$ of its associated tracks. The transverse and longitudinal impact parameters of a track are denoted by d_0 and z_0 respectively. This analysis categorises jets and leptons as *preselected* or *signal*, whose definitions are summarised in Table 5.2 and detailed below.

5.3.1 Preselected objects

Jets Energetic quarks and gluons hadronise to form collimated sprays of particles. These particles are grouped into jets, based on topological clusters of calorimeter energy deposits [353]. The anti-k_t algorithm [262,263] is used with distance parameter $R = 0.4$, which results in geometrically conical jets, when not overlapping. This analysis treats both photons and hadronically decaying tau leptons as jets. Jets must satisfy $p_{\mathrm{T}} > 20$ GeV after being calibrated in accord with Ref. [354].

Pileup can undesirably alter jet kinematics and two mitigation strategies are employed. One is based on calorimeter information where the expected energy contribution from pileup is subtracted according to the jet area [355]. The other is based on tracking

information where jets with $p_{\mathrm{T}} < 60$ GeV and $|\eta| < 2.4$ must satisfy the *Medium* working point of the Jet Vertex Tagger [355]. Further, events consistent with detector noise or non-collision backgrounds (such as muons from cosmic rays mis-reconstructed as jets) are rejected if they fail basic quality criteria [356].

Jets may contain hadrons composed of heavy flavour quarks. In particular, B-hadrons are sufficiently long-lived such that their vertices are displaced from the primary vertex by a few millimetres. This property is used to identify *b-tagged jets* using the multivariate *MV2c10* algorithm [357, 358]. This uses information from tracks, thus limiting its application to $|\eta| < 2.5$. A working point is chosen such that jets with B-hadrons from simulated $t\bar{t}$ events are identified with 85% efficiency. The corresponding rejection factors for jets initiated from charm quarks (light-flavour quarks or gluons) are 3 (34).

Electrons and muons Preselected electrons are reconstructed with $p_{\mathrm{T}} > 4.5$ GeV and $|\eta| < 2.47$. These satisfy the likelihood-based *VeryLoose* identification [359]. The calorimeter shower shapes of electrons and tracking information are used as inputs to the likelihood-based identification criteria.

Preselected muons are reconstructed using information from the tracker and muon spectrometer. These are identified using the *Medium* criterion defined in Ref. [360] and required to satisfy $p_{\mathrm{T}} > 4$ GeV, $|\eta| < 2.5$, and $|z_0 \sin\theta| < 0.5$ mm.

Overlap removal Preselected jets, electrons and muons are reconstructed independently, so an *overlap removal* procedure is employed to avoid ambiguity of identification. This is based on the distance measure $\Delta R_y = \sqrt{(\Delta y)^2 + (\Delta\phi)^2}$, where y is the rapidity. The procedure is as follows. For an electron sharing a track with a muon, discard the electron; this suppresses muon bremsstrahlung followed by a photon conversion. When a non-b-tagged jet and an electron are separated within $\Delta R_y < 0.2$, remove the jet. If a jet having fewer than three tracks with $p_{\mathrm{T}} > 0.5$ GeV is within $\Delta R_y < 0.4$ from a muon, discard the jet to suppress muon bremsstrahlung. Finally, for jets within $\Delta R_y < 0.4$ of electrons or muons, retain the jets and remove the electrons and muons to suppress heavy flavour quark decays.

5.3.2 Signal objects

Signal objects are a subset of those preselected, which are now described.

Jets and leptons Signal jets are required to have $p_{\mathrm{T}} > 30$ GeV, except that the b-tagging is applied to jets down to $p_{\mathrm{T}} > 20$ GeV to maximise rejection of top quark backgrounds.

Of the remaining electron candidates, signal electrons must additionally satisfy the likelihood-based *Tight* identification criteria [359], and the significance of the transverse impact parameter is required to be $|d_0/\sigma(d_0)| < 5$. For signal muons, the requirement $|d_0/\sigma(d_0)| < 3$ is imposed.

Isolation requirements are imposed on the remaining lepton candidates to suppress processes including jets mis-identified as leptons, photon conversions, and semi-leptonic decays of heavy-flavour hadrons, which are collectively referred to as *fake/nonprompt leptons*. Such processes contribute additional tracks or calorimeter deposits in a small cone around the candidate lepton compared with prompt leptons. Selections on various metrics are defined to quantify the activity nearby such leptons and define isolation criteria. These are detailed in Refs. [359, 360], where this analysis uses the *GradientLoose* [359] and *FixedCutTightTrackOnly* [360, 361] isolation criteria, which signal electrons and muons are required to satisfy, respectively. These are chosen based on signal efficiency and background rejection optimisation studies. However, if nearby tracks or calorimeter deposits are associated with preselected leptons, these are excluded from consideration in the isolation requirements. This is referred to as the *nearby isolation correction* developed in Ref. [362] and is applied in order to preserve efficiency for two leptons with low invariant mass, as often the case with the signals considered.

To correct for differences in the reconstruction efficiencies of electrons, muons and b-tagged jets between the simulated samples and data, small corrections referred to as *scale factors* are applied to the Monte Carlo. These scale factors for b-tagged jets correct differences in b-jet identification efficiencies as well as mis-identification rates of charm quark, and light-flavour quark (up, down or strange) or gluon initiated jets. The *tag-and-probe methods* detailed further in Refs. [359, 360] use $J/\psi \to ee/\mu\mu$ events to derive scale factors for the identification efficiencies of electrons and muons. Similar scale factors are applied for the isolation of electrons and muons, where Figure 5.5

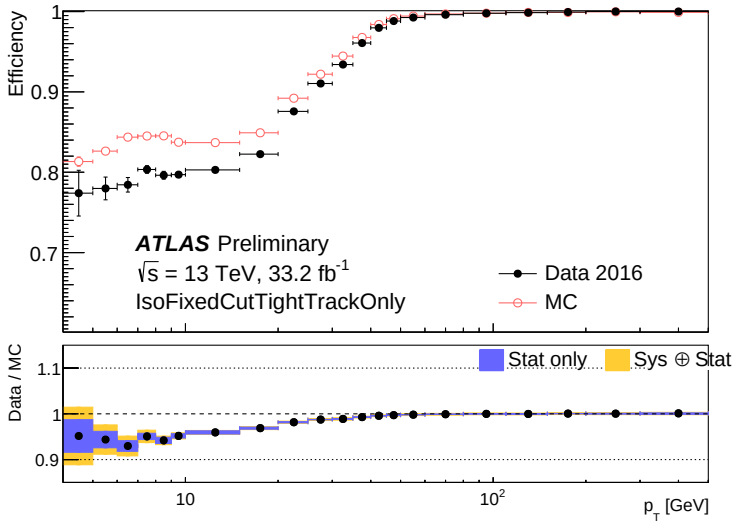

Figure 5.5: Figure reproduced from Ref. [361] showing the efficiency of the FixedCutTightTrackOnly isolation working point as a function of muon p_{T}. The black filled (red unfilled) circles denote the efficiencies measured in data (predicted from MC). The ratio of data / MC defines the scale factors used to correct MC in the analysis. This is determined using $Z \to \mu\mu$ events using the tag-and-probe method.

exemplifies this for muons used in this analysis.

The total electron and muon reconstruction efficiencies after imposing all these quality requirements are shown in Figure 5.6.

Missing transverse momentum If particles in the final state escape detection e.g. neutrinos and dark matter, the missing transverse momentum $\mathbf{p}_{\mathrm{T}}^{\mathrm{miss}}$ with magnitude $E_{\mathrm{T}}^{\mathrm{miss}}$ can be non-zero. This is defined as the negative vectorial sum of the transverse momenta $\mathbf{p}_{\mathrm{T}}^{i}$ of all reconstructed objects (electrons, muons and jets) and an additional soft term i.e. $\mathbf{p}_{\mathrm{T}}^{\mathrm{miss}} = -\sum_{i\in\{\mathrm{obj}\}} \mathbf{p}_{\mathrm{T}}^{i}$, where $\{\mathrm{obj}\} = \{\mathrm{electrons}, \mathrm{muons}, \mathrm{jets}, \mathrm{soft\ term}\}$. The soft term is constructed from all tracks that are not associated with any object, but remain associated with the primary vertex [363].

5.4 Search strategy

Existing searches for electroweakinos and sleptons use lepton triggers [197, 217, 277, 278], whose high thresholds have insufficient acceptance on low momentum leptons of compressed scenarios to allow sensitivity (Figure 5.7 left). Our strategy instead selects

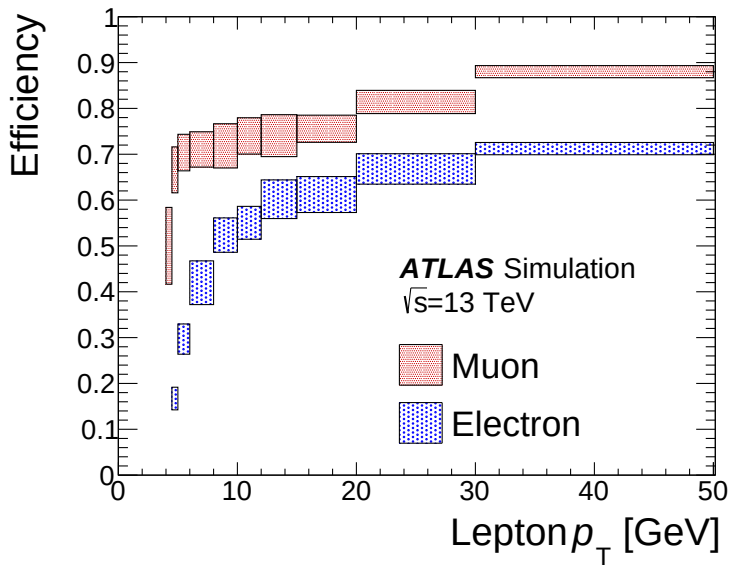

Figure 5.6: Summary of the lepton efficiencies when all the signal selections are applied for electrons (blue) and muons (red). This includes reconstruction, identification and isolation. This plot is made by a collaborator. Shown bands capture the range of values over all the signal Monte Carlo considered.

events using $E_{\mathrm{T}}^{\mathrm{miss}}$ triggers. For our signals, the large $E_{\mathrm{T}}^{\mathrm{miss}}$ arises from the invisible $\widetilde{\chi}_1^0$ states recoiling against hadronic initial state radiation (ISR), as illustrated in Figure 5.7 (right). Without ISR, the $E_{\mathrm{T}}^{\mathrm{miss}}$ is substantially lower as the $\widetilde{\chi}_1^0$ states carry away much of the momentum in nearly back-to-back configuration. This analysis targets decays from an off-shell Z boson or from slepton pairs, which always produce two same-flavour leptons with opposite electric charge (e^+e^- or $\mu^+\mu^-$).

The dominant backgrounds mimicking the signal are divided into two categories:

- *Irreducible*: two prompt leptons and $E_{\mathrm{T}}^{\mathrm{miss}}$ from neutrinos largely arise from $t\bar{t}, WW$ and $Z^{(*)}/\gamma^*(\rightarrow \tau\tau)$ + jets processes. These are estimated with the aid of MC simulation, as described in Subsection 5.5.1.

- *Reducible*: leptons that are nonprompt or fake (such as jets passing lepton requirements) arise from processes such as $W(\rightarrow \ell\nu)$ + jets. These fake/nonprompt leptons are the dominant reducible backgrounds and are estimated using the data-driven *Fake Factor* method outlined in Subsection 5.5.2.

Several kinematic variables are used to maximise the Higgsino and slepton signal and rejection of background processes. The search strategy first exploits features common to

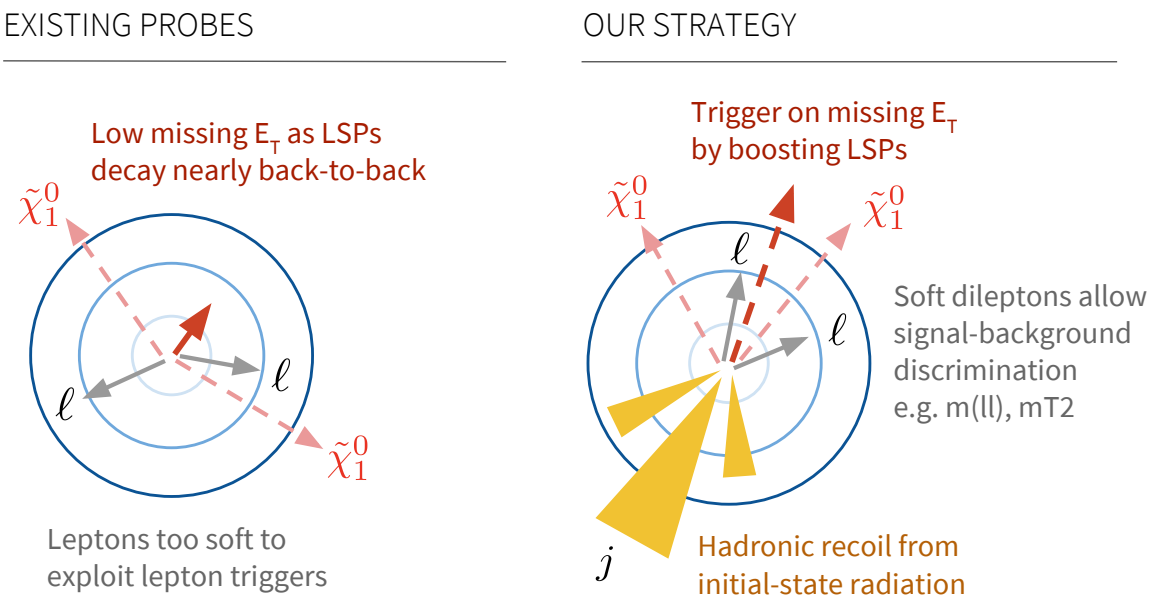

Figure 5.7: Schematic of the decays of compressed electroweak states and their detector kinematics. Left shows the issues of using existing lepton-trigger based strategies for probing compressed electroweak states. Right illustrates the initial-state radiation strategy to use the $E_{\mathrm{T}}^{\mathrm{miss}}$ triggers employed by this analysis.

these two signal scenarios (Subsection 5.4.1), before tuning the final signal regions (SRs) to target each optimally (Subsection 5.4.2). This optimisation was performed blinded without considering the data counts in the SRs, but kinematic distributions displayed in this section are produced after unblinding. The results of this sensitivity optimisation are summarised in Table 5.3 and discussed in detail below.

5.4.1 Selection common to all signal regions

The requirements on the following variables capitalise on features common to both the Higgsino and slepton signals.

Jet and $\mathbf{p}_{\mathrm{T}}^{\mathrm{miss}}$ back-to-back $E_{\mathrm{T}}^{\mathrm{miss}} > 200$ GeV, $p_{\mathrm{T}}^{j_1} > 100$ GeV and $\Delta\phi(j_1, \mathbf{p}_{\mathrm{T}}^{\mathrm{miss}}) > 2.0$. The $E_{\mathrm{T}}^{\mathrm{miss}}$ requirement ensures that data events are selected with $> 95\%$ efficiency by the trigger. The leading jet p_{T}, denoted as $p_{\mathrm{T}}^{j_1}$, must be large as significant hadronic activity is required to balance the $\mathbf{p}_{\mathrm{T}}^{\mathrm{miss}}$. In the case of the signal, this arises from initial state radiation to balance the $E_{\mathrm{T}}^{\mathrm{miss}}$. A large magnitude of the azimuthal angle $\Delta\phi(j_1, \mathbf{p}_{\mathrm{T}}^{\mathrm{miss}})$ between the leading jet and $\mathbf{p}_{\mathrm{T}}^{\mathrm{miss}}$ ensures such topologies are selected. The azimuthal angle between any jet and $\mathbf{p}_{\mathrm{T}}^{\mathrm{miss}}$ must satisfy $\min(\Delta\phi(\text{any jet}, \mathbf{p}_{\mathrm{T}}^{\mathrm{miss}})) > 0.4$ to reduce

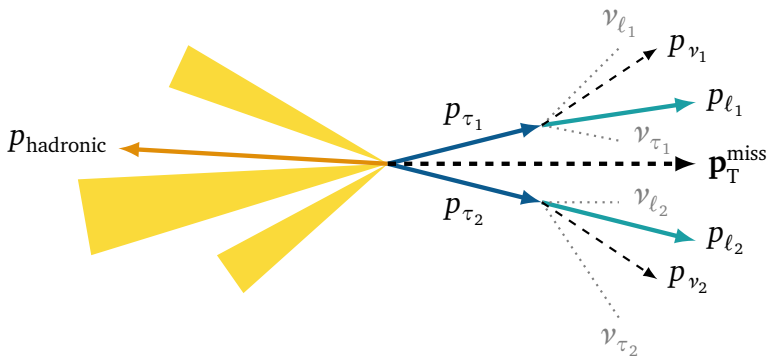

Figure 5.8: Schematic of the fully leptonic decays $\tau \to \nu_\tau \ell \nu_\ell$ of the $Z^{(*)}/\gamma^*(\to \tau\tau)$ + jets system used to define the $m_{\tau\tau}$ variable.

instrumental $E_{\text{T}}^{\text{miss}}$ from mis-measured jets. Jets with $p_{\text{T}} > 30$ GeV are used in this variable.

Veto b-tagged jets. The number of b-tagged jets is required to be zero. The b-tagging is applied to jets with $p_{\text{T}} > 20$ GeV using a configuration which identifies 85% of jets with b-hadrons from $t\bar{t}$ MC to maximise rejection of backgrounds with top quarks.

Lepton p_{T}. The lepton with the higher (lower) p_{T} in each pair is referred to as leading (subleading) lepton, which is written as $\ell_1(\ell_2)$. The leading lepton is required to satisfy $p_{\text{T}} > 5$ GeV, which is found to suppress fake/nonprompt leptons. The p_{T} thresholds for the subleading lepton remains as low as reconstruction is supported, at $p_{\text{T}} > 4.5$ (4) GeV for electrons (muons), to maximise signal acceptance.

Ditau mass $m_{\tau\tau} \notin [0, 160]$ GeV. The $m_{\tau\tau}$ variable [290, 306, 312] is used to reconstruct $Z^{(*)}/\gamma^*(\to \tau\tau)$ + jets processes where both τ particles decay leptonically $\tau \to \nu_\tau \ell \nu_\ell$. Figure 5.8 illustrates the kinematics of this system schematically. This is defined by the signed square root of $m_{\tau\tau}^2 = 2p_{\ell_1} \cdot p_{\ell_2}(1+\xi_1)(1+\xi_2)$, i.e.

$$m_{\tau\tau} = \text{sign}\left(m_{\tau\tau}^2\right)\sqrt{\left|m_{\tau\tau}^2\right|}, \tag{5.2}$$

working in the boosted tau limit $p_\tau^2 \to 0$ GeV while p_{ℓ_1} and p_{ℓ_2} are the visible lepton four-momenta. The scalar ξ_i parameters are obtained by inverting the equation $\mathbf{p}_{\text{T}}^{\text{miss}} = \xi_1 \mathbf{p}_{\text{T}}^{\ell_1} + \xi_2 \mathbf{p}_{\text{T}}^{\ell_2}$, which uses the $\mathbf{p}_{\text{T}}^{\text{miss}}$ to constrain the momenta of the neutrino system p_{ν_i} from each i-th tau. This assumes that the taus from the Z are boosted such that the neutrinos and lepton are collinear with the parent tau. The p_{ν_i} is then well-approximated by a linear rescaling of the visible lepton momentum $p_{\nu_i} \approx \xi_i p_{\ell_i}$, resulting in the tau

momentum being $p_{\tau_i} = (1+\xi_i)p_{\ell_i}$. The $m^2_{\tau\tau}$ variable can have negative values when one of the p_{ℓ_i} has smaller magnitude than $E_{\mathrm{T}}^{\mathrm{miss}}$ and points in the opposite hemisphere to the $\mathbf{p}_{\mathrm{T}}^{\mathrm{miss}}$, as often the case in processes such as WW and the signal.

Figure 5.9a shows the kinematic distributions for this variable after all the requirements common to all SRs (Table 5.3) are imposed. When all the selections defining the electroweakino SRs in Table 5.3 are applied, the $m_{\tau\tau} \in [0, 160]$ GeV veto has a signal efficiency of 75% for the Higgsino model point $m(\widetilde{\chi}_2^0, \widetilde{\chi}_1^0) = (110, 100)$ GeV, and 87% of the $Z^{(*)}/\gamma^*(\rightarrow \tau\tau)$+jets background is rejected.

5.4.2 Signal regions optimised for Higgsinos and sleptons

For the Higgsino signals, the two leptons arise predominantly from a three-body decay $\widetilde{\chi}_2^0 \rightarrow \ell\ell\widetilde{\chi}_1^0$. Meanwhile, a pair of two-body decays $\tilde{\ell} \rightarrow \ell\widetilde{\chi}_1^0$ yield the two leptons for slepton signals. Two sets of SRs are therefore optimised to exploit the kinematic differences between these distinct classes of decays. The SRs optimised for Higgsinos are also referred to as electroweakino SRs, given these are also used for the forthcoming wino–bino interpretation. Additional requirements are made on the following variables.

Dilepton distance $\Delta R_{\ell\ell} = \sqrt{(\Delta\eta_{\ell\ell})^2 + (\Delta\phi_{\ell\ell})^2}$. This is required in all cases to fulfil $\Delta R_{\ell\ell} > 0.05$ to suppress nearly collinear lepton pairs from photon conversions or muons with spurious tracks from shared inner detector hits. Due to the Lorentz boost of $\widetilde{\chi}_2^0$ from the hadronic recoil, the dilepton pair from the $\widetilde{\chi}_2^0$ decay typically has smaller separation in electroweakino signals than those from background or slepton signals as shown in Figure 5.9b, where the two leptons typically arise from different legs of the decay. Thus, the $\Delta R_{\ell\ell} < 2.0$ selection is imposed for electroweakino SRs.

Transverse mass $m_{\mathrm{T}}^{\ell_1}$. This variable is defined as

$$m_{\mathrm{T}}^{\ell_1} = \sqrt{2\left(E_{\mathrm{T}}^{\mathrm{miss}} E_{\mathrm{T}}^{\ell_1} - \mathbf{p}_{\mathrm{T}}^{\mathrm{miss}} \cdot \mathbf{p}_{\mathrm{T}}^{\ell_1}\right)}, \tag{5.3}$$

which is required to be less than 70 GeV only for electroweakino SRs. For electroweakinos, the leading lepton from the signals tend to be closer to $\mathbf{p}_{\mathrm{T}}^{\mathrm{miss}}$ than for background processes. This selection is not imposed on the slepton signals as the leading lepton tends to be more well separated from the $\mathbf{p}_{\mathrm{T}}^{\mathrm{miss}}$ (the requirement on $m_{\mathrm{T2}}^{m_\chi}$ to be described below is an implicit requirement on the transverse mass). Figure 5.9d shows signal and background distributions in this variable.

Variable	Requirement	
Number of leptons	$= 2$	
Lepton charge and flavour	e^+e^- or $\mu^+\mu^-$	
Leading lepton $p_{\mathrm{T}}^{\ell_1}$	> 5 (5) GeV for electron (muon)	
Subleading lepton $p_{\mathrm{T}}^{\ell_2}$	> 4.5 (4) GeV for electron (muon)	
$\Delta R_{\ell\ell}$	> 0.05	
$m_{\ell\ell}$	$\in [1, 60]$ GeV excluding $[3.0, 3.2]$ GeV	
$E_{\mathrm{T}}^{\mathrm{miss}}$	> 200 GeV	
Leading jet $p_{\mathrm{T}}^{j_1}$	> 100 GeV	
$\Delta\phi(j_1, \mathbf{p}_{\mathrm{T}}^{\mathrm{miss}})$	> 2.0	
$\min\big(\Delta\phi(\text{any jet}, \mathrm{p}_{\mathrm{T}}^{\mathrm{miss}})\big)$	> 0.4	
Number of b-jets $N_{\text{b-jets}}$	$= 0$	
$m_{\tau\tau}$	< 0 or > 160 GeV	
	Electroweakino SRs	Slepton SRs
$\Delta R_{\ell\ell}$	< 2	—
$m_{\mathrm{T}}^{\ell_1}$	< 70 GeV	—
$E_{\mathrm{T}}^{\mathrm{miss}}/H_{\mathrm{T}}^{\mathrm{lep}}$	$> \max(5, 15 - 2m_{\ell\ell}/\mathrm{GeV})$	$> \max\big(3, 15 - 2\big(m_{\mathrm{T2}}^{100}/\mathrm{GeV} - 100\big)\big)$
Binned in	$m_{\ell\ell}$	m_{T2}^{100}

Table 5.3: Summary of event selection common to all SRs, as well as those only required for the electroweakino and slepton SRs. The binning scheme used to define the final SRs is shown in Table 5.4.

Dilepton invariant mass $m_{\ell\ell}$. This is correlated with the electroweakino mass splittings. The $m_{\ell\ell}$ from the $\widetilde{\chi}_2^0$ decay is kinematically bound by the mass splitting $\Delta m(\widetilde{\chi}_2^0, \widetilde{\chi}_1^0)$, i.e. $m_{\ell\ell} \leq \Delta m(\widetilde{\chi}_2^0, \widetilde{\chi}_1^0)$, whereas this endpoint is absent in background processes (and for the slepton signals), as illustrated by Figure 5.10a. The $m_{\ell\ell}$ is binned to define the electroweakino SRs, to be further described below. The range $m_{\ell\ell} \in [3, 3.2]$ GeV is vetoed to suppress J/ψ resonances. The requirement of $m_{\ell\ell} > 1$ GeV is applied throughout for the same reason as the $\Delta R_{\ell\ell} > 0.05$ described above. Meanwhile, the condition $m_{\ell\ell} < 60$ GeV is imposed to reduce leptonically decay Z boson processes.

Stransverse mass $m_{\mathrm{T2}}^{m_\chi}$. This quantity is correlated with the slepton mass splitting. It is defined by [159, 160]

$$m_{\mathrm{T2}}^{m_\chi}\left(p_{\ell_1}, p_{\ell_2}, \mathbf{p}_{\mathrm{T}}^{\mathrm{miss}}\right) = \min_{\mathbf{q}_{\mathrm{T}}}\Big(\max\Big[m_{\mathrm{T}}\left(\mathbf{p}_{\mathrm{T}}^{\ell_1}, \mathbf{p}_{\mathrm{T}}^{\mathrm{miss}}, m_\chi\right), m_{\mathrm{T}}\left(\mathbf{p}_{\mathrm{T}}^{\ell_2}, \mathbf{p}_{\mathrm{T}}^{\mathrm{miss}} - \mathbf{q}_{\mathrm{T}}, m_\chi\right)\Big]\Big), \quad (5.4)$$

where m_χ is the hypothesised mass of the invisible particles and the transverse vector $\mathbf{q}_{\mathrm{T}}$ with magnitude q_{T} is required to minimise the larger of the two transverse masses

Electroweakino SRs							
SRee-$m_{\ell\ell}$, SR$\mu\mu$-$m_{\ell\ell}$	$[1,3]$	$[3.2,5]$	$[5,10]$	$[10,20]$	$[20,30]$	$[30,40]$	$[40,60]$
SR$\ell\ell$-$m_{\ell\ell}$	$[1,3]$	$[1,5]$	$[1,10]$	$[1,20]$	$[1,30]$	$[1,40]$	$[1,60]$
Slepton SRs							
SRee-m_{T2}^{100}, SR$\mu\mu$-m_{T2}^{100}		$[100,102]$	$[102,105]$	$[105,110]$	$[110,120]$	$[120,130]$	$[130,\infty]$
SR$\ell\ell$-m_{T2}^{100}		$[100,102]$	$[100,105]$	$[100,110]$	$[100,120]$	$[100,130]$	$[100,\infty]$

Table 5.4: Binning scheme for the $m_{\ell\ell}$ (electroweakino SRs) and m_{T2}^{100} (slepton SRs) variables. Units are in GeV.

defined by

$$m_{\mathrm{T}}\left(\mathbf{p}_{\mathrm{T}}^{\ell}, \mathbf{q}_{\mathrm{T}}, m_{\chi}\right) = \sqrt{m_{\ell}^2 + m_{\chi}^2 + 2\left(\sqrt{m_{\ell}^2 + p_{\mathrm{T}}^2}\sqrt{m_{\chi}^2 + q_{\mathrm{T}}^2} - \mathbf{p}_{\mathrm{T}}^{\ell} \cdot \mathbf{q}_{\mathrm{T}}\right)}. \tag{5.5}$$

For a given slepton signal with slepton mass $m(\tilde{\ell})$ and LSP mass $m(\tilde{\chi}_1^0)$, the inequality $m_{\mathrm{T2}}^{m_\chi} \leq m(\tilde{\ell})$ is satisfied for the choice $m_\chi = m(\tilde{\chi}_1^0)$. Background events do not have such kinematic endpoints, allowing greater discrimination for smaller $\Delta m(\tilde{\ell}, \tilde{\chi}_1^0)$. This analysis chooses $m_{\mathrm{T2}}^{m_\chi}$ with a single $m_\chi = 100$ GeV for simplicity, denoted m_{T2}^{100}, based on the expected sensitivity of this analysis. Figure 5.10b shows the distribution of slepton signals and the correlation with the mass splitting absent in background events.

Missing momentum vs lepton ratio $E_{\mathrm{T}}^{\mathrm{miss}}/H_{\mathrm{T}}^{\mathrm{lep}}$. This variable exploits the large scale separation between the low momentum leptons typically of order 10 GeV relative to the $E_{\mathrm{T}}^{\mathrm{miss}} > 200$ GeV in the signals. By contrast, background processes such as $WW \to \ell\nu\ell\nu$ have significantly more energetic leptons, such that the scalar sum of the lepton momenta $H_{\mathrm{T}}^{\mathrm{lep}} = \sum_i p_{\mathrm{T}}^{\ell_i}$ favours larger values than those from the signals.

The discriminating power of $E_{\mathrm{T}}^{\mathrm{miss}}/H_{\mathrm{T}}^{\mathrm{lep}}$ improves for smaller mass splittings. This is illustrated in Figure 5.10, which shows the kinematic distributions of the total background and various benchmark signals, projected into the $E_{\mathrm{T}}^{\mathrm{miss}}/H_{\mathrm{T}}^{\mathrm{lep}}$ vs $m_{\ell\ell}$ (m_{T2}^{100}) plane for the electroweakino (slepton) SRs. The signals are bounded from above by the $m_{\ell\ell}$ or m_{T2}^{100} variable due to the aforementioned kinematic endpoints. The red solid line denotes the requirements imposed on $E_{\mathrm{T}}^{\mathrm{miss}}/H_{\mathrm{T}}^{\mathrm{lep}}$, which are allowed to vary according to the inferred signal mass splitting:

$$E_{\mathrm{T}}^{\mathrm{miss}}/H_{\mathrm{T}}^{\mathrm{lep}} > \begin{cases} \max\left(5, 15 - 2m_{\ell\ell}/\mathrm{GeV}\right), & \text{electroweakino SRs,} \\ \max\left(3, 15 - 2\left[m_{\mathrm{T2}}^{100}/\mathrm{GeV} - 100\right]\right), & \text{slepton SRs.} \end{cases} \tag{5.6}$$

The factor of two is applied as the values of the $m_{\ell\ell}$ or $(m_{\mathrm{T2}}^{100} - 100$ GeV) proxies for signal

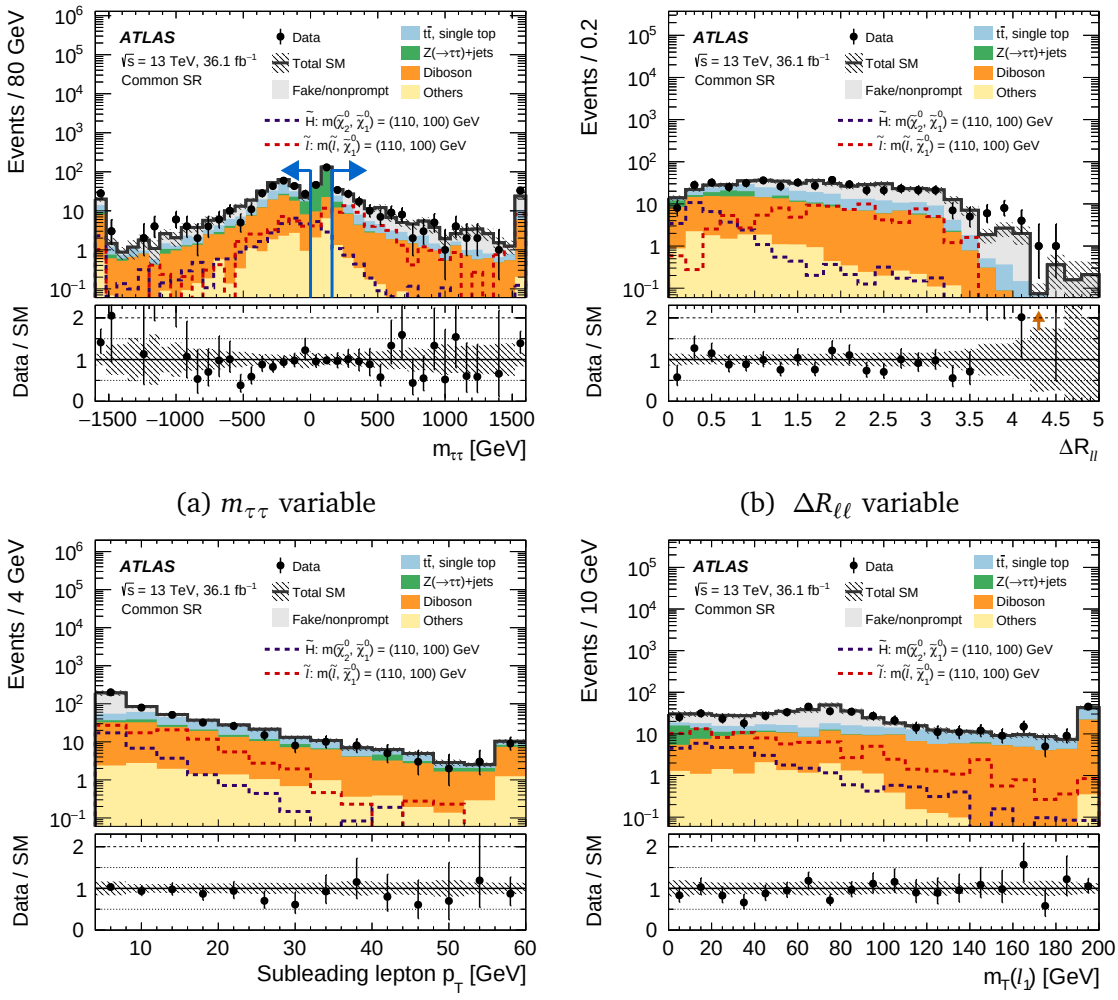

(a) $m_{\tau\tau}$ variable

(b) $\Delta R_{\ell\ell}$ variable

(c) Subleading lepton p_{T}

(d) $m_{\mathrm{T}}(\ell_1)$ variable

Figure 5.9: Kinematic distributions in a selection of variables when the requirements common to both the electroweakino and slepton SRs in Table 5.3 are applied. The blue arrow indicates the selection to be imposed. Background processes containing fewer than two prompt leptons are categorised as 'Fake/nonprompt'. The category 'Others' contains rare backgrounds such as triboson and Higgs boson. The dashed lines denote the benchmark signals for the Higgsino (dark purple) and slepton (red) models.

mass splitting are on average approximately half of the underlying signal Δm. A lower minimum value of 3 is used for sleptons to retain sensitivity to moderately compressed mass splittings $\Delta m(\tilde{\ell}, \tilde{\chi}_1^0) \sim 15$ GeV.

Table 5.4 (upper) defines the SRs optimised for Higgsino sensitivity. The $m_{\ell\ell}$ variable is used to construct several non-overlapping regions for analysis. These are further divided into ee and $\mu\mu$ channels, labelled by SRee-$m_{\ell\ell}$ and SR$\mu\mu$-$m_{\ell\ell}$ respectively. The

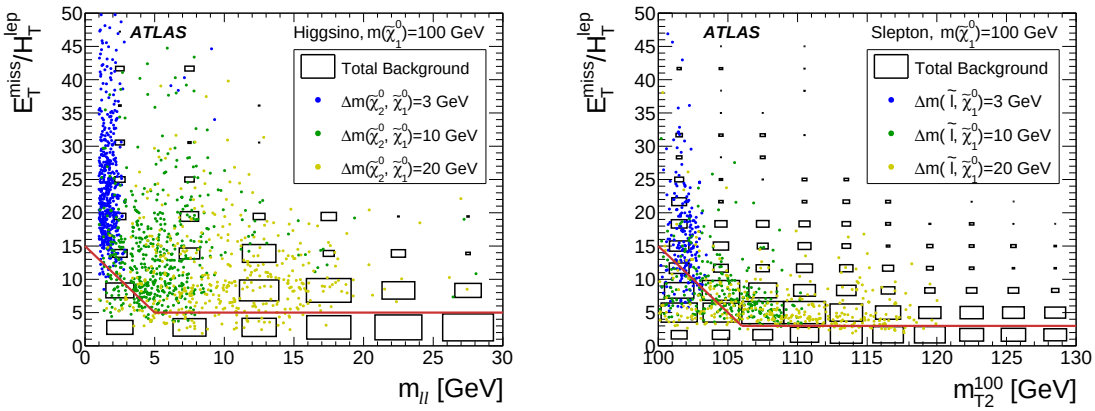

(a) Electroweakino SRs (b) Slepton SRs

Figure 5.10: Two-dimensional distributions of the backgrounds (boxes) and benchmark signals (circles) in the electroweakino (left) and slepton (right) SRs before the requirement in the variables plotted are imposed. Events below the red solid lines are rejected by the requirement on $E_{\mathrm{T}}^{\mathrm{miss}}/H_{\mathrm{T}}^{\mathrm{lep}}$. These plots were made by a collaborator.

$E_{\mathrm{T}}^{\mathrm{miss}}/H_{\mathrm{T}}^{\mathrm{lep}}$, $\Delta R_{\ell\ell}$, and $m_{\mathrm{T}}^{\ell_1}$ requirements are applied to all these SRs. An analogous set of bins are defined in Table 5.4 (lower) optimised for slepton sensitivity. Twelve non-overlapping regions binned in m_{T2}^{100} are defined, which are then also split by ee and $\mu\mu$ channels. When setting exclusion limits on the electroweakino (slepton) signals, only the non-overlapping $m_{\ell\ell}$ (m_{T2}^{100}) regions are simultaneously fit and statistically combined to improve sensitivity, as described in Section 5.7.

Figure 5.11 shows the signal acceptances $\mathscr{A}$ in the SRs prior to any detector effects, and before any of the binned selection has been applied. These selections are implemented in the SimpleAnalysis package, whose code is available on HepData in the auxiliary material of Ref. [4]. For Higgsino signals in the $\widetilde{\chi}_2^0\widetilde{\chi}_1^\pm, \widetilde{\chi}_2^0\widetilde{\chi}_1^0$ processes, the $\mathscr{A}$ are typically $\sim 10^{-3}$ to 10^{-4} in the electroweakino SR, whereas $\mathscr{A}$ for the $\widetilde{\chi}_1^+\widetilde{\chi}_1^-$ process are typically an order of magnitude lower. Meanwhile for slepton signals in the slepton SR, these are typically an order of magnitude larger at $\sim 10^{-2}$ to 10^{-3}. This difference dominantly arises due to the $Z^* \to \ell\ell$ branching fraction for electroweakinos.

Figure 5.12 shows the efficiency ϵ of the SR selection, which characterises the effects of the detector response and reconstruction algorithms. These are the fraction of events that enter the SR after these effects are included out of those produced, divided by the acceptance $\mathscr{A}$ calculated by SimpleAnalysis. For the signals considered, the typical values of ϵ are around 30 to 50%, dominated by lepton reconstruction efficiencies.

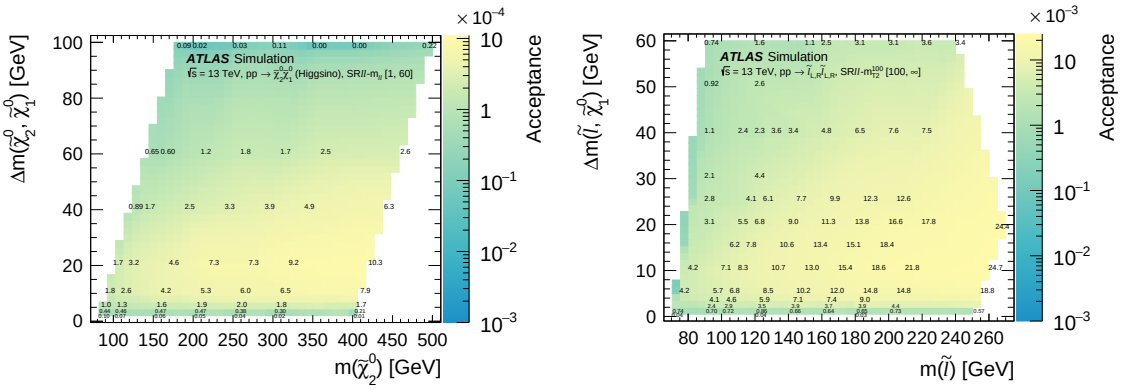

(a) Higgsino $\tilde{\chi}_2^0\tilde{\chi}_1^0$ SR$\ell\ell$-$m_{\ell\ell}$ $[1, 60]$ (b) Slepton $\tilde{\ell}\tilde{\ell}$ SR$\ell\ell$-m_{T2}^{100} $[100, \infty]$

Figure 5.11: Signal acceptance $\mathscr{A}$ in the SRs labelled by the captions without detector effects applied. This is defined as the number of events passing the SR selections N_{SR} divided by cross-section times luminosity $\sigma \times L$, i.e. $\mathscr{A} = N_{\mathrm{SR}}^{\text{no detector}}/(\sigma \times L)$.

5.5 Background estimation

Standard Model processes with jets, two leptons and missing transverse momentum can mimic the signals considered. Figure 5.13 schematically summarises how the background processes enter the SRs and their estimation strategy detailed below.

5.5.1 Irreducible backgrounds

The dominant irreducible background processes include $t\bar{t}$, single top (mainly tW), diboson WW, WZ where the third lepton is not identified, and $Z^{(*)}/\gamma^*(\rightarrow \tau\tau)+$jets. For the $t\bar{t}$, single top, and $Z^{(*)}/\gamma^*(\rightarrow \tau\tau)+$jets processes, the MC simulations are normalised in a simultaneous fit to the observed data counts in control regions (CR) using statistical procedures outlined in Section 5.7. The CRs are designed to be statistically disjoint from the SRs, enriched in a particular background process, have minimal contamination from signals considered, and exhibit kinematic properties similar to the SRs. The event rates in the SRs are then predicted by extrapolating the simulated MC distributions from the CRs. This extrapolation and the modelling of remaining backgrounds are validated using events in dedicated validation regions (VR). The VRs do not constrain the fit, and are orthogonal to the CRs and SRs. These regions are summarised in Table 5.5.

The prompt dileptonic decays of $t\bar{t}$ and tW, diboson WW, and $Z^{(*)}/\gamma^*(\rightarrow \tau\tau)+$jets processes yield same-flavour (SF) lepton pairs ($ee+\mu\mu$) with equal rate as those with

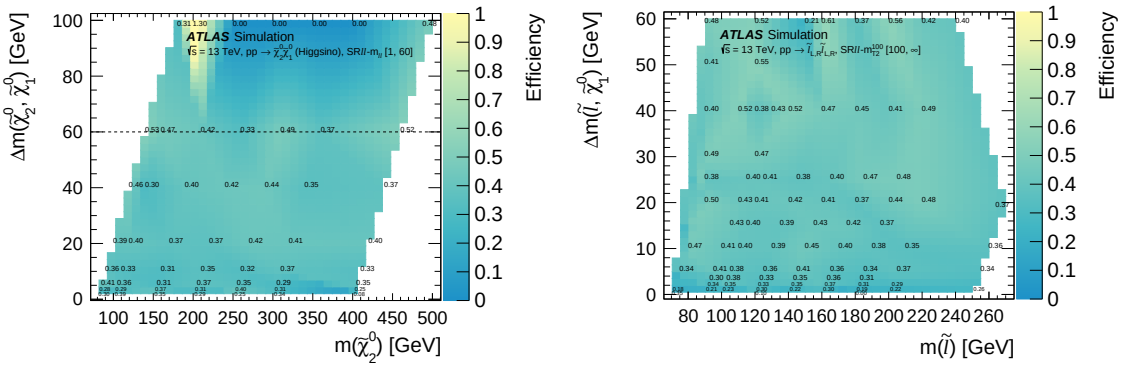

(a) Higgsino $\widetilde{\chi}_2^0\widetilde{\chi}_1^0$ SR$\ell\ell$-$m_{\ell\ell}$ $[1, 60]$ (b) Slepton $\tilde{\ell}\tilde{\ell}$ SR$\ell\ell$-m_{T2}^{100} $[100, \infty]$

Figure 5.12: Efficiency ϵ in the SRs labelled by the subfigure captions. This is defined as the fraction of events passing SR selection including detector effects $N_{\mathrm{SR}}^{\mathrm{detector}}/(\sigma \times L)$, where $\sigma \times L$ is the cross-section times luminosity, divided by the acceptance $\mathscr{A}$, i.e. $\epsilon = N_{\mathrm{SR}}^{\mathrm{detector}}/(\mathscr{A} \times \sigma \times L)$. The dashed line indicates the maximum value of the $m_{\ell\ell}$ considered in the SR.

different-flavour (DF) pairs ($e\mu + \mu e$), where the left (right) lepton of each pair denotes the leading (subleading) lepton. To enhance the statistical constraining power of the CRs, the definitions consider all possible flavour assignments ($ee + \mu\mu + e\mu + \mu e$).

Control regions Two single-bin CRs are considered, denoted CR-top and CR-tau. Requirements common to all SRs in Table 5.3 are imposed, except otherwise stated in Table 5.5. Event yields before the fit are displayed in Table 5.6 under 'pre-fit SM events'. CR-top is a sample enhanced in top quarks, selected by requiring at least one b-tagged jet and has 1100 observed events. The $N_{\text{b-jet}}$ distribution (Figure 5.14a) shows MC predictions of the data being compatible within the uncertainties. A similar compatibility is observed for the subleading lepton p_{T} down to 4 GeV (Figure 5.14b). These data are used to normalise the tW and $t\bar{t}$ MC samples, which have 72% purity in this region. Between these two processes, top quark pairs dominate over single top contributions, comprising 90% and 10% respectively.

A sample enriched in the $Z^{(*)}/\gamma^*(\rightarrow \tau\tau)$ + jets processes, with 80% purity, used to construct CR-tau. This has 68 observed events and is obtained by selecting events satisfying $60 < m_{\tau\tau} < 120$ GeV. The $m_{\tau\tau}$ (Figure 5.14c) and $m_{\ell\ell}$ (Figure 5.14d) distributions show MC modelling the data, which are compatible within the uncertainties. The ratio

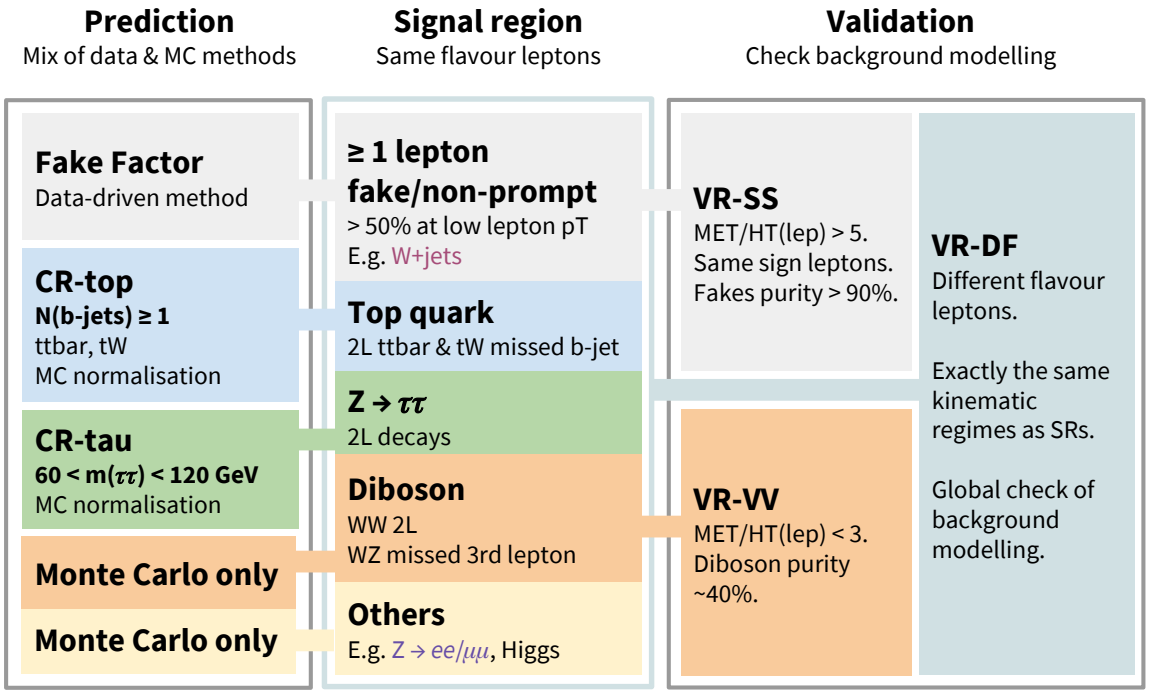

Figure 5.13: Schematic overview of the background estimation strategy. Displayed are the main categories of background processes which enter the signal region (centre), the methods used to predict their yields (left), and event samples selected to validate the background modelling (right).

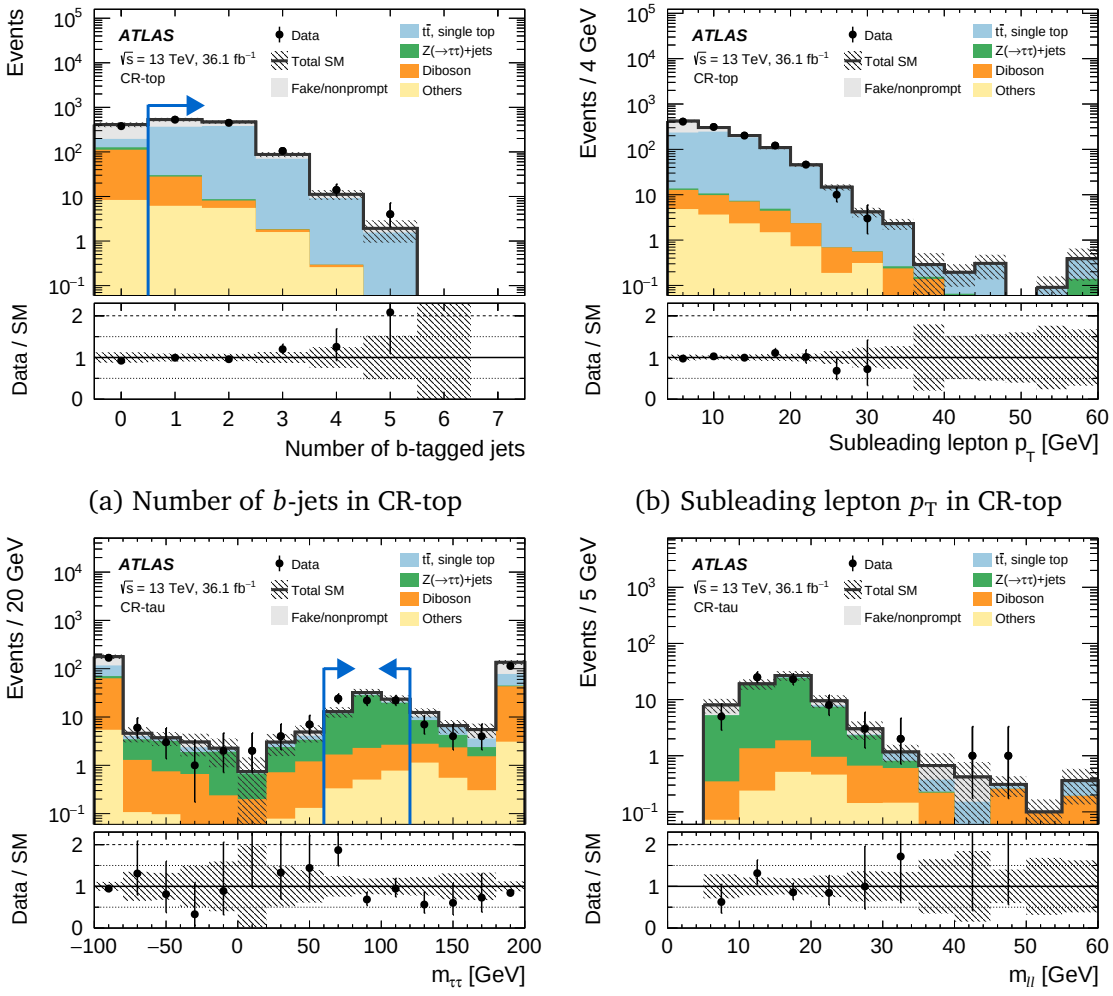

(a) Number of b-jets in CR-top

(b) Subleading lepton p_{T} in CR-top

(c) $m_{\tau\tau}$ variable in CR-tau

(d) $m_{\ell\ell}$ variable in CR-tau

Figure 5.14: The distributions of the control regions in a selection of kinematic variables, where the arrow, if present, indicates the final requirement used to define the region. Background processes containing fewer than two prompt leptons are categorised as 'Fake/nonprompt'. The category 'Others' contains rare backgrounds such as triboson and Higgs boson. The uncertainty bands plotted include all statistical and systematic uncertainties. The far left (right) bin includes underflow (overflow).

$E_{\mathrm{T}}^{\mathrm{miss}}/H_{\mathrm{T}}^{\mathrm{lep}}$ is required to take values between 4 and 8 to reduce potential contamination from signal events.

For all the Higgsino, wino–bino and slepton signals considered, the signal contamination is on average 3% and at most 11% in these CRs.

Validation regions A sample enriched in diboson events is selected using a $E_{\mathrm{T}}^{\mathrm{miss}}/H_{\mathrm{T}}^{\mathrm{lep}} < 3$ requirement. This defines a validation region VR-VV to check the modelling of the diboson background and the assigned systematic uncertainties. This has a purity of approximately 40% diboson, with the remainder mostly from fake/nonprompt and $t\bar{t}$. The diboson samples are generated in SHERPA according to lepton multiplicity, and is dominated by 2ℓ processes at 85% followed by 15% 3ℓ contributions from $WZ \to \ell\nu\ell\ell$ where one of the leptons is not reconstructed, while 4ℓ processes are negligible. Studies using diboson samples generated using POWHEG show that $WW \to \ell\nu\ell\nu$ dominates in 2ℓ processes, while $ZZ \to \ell\ell\nu\nu$ is negligible. The signal contamination is 8% at most.

Given that this analysis only probes signals decaying to same flavour ($ee, \mu\mu$) lepton pairs, VRs are constructed to have identical kinematic selection as the SRs, except requiring different flavour pairs ($e\mu, \mu e$), which are denoted by VRDF-$m_{\ell\ell}$ and VRDF-m_{T2}^{100}. These are used to validate the overall background estimation within the same kinematic regime as the SR, whose yields will be displayed in Figure 5.17.

Backgrounds estimated using MC labelled 'Others' comprise the remaining rare top ($3t, 4t, t\bar{t}+WW,\ t+Z$), Higgs boson, and triboson processes in Table 5.1. These contribute at most 10% and is typically less than 5% in different regions. Within 'Others', Higgs boson processes typically contribute more than half, except in CR-top where top quark pairs produced in association with a vector boson $t\bar{t}+V$ dominates. No Drell–Yan MC processes are included as these are found to be negligible.

5.5.2 Reducible backgrounds

Two sources of reducible backgrounds are considered: processes where fewer than two leptons are prompt, and those where the $E_{\mathrm{T}}^{\mathrm{miss}}$ is instrumental in origin.

Fake/nonprompt leptons Backgrounds with fewer than two prompt leptons, such as from photon conversions or semi-leptonic decays of b-hadrons, are categorised as

Region	SR orthogonality	Additional requirements	Flavour
CR-top	$N_{\text{b-jets}} \geq 1$	$E_{\text{T}}^{\text{miss}}/H_{\text{T}}^{\text{lep}} > 5$	$ee + \mu\mu + e\mu + \mu e$
CR-tau	$m_{\tau\tau} \in [60, 120]$ GeV	$E_{\text{T}}^{\text{miss}}/H_{\text{T}}^{\text{lep}} \in [4, 8]$	$ee + \mu\mu + e\mu + \mu e$
VR-VV	$E_{\text{T}}^{\text{miss}}/H_{\text{T}}^{\text{lep}} < 3$	—	$ee + \mu\mu + e\mu + \mu e$
VR-SS	Same sign $\ell^{\pm}\ell^{\pm}$	$E_{\text{T}}^{\text{miss}}/H_{\text{T}}^{\text{lep}} > 5$	$ee + \mu e, \mu\mu + e\mu$
VRDF-$m_{\ell\ell}$	$e\mu + \mu e$	$E_{\text{T}}^{\text{miss}}/H_{\text{T}}^{\text{lep}} > \max(5, 15 - 2m_{\ell\ell}/\text{GeV}), \Delta R_{\ell\ell} < 2, m_{\text{T}}^{\ell_1} < 70$ GeV	$e\mu + \mu e$
VRDF-m_{T2}^{100}	$e\mu + \mu e$	$E_{\text{T}}^{\text{miss}}/H_{\text{T}}^{\text{lep}} > \max\left(3, 15 - 2\left(m_{\text{T2}}^{100}/\text{GeV} - 100\right)\right)$	$e\mu + \mu e$

Table 5.5: Control (CR) and validation regions (VR) defined to have the same selection common to all regions in Table 5.3, except those listed here. The left (right) lepton of each pair denotes the leading (subleading) lepton.

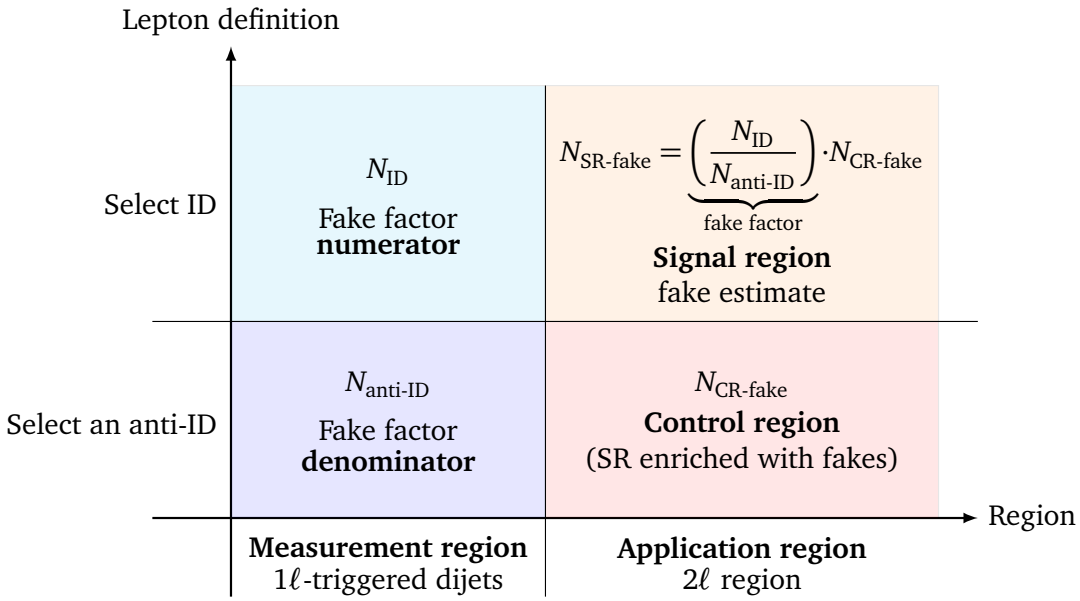

Figure 5.15: Schematic of the Fake Factor method.

fake/nonprompt. An example such source is the $W(\rightarrow \ell\nu)$ + jets process. Since MC simulation is not expected to model these processes accurately, the data-driven Fake Factor method [364] is employed.

The Fake Factor method is schematically illustrated in Figure 5.15. First, a set of criteria, denoted ID, are the same as signal leptons. A second set has at least one of the identification, isolation or impact parameter requirements loosened or inverted with respect to ID leptons. These are referred to as anti-ID and are an orthogonal sample enriched in fake/nonprompt leptons. Table 5.7 summarises these definitions.

The Fake Factor procedure aims to quantify what fraction of fake/nonprompt leptons passes the ID criteria and therefore enters the SR; this kinematic regime is the *application*

Region	CR-top	CR-tau	VR-VV	VR-SS $ee + \mu e$	VR-SS $\mu\mu + e\mu$
Observed events	1100	68	241	51	125
Fitted SM events	1100 ± 33	68 ± 8	245 ± 27	72 ± 29	111 ± 25
Fake/nonprompt leptons	270 ± 60	6 ± 4	49 ± 13	67 ± 29	104 ± 25
Diboson	24.7 ± 3.3	5.0 ± 1.0	99 ± 17	4.4 ± 1.0	6.2 ± 1.0
$Z(\to \tau\tau)$+jets	2.7 ± 1.7	53 ± 9	22 ± 5	$0.012^{+0.012}_{-0.012}$	$0.01^{+0.21}_{-0.01}$
$t\bar{t}$, single top	790 ± 70	2.4 ± 0.9	61 ± 14	$0.01^{+0.10}_{-0.01}$	$0.01^{+0.10}_{-0.01}$
Others	14 ± 7	1.6 ± 0.9	14 ± 7	0.19 ± 0.12	$0.19^{+0.28}_{-0.19}$
Pre-fit SM events	1080 ± 60	89 ± 6	252 ± 27	72 ± 29	111 ± 25
Fake/nonprompt leptons	270 ± 60	5.9 ± 3.5	49 ± 13	67 ± 29	104 ± 25
Diboson	24.7 ± 3.3	5.0 ± 1.1	99 ± 17	4.4 ± 1.0	6.2 ± 1.0
$Z(\to \tau\tau)$+jets	3.8 ± 2.1	74 ± 5	30 ± 5	$0.016^{+0.016}_{-0.016}$	$0.01^{+0.30}_{-0.01}$
$t\bar{t}$, single top	771 ± 10	2.4 ± 0.8	59 ± 13	$0.01^{+0.10}_{-0.01}$	$0.01^{+0.10}_{-0.01}$
Others	14 ± 7	1.6 ± 0.9	14 ± 7	0.19 ± 0.12	$0.19^{+0.29}_{-0.19}$

Table 5.6: Event yields in the CR and VRs common to the analysis, normalised to an integrated luminosity of 36.1 fb^{-1}. The fitted SM events are obtained from the control regions using the background-only fit. Pre-fit SM events expectations are given for comparison. Background processes containing fewer than two prompt leptons are categorized as 'Fake/nonprompt'. The category 'Others' contains rare backgrounds from triboson, Higgs boson, and the remaining top-quark production processes listed in Table 5.1. The uncertainties shown are the combined statistical and systematic uncertainties. Uncertainties on the fitted yields are symmetric by construction, where the negative error is truncated when reaching to zero event yield.

Electrons	Muons
ID leptons	
$p_{\mathrm{T}} > 4.5$ GeV, $\lvert\eta\rvert < 2.47$	$p_{\mathrm{T}} > 4$ GeV, $\lvert\eta\rvert < 2.5$
$\lvert z_0 \sin\theta\rvert < 0.5$ mm, $\lvert d_0/\sigma(d_0)\rvert < 5$	$\lvert z_0 \sin\theta\rvert < 0.5$ mm, $\lvert d_0/\sigma(d_0)\rvert < 3$
Tight identification	Medium identification,
GradientLoose isolation	FixedCutTightTrackOnly isolation
Anti-ID leptons defined as ID leptons except the following requirements	
LooseAndBLayer identification	
AND (NOT Tight identification	($\lvert d_0/\sigma(d_0)\rvert > 3$
OR $\lvert d_0/\sigma(d_0)\rvert > 5$	OR NOT FixedCutTightTrackOnly isolation)
OR NOT GradientLoose isolation)	

Table 5.7: Definitions of ID and anti-ID leptons used for the Fake Factor method.

region. To calculate this, a sample of events is selected using prescaled single-lepton triggers, which is dominated by multijet processes enhanced in fake/nonprompt leptons, which is denoted the *measurement region*. Out of this sample, one can then measure the fraction of these events whose fake/nonprompt leptons pass the ID criteria, which is the *numerator*. The complement of this sample is the fraction of events with fake/nonprompt leptons that fail the ID requirements (they satisfy anti-ID), which forms the *denominator*. The ratio of yields in the numerator N_{ID} and denominator $N_{\text{anti-ID}}$ defines *fake factors*. These are p_{T}-dependent for electrons and muons. For muons, these are also computed separately for $N_{\text{b-jets}} = 0$ and $N_{\text{b-jets}} \geq 1$ selections.

To obtain the fake/nonprompt estimate $N_{\text{SR-fake}}$ in the SR, these fake factors are applied to the events satisfying the corresponding selection requirements $N_{\text{CR-fake}}$, except with an anti-ID lepton replacing an ID lepton, thus defining a 'CR-fake'. To a first order, this is applied event-by-event as

$$N_{\text{SR-fake}} = \underbrace{\left(\frac{N_{\text{ID}}}{N_{\text{anti-ID}}}\right)}_{\text{fake factor}} \cdot N_{\text{CR-fake}}. \tag{5.7}$$

More precisely, there are small contributions from prompt leptons to the N_{ID} and $N_{\text{anti-ID}}$, which are subtracted based on estimates using MC.

The yields from this procedure are cross-checked in validation regions, denoted VR-SS, which have similar kinematic selection as the SRs, but are enriched in fake/nonprompt leptons by requiring two leptons with the same electric charge. Fake/nonprompt leptons are found to be dominantly the subleading one, so the VR-SS is divided into $ee + \mu e$ and $\mu\mu + e\mu$ samples. Processes in which both leptons are fake/nonprompt are verified in data as negligible based on the rate of anti-ID leptons.

Instrumental $E_{\text{T}}^{\text{miss}}$ Background processes with no neutrinos can enter the SRs when the $E_{\text{T}}^{\text{miss}}$ is instrumental in origin, which occurs when the kinematics of visible objects are mis-measured by the detector. One such process is Drell–Yan $ee/\mu\mu$ production, where one of the associated jets is mis-measured. This contribution is estimated by MC, cross-checked with a data-driven procedure, and is found to be negligible.

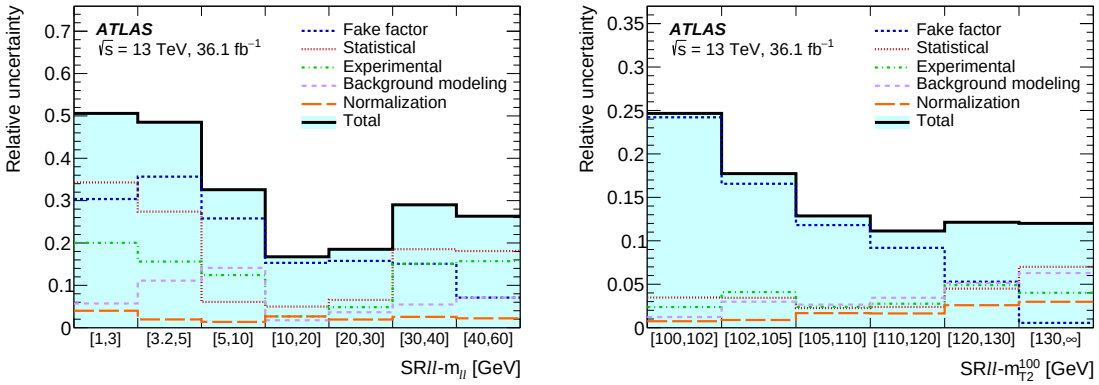

Figure 5.16: The relative systematic uncertainties in the background prediction in the exclusive electroweakino (left) and slepton (right) SRs using the background-only fit. Individual uncertainties can be correlated and do not necessarily add up in quadrature to the total uncertainty. I calculated the components and total systematic uncertainties using HISTFITTER, which were provided to a collaborator who made this plot.

5.6 Systematic uncertainties

The systematic uncertainties considered in the analysis originate from experimental sources, which include those from the Fake Factor method, and theoretical modelling of the MC samples. Figure 5.16 summarises the relative contributions of the various classes of systematic uncertainty to the background estimate in the exclusive SRs.

5.6.1 Experimental uncertainties

The largest source of systematic uncertainty arises from the Fake Factor method. Systematic uncertainties are treated as nuisance parameters in the likelihood fit in Section 5.7. These arise from the following sources:

- *Statistical uncertainties*. These arise from the limited sample size of measurement regions where the fake factors are derived. The uncertainties are implemented as independent nuisance parameters such that those for electrons are uncorrelated from muons, each of the anti-ID lepton p_{T} bins used are uncorrelated from one another. However, the same nuisance parameter is used regardless of CR, VR or SR, so are correlated across these regions. This source of systematic uncertainty is categorised under 'Statistical' (red), while the remaining sources discussed below are under 'Fake factor' (blue) in Figure 5.16.

- *Kinematic differences between measurement region and SR*. The measurement and signal regions can have different event and lepton kinematic properties, such as different proportions of fake/nonprompt leptons originating from heavy flavour decays. A systematic uncertainty of 25% is assigned based on the variations observed in the measured fake factors as a function of $|\eta|$.

- *VR-SS data vs predicted agreement*. Differences between the Fake Factor prediction and the observed yields in the VR-SS regions are used to assign further systematic uncertainties. These uncertainties and the *kinematic differences* uncertainties described above are uncorrelated between electrons and muons, while uncertainties for each of the two CRs are also uncorrelated from the SRs, but are otherwise correlated between all the SRs.

- *Prompt subtraction*. Uncertainties related to the subtraction of prompt leptons based on MC are considered but found to be negligible due to the small contributions of prompt leptons.

The remaining sources of systematic uncertainty categorised under 'Experimental' in Figure 5.16 are considered for both background and signal samples. These are predominantly due to jet energy scale and resolution, flavour-tagging, and the pileup reweighting procedure applied to samples. Contributions from the reconstruction and identification efficiencies of leptons, together with energy/momentum scale and resolution are considered but are typically subdominant, as indicated by 'Experimental' in Figure 5.16. The systematic uncertainties in the normalisation factors derived from the CRs are labelled 'Normalization' in Figure 5.16, which are typically a few percent at most.

5.6.2 Theoretical uncertainties

Background modelling Uncertainties in the theoretical modelling of background processes are labelled 'Background modeling' in Figure 5.16, which is not the dominant source in any SR. These are considered for the dominant backgrounds where MC samples are used, namely top ($t\bar{t}$ and tW), $Z^{(*)}/\gamma^{*}(\rightarrow \tau\tau)$ + jets, and diboson samples. For the remaining MC samples in the 'Other' category, a single 50% uncertainty is assigned. The following contributions are considered:

- *Generator parameters*. The generator parameters for the QCD renormalisation and factorisation scales are varied independently up and down by a factor or two, to evaluate its impact on the acceptance for each sample. Variations in the strong coupling α_s are also considered.

- *Choice of parton distribution function (PDF) set*. Uncertainties associated with the choice of PDF set are evaluated by taking the envelope of changes in acceptance after reweighting samples to the central values of the CT10 and MMHT PDF sets.

For the samples involving top quarks and $Z^{(*)}/\gamma^*(\rightarrow \tau\tau)$ + jets, these effects only affect the $m_{\ell\ell}$ and m_{T2}^{100} shape as the normalisation is constrained by the corresponding CRs in the fit. In the case of the diboson sample, variations in the QCD scale are found to dominate the modelling uncertainties in the SRs. These modelling uncertainties are calculated in each of the CRs and SR bins, but one nuisance parameter is used for each of the three sets of background samples considered such that their effects are correlated across all regions.

Signal modelling The most significant modelling uncertainty for the SUSY signals are those associated with ISR jets and the jet–parton matching. Uncertainties due to the choice of QCD renormalisation and factorisation scales are calculated by varying the `scalefact` parameter in MG5_aMC@NLO up and down by a factor of two. Uncertainties in choice of jet–parton matching scale are evaluated by simultaneously varying the `ktdurham` in MG5_aMC@NLO and `Merging::TMS` parameters in PYTHIA up and down by a factor of two. For the modelling of underlying event, along with initial and final state radiation in the PYTHIA tunes, five sets of variations defined in Ref. [319] with respect to the default A14 are used to evaluate these uncertainties. Following PDF4LHC recommendations [365], uncertainties from the choice of PDF sets are found to contribute 15%.

Each uncertainty is calculated as half the acceptance variation after imposing $E_{\mathrm{T}}^{\mathrm{miss}}$ and jet signal region requirements, before detector simulation. These are summed in quadrature, resulting in uncertainties of 25% for electroweakinos. For sleptons, the uncertainties increase with smaller mass splittings up to 50%, 40%, 30% for $\Delta m(\tilde{\ell}, \tilde{\chi}_1^0) \in [0,1], [1,2], [2,4]$ GeV. One way to constrain these ISR uncertainties is by measuring the

Normalisation parameter	Control region	MC samples applied	Value
μ_{top}	CR-top	$t\bar{t}$, tW	1.02 ± 0.09
$\mu_{Z^{(*)}/\gamma^* \to \tau\tau}$	CR-tau	$Z^{(*)}/\gamma^*(\to \tau\tau)$ + jets	0.72 ± 0.13

Table 5.8: Normalisation parameters from the background-only fit, the control region used to derive these, the MC samples in which these are applied to, and the extracted value whose uncertainties include statistical and systematic contributions combined.

dilepton p_{T} as a proxy for the hadronic recoil, as done by CMS [304]. This procedure is not pursued in the results presented, and is deferred for future work. The effect on the $m_{\ell\ell}$ and m_{T2}^{100} signal shapes are found to be negligible, so a single nuisance parameter correlated across all SR bins is considered in the exclusion fits described in Section 5.7.

5.7 Results and interpretation

The HISTFITTER package [366] implements the statistical analysis based on a profile-likelihood method [367]. To determine the SM background predictions independent of the signal regions, only the control regions are used to constrain the fit parameters by likelihood maximisation assuming no signal events in the CRs; this is referred to as the *background-only fit*. The normalisations for the $t\bar{t}$, tW, and $Z^{(*)}/\gamma^*(\to \tau\tau)$ + jets MC are extracted in a simultaneous fit to the data events in CR-top and CR-tau respectively. Data events in the SRs are not considered in the fit. The corresponding normalisation parameters obtained from the background-only fit, are displayed in Table 5.8. That $\mu_{Z^{(*)}/\gamma^* \to \tau\tau}$ is more than 1 standard deviation from unity suggests mild mis-modelling in this high $E_{\text{T}}^{\text{miss}}$ regime, whose investigations are deferred for future work.

The background rates extrapolated into the validation regions using the background-only fit are displayed in Figure 5.17, with example yields in Table 5.6. Figure 5.18 illustrates example kinematic distributions in these VRs. Overall, the data and SM predictions are compatible within the uncertainties. This indicates that the background model is sufficiently accurate to describe SM processes for the SRs to be unblinded and perform the search for evidence of signals beyond the SM.

The predicted yields N_{exp} and observed data counts N_{obs} in each overlapping single-bin SRs are shown in Table 5.9. The discovery p-values quantify the probability that

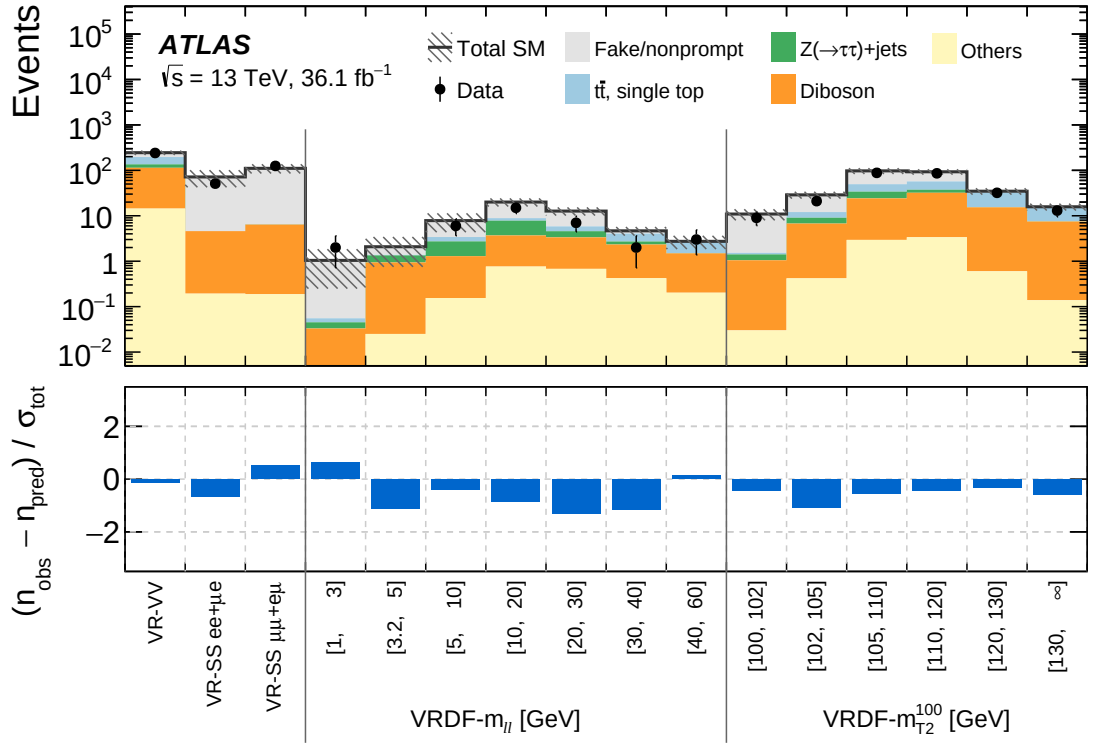

Figure 5.17: Summary of data and predicted yields in the validation regions after the background-only fit. Background processes containing fewer than two prompt leptons are categorised as 'Fake/nonprompt'. The category 'Others' contains rare backgrounds such as triboson and Higgs boson.

the background model alone is compatible with any excess of observed events due to a statistical fluctuation, whose calculations assume a signal strength of zero $\mu_{\text{SIG}} = 0$. None of the p-values are statistically significant in these hypothesis tests, showing the data are compatible with the prediction within the uncertainties.

Figure 5.19 shows the kinematic distributions of the $m_{\ell\ell}$ and m_{T2}^{100} variables in the SRs together with expected signal shapes. Figure 5.20 shows the data and SM expectation in the non-overlapping SRs divided by ee and $\mu\mu$. No significant excesses of the data above the background expectation are observed. These results constrain the presence of new phenomena beyond the SM, for which we derive limits of generic signals (Subsection 5.7.1) and on simplified models (Subsection 5.7.2).

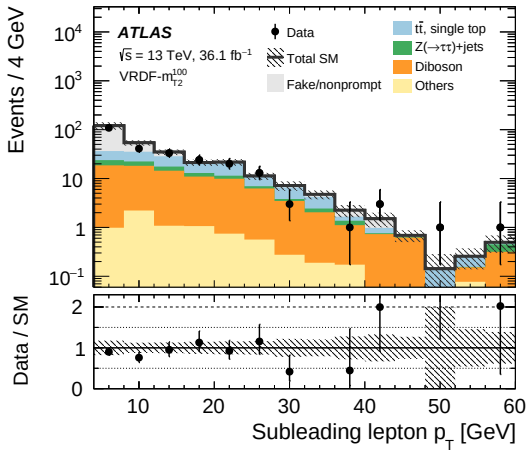

(a) VRDF-m_{T2}^{100} $p_{\mathrm{T}}^{\ell_2}$

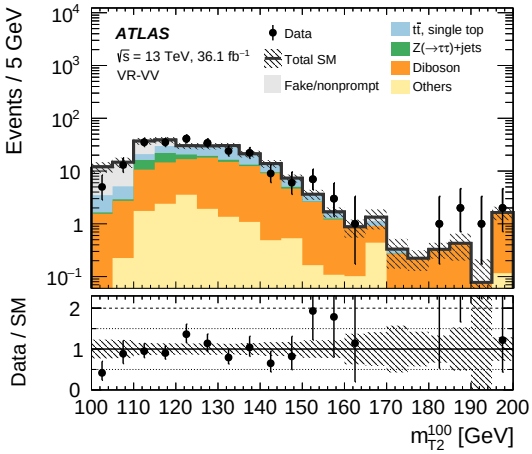

(b) VR-VV m_{T2}^{100}

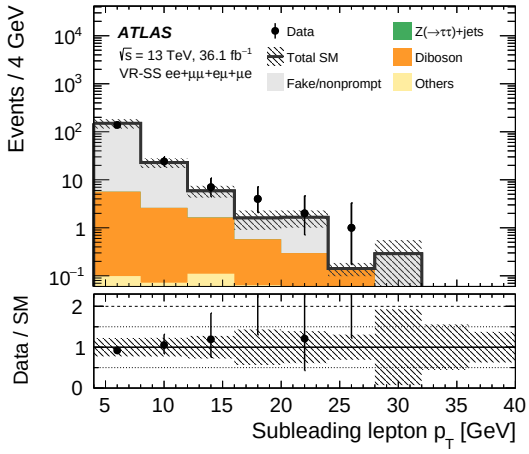

(c) VR-SS $p_{\mathrm{T}}^{\ell_2}$

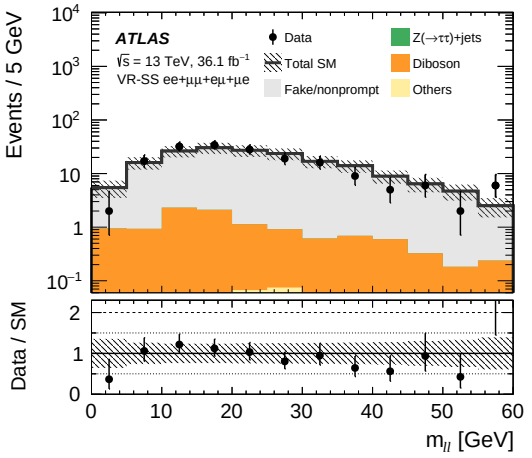

(d) VR-SS $m_{\ell\ell}$

Figure 5.18: Distributions of the data and background prediction with the VR selections. The last bin includes overflow. Background processes containing fewer than two prompt leptons are categorised as 'Fake/nonprompt'. The category 'Others' contains rare backgrounds such as triboson and Higgs boson. The uncertainty bands plotted include all statistical and systematic uncertainties.

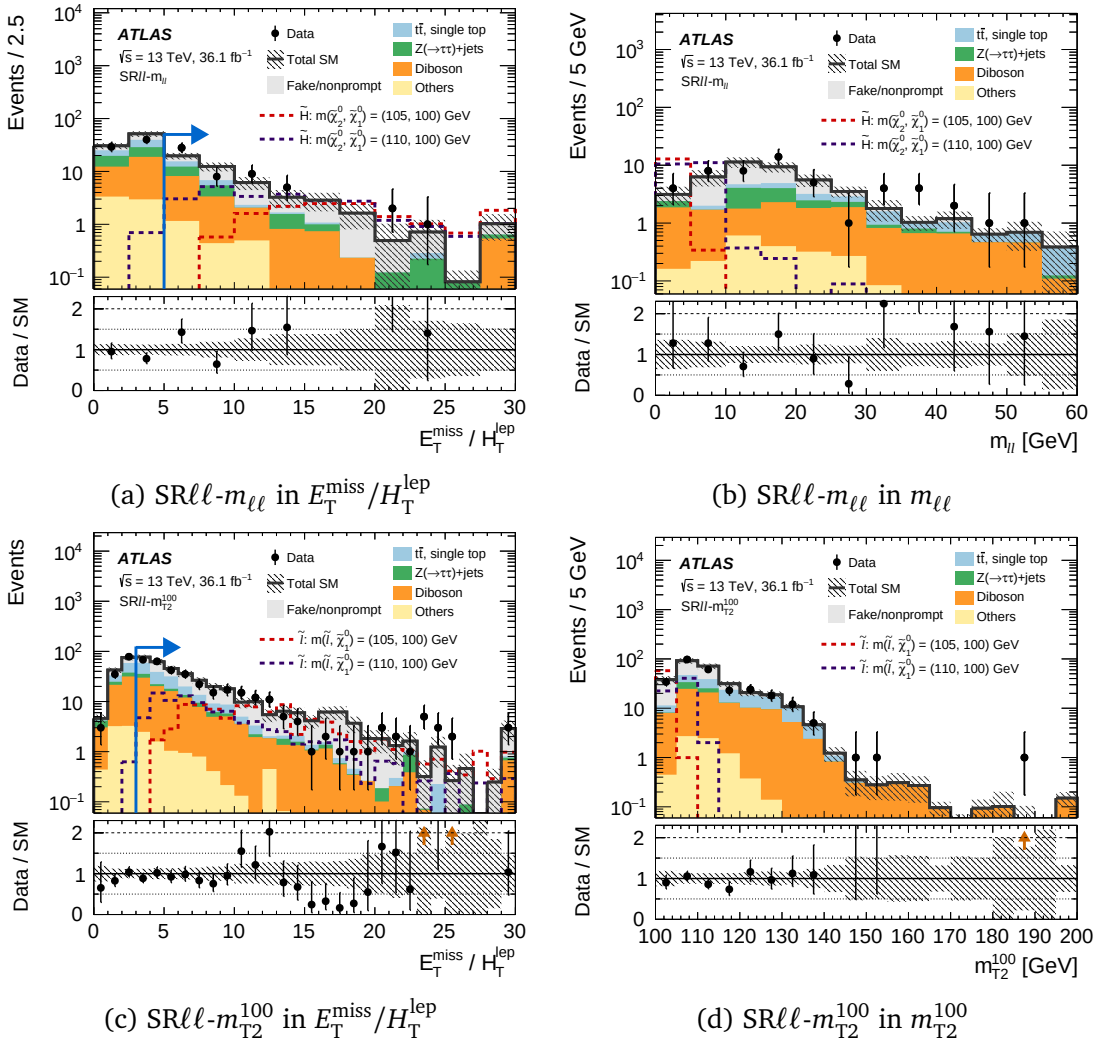

(a) SR$\ell\ell$-$m_{\ell\ell}$ in $E_{\mathrm{T}}^{\mathrm{miss}}/H_{\mathrm{T}}^{\mathrm{lep}}$

(b) SR$\ell\ell$-$m_{\ell\ell}$ in $m_{\ell\ell}$

(c) SR$\ell\ell$-m_{T2}^{100} in $E_{\mathrm{T}}^{\mathrm{miss}}/H_{\mathrm{T}}^{\mathrm{lep}}$

(d) SR$\ell\ell$-m_{T2}^{100} in m_{T2}^{100}

Figure 5.19: Distributions of the data and background prediction with the SR selections applied from Table 5.3, before being binned as in Table 5.4. The last bin includes overflow. Background processes containing fewer than two prompt leptons are categorised as 'Fake/nonprompt'. The category 'Others' contains rare backgrounds such as triboson and Higgs boson. The uncertainty bands plotted include all statistical and systematic uncertainties. Dashed lines represent signal points for the Higgsino $\widetilde{H}$ and slepton $\widetilde{\ell}$ simplified models.

5.7.1 Model-independent upper limits on new phenomena

The seven overlapping SR$\ell\ell$-$m_{\ell\ell}$ and six SR$\ell\ell$-m_{T2}^{100} regions are used to set model-independent upper limits on processes beyond the SM in these SRs. Only one SR is considered at a time as considering more than one subregion of the $m_{\ell\ell}$ or m_{T2}^{100} spectrum would assume greater model-dependence. These results are shown in Table 5.9.

For each SR, the limit setting procedure considers three inputs: the predicted number of events N_{exp} and its corresponding uncertainty δN_{exp} from the background-only fit, together with the observed yield N_{obs}. A non-negative signal strength parameter μ_{SIG} is defined such that a value of unity corresponds to one signal event in the SR. Signal contamination in the CRs is assumed to be negligible.

Using the $\mathrm{CL_s}$ prescription [269], the μ_{SIG} is scanned until the $\mathrm{CL_s}$ value of the hypothesis test reaches 0.05. The value $\mu_{\mathrm{SIG}}(\mathrm{CL_s} = 0.05)$ then corresponds to an upper limit at the 95% confidence level (CL) on the observed (expected) signal events $S^{95}_{\mathrm{obs\ (exp)}}$ that enter each SR. This is translated into upper limits on the visible cross-sections $\langle \epsilon \mathscr{A} \sigma \rangle^{95}_{\mathrm{obs}}$ (cross-section σ of generic signal multiplied by acceptance $\mathscr{A}$ and reconstruction efficiency ϵ), defined as S^{95}_{obs} divided by the integrated luminosity of 36.1 fb^{-1}.

5.7.2 Exclusion limits on simplified models

Results are interpreted as constraints on the simplified models of SUSY discussed in Section 5.2.1. The background-only fit is extended to allow a signal model with a corresponding signal strength parameter in a simultaneous fit of all control and relevant signal regions; this is referred to as the *exclusion fit*.

When a Higgsino or wino–bino signal is considered, only the 14 non-overlapping SRs binned in $m_{\ell\ell}$ are considered with the two CRs. By statistically combining these SRs, correlations in the signal shape of the $m_{\ell\ell}$ spectrum can be exploited to improve sensitivity. These are also referred to as *shape fits*. This is more effective for signals that are modestly distributed across several several bins, namely larger $\Delta m(\widetilde{\chi}_2^0, \widetilde{\chi}_1^0)$. Heuristically, this is because it is more difficult for the fit to ascribe signal-induced excesses to background fluctuations in multiple bins than one. The ee channel is fit separately from the $\mu\mu$ to exploit differences in expected sensitivity due to lepton flavour dependence of signal efficiency and background rejection. Similarly, when a slepton

Signal Region	N_{obs}	N_{exp}	$\langle\epsilon\mathscr{A}\sigma\rangle^{95}_{\text{obs}}$ [fb]	S^{95}_{obs}	S^{95}_{exp}	$p(\mu_{\text{SIG}}=0)$
SR$\ell\ell$-$m_{\ell\ell}$ $[1,3]$	1	1.7 ± 0.9	0.10	3.8	$4.3^{+1.7}_{-0.7}$	0.50
SR$\ell\ell$-$m_{\ell\ell}$ $[1,5]$	4	3.1 ± 1.2	0.18	6.6	$5.6^{+2.3}_{-1.0}$	0.32
SR$\ell\ell$-$m_{\ell\ell}$ $[1,10]$	12	8.9 ± 2.5	0.34	12.3	$9.6^{+3.2}_{-1.9}$	0.21
SR$\ell\ell$-$m_{\ell\ell}$ $[1,20]$	34	29 ± 6	0.61	22	17^{+7}_{-6}	0.25
SR$\ell\ell$-$m_{\ell\ell}$ $[1,30]$	40	38 ± 6	0.59	21	20^{+9}_{-5}	0.38
SR$\ell\ell$-$m_{\ell\ell}$ $[1,40]$	48	41 ± 7	0.72	26	20^{+8}_{-5}	0.20
SR$\ell\ell$-$m_{\ell\ell}$ $[1,60]$	52	43 ± 7	0.80	29	24^{+5}_{-10}	0.18
SR$\ell\ell$-m^{100}_{T2} $[100,102]$	8	12.4 ± 3.1	0.18	7	9^{+4}_{-2}	0.50
SR$\ell\ell$-m^{100}_{T2} $[100,105]$	34	38 ± 7	0.49	18	23^{+7}_{-7}	0.50
SR$\ell\ell$-m^{100}_{T2} $[100,110]$	131	129 ± 18	1.3	48	47^{+13}_{-15}	0.37
SR$\ell\ell$-m^{100}_{T2} $[100,120]$	215	232 ± 29	1.4	52	62^{+21}_{-15}	0.50
SR$\ell\ell$-m^{100}_{T2} $[100,130]$	257	271 ± 32	1.7	61	69^{+22}_{-17}	0.50
SR$\ell\ell$-m^{100}_{T2} $[100,\infty]$	277	289 ± 33	1.8	66	72^{+24}_{-17}	0.50

Table 5.9: Summary of yields and model-independent limits in SR$\ell\ell$-$m_{\ell\ell}$ and SR$\ell\ell$-m^{100}_{T2} signal regions. Left to right: The first two columns present observed (N_{obs}) and expected (N_{exp}) event yields in the inclusive signal regions. The latter are obtained by the background-only fit of the control regions, and the uncertainties displayed include both statistical and systematic contributions. The next two columns show the observed 95% CL upper limits on the visible cross-section $\left(\langle\epsilon\mathscr{A}\sigma\rangle^{95}_{\text{obs}}\right)$ and on the number of signal events $\left(S^{95}_{\text{obs}}\right)$. The fifth column $\left(S^{95}_{\text{exp}}\right)$ shows what the 95% CL upper limit on the number of signal events would be, given an observed number of events equal to the expected number (and $\pm1\sigma$ deviations from the expectation) of background events. The last column shows the discovery p-value ($p(\mu_{\text{SIG}})=0$)), which is capped at 0.5.

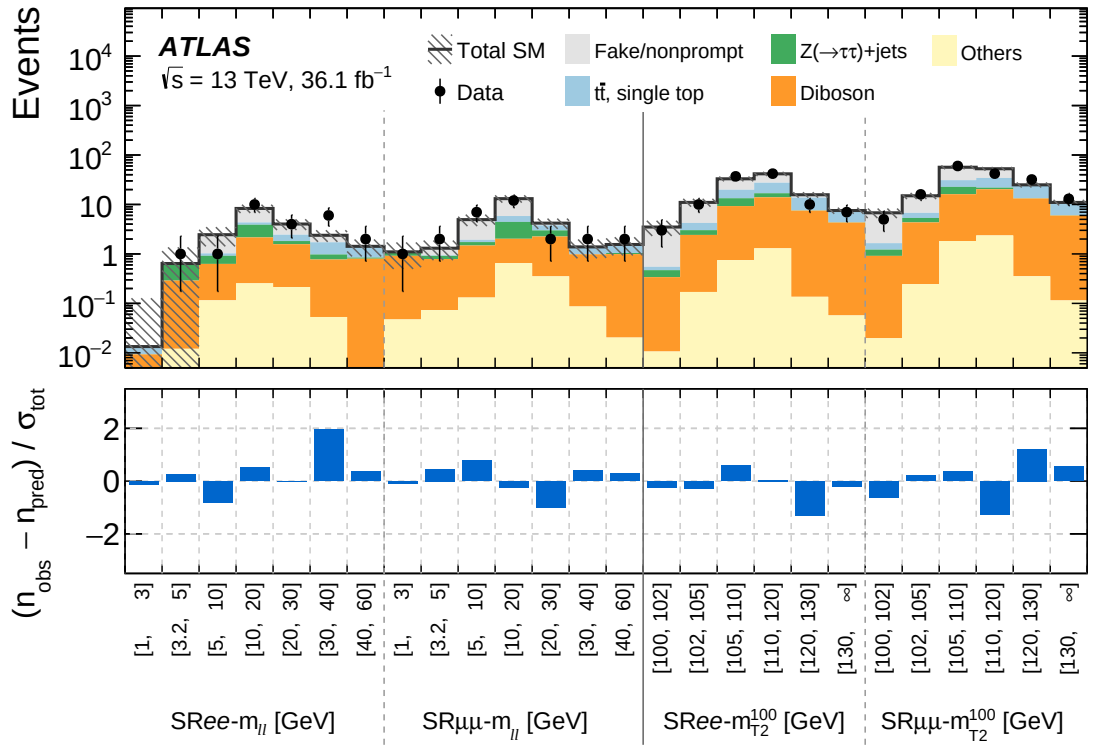

Figure 5.20: Summary of data and predicted yields in the signal (SR) regions after the exclusion fit with signal strength parameter set to zero. Background processes containing fewer than two prompt leptons are categorised as 'Fake/nonprompt'. The category 'Others' contains rare backgrounds such as triboson and Higgs boson.

signal is assumed, only the 12 non-overlapping SRs binned in m_{T2}^{100} are used with the two CRs for the exclusion fit.

Table 5.10 shows the yields for the two exclusion fits, both performed with the signal strength parameter set to zero, whose yields are illustrated in Figure 5.20. These are expected to have small differences from those obtained in the background-only fit (Table 5.9) as the exclusion fits are now overconstrained. This means there are more independent regions than there are floating parameters (e.g. normalisation μ_{top}) for the background model to accommodate the observed data in the fit. The likelihood is extremised by also allowing the nuisance parameters to be adjusted.

To set limits on simplified models, the signal strength parameter is allowed to be non-zero. A hypothesis test is performed to set 95% CL limits based on the $\mathrm{CL_s}$ prescription [269]. Expected and observed limits on simplified model masses are derived by interpolating the corresponding logarithm of $\mathrm{CL_s}$ values across a grid of points that

SRee-$m_{\ell\ell}$ [GeV]	[1, 3]	[3.2, 5]	[5, 10]	[10, 20]	[20, 30]	[30, 40]	[40, 60]
Observed events	0	1	1	10	4	6	2
Fitted SM events	$0.01^{+0.11}_{-0.01}$	$0.6^{+0.7}_{-0.6}$	2.4 ± 1.0	8.3 ± 1.6	4.0 ± 1.0	2.4 ± 0.6	1.4 ± 0.5
Fake/nonprompt leptons	$0.00^{+0.08}_{-0.00}$	$0.02^{+0.12}_{-0.02}$	1.4 ± 0.9	4.0 ± 1.5	1.6 ± 0.9	0.7 ± 0.6	$0.02^{+0.11}_{-0.02}$
Diboson	$0.007^{+0.014}_{-0.007}$	$0.28^{+0.29}_{-0.28}$	0.51 ± 0.28	1.9 ± 0.6	1.36 ± 0.31	0.72 ± 0.22	0.80 ± 0.28
$Z^{(*)}/\gamma^*(\to \tau\tau)$+jets	$0.000^{+0.007}_{-0.000}$	$0.3^{+0.8}_{-0.3}$	$0.3^{+0.5}_{-0.3}$	1.7 ± 0.7	$0.25^{+0.26}_{-0.25}$	0.20 ± 0.18	$0.04^{+0.28}_{-0.04}$
$t\bar{t}$, single top	$0.00^{+0.08}_{-0.00}$	$0.02^{+0.12}_{-0.02}$	$0.11^{+0.14}_{-0.11}$	0.44 ± 0.29	0.63 ± 0.35	0.7 ± 0.4	0.6 ± 0.4
Others	$0.002^{+0.015}_{-0.002}$	$0.012^{+0.013}_{-0.012}$	0.12 ± 0.11	0.25 ± 0.16	0.21 ± 0.12	$0.05^{+0.06}_{-0.05}$	$0.0018^{+0.0033}_{-0.0018}$
SR$\mu\mu$-$m_{\ell\ell}$ [GeV]	[1, 3]	[3.2, 5]	[5, 10]	[10, 20]	[20, 30]	[30, 40]	[40, 60]
Observed events	1	2	7	12	2	2	2
Fitted SM events	1.1 ± 0.6	1.3 ± 0.6	4.9 ± 1.3	13.1 ± 2.2	4.2 ± 1.0	1.4 ± 0.6	1.6 ± 0.6
Fake/nonprompt leptons	$0.00^{+0.33}_{-0.00}$	$0.4^{+0.5}_{-0.4}$	3.0 ± 1.3	7.3 ± 2.1	$0.4^{+0.8}_{-0.4}$	$0.03^{+0.19}_{-0.03}$	$0.0^{+0.5}_{-0.0}$
Diboson	0.9 ± 0.5	0.7 ± 0.4	1.3 ± 0.6	1.4 ± 0.5	1.9 ± 0.4	0.9 ± 0.5	0.97 ± 0.28
$Z^{(*)}/\gamma^*(\to \tau\tau)$+jets	$0.18^{+0.25}_{-0.18}$	0.13 ± 0.12	$0.3^{+0.5}_{-0.3}$	2.4 ± 0.8	0.7 ± 0.4	$0.001^{+0.011}_{-0.001}$	$0.05^{+0.06}_{-0.05}$
$t\bar{t}$, single top	$0.01^{+0.10}_{-0.01}$	$0.02^{+0.12}_{-0.02}$	0.19 ± 0.13	1.4 ± 0.6	0.8 ± 0.4	0.37 ± 0.21	0.51 ± 0.33
Others	0.047 ± 0.030	$0.07^{+0.09}_{-0.07}$	0.13 ± 0.12	0.7 ± 0.5	0.35 ± 0.20	0.09 ± 0.07	0.020 ± 0.020

SRee-m_{T2}^{100} [GeV]	[100, 102]	[102, 105]	[105, 110]	[110, 120]	[120, 130]	[130, ∞]
Observed events	3	10	37	42	10	7
Fitted SM events	3.5 ± 1.2	11.0 ± 2.0	33 ± 4	42 ± 4	15.7 ± 2.0	7.5 ± 1.1
Fake/nonprompt leptons	2.9 ± 1.2	6.8 ± 2.0	13 ± 4	14 ± 4	1.9 ± 1.2	$0.01^{+0.10}_{-0.01}$
Diboson	0.33 ± 0.12	2.3 ± 0.6	8.5 ± 1.6	12.7 ± 2.4	7.4 ± 1.4	4.3 ± 0.9
$Z^{(*)}/\gamma^*(\to \tau\tau)$+jets	$0.13^{+0.23}_{-0.13}$	0.6 ± 0.4	4.1 ± 1.8	2.9 ± 1.0	$0.00^{+0.08}_{-0.00}$	$0.00^{+0.20}_{-0.00}$
$t\bar{t}$, single top	0.08 ± 0.08	1.2 ± 0.5	6.5 ± 1.6	10.7 ± 2.4	6.3 ± 1.4	3.2 ± 0.9
Others	$0.011^{+0.012}_{-0.011}$	0.17 ± 0.11	0.8 ± 0.4	1.3 ± 0.7	0.14 ± 0.09	0.06 ± 0.04
SR$\mu\mu$-m_{T2}^{100} [GeV]	[100, 102]	[102, 105]	[105, 110]	[110, 120]	[120, 130]	[130, ∞]
Observed events	5	16	60	42	32	13
Fitted SM events	6.8 ± 1.5	15.0 ± 2.1	57 ± 5	53 ± 4	24.9 ± 2.9	11.0 ± 1.4
Fake/nonprompt leptons	5.1 ± 1.5	8.2 ± 2.1	26 ± 5	18 ± 4	1.2 ± 0.8	$0.02^{+0.17}_{-0.02}$
Diboson	0.89 ± 0.22	4.1 ± 0.9	14.3 ± 2.2	18.0 ± 2.7	12.9 ± 2.2	5.9 ± 1.1
$Z^{(*)}/\gamma^*(\to \tau\tau)$+jets	0.31 ± 0.23	$1.0^{+1.3}_{-1.0}$	6.6 ± 1.7	$1.6^{+1.8}_{-1.6}$	$0.03^{+0.25}_{-0.03}$	$0.02^{+0.24}_{-0.02}$
$t\bar{t}$, single top	0.43 ± 0.22	1.4 ± 0.5	8.3 ± 2.2	12.4 ± 2.9	10.5 ± 2.6	5.0 ± 1.3
Others	$0.020^{+0.024}_{-0.020}$	0.24 ± 0.15	1.8 ± 1.0	2.4 ± 1.3	0.35 ± 0.23	0.11 ± 0.07

Table 5.10: Observed event yields and exclusion fit results with the signal strength parameter set to zero for the exclusive electroweakino and slepton signal regions. Background processes containing fewer than two prompt leptons are categorized as 'Fake/nonprompt'. The category 'Others' contains rare backgrounds from triboson, Higgs boson, and the remaining top-quark production processes listed in Table 5.1. Uncertainties in the fitted background estimates combine statistical and systematic uncertainties.

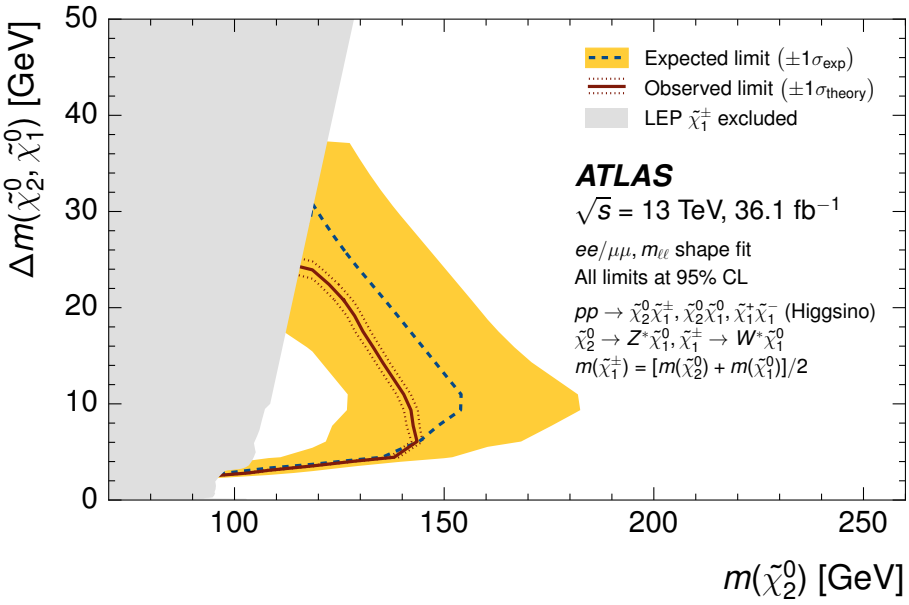

(a) Higgsino simplified model.

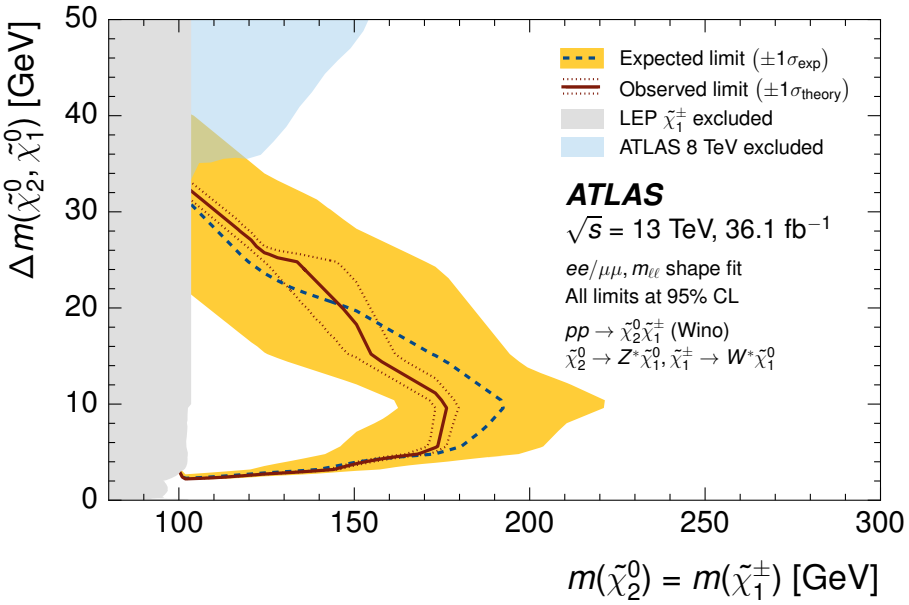

(b) Wino–bino simplified model.

Figure 5.21: Exclusion limits for (a) Higgsino and (b) wino–bino models. Displayed are the expected 95% CL exclusion sensitivity (blue dashed line) with $\pm 1\sigma_{\text{exp}}$ (yellow band) from systematic uncertainties and observed limits (red solid line) with $\pm 1\sigma_{\text{theory}}$ (dotted red line) from signal cross-section uncertainties. The shape fit to the $m_{\ell\ell}$ spectrum is used to derive the limits. For Higgsino production, the chargino $\tilde{\chi}_1^{\pm}$ mass is assumed to be halfway between the two lightest neutralino masses, while $m(\tilde{\chi}_2^0) = m(\tilde{\chi}_1^{\pm})$ is assumed for the wino–bino model. The grey regions denote the lower chargino mass limit from LEP [22]. The blue region in (5.21b) is the limit from the $2\ell + 3\ell$ combination of ATLAS Run 1 [277, 278].

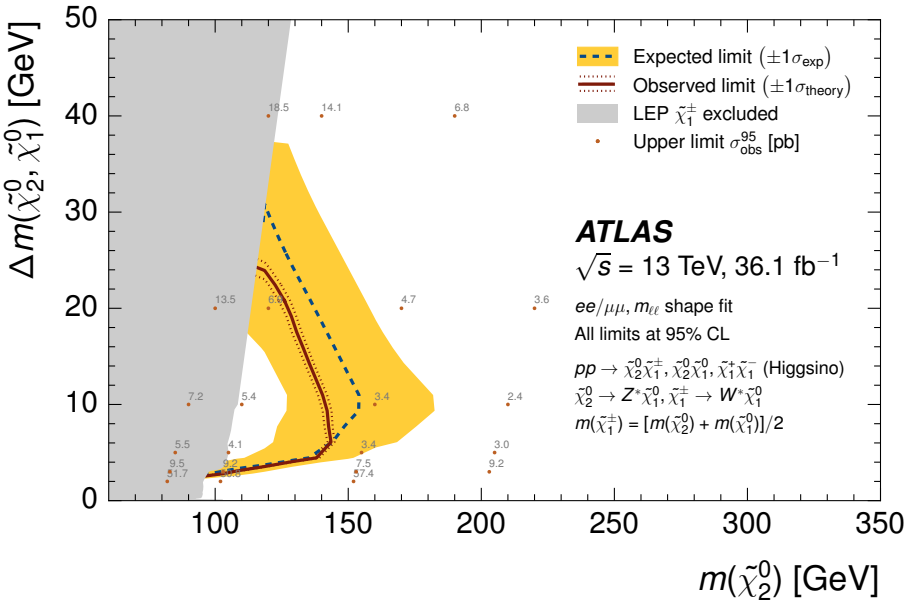

Figure 5.22: Same as Figure 5.22 with the 95% CL upper limits on the Higgsino model signal cross-sections σ_{obs}^{95} overlayed for the mass points indicated by orange circles.

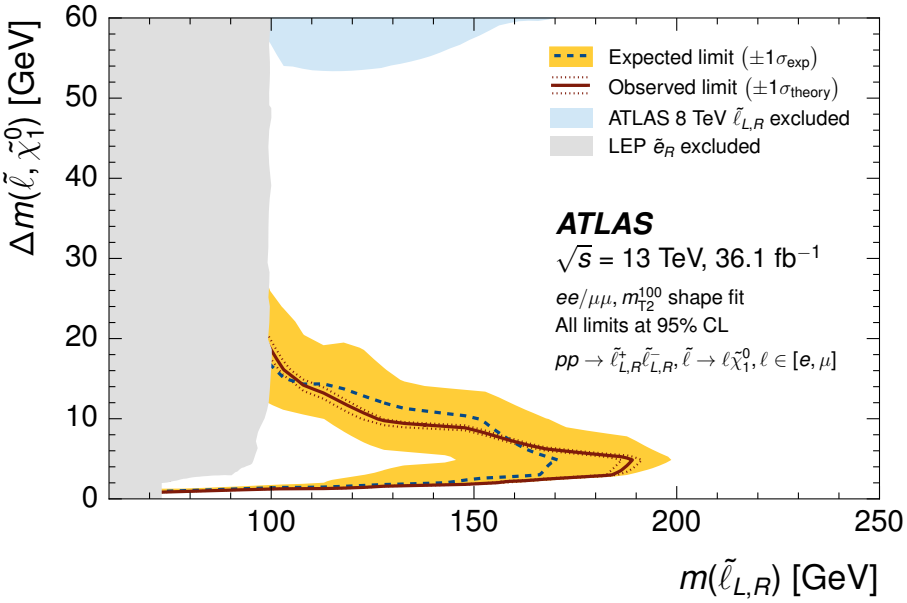

Figure 5.23: Exclusion limits for slepton model. Displayed are the expected 95% CL exclusion sensitivity (blue dashed line) with $\pm1\sigma_{\text{exp}}$ (yellow band) from systematic uncertainties and observed limits (red solid line) with $\pm1\sigma_{\text{theory}}$ (dotted red line) from signal cross-section uncertainties. The m_{T2}^{100} shape fit is used to derive the limit. Slepton $\tilde{\ell}$ refers to the scalar partners of left- and right-handed electrons and muons with a four-fold mass degeneracy $m(\tilde{e}_L) = m(\tilde{e}_R) = m(\tilde{\mu}_L) = m(\tilde{\mu}_R)$. Also shown are the LEP $\tilde{e}_R$ limit (grey filled) [24, 282] and the ATLAS Run 1 limit (blue filled) [277].

sample the mass plane. In general, observed limits are weaker (stronger) than expected if there is an excess (deficit) of observed events than predicted in the SRs used to constrain the signal. The results of these constraints are discussed below:

Higgsino model Figure 5.21a shows the 95% CL exclusion limits on the Higgsino simplified model from a shape fit to the $m_{\ell\ell}$ spectrum. This is projected into the $\Delta m(\widetilde{\chi}_2^0, \widetilde{\chi}_1^0)$ vs $m(\widetilde{\chi}_2^0)$ mass plane, where $\widetilde{\chi}_2^0$ are excluded up to 145 GeV for $\Delta m(\widetilde{\chi}_2^0, \widetilde{\chi}_1^0)$ of 5 to 10 GeV. The sensitivity extends down to $\Delta m(\widetilde{\chi}_2^0, \widetilde{\chi}_1^0) \sim 3$ GeV for neutralino masses of $m(\widetilde{\chi}_2^0) \sim 110$ GeV. Limits extends those from LEP, whose lower bound on the chargino mass is taken from the 'Higgsino region' of Ref. [22] in the case of $\Delta m(\widetilde{\chi}_1^\pm, \widetilde{\chi}_1^0) < 10$ GeV, and 103.5 GeV above that [23].

Figure 5.22 also displays the 95% CL upper limits on the Higgsino model cross-sections for the mass points sampled in the $\Delta m(\widetilde{\chi}_2^0, \widetilde{\chi}_1^0)$ vs $m(\widetilde{\chi}_2^0)$ plane. These are the maximum cross-sections of any generic signal model with the same acceptance, efficiency and shape distributed across the multiple $m_{\ell\ell}$ SRs, which may also be realised in non-minimal versions of SUSY or other scenarios.

Wino–bino model The $m_{\ell\ell}$ shape fit is also used to set limits on the wino–bino model, as displayed in Figure 5.21b. Wino masses $m(\widetilde{\chi}_2^0) = m(\widetilde{\chi}_1^\pm)$ are excluded up to 175 GeV for mass splittings $\Delta m(\widetilde{\chi}_2^0, \widetilde{\chi}_1^0)$ of 10 GeV, and down to $\Delta m(\widetilde{\chi}_2^0, \widetilde{\chi}_1^0) \sim 2.5$ GeV for $m(\widetilde{\chi}_2^0) \sim 110$ GeV. Limits complement the $2\ell + 3\ell$ combination from ATLAS Run 1 [277, 278] and surpass those from LEP. The LEP lower chargino mass bound is taken from the 'gaugino region' of Ref. [22] for the $\Delta m(\widetilde{\chi}_1^\pm, \widetilde{\chi}_1^0) < 10$ GeV regime, and 103.5 GeV above that.

Slepton model Figure 5.23 shows the 95% CL limits on the slepton simplified model. This uses the exclusion fits that exploit the signal shape of the m_{T2}^{100} spectrum using the exclusive slepton SRs. Here, slepton masses of up to $m(\tilde{\ell}) \sim 190$ GeV are excluded for $\Delta m(\tilde{\ell}, \widetilde{\chi}_1^0) \sim 5$ GeV, and down to mass splittings $\Delta m(\tilde{\ell}, \widetilde{\chi}_1^0)$ of approximately 1 GeV for $m(\tilde{\ell}) \sim 75$ GeV. A four-fold degeneracy is assumed in the masses of the scalar partners of the left- and right-handed electron and muon $m(\widetilde{e}_L) = m(\widetilde{e}_R) = m(\widetilde{\mu}_L) = m(\widetilde{\mu}_R)$. For the LEP limit, the lower limit on $m(\widetilde{e}_R)$ is used from the combination of the four experiments [24]. In the region $\Delta m(\tilde{\ell}, \widetilde{\chi}_1^0) \lesssim 3$ GeV, the universal $m(\widetilde{e}_R) > 73$ GeV limit

is used, which is independent of mass splitting [282]. This sensitivity complements that of ATLAS Run 1 [277], but for $20 \lesssim \Delta m(\tilde{\ell}, \widetilde{\chi}_1^0) \lesssim 60$ GeV, there remains no hadron collider sensitivity at the time this analysis was published.

In these simplified model interpretations, sensitivity is lost when the mass splitting between the produced SUSY state and LSP becomes less than a few GeV due to the reduced acceptance of the soft leptons (Figure 5.6). Meanwhile, sensitivity decreases for larger mass splittings above approximately 20 to 30 GeV due to the $m_{\ell\ell}$ or m_{T2}^{100} shapes of the signal becoming increasingly similar to that of the SM background.

5.8 Summary plots of simplified model sensitivity

Summary plots of sensitivity from this chapter and other ATLAS results are presented in Figures 5.24 to 5.26 for the Higgsino dark matter, wino–bino and slepton–bino scenarios considered. Two of these (Higgsino and slepton) are newly produced in the context of this thesis. These identify striking gaps in collider sensitivity, and brief comments on how they may be probed in future work are discussed.

Higgsinos and the prompt–long-lived gap Figure 5.24 shows the ATLAS summary plot for direct Higgsino production. The exclusion limits set by this chapter (labelled by 2ℓ compressed in solid blue) are presented in the mass plane involving the chargino mass $m(\widetilde{\chi}_1^\pm)$ and splitting $\Delta m(\widetilde{\chi}_1^\pm, \widetilde{\chi}_1^0)$ to compare with the LEP constraints (solid grey). This is compared with constraints from the disappearing track search (solid orange). This probes ultra-compressed mass splittings whereby the chargino is sufficiently long-lived to leave 'tracklets' of silicon hits in the innermost silicon layers; the details of this analysis are found in Refs. [368,369]. Care should be taken when interpreting the 2ℓ compressed limit, as the impact on the sensitivity of this analysis is dominated by $\Delta m(\widetilde{\chi}_2^0, \widetilde{\chi}_1^0)$ and the chargino mass was a model-dependent choice of the model.

Nonetheless, the prompt–long-lived gap in sensitivity for $0.3 \lesssim \Delta m(\widetilde{\chi}_1^\pm, \widetilde{\chi}_1^0) \lesssim 2$ GeV is evident. Here, the phenomenology of the Higgsinos states transitions from prompt decays to being considered long-lived on detector scales. The 2ℓ compressed analysis can open sensitivity to smaller $\Delta m(\widetilde{\chi}_1^\pm, \widetilde{\chi}_1^0)$ by reconstructing softer or fewer leptons. For the disappearing track to probe larger $\Delta m(\widetilde{\chi}_1^\pm, \widetilde{\chi}_1^0)$ requires smaller chargino lifetimes

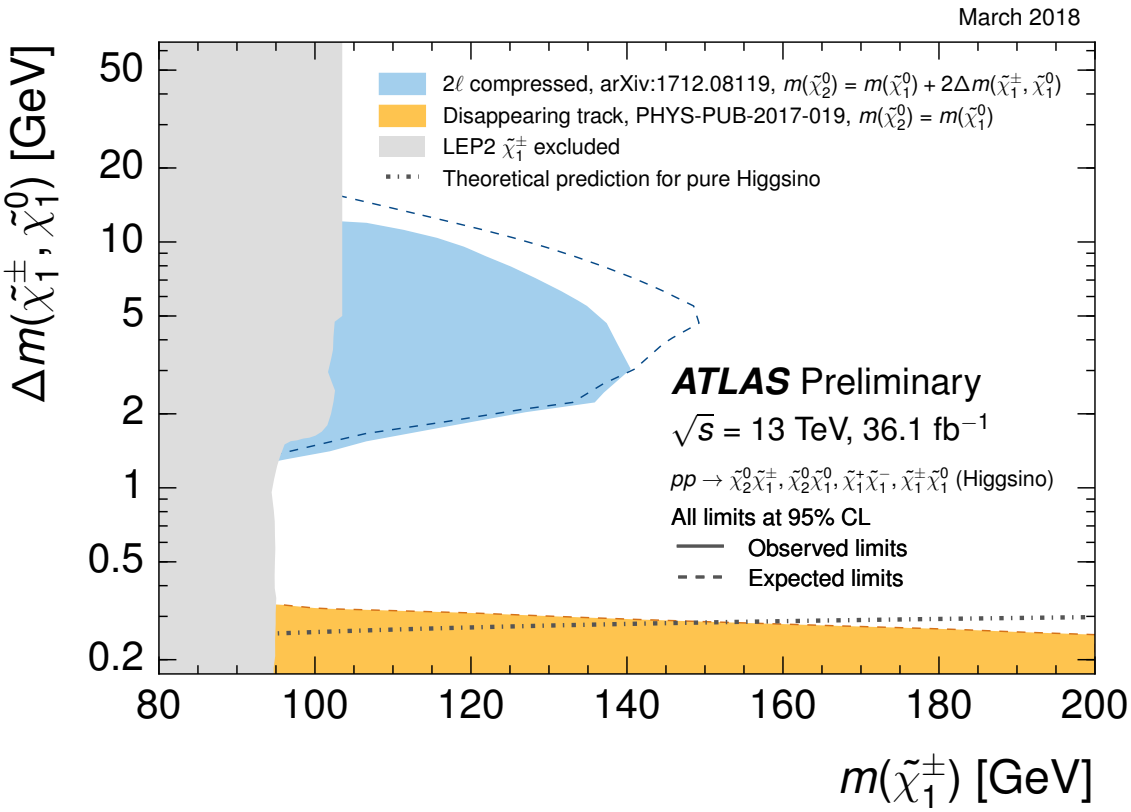

Figure 5.24: Summary of ATLAS sensitivity to direct production of Higgsino dark matter [5]. This thesis presented sensitivity resulting from the 2ℓ compressed analysis [3] (blue, this thesis); this is the limit corresponding to that shown in Figure 5.21a. Here, the mass plane shows the chargino–neutralino mass splitting $\Delta m(\tilde{\chi}_1^\pm, \tilde{\chi}_1^0)$ vs chargino mass $m(\tilde{\chi}_1^\pm)$. Constraints from the disappearing track search [368, 369] are also shown (orange grey). The mass of the next-to-lightest neutralino $m(\tilde{\chi}_2^0)$ for the simplified models used to derive the ATLAS limits are indicated in the legend. The four $\tilde{\chi}_2^0\tilde{\chi}_1^\pm$, $\tilde{\chi}_2^0\tilde{\chi}_1^0$, $\tilde{\chi}_1^+\tilde{\chi}_1^-$, and $\tilde{\chi}_1^\pm\tilde{\chi}_1^0$ production processes are considered, assuming pure Higgsino cross-sections. Previous constraints on chargino production are from a combination of results from LEP experiments [22, 23] (grey filled). The grey dot-dashed line indicates a particular benchmark mass splitting that corresponds to the pure Higgsino prediction [289, 370].

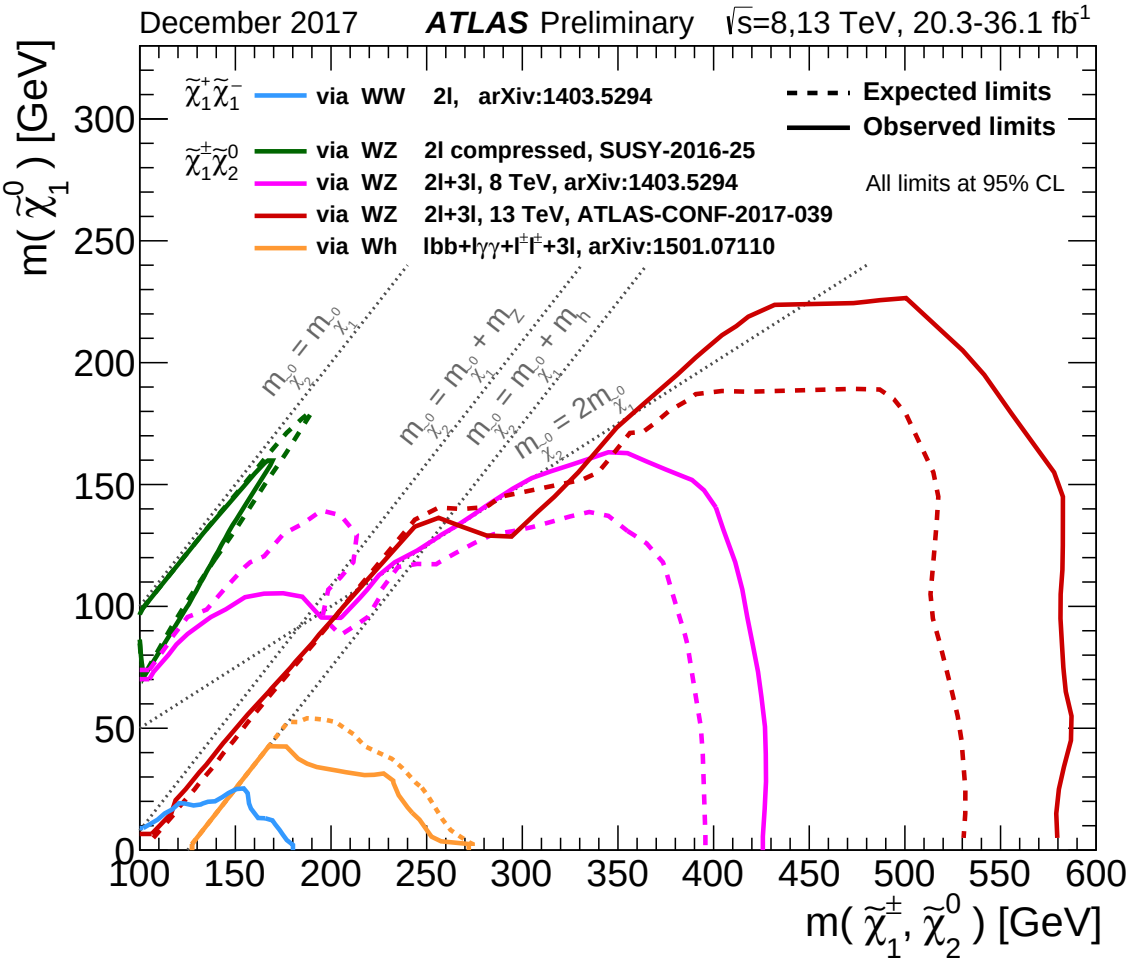

Figure 5.25: Summary of ATLAS sensitivity to direct wino production decaying via bosons [5]. This is the same as Figure 5.2a but with the constraint the soft 2ℓ compressed search [3] included (green line, this thesis), corresponding to the limit presented in Figure 5.21b. This may be compared directly with the other WZ decay limits. Constraints are also presented from the $2+3\ell$ analyses at 8 TeV with 20.3 fb^{-1} [197, 217, 277, 278] (pink) and 13 TeV with 36.1 fb^{-1} [279] (red). The wino–bino simplified model assumes pure wino production cross-sections and mass degenerate chargino–neutralino $m(\tilde{\chi}_2^0) = m(\tilde{\chi}_1^\pm)$, with the different decays indicated in the legend with 100% branching ratio. Also displayed in this figure are 8 TeV ATLAS constraints on simplified wino–bino models with WW [277] (blue) and Wh [371] (yellow) decays, but cannot be directly compared to limits with WZ decays. I provided the input (green line) to a collaborator who made this plot.

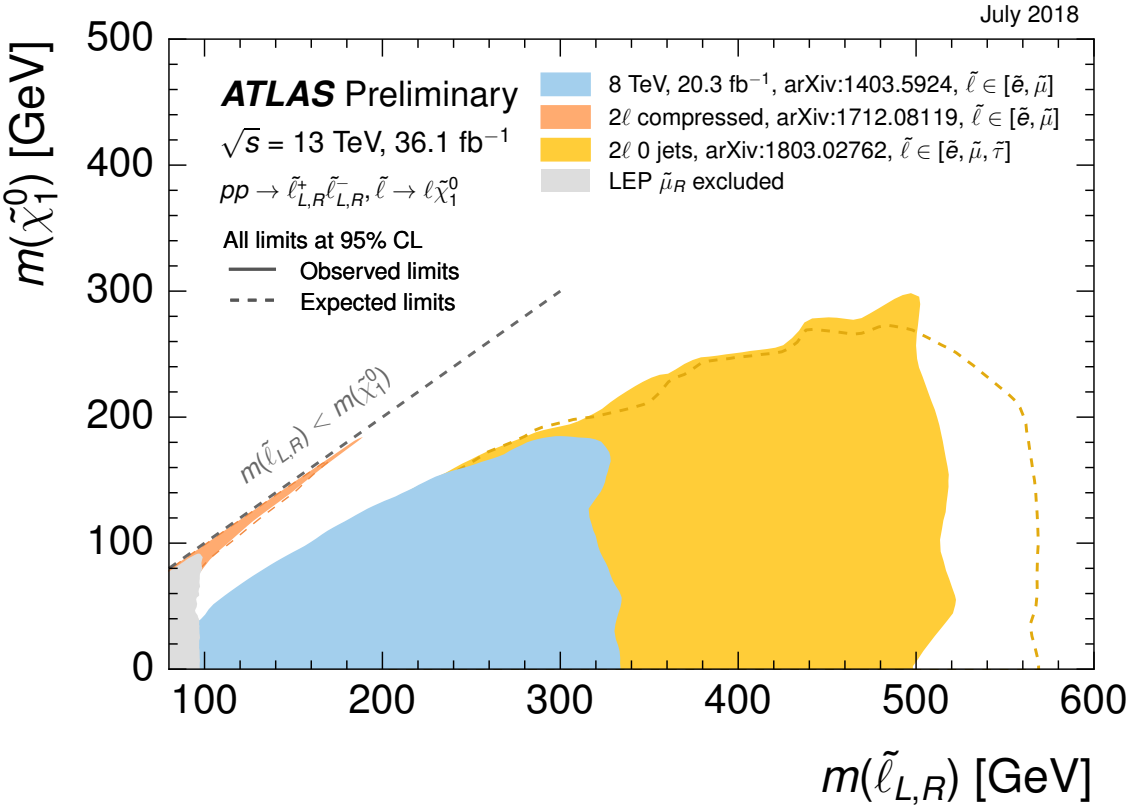

Figure 5.26: Summary of ATLAS sensitivity to direct slepton production [5]. This thesis presented the constraint from soft 2ℓ compressed search [3] (orange, this thesis); this corresponds to the limit presented in Figure 5.23. Constraints are also presented from the 2ℓ 0 jets analyses at 8 TeV with 20.3 fb^{-1} [277] (blue filled, as presented in Figure 5.2b) and 13 TeV with 36.1^{-1} [279] (yellow filled). Also displayed is the LEP limit on scalar partners of the right-handed muon $\tilde{\mu}_R$ (grey solid) [24, 280, 286]. The simplified slepton model for the ATLAS limits assume a four-fold mass degeneracy $m(\tilde{e}_L) = m(\tilde{e}_R) = m(\tilde{\mu}_L) = m(\tilde{\mu}_R)$ (for the 2ℓ 0 jets 13 TeV analysis, staus $\tilde{\tau}$ are also included in the mass degeneracy), as indicated in the legend. The slepton is assumed to decay to the corresponding lepton and bino neutralino dark matter via $\tilde{\ell} \to \ell\tilde{\chi}^{0}_{1}$ with 100% branching ratio.

by reconstructing shorter tracklets closer to the beam pipe. Both these avenues to bridge this gap are experimentally very challenging.

Wino–bino and the WZ corridor Figure 5.25 shows the ATLAS summary plot for boson decays of direct wino production decaying to bino $\widetilde{\chi}_1^0$. This figure is the same as Figure 5.2a but with the constraint the soft 2ℓ search [3] presented in this chapter included (green line), corresponding to the limit presented in Figure 5.21b. The moderately compressed region $30 \lesssim \Delta m(\widetilde{\chi}_1^\pm, \widetilde{\chi}_1^0) \lesssim 100$ GeV is particularly poorly constrained, primarily because the 3ℓ analysis was not optimised for this region in the most recent 13 TeV search [279]. When the mass splitting is of the order of the W or Z boson masses, this is also known as the WZ corridor. Here, the signal becomes kinematically very similar to the corresponding diboson background, making sensitivity especially challenging. Exploring a 3ℓ channel may improve sensitivity, as well as multi-variate techniques to better exploit signal–background kinematic differences.

Sleptons and the coannihilation corridor Figure 5.26 shows the ATLAS summary plot for direct slepton production in the mass plane of $m(\widetilde{\chi}_1^0)$ vs $m(\tilde{\ell})$. This chapter sets exclusion limits labelled by the 2ℓ compressed (orange filled). These are compared with partners of the right-handed muon ($\widetilde{\mu}_R$) from LEP constraints, and with limits obtained from the 2ℓ 0 jets searches at 8 TeV with 20.3 fb^{-1} [277]. Particularly striking is the gap in sensitivity beyond those from LEP in the so-called coannihilation corridor $15 \lesssim \Delta m(\tilde{\ell}, \widetilde{\chi}_1^0) \lesssim 60$ GeV. Indeed, the sensitivity of the 13 TeV 2ℓ 0 jets search [279] did not improve on the 8 TeV counterpart for $\Delta m(\tilde{\ell}, \widetilde{\chi}_1^0) \lesssim 60$ GeV. Here, the m_{T2} signal shape becomes very difficult to distinguish from the SM $WW \to \ell\nu\ell\nu$ process. A possible improvement is an angular analysis to distinguish between the spin-1 WW background from spin-0 $\tilde{\ell}\tilde{\ell}$ signal. Recently, the author proposed a solution using proton-tagged photon fusion production of sleptons $pp \to p(\gamma\gamma \to \tilde{\ell}\tilde{\ell})p$ to open sensitivity to this region by measuring initial state kinematics and the full missing momentum 4-vector [14].

5.9 Conclusions

This chapter presented a search for electroweak production of supersymmetric states in scenarios with compressed mass spectra using 36.1 fb^{-1} of $\sqrt{s} = 13$ TeV pp collisions recorded by ATLAS. Events were selected using the missing transverse momentum trigger. This allowed electrons (muons) down to 4.5 (4) GeV transverse momenta to be reconstructed, among the lowest used in ATLAS, in order to probe compressed scenarios. The dilepton invariant mass $m_{\ell\ell}$ and stranverse mass m_{T2} were the main discriminants used to construct signal regions, which exploit kinematic endpoints in the signals.

This is the first LHC publication to open sensitivity beyond LEP for Higgsino dark matter, and bino dark matter with wino or slepton coannihilators. However, no significant excesses were observed above the Standard Model expectation. For the Higgsino simplified model, exclusion limits at 95% CL were set on the next-to-lightest neutralino $\widetilde{\chi}_2^0$ up to masses of 145 GeV for 10 GeV mass splittings. For the wino–bino simplified model, the exclusion reached $\widetilde{\chi}_2^0$ up to masses of 175 GeV for 10 GeV mass splittings. For the slepton simplified model, which involves direct production of mass degenerate left and right-handed partners of the electrons and muons, signals were excluded up to masses of 190 GeV for mass splittings of 5 GeV. Using among the lowest momentum leptons supported by ATLAS allowed mass splittings down to 2.5, 2 and 1 GeV to be probed for the Higgsino, wino–bino, and slepton simplified models, respectively.

Finally, summary plots demonstrated the complementarity of sensitivity for these searches at the compressed frontier with other ATLAS searches. Striking gaps in sensitivity are identified, which serve as key targets for future work.

6

Summary

Weak scale supersymmetry provides solutions to the dark matter and electroweak hierarchy problems, while giving rich collider phenomenology explored in this thesis. Two pieces of original research were presented in Chapters 4 and 5, which examine and develop strategies to discover new dynamics accessible to the LHC. We now summarise the conclusions of these chapters.

Chapter 4 presented a theoretical study interpreting six early $\sqrt{s} = 13$ TeV searches for supersymmetry using 3.2 fb^{-1} of luminosity in the 19-dimensional parameter space of the phenomenological MSSM. These evaluate the robustness of early Run 2 search strategies and are compared to non-collider experiments, such as direct detection experiments searching for dark matter. The LHC searches primarily target production of gluinos and squarks, exhibiting striking complementarity in sensitivity for various scenarios of neutralino dark matter. Notably, Higgsino dark matter near 100 GeV remained promising even after these early Run 2 LHC constraints and served as a key target to design a new search in the subsequent chapter.

Chapter 5 presented a new experimental search strategy for electroweak production of supersymmetric states in scenarios with compressed mass spectra. Events are selected from 36.1 fb^{-1} of 13 TeV proton–proton collisions recorded by ATLAS. Two electrons (muons) down to $p_{\mathrm{T}} > 4.5$ (4) GeV are required, among the lowest used by ATLAS. In the supersymmetry signals, the invisible states recoil against initial state radiation, aligning their momenta to pass the missing transverse momentum trigger. These innovations are required to overcome long-standing difficulties to probe compressed scenarios, and this strategy has become a new cornerstone in the LHC search programme. This work is the first LHC publication with sensitivity to Higgsino dark matter and the coannihilation corridor involving winos or sleptons as the coannihilator. Sensitivity to all these scenarios

surpassed LEP constraints for the first time in nearly two decades. Nonetheless, striking gaps are revealed, with lower mass bounds on electroweakinos and sleptons being as low as or even below 100 GeV, which motivate future work to open sensitivity.

No statistically significant deviations from Standard Model predictions were observed in any of the work presented in this thesis. Despite this, the arguments for new physics beyond the Standard Model remain convincing—from stabilising the electroweak hierarchy to the particle identity of dark matter and tantalising tensions in the flavour sector. This thesis pioneered a new discovery strategy targeting otherwise inaccessible regimes of the energy frontier. Probing the remaining blind spots will require experimental creativity. Just as Hooke and Galileo did not anticipate the wealth of cellular biology and extraterrestrial moons when they inspected nature using their improved optical instruments, we should equally be prepared for profound surprises as we probe the unknown with upgraded tools and new techniques. We look forward with excitement to the innovation and ingenuity required to discover new physics and transform our understanding of fundamental physics.

Bibliography

[1] A. Barr and J. Liu, *First interpretation of 13 TeV supersymmetry searches in the pMSSM*, arXiv:1605.09502.

[2] A. Barr and J. Liu, *Analysing parameter space correlations of recent 13 TeV gluino and squark searches in the pMSSM*, *Eur. Phys. J. C* **77** (2017), no. 3 202, [arXiv:1608.05379].

[3] ATLAS Collaboration, *Search for electroweak production of supersymmetric states in scenarios with compressed mass spectra at* $\sqrt{s} = 13$ *TeV with the ATLAS detector*, *Phys. Rev. D* **97** (2018) 052010, [arXiv:1712.08119].

[4] ATLAS Collaboration, *HEPData for Search for electroweak production of supersymmetric states in scenarios with compressed mass spectra at* $\sqrt{s} = 13$ *TeV with the ATLAS detector*, 2018. doi.org/10.17182/hepdata.80609.

[5] ATLAS Collaboration, *ATLAS supersymmetry searches summary plots*, 2018. https://twiki.cern.ch/twiki/bin/view/AtlasPublic/SupersymmetryPublicResults.

[6] M. Hance, J. Liu, et al., *Searches for Weak Production of Compressed Supersymmetry in* pp *Collisions at* $\sqrt{s} = 13$ *TeV with the ATLAS Detector*, *ATL-COM-PHYS-2016-1708*. https://cds.cern.ch/record/2235272.

[7] ATLAS Collaboration, *Search for electroweak production of charginos and sleptons decaying in final states with two leptons and missing transverse momentum in* $\sqrt{s} = 13$ *TeV* pp *collisions using the ATLAS detector*, Tech. Rep. ATLAS-CONF-2019-008, CERN, Geneva, Mar, 2019.

[8] O. Abouzeid, J. Liu, et al., *Searches for weak production of compressed SUSY using soft leptons and missing transverse momentum in* $\sim$*140* fb^{-1} *of* pp *collisions at* $\sqrt{s} = 13$ *TeV with the ATLAS detector*, *ATL-COM-PHYS-2018-230*.

[9] ATLAS Collaboration, *Searches for electroweak production of supersymmetric particles with compressed mass spectra in* $\sqrt{s} = 13$ *TeV* pp *collisions with the ATLAS detector*, Tech. Rep. ATLAS-CONF-2019-014, CERN, Geneva, May, 2019.

[10] I. Dawson, B. Gallop, J. Liu, P. S. Miyagawa, P. W. Phillips, G. D. Pownall, D. Robinson, and A. R. Weidberg, *In Situ Radiation Damage Studies of Optoelectronics in the ATLAS SemiConductor*, 2019. Accepted Journal of Instrumentation.

[11] J. Liu, *Luminosity correlation of photodiode currents for SCT optical links*, *ATL-INDET-INT-2017-002* (Jan, 2017).

[12] ATLAS SCT Collaboration, *Bandwidth limitations, IPIN trends, SEU impact on chips, long term depletion projections, long term current projections, noisy strips vs time, active strips vs time. 2016 data*, Sep, 2016. https://atlas.web.cern.ch/Atlas/SCT-2016-002.

[13] ATLAS SCT Collaboration, *SCT p-i-n diode radiation damage effects during 2015 and 2016.*, Sep, 2017. https://atlas.web.cern.ch/Atlas/GROUPS/PHYSICS/PLOTS/SCT-2017-003.

[14] L. Beresford and J. Liu, *Photon collider search strategy for sleptons and dark matter at the LHC*, arXiv:1811.06465.

[15] H. Geiger and E. Marsden, *On a diffuse reflection of the α-particles*, *Proceedings of the Royal Society of London A: Mathematical, Physical and Engineering Sciences* **82** (1909), no. 557 495–500, [http://rspa.royalsocietypublishing.org/content/82/557/495.full.pdf].

[16] E. Rutherford, *The scattering of alpha and beta particles by matter and the structure of the atom*, *Phil. Mag. Ser.6* **21** (1911) 669–688.

[17] H. Geiger and E. Marsden, *The laws of deflexion of a particles through large angles*, *The London, Edinburgh, and Dublin Philosophical Magazine and Journal of Science* **25** (1913), no. 148 604–623.

[18] Lyndon Evans and Philip Bryant, *LHC Machine*, *Journal of Instrumentation* **3** (2008), no. 08 S08001.

[19] ATLAS Collaboration, *The ATLAS Experiment at the CERN Large Hadron Collider*, *JINST* **3** (2008), no. 08 S08003.

[20] *LEP design report*. CERN, Geneva, 1984. Copies shelved as reports in LEP, PS and SPS libraries.

[21] SLD Electroweak Group, DELPHI, ALEPH, SLD, SLD Heavy Flavour Group, OPAL, LEP Electroweak Working Group, L3, *Precision electroweak measurements on the Z resonance*, *Phys. Rept.* **427** (2006) 257–454, [hep-ex/0509008].

[22] ALEPH, DELPHI, L3, OPAL Experiments, "Combined LEP Chargino Results, up to 208 GeV for low DM." LEPSUSYWG/02-04.1, 2002.

[23] ALEPH, DELPHI, L3, OPAL Experiments, "Combined LEP Chargino Results, up to 208 GeV for large m0." LEPSUSYWG/01-03.1, 2001.

[24] ALEPH, DELPHI, L3, OPAL Experiments, "Combined LEP Selectron/Smuon/Stau Results, 183-208 GeV." LEPSUSYWG/04-01.1, 2004.

[25] TeVI Group, *Design Report Tevatron 1 project*, *Fermilab* (1984).

[26] **D0** Collaboration, S. Abachi et al., *Observation of the top quark*, *Phys. Rev. Lett.* **74** (1995) 2632–2637, [hep-ex/9503003].

[27] **CDF** Collaboration, F. Abe et al., *Observation of top quark production in $\bar{p}p$ collisions*, *Phys. Rev. Lett.* **74** (1995) 2626–2631, [hep-ex/9503002].

[28] **D0** Collaboration, V. M. Abazov et al., *Search for squarks and gluinos in events with jets and missing transverse energy using 2.1 $f\,b^{-1}$ of $p\bar{p}$ collision data at $\sqrt{s} = 1.96$- TeV*, *Phys. Lett.* **B660** (2008) 449–457, [arXiv:0712.3805].

[29] **CDF** Collaboration, T. Aaltonen et al., *Search for Direct Pair Production of Supersymmetric Top and Supersymmetric Bottom Quarks in $p\bar{p}$ Collisions at $\sqrt{s} = 1.96$-TeV*, *Phys. Rev.* **D76** (2007) 072010, [arXiv:0707.2567].

[30] ATLAS Collaboration, *Observation of a new particle in the search for the Standard Model Higgs boson with the ATLAS detector at the LHC*, *Phys. Lett. B* **716** (2012) 1, [arXiv:1207.7214].

[31] CMS Collaboration, *Observation of a new boson at a mass of 125 GeV with the CMS experiment at the LHC*, *Phys. Lett. B* **716** (2012) 30, [arXiv:1207.7235].

[32] ALICE Collaboration, *The ALICE experiment at the CERN LHC*, *JINST* **3** (2008) S08002.

[33] CMS Collaboration, *The CMS experiment at the CERN LHC*, *JINST* **3** (2008) S08004.

[34] LHCb Collaboration, *The LHCb Detector at the LHC*, *JINST* **3** (2008) S08005.

[35] C. Lefèvre, *The CERN accelerator complex*, Dec, 2008. CERN-DI-0812015.

[36] ATLAS Collaboration, *ATLAS luminosity public Run 2 results*, 2017.

[37] ATLAS Collaboration, *Expected Performance of the ATLAS Experiment – Detector, Trigger and Physics*, arXiv:0901.0512.

[38] **Particle Data Group** Collaboration, K. A. Olive et al., *Review of Particle Physics*, *Chin. Phys.* **C38** (2014) 090001.

[39] ATLAS Collaboration, *ATLAS Inner Detector: Technical Design Report, 1*. Technical Design Report ATLAS. CERN, Geneva, 1997.

[40] F. Hartmann, *Silicon tracking detectors in high-energy physics*, *Nucl. Instrum. Meth.* **A666** (2012) 25 – 46. Advanced Instrumentation.

[41] **ATLAS** Collaboration, B. Mindur, *ATLAS Transition Radiation Tracker (TRT): Straw tubes for tracking and particle identification at the Large Hadron Collider*, *Nucl. Instrum. Meth.* **A845** (2017) 257–261.

[42] ATLAS Collaboration, *ATLAS pixel detector electronics and sensors*, *JINST* **3** (2008) P07007.

[43] **ATLAS** Collaboration, M. Backhaus, *The upgraded Pixel Detector of the ATLAS Experiment for Run 2 at the Large Hadron Collider*, *Nucl. Instrum. Meth.* **A831** (2016) 65–70.

[44] ATLAS Collaboration, "ATLAS Insertable B-Layer Technical Design Report." ATLAS-TDR-19, 2010.

[45] **ATLAS IBL** Collaboration, B. Abbott et al., *Production and Integration of the ATLAS Insertable B-Layer*, *JINST* **13** (2018), no. 05 T05008, [arXiv:1803.00844].

[46] A. Ahmad et al, *The silicon microstrip sensors of the ATLAS semiconductor tracker*, .

[47] ATLAS Collaboration, *Operation and performance of the ATLAS semiconductor tracker*, *JINST* **9** (2014) P08009, [arXiv:1404.7473].

[48] ATLAS Collaboration, *Particle Identification Performance of the ATLAS Transition Radiation Tracker*, Tech. Rep. ATLAS-CONF-2011-128, CERN, Geneva, Sep, 2011.

[49] C. W. Fabjan and F. Gianotti, *Calorimetry for particle physics*, *Rev. Mod. Phys.* **75** (Oct, 2003) 1243–1286.

[50] ATLAS Collaboration, *ATLAS liquid-argon calorimeter: Technical Design Report*. Technical Design Report ATLAS. CERN, Geneva, 1996.

[51] ATLAS Collaboration, *ATLAS tile calorimeter: Technical Design Report*. Technical Design Report ATLAS. CERN, Geneva, 1996.

[52] ATLAS Collaboration, *Readiness of the ATLAS Liquid Argon Calorimeter for LHC Collisions*, *Eur. Phys. J.* **C70** (2010) 723–753, [arXiv:0912.2642].

[53] **ATLAS** Collaboration, N. Nikiforou, *Performance of the ATLAS Liquid Argon Calorimeter after three years of LHC operation and plans for a future upgrade*, in *Proceedings, 3rd International Conference on Advancements in Nuclear Instrumentation Measurement Methods and their Applications (ANIMMA 2013): Marseille, France, June 23-27, 2013*, 2013. arXiv:1306.6756.

[54] A. Artamonov et al., *The ATLAS forward calorimeters*, *JINST* **3** (2008) P02010.

[55] ATLAS Collaboration, *Readiness of the ATLAS Tile Calorimeter for LHC collisions*, *Eur. Phys. J.* **C70** (2010) 1193–1236, [arXiv:1007.5423].

[56] A. Hrynevich, *Performance of the ATLAS Tile Calorimeter*, Tech. Rep. ATL-TILECAL-PROC-2017-004. 06, CERN, Geneva, May, 2017.

[57] M. Mlynarikova, *Performance of the ATLAS hadronic Tile calorimeter*, in *5th Large Hadron Collider Physics Conference (LHCP 2017) Shanghai, China, May 15-20, 2017*, 2017. arXiv:1709.00100.

[58] ATLAS Collaboration, *ATLAS muon spectrometer: Technical Design Report*. Technical Design Report ATLAS. CERN, Geneva, 1997.

[59] **ATLAS** Collaboration, E. Diehl, *Calibration and Performance of the ATLAS Muon Spectrometer*, in *Particles and fields. Proceedings, Meeting of the Division of the American Physical Society, DPF 2011, Providence, USA, August 9-13, 2011*, 2011. arXiv:1109.6933.

[60] G. Aielli, M. Bindi, and A. Polini, *Performance, Operation and Detector Studies with the ATLAS Resistive Plate Chambers*, Tech. Rep. ATL-MUON-PROC-2012-006, CERN, Geneva, Sep, 2012.

[61] K. Nagai, *Thin gap chambers in ATLAS*, *Nucl. Instrum. Meth.* **A384** (1996), no. 1 219 – 221. BEAUTY '96.

[62] F. Bauer et al., *Construction and Test of MDT Chambers for the ATLAS Muon Spectrometer*, *Nucl. Instrum. Meth.* **A461** (2001) 17–20, [arXiv:1604.02000].

[63] T. Argyropoulos et al., *Cathode strip chambers in ATLAS: Installation, commissioning and in situ performance*, *IEEE Trans. Nucl. Sci.* **56** (2009) 1568–1574.

[64] ATLAS Collaboration, *Performance of the ATLAS trigger system in 2015*, *Eur. Phys. J. C* **77** (2017) 317, [arXiv:1611.09661].

[65] ATLAS Collaboration, *Missing Energy Trigger Public Results*, 2017.

[66] **ATLAS** Collaboration, G. Duckeck, D. Barberis, R. Hawkings, R. Jones, N. McCubbin, G. Poulard, D. Quarrie, T. Wenaus, and E. Obreshkov, *ATLAS computing: Technical design report*, *CERN* (2005).

[67] R. Brun and F. Rademakers, *ROOT: An object oriented data analysis framework*, *Nucl. Instrum. Meth.* **A389** (1997) 81–86.

[68] ATLAS Collaboration, *Search for dark matter and other new phenomena in events with an energetic jet and large missing transverse momentum using the ATLAS detector*, 2016. ATLAS-CONF-2017-060.

[69] ATLAS Collaboration, *$H \to 2e2\mu$ candidate event with 25 additional reconstructed primary vertices recorded in 2016*, 2016. https://twiki.cern.ch/twiki/bin/view/AtlasPublic/EventDisplayRun2Physics.

[70] M. Schwartz, *Quantum Field Theory and the Standard Model*. Cambridge University Press, 2013.

[71] S. Weinberg, *The Quantum theory of fields. Vol. 1: Foundations*. Cambridge University Press, 2005.

[72] G. Altarelli, *Collider Physics within the Standard Model: a Primer*, arXiv:1303.2842.

[73] S. F. Novaes, *Standard model: An Introduction*, in *Particles and fields. Proceedings, 10th Jorge Andre Swieca Summer School, Sao Paulo, Brazil, February 6-12, 1999*, 1999. hep-ph/0001283.

[74] M. B. Robinson, K. R. Bland, G. B. Cleaver, and J. R. Dittmann, *A Simple Introduction to Particle Physics. Part I - Foundations and the Standard Model*, arXiv:0810.3328.

[75] C. P. Burgess and G. D. Moore, *The standard model: A primer*. Cambridge University Press, 2006.

[76] ATLAS Collaboration, *Standard Model summary plots*, 2018. https://twiki.cern.ch/twiki/bin/view/AtlasPublic/StandardModelPublicResults.

[77] **LHCb** Collaboration, R. Aaij et al., *Test of lepton universality using $B^+ \to K^+\ell^+\ell^-$ decays*, *Phys. Rev. Lett.* **113** (2014) 151601, [arXiv:1406.6482].

[78] **LHCb** Collaboration, R. Aaij et al., *Test of Lepton Flavor Universality by the measurement of the $B^0 \to D^{*-}\tau^+\nu_\tau$ branching fraction using three-prong τ decays*, *Phys. Rev.* **D97** (2018), no. 7 072013, [arXiv:1711.02505].

[79] F. Archilli, M.-O. Bettler, P. Owen, and K. Petridis, *Flavour-changing neutral currents making and breaking the standard model*, *Nature* **546** (2017), no. 7657 221.

[80] G. Ciezarek, M. Franco Sevilla, B. Hamilton, R. Kowalewski, T. Kuhr, V. LÃijth, and Y. Sato, *A Challenge to Lepton Universality in B Meson Decays*, *Nature* **546** (2017) 227–233, [arXiv:1703.01766].

[81] **Muon g-2** Collaboration, G. W. Bennett et al., *Final Report of the Muon E821 Anomalous Magnetic Moment Measurement at BNL*, *Phys. Rev. D* **73** (2006) 072003, [hep-ex/0602035].

[82] K. Hagiwara, R. Liao, A. D. Martin, D. Nomura, and T. Teubner, $(g-2)_\mu$ *and* $\alpha(M_Z^2)$ *re-evaluated using new precise data*, *J. Phys. G* **38** (2011) 085003, [arXiv:1105.3149].

[83] **SNO** Collaboration, Q. R. Ahmad et al., *Measurement of the rate of* $\nu_e + d \to p + p + e^-$ *interactions produced by* ^8B *solar neutrinos at the Sudbury Neutrino Observatory*, *Phys. Rev. Lett.* **87** (2001) 071301, [nucl-ex/0106015].

[84] **Super-Kamiokande** Collaboration, Y. Fukuda et al., *Evidence for oscillation of atmospheric neutrinos*, *Phys. Rev. Lett.* **81** (1998) 1562–1567, [hep-ex/9807003].

[85] **LSND** Collaboration, A. Aguilar-Arevalo et al., *Evidence for neutrino oscillations from the observation of anti-neutrino(electron) appearance in a anti-neutrino(muon) beam*, *Phys. Rev.* **D64** (2001) 112007, [hep-ex/0104049].

[86] G. Mention, M. Fechner, T. Lasserre, T. A. Mueller, D. Lhuillier, M. Cribier, and A. Letourneau, *The Reactor Antineutrino Anomaly*, *Phys. Rev.* **D83** (2011) 073006, [arXiv:1101.2755].

[87] **MiniBooNE** Collaboration, A. A. Aguilar-Arevalo et al., *Observation of a Significant Excess of Electron-Like Events in the MiniBooNE Short-Baseline Neutrino Experiment*, arXiv:1805.12028.

[88] J. M. Cline, *Baryogenesis*, in *Les Houches Summer School - Session 86: Particle Physics and Cosmology: The Fabric of Spacetime Les Houches, France, July 31-August 25, 2006*, 2006. hep-ph/0609145.

[89] S. Davidson, E. Nardi, and Y. Nir, *Leptogenesis*, *Phys. Rept.* **466** (2008) 105–177, [arXiv:0802.2962].

[90] R. D. Peccei and H. R. Quinn, *CP Conservation in the Presence of Instantons*, *Phys. Rev. Lett.* **38** (1977) 1440–1443.

[91] C. A. Baker et al., *An Improved experimental limit on the electric dipole moment of the neutron*, *Phys. Rev. Lett.* **97** (2006) 131801, [hep-ex/0602020].

[92] **Supernova Search Team** Collaboration, A. G. Riess et al., *Observational evidence from supernovae for an accelerating universe and a cosmological constant*, *Astron. J.* **116** (1998) 1009–1038, [astro-ph/9805201].

[93] **Supernova Cosmology Project** Collaboration, S. Perlmutter et al., *Measurements of Omega and Lambda from 42 high redshift supernovae*, *Astrophys. J.* **517** (1999) 565–586, [astro-ph/9812133].

[94] **SDSS** Collaboration, M. Tegmark et al., *Cosmological parameters from SDSS and WMAP*, *Phys. Rev.* **D69** (2004) 103501, [astro-ph/0310723].

[95] **Planck** Collaboration, P. A. R. Ade et al., *Planck 2015 results. XIII. Cosmological parameters*, *Astron. Astrophys.* **594** (2016) A13, [arXiv:1502.01589].

[96] **WMAP** Collaboration, E. Komatsu et al., *Seven-Year Wilkinson Microwave Anisotropy Probe (WMAP) Observations: Cosmological Interpretation*, *Astrophys. J. Suppl.* **192** (2011) 18, [arXiv:1001.4538].

[97] S. Weinberg, *The Cosmological Constant Problem*, *Rev. Mod. Phys.* **61** (1989) 1–23.

[98] J. Martin, *Everything You Always Wanted To Know About The Cosmological Constant Problem (But Were Afraid To Ask)*, *Comptes Rendus Physique* **13** (2012) 566–665, [arXiv:1205.3365].

[99] A. H. Guth, *The Inflationary Universe: A Possible Solution to the Horizon and Flatness Problems*, *Phys. Rev.* **D23** (1981) 347–356.

[100] D. Baumann, *Inflation*, in *Physics of the large and the small, TASI 09, proceedings of the Theoretical Advanced Study Institute in Elementary Particle Physics, Boulder, Colorado, USA, 1-26 June 2009*, pp. 523–686, 2011. arXiv:0907.5424.

[101] A. Linde, *Inflationary Cosmology after Planck 2013*, in *100e Ecole d'Ete de Physique: Post-Planck Cosmology Les Houches, France, July 8-August 2, 2013*, pp. 231–316, 2015. arXiv:1402.0526.

[102] H. Georgi and S. L. Glashow, *Unity of All Elementary Particle Forces*, *Phys. Rev. Lett.* **32** (1974) 438–441.

[103] S. Dimopoulos, S. Raby, and F. Wilczek, *Supersymmetry and the Scale of Unification*, *Phys. Rev.* **D24** (1981) 1681–1683.

[104] S. Dimopoulos and H. Georgi, *Softly Broken Supersymmetry and SU(5)*, *Nucl. Phys.* **B193** (1981) 150.

[105] G. Bertone, D. Hooper, and J. Silk, *Particle dark matter: Evidence, candidates and constraints*, *Phys. Rept.* **405** (2005) 279–390, [hep-ph/0404175].

[106] D. Hooper, *Particle Dark Matter*, in *Proceedings of Theoretical Advanced Study Institute in Elementary Particle Physics on The dawn of the LHC era (TASI 2008)*, pp. 709–764, 2010. arXiv:0901.4090.

[107] K. Garrett and G. Duda, *Dark Matter: A Primer*, *Adv. Astron.* **2011** (2011) 968283, [arXiv:1006.2483].

[108] J. L. Feng, *Dark Matter Candidates from Particle Physics and Methods of Detection*, *Ann. Rev. Astron. Astrophys.* **48** (2010) 495–545, [arXiv:1003.0904].

[109] **Snowmass 2013 Cosmic Frontier Working Groups 1–4** Collaboration, D. Bauer et al., *Dark Matter in the Coming Decade: Complementary Paths to Discovery and Beyond*, vol. 7-8, pp. 16–23, 2015. arXiv:1305.1605.

[110] V. C. Rubin and W. K. Ford, Jr., *Rotation of the Andromeda Nebula from a Spectroscopic Survey of Emission Regions*, *Astrophys. J.* **159** (1970) 379–403.

[111] V. C. Rubin, N. Thonnard, and W. K. Ford, Jr., *Rotational properties of 21 Sc galaxies with a large range of luminosities and radii, from NGC 4605 ($R = 4$ kpc) to UGC 2885 ($R = 122$ kpc)*, *Astrophys. J.* **238** (1980) 471.

[112] F. Zwicky, *Die Rotverschiebung von extragalaktischen Nebeln*, *Helv. Phys. Acta* **6** (1933) 110–127.

[113] A. D. Lewis, D. A. Buote, and J. T. Stocke, *Chandra Observations of Abell 2029: The Dark Matter Profile Down to $< 0.01 R_{vir}$ in an Unusually Relaxed Cluster*, *Astrophys. J.* **586** (2003) 135–142, [astro-ph/0209205].

[114] J. A. Tyson, G. P. Kochanski, and I. P. Dell'Antonio, *Detailed mass map of CL0024+1654 from strong lensing*, *Astrophys. J.* **498** (1998) L107, [astro-ph/9801193].

[115] A. Refregier, *Weak gravitational lensing by large scale structure*, *Ann. Rev. Astron. Astrophys.* **41** (2003) 645–668, [astro-ph/0307212].

[116] D. Clowe, M. Bradac, A. H. Gonzalez, M. Markevitch, S. W. Randall, et al., *A direct empirical proof of the existence of dark matter*, *Astrophys.J.* **648** (2006) L109–L113, [astro-ph/0608407].

[117] P. Van Dokkum, S. Danieli, Y. Cohen, A. Merritt, A. J. Romanowsky, R. Abraham, J. Brodie, C. Conroy, D. Lokhorst, L. Mowla, et al., *A galaxy lacking dark matter*, *Nature* **555** (2018), no. 7698 629.

[118] S. Dodelson, *Supersymmetric unification*. Academic Press, San Diego, CA, 2003.

[119] M. Lisanti, *Lectures on Dark Matter Physics*, in *Proceedings, Theoretical Advanced Study Institute in Elementary Particle Physics: New Frontiers in Fields and Strings (TASI 2015): Boulder, CO, USA, June 1-26, 2015*, pp. 399–446, 2017. arXiv:1603.03797.

[120] **Planck** Collaboration, N. Aghanim et al., *Planck 2018 results. VI. Cosmological parameters*, arXiv:1807.06209.

[121] S. Weinberg, *Implications of Dynamical Symmetry Breaking*, *Phys. Rev.* **D13** (1976) 974–996.

[122] L. Susskind, *Dynamics of Spontaneous Symmetry Breaking in the Weinberg-Salam Theory*, *Phys. Rev.* **D20** (1979) 2619–2625.

[123] S. Weinberg, *A Model of Leptons*, *Phys. Rev. Lett.* **19** (1967) 1264–1266.

[124] S. L. Glashow, *Partial Symmetries of Weak Interactions*, *Nucl. Phys.* **22** (1961) 579–588.

[125] T. W. B. Kibble, *Symmetry breaking in nonAbelian gauge theories*, *Phys. Rev.* **155** (1967) 1554–1561.

[126] P. W. Higgs, *Broken symmetries, massless particles and gauge fields*, *Phys. Lett.* **12** (1964) 132–133.

[127] F. Englert and R. Brout, *Broken Symmetry and the Mass of Gauge Vector Mesons*, *Phys. Rev. Lett.* **13** (1964) 321–323.

[128] G. 't Hooft, *Naturalness, chiral symmetry, and spontaneous chiral symmetry breaking*, *NATO Sci. Ser. B* **59** (1980) 135–157.

[129] C. P. Burgess, *Introduction to Effective Field Theory*, *Ann. Rev. Nucl. Part. Sci.* **57** (2007) 329–362, [hep-th/0701053].

[130] N. Arkani-Hamed, S. Dimopoulos, and G. R. Dvali, *The Hierarchy problem and new dimensions at a millimeter*, *Phys. Lett.* **B429** (1998) 263–272, [hep-ph/9803315].

[131] L. Randall and R. Sundrum, *A Large mass hierarchy from a small extra dimension*, *Phys. Rev. Lett.* **83** (1999) 3370–3373, [hep-ph/9905221].

[132] N. Arkani-Hamed, A. G. Cohen, E. Katz, and A. E. Nelson, *The Littlest Higgs*, *JHEP* **07** (2002) 034, [hep-ph/0206021].

[133] S. Dimopoulos, *Supersymmetric unification*, in *History of Original Ideas and Basic Discoveries in Particle Physics* (H. B. Newman and T. Ypsilantis, eds.), ch. 32, pp. 623–638. Nato Science Series B, 1996.

[134] Yu. A. Golfand and E. P. Likhtman, *Extension of the Algebra of Poincare Group Generators and Violation of p Invariance*, *JETP Lett.* **13** (1971) 323–326. [Pisma Zh. Eksp. Teor. Fiz.13,452(1971)].

[135] D. V. Volkov and V. P. Akulov, *Is the Neutrino a Goldstone Particle?*, *Phys. Lett. B* **46** (1973) 109–110.

[136] J. Wess and B. Zumino, *Supergauge Transformations in Four-Dimensions*, *Nucl. Phys. B* **70** (1974) 39–50.

[137] J. Wess and B. Zumino, *Supergauge Invariant Extension of Quantum Electrodynamics*, *Nucl. Phys. B* **78** (1974) 1.

[138] S. Ferrara and B. Zumino, *Supergauge Invariant Yang-Mills Theories*, *Nucl. Phys. B* **79** (1974) 413.

[139] A. Salam and J. A. Strathdee, *Supersymmetry and Nonabelian Gauges*, *Phys. Lett. B* **51** (1974) 353–355.

[140] R. Haag, J. T. Lopuszánski, and M. F. Sohnius, *All possible generators of supersymmetries of the S-matrix*, *Nucl. Phys. B* **88** (Nov, 1974) 257–74. 45 p.

[141] S. P. Martin, *A Supersymmetry primer*, hep-ph/9709356. [Adv. Ser. Direct. High Energy Phys.18,1(1998)].

[142] I. J. R. Aitchison, *Supersymmetry and the MSSM: An Elementary introduction*, hep-ph/0505105.

[143] P. Fayet, *Supersymmetry and Weak, Electromagnetic and Strong Interactions*, *Phys. Lett.* **B64** (1976) 159.

[144] P. Fayet, *Spontaneously Broken Supersymmetric Theories of Weak, Electromagnetic and Strong Interactions*, *Phys. Lett.* **B69** (1977) 489.

[145] **MSSM Working Group** Collaboration, A. Djouadi et al., *The Minimal supersymmetric standard model: Group summary report*, in *GDR (Groupement De Recherche) - Supersymetrie Montpellier, France, April 15-17, 1998*, 1998. hep-ph/9901246.

[146] G. R. Farrar and P. Fayet, *Phenomenology of the Production, Decay, and Detection of New Hadronic States Associated with Supersymmetry*, *Phys. Lett. B* **76** (1978) 575–579.

[147] P. Z. Skands et al., *SUSY Les Houches accord: Interfacing SUSY spectrum calculators, decay packages, and event generators*, *JHEP* **07** (2004) 036, [hep-ph/0311123].

[148] H. Goldberg, *Constraint on the Photino Mass from Cosmology*, *Phys. Rev. Lett.* **50** (1983) 1419. [Erratum: Phys. Rev. Lett.103,099905(2009)].

[149] J. R. Ellis, J. S. Hagelin, D. V. Nanopoulos, K. A. Olive, and M. Srednicki, *Supersymmetric Relics from the Big Bang*, *Nucl. Phys.* **B238** (1984) 453–476.

[150] R. Barbieri and D. Pappadopulo, *S-particles at their naturalness limits*, *JHEP* **10** (2009) 061, [arXiv:0906.4546].

[151] M. Papucci, J. T. Ruderman, and A. Weiler, *Natural SUSY endures*, *JHEP* **09** (2012) 035, [arXiv:1110.6926].

[152] R. Barbieri and G. F. Giudice, *Upper Bounds on Supersymmetric Particle Masses*, *Nucl. Phys. B* **306** (1988) 63.

[153] B. de Carlos and J. A. Casas, *One loop analysis of the electroweak breaking in supersymmetric models and the fine tuning problem*, *Phys. Lett. B* **309** (1993) 320–328, [hep-ph/9303291].

[154] N. Arkani-Hamed and S. Dimopoulos, *Supersymmetric unification without low energy supersymmetry and signatures for fine-tuning at the LHC*, *JHEP* **06** (2005) 073, [hep-th/0405159].

[155] G. F. Giudice and A. Romanino, *Split supersymmetry*, *Nucl. Phys.* **B699** (2004) 65–89, [hep-ph/0406088]. [Erratum: Nucl. Phys.B706,487(2005)].

[156] K. Griest and D. Seckel, *Three exceptions in the calculation of relic abundances*, *Phys. Rev. D* **43** (1991) 3191–3203.

[157] J. Edsjo and P. Gondolo, *Neutralino relic density including coannihilations*, *Phys. Rev. D* **56** (1997) 1879–1894, [hep-ph/9704361].

[158] ATLAS Collaboration, *Search for New Phenomena in Dijet Mass and Angular Distributions from pp Collisions at $\sqrt{s} = 13$ TeV with the ATLAS Detector*, *Phys. Lett. B* **754** (2016) 302, [arXiv:1512.01530].

[159] C. G. Lester and D. J. Summers, *Measuring masses of semi-invisibly decaying particles pair produced at hadron colliders*, *Phys. Lett. B* **463** (1999) 99–103, [hep-ph/9906349].

[160] A. Barr, C. Lester, and P. Stephens, *A variable for measuring masses at hadron colliders when missing energy is expected; m_{T2}: the truth behind the glamour*, *J. Phys. G* **29** (2003) 2343–2363, [hep-ph/0304226].

[161] A. J. Barr, *Measuring slepton spin at the LHC*, *JHEP* **02** (2006) 042, [hep-ph/0511115].

[162] A. J. Barr, B. Gripaios, and C. G. Lester, *Weighing Wimps with Kinks at Colliders: Invisible Particle Mass Measurements from Endpoints*, *JHEP* **02** (2008) 014, [arXiv:0711.4008].

[163] A. J. Barr and C. G. Lester, *A Review of the Mass Measurement Techniques proposed for the Large Hadron Collider*, *J. Phys.* **G37** (2010) 123001, [arXiv:1004.2732].

[164] A. J. Barr, T. J. Khoo, P. Konar, K. Kong, C. G. Lester, K. T. Matchev, and M. Park, *Guide to transverse projections and mass-constraining variables*, *Phys. Rev.* **D84** (2011) 095031, [arXiv:1105.2977].

[165] N. Arkani-Hamed, P. Schuster, N. Toro, J. Thaler, L.-T. Wang, B. Knuteson, and S. Mrenna, *MARMOSET: The Path from LHC Data to the New Standard Model via On-Shell Effective Theories*, hep-ph/0703088.

[166] J. Alwall, P. Schuster, and N. Toro, *Simplified Models for a First Characterization of New Physics at the LHC*, *Phys. Rev. D* **79** (2009) 075020, [arXiv:0810.3921].

[167] J. Alwall, M.-P. Le, M. Lisanti, and J. G. Wacker, *Model-Independent Jets plus Missing Energy Searches*, *Phys. Rev.* **D79** (2009) 015005, [arXiv:0809.3264].

[168] E. Izaguirre, M. Manhart, and J. G. Wacker, *Bigger, Better, Faster, More at the LHC*, *JHEP* **12** (2010) 030, [arXiv:1003.3886].

[169] D. S. M. Alves, E. Izaguirre, and J. G. Wacker, *Where the Sidewalk Ends: Jets and Missing Energy Search Strategies for the 7 TeV LHC*, *JHEP* **10** (2011) 012, [arXiv:1102.5338].

[170] **LHC New Physics Working Group** Collaboration, D. Alves, *Simplified Models for LHC New Physics Searches*, *J. Phys. G* **39** (2012) 105005, [arXiv:1105.2838].

[171] R. Essig, E. Izaguirre, J. Kaplan, and J. G. Wacker, *Heavy Flavor Simplified Models at the LHC*, *JHEP* **01** (2012) 074, [arXiv:1110.6443].

[172] LHC SUSY Cross Section Working Group, *Cross sections for various sub-process – 13 TeV*, 2017. https://twiki.cern.ch/twiki/bin/view/LHCPhysics/SUSYCrossSections.

[173] B. Fuks, M. Klasen, D. R. Lamprea, and M. Rothering, *Gaugino production in proton-proton collisions at a center-of-mass energy of 8 TeV*, *JHEP* **1210** (2012) 081, [arXiv:1207.2159].

[174] B. Fuks, M. Klasen, D. R. Lamprea, and M. Rothering, *Precision predictions for electroweak superpartner production at hadron colliders with Resummino*, *Eur.Phys.J.* **C73** (2013) 2480, [arXiv:1304.0790].

[175] B. Fuks, M. Klasen, D. R. Lamprea, and M. Rothering, *Revisiting slepton pair production at the Large Hadron Collider*, *JHEP* **01** (2014) 168, [arXiv:1310.2621].

[176] W. Beenakker, C. Borschensky, M. KrÃď mer, A. Kulesza, and E. Laenen, *NNLL-fast: predictions for coloured supersymmetric particle production at the LHC with threshold and Coulomb resummation*, *JHEP* **12** (2016) 133, [arXiv:1607.07741].

[177] ATLAS Collaboration, *Search for squarks and gluinos in final states with jets and missing transverse momentum using* $36\,fb^{-1}$ *of* $\sqrt{s} = 13$ *TeV* pp *collision data with the ATLAS detector*, *Phys. Rev. D* **97** (2018) 112001, [arXiv:1712.02332].

[178] ATLAS Collaboration, *Search for new phenomena with large jet multiplicities and missing transverse momentum using large-radius jets and flavour-tagging at ATLAS in 13 TeV* pp *collisions*, *JHEP* **12** (2017) 034, [arXiv:1708.02794].

[179] ATLAS Collaboration, *Search for squarks and gluinos in final states with jets and missing transverse momentum at* $\sqrt{s} = 13$ *TeV with the ATLAS detector*, *Eur. Phys. J. C* **76** (2016) 392, [arXiv:1605.03814].

[180] ATLAS Collaboration, *Search for new phenomena in final states with large jet multiplicities and missing transverse momentum with ATLAS using* $\sqrt{s} = 13$ *TeV proton–proton collisions*, *Phys. Lett. B* **757** (2016) 334, [arXiv:1602.06194].

[181] ATLAS Collaboration, *Search for gluinos in events with an isolated lepton, jets and missing transverse momentum at* $\sqrt{s} = 13$ *TeV with the ATLAS detector*, *Eur. Phys. J. C* **76** (2016) 565, [arXiv:1605.04285].

[182] ATLAS Collaboration, *Search for pair production of gluinos decaying via stop and sbottom in events with b-jets and large missing transverse momentum in* pp *collisions at* $\sqrt{s} = 13$ *TeV with the ATLAS detector*, *Phys. Rev. D* **94** (2016) 032003, [arXiv:1605.09318].

[183] ATLAS Collaboration, *Search for supersymmetry at $\sqrt{s} = 13$ TeV in final states with jets and two same-sign leptons or three leptons with the ATLAS detector*, *Eur. Phys. J. C* **76** (2016) 259, [arXiv:1602.09058].

[184] ATLAS Collaboration, *Search for new phenomena in final states with an energetic jet and large missing transverse momentum in pp collisions at $\sqrt{s} = 13$ TeV using the ATLAS detector*, *Phys. Rev. D* **94** (2016) 032005, [arXiv:1604.07773].

[185] ATLAS Collaboration, *Search for metastable heavy charged particles with large ionization energy loss in pp collisions at $\sqrt{s} = 13$ TeV using the ATLAS experiment*, *Phys. Rev. D* **93** (2016) 112015, [arXiv:1604.04520].

[186] ATLAS Collaboration, *Search for top squarks in final states with one isolated lepton, jets, and missing transverse momentum in $\sqrt{s} = 13$ TeV pp collisions with the ATLAS detector*, *Phys. Rev. D* **94** (2016) 052009, [arXiv:1606.03903].

[187] ATLAS Collaboration, *Search for heavy long-lived charged R-hadrons with the ATLAS detector in 3.2 fb^{-1} of proton–proton collision data at $\sqrt{s} = 13$ TeV*, *Phys. Lett. B* **760** (2016) 647, [arXiv:1606.05129].

[188] ATLAS Collaboration, *Search for bottom squark pair production in proton–proton collisions at $\sqrt{s} = 13$ TeV with the ATLAS detector*, *Eur. Phys. J. C* **76** (2016) 547, [arXiv:1606.08772].

[189] CMS Collaboration, *Search for new physics with the M_{T2} variable in all-jets final states produced in pp collisions at $\sqrt{s} = 13$ TeV*, *JHEP* **10** (2016) 006, [arXiv:1603.04053].

[190] CMS Collaboration, *Search for supersymmetry in the multijet and missing transverse momentum final state in pp collisions at 13 TeV*, *Phys. Lett. B* **758** (2016) 152, [arXiv:1602.06581].

[191] CMS Collaboration, *Search for new physics in same-sign dilepton events in proton–proton collisions at $\sqrt{s} = 13$ TeV*, *Eur. Phys. J. C* **76** (2016) 439, [arXiv:1605.03171].

[192] CMS Collaboration, *Search for supersymmetry in pp collisions at $\sqrt{s} = 13$ TeV in the single-lepton final state using the sum of masses of large-radius jets*, *JHEP* **08** (2016) 122, [arXiv:1605.04608].

[193] ATLAS Collaboration, *Search for squarks and gluinos with the ATLAS detector in final states with jets and missing transverse momentum using $\sqrt{s} = 8$ TeV proton–proton collision data*, *JHEP* **09** (2014) 176, [arXiv:1405.7875].

[194] ATLAS Collaboration, *Search for charginos nearly mass degenerate with the lightest neutralino based on a disappearing-track signature in pp collisions at $\sqrt{s} = 8$ TeV with the ATLAS detector*, *Phys. Rev. D* **88** (2013) 112006, [arXiv:1310.3675].

[195] ATLAS Collaboration, *Summary of the searches for squarks and gluinos using $\sqrt{s} = 8$ TeV pp collisions with the ATLAS experiment at the LHC*, *JHEP* **10** (2015) 054, [arXiv:1507.05525].

[196] ATLAS Collaboration, *ATLAS Run 1 searches for direct pair production of third-generation squarks at the Large Hadron Collider*, *Eur. Phys. J. C* **75** (2015) 510, [arXiv:1506.08616].

[197] ATLAS Collaboration, *Search for the electroweak production of supersymmetric particles in $\sqrt{s} = 8$ TeV pp collisions with the ATLAS detector*, *Phys. Rev. D* **93** (2016) 052002, [arXiv:1509.07152].

[198] CMS Collaboration, *Searches for third-generation squark production in fully hadronic final states in proton–proton collisions at $\sqrt{s} = 8$ TeV*, *JHEP* **06** (2015) 116, [arXiv:1503.08037].

[199] CMS Collaboration, *Searches for supersymmetry using the M_{T2} variable in hadronic events produced in pp collisions at 8 TeV*, *JHEP* **05** (2015) 078, [arXiv:1502.04358].

[200] L. J. Hall and L. Randall, *Weak scale effective supersymmetry*, *Phys. Rev. Lett.* **65** (1990) 2939–2942.

[201] C. F. Berger, J. S. Gainer, J. L. Hewett, and T. G. Rizzo, *Supersymmetry Without Prejudice*, *JHEP* **02** (2009) 023, [arXiv:0812.0980].

[202] M. W. Cahill-Rowley, J. L. Hewett, S. Hoeche, A. Ismail, and T. G. Rizzo, *The New Look pMSSM with Neutralino and Gravitino LSPs*, *Eur. Phys. J.* **C72** (2012) 2156, [arXiv:1206.4321].

[203] M. W. Cahill-Rowley, J. L. Hewett, A. Ismail, and T. G. Rizzo, *More energy, more searches, but the phenomenological MSSM lives on*, *Phys. Rev.* **D88** (2013), no. 3 035002, [arXiv:1211.1981].

[204] M. Cahill-Rowley, J. L. Hewett, A. Ismail, and T. G. Rizzo, *Lessons and prospects from the pMSSM after LHC Run I*, *Phys. Rev.* **D91** (2015), no. 5 055002, [arXiv:1407.4130].

[205] S. S. AbdusSalam, B. C. Allanach, F. Quevedo, F. Feroz, and M. Hobson, *Fitting the Phenomenological MSSM*, *Phys. Rev.* **D81** (2010) 095012, [arXiv:0904.2548].

[206] B. C. Allanach, A. J. Barr, A. Dafinca, and C. Gwenlan, *Discovery reach for generic supersymmetry at the LHC: M_{T2} versus missing transverse momentum selections for pMSSM searches*, *JHEP* **07** (2011) 104, [arXiv:1105.1024].

[207] S. Sekmen, S. Kraml, J. Lykken, F. Moortgat, S. Padhi, L. Pape, M. Pierini, H. B. Prosper, and M. Spiropulu, *Interpreting LHC SUSY searches in the phenomenological MSSM*, *JHEP* **02** (2012) 075, [arXiv:1109.5119].

[208] C. Strege, G. Bertone, G. J. Besjes, S. Caron, R. Ruiz de Austri, A. Strubig, and R. Trotta, *Profile likelihood maps of a 15-dimensional MSSM*, *JHEP* **09** (2014) 081, [arXiv:1405.0622].

[209] K. J. de Vries et al., *The pMSSM10 after LHC Run 1*, *Eur. Phys. J. C* **75** (2015), no. 9 422, [arXiv:1504.03260].

[210] A. Arbey, M. Battaglia, and F. Mahmoudi, *Light Neutralino Dark Matter in the pMSSM: Implications of LEP, LHC and Dark Matter Searches on SUSY Particle Spectra*, *Eur. Phys. J.* **C72** (2012) 2169, [arXiv:1205.2557].

[211] C. Boehm, P. S. B. Dev, A. Mazumdar, and E. Pukartas, *Naturalness of Light Neutralino Dark Matter in pMSSM after LHC, XENON100 and Planck Data*, *JHEP* **06** (2013) 113, [arXiv:1303.5386].

[212] A. Fowlie, K. Kowalska, L. Roszkowski, E. M. Sessolo, and Y.-L. S. Tsai, *Dark matter and collider signatures of the MSSM*, *Phys. Rev.* **D88** (2013) 055012, [arXiv:1306.1567].

[213] M. Cahill-Rowley, R. Cotta, A. Drlica-Wagner, S. Funk, J. Hewett, A. Ismail, T. Rizzo, and M. Wood, *Complementarity of dark matter searches in the phenomenological MSSM*, *Phys. Rev.* **D91** (2015), no. 5 055011, [arXiv:1405.6716].

[214] L. Roszkowski, E. M. Sessolo, and A. J. Williams, *Prospects for dark matter searches in the pMSSM*, *JHEP* **02** (2015) 014, [arXiv:1411.5214].

[215] G. Bertone, F. Calore, S. Caron, R. Ruiz, J. S. Kim, R. Trotta, and C. Weniger, *Global analysis of the pMSSM in light of the Fermi GeV excess: prospects for the LHC Run-II and astroparticle experiments*, *JCAP* **1604** (2016), no. 04 037, [arXiv:1507.07008].

[216] M. E. Cabrera-Catalan, S. Ando, C. Weniger, and F. Zandanel, *Indirect and direct detection prospect for TeV dark matter in the nine parameter MSSM*, *Phys. Rev.* **D92** (2015), no. 3 035018, [arXiv:1503.00599].

[217] ATLAS Collaboration, *Dark matter interpretations of ATLAS searches for the electroweak production of supersymmetric particles in $\sqrt{s} = 8$ TeV proton–proton collisions*, *JHEP* **09** (2016) 175, [arXiv:1608.00872].

[218] ATLAS Collaboration, *Summary of the ATLAS experiment's sensitivity to supersymmetry after LHC Run 1 — interpreted in the phenomenological MSSM*, *JHEP* **10** (2015) 134, [arXiv:1508.06608].

[219] CMS Collaboration, *Phenomenological MSSM interpretation of CMS searches in pp collisions at $\sqrt{s} = 7$ and 8 TeV*, *JHEP* **10** (2016) 129, [arXiv:1606.03577].

[220] K. Kowalska, *Phenomenological MSSM in light of new 13 TeV LHC data*, *Eur. Phys. J.* **C76** (2016), no. 12 684, [arXiv:1608.02489].

[221] J. Abdallah et al., *Simplified Models for Dark Matter and Missing Energy Searches at the LHC*, arXiv:1409.2893.

[222] J. Abdallah et al., *Simplified Models for Dark Matter Searches at the LHC*, *Phys. Dark Univ.* **9-10** (2015) 8–23, [arXiv:1506.03116].

[223] D. Abercrombie et al., *Dark Matter Benchmark Models for Early LHC Run-2 Searches: Report of the ATLAS/CMS Dark Matter Forum*, arXiv:1507.00966.

[224] G. Busoni et al., *Recommendations on presenting LHC searches for missing transverse energy signals using simplified s-channel models of dark matter*, arXiv:1603.04156.

[225] M. Bauer et al., *Towards the next generation of simplified Dark Matter models*, arXiv:1607.06680.

[226] ATLAS Collaboration, *Search for dark matter produced in association with a Higgs boson decaying to two bottom quarks in pp collisions at $\sqrt{s} = 8$ TeV with the ATLAS detector*, *Phys. Rev. D* **93** (2016) 072007, [arXiv:1510.06218].

[227] ATLAS Collaboration, *Search for new phenomena in events with a photon and missing transverse momentum in pp collisions at $\sqrt{s} = 13$ TeV with the ATLAS detector*, *JHEP* **06** (2016) 059, [arXiv:1604.01306].

[228] ATLAS Collaboration, *Search for dark matter produced in association with a hadronically decaying vector boson in pp collisions at $\sqrt{s} = 13$ TeV with the ATLAS detector*, *Phys. Lett. B* **763** (2016) 251, [arXiv:1608.02372].

[229] CMS Collaboration, *Search for dark matter, extra dimensions, and unparticles in monojet events in proton–proton collisions at $\sqrt{s} = 8$ TeV*, *Eur. Phys. J. C* **75** (2015) 235, [arXiv:1408.3583].

[230] CMS Collaboration, *Search for dark matter particles in proton–proton collisions at $\sqrt{s} = 8$ TeV using the razor variables*, *JHEP* **12** (2016) 088, [arXiv:1603.08914].

[231] CMS Collaboration, *Search for dark matter in proton–proton collisions at 8 TeV with missing transverse momentum and vector boson tagged jets*, *JHEP* **12** (2016) 083, [arXiv:1607.05764].

[232] T. A. W. Martin and D. Morrissey, *Electroweakino constraints from LHC data*, *JHEP* **12** (2014) 168, [arXiv:1409.6322].

[233] J. Bramante, N. Desai, P. Fox, A. Martin, B. Ostdiek, and T. Plehn, *Towards the Final Word on Neutralino Dark Matter*, *Phys. Rev.* **D93** (2016), no. 6 063525, [arXiv:1510.03460].

[234] D. Barducci, A. Belyaev, A. K. M. Bharucha, W. Porod, and V. Sanz, *Uncovering Natural Supersymmetry via the interplay between the LHC and Direct Dark Matter Detection*, *JHEP* **07** (2015) 066, [arXiv:1504.02472].

[235] **PandaX-II** Collaboration, A. Tan et al., *Dark Matter Results from First 98.7 Days of Data from the PandaX-II Experiment*, *Phys. Rev. Lett.* **117** (2016), no. 12 121303, [arXiv:1607.07400].

[236] **LUX** Collaboration, D. S. Akerib et al., *Results from a search for dark matter in the complete LUX exposure*, *Phys. Rev. Lett.* **118** (2017), no. 2 021303, [arXiv:1608.07648].

[237] J. Berger, M. W. Cahill-Rowley, D. Ghosh, J. L. Hewett, A. Ismail, and T. G. Rizzo, *CP-violating phenomenological MSSM*, *Phys. Rev.* **D93** (2016), no. 3 035017, [arXiv:1510.08840].

[238] M. Baak, M. Goebel, J. Haller, A. Hoecker, D. Kennedy, R. Kogler, K. Moenig, M. Schott, and J. Stelzer, *The Electroweak Fit of the Standard Model after the Discovery of a New Boson at the LHC*, *Eur. Phys. J.* **C72** (2012) 2205, [arXiv:1209.2716].

[239] T. Aoyama, M. Hayakawa, T. Kinoshita, and M. Nio, *Complete Tenth-Order QED Contribution to the Muon g-2*, *Phys. Rev. Lett.* **109** (2012) 111808, [arXiv:1205.5370].

[240] A. Nyffeler, *Hadronic light-by-light scattering in the muon g-2: A New short-distance constraint on pion-exchange*, *Phys. Rev.* **D79** (2009) 073012, [arXiv:0901.1172].

[241] A. Czarnecki, W. J. Marciano, and A. Vainshtein, *Refinements in electroweak contributions to the muon anomalous magnetic moment*, *Phys. Rev.* **D67** (2003) 073006, [hep-ph/0212229]. [Erratum: Phys. Rev.D73,119901(2006)].

[242] **Muon g-2** Collaboration, G. W. Bennett et al., *Measurement of the negative muon anomalous magnetic moment to 0.7 ppm*, *Phys. Rev. Lett.* **92** (2004) 161802, [hep-ex/0401008].

[243] P. J. Mohr, B. N. Taylor, and D. B. Newell, *Codata recommended values of the fundamental physical constants: 2006**, *Rev. Mod. Phys.* **80** (Jun, 2008) 633–730.

[244] B. L. Roberts, *Status of the Fermilab Muon* $(g-2)$ *Experiment*, *Chin. Phys.* **C34** (2010) 741–744, [arXiv:1001.2898].

[245] **Heavy Flavor Averaging Group** Collaboration, Y. Amhis et al., *Averages of B-Hadron, C-Hadron, and tau-lepton properties as of early 2012*, arXiv:1207.1158.

[246] K. De Bruyn, R. Fleischer, R. Knegjens, P. Koppenburg, M. Merk, A. Pellegrino, and N. Tuning, *Probing New Physics via the* $B_s^0 \to \mu^+\mu^-$ *Effective Lifetime*, *Phys. Rev. Lett.* **109** (2012) 041801, [arXiv:1204.1737].

[247] **LHCb, CMS** Collaboration, V. Khachatryan et al., *Observation of the rare* $B_s^0 \to \mu^+\mu^-$ *decay from the combined analysis of CMS and LHCb data*, *Nature* **522** (2015) 68–72, [arXiv:1411.4413].

[248] **BaBar** Collaboration, B. Aubert et al., *A Search for* $B^+ \to \ell^+ \nu_\ell$ *Recoiling Against* $B^- \to D^0 \ell^- \bar{\nu} X$, *Phys. Rev.* **D81** (2010) 051101, [arXiv:0912.2453].

[249] **Belle** Collaboration, K. Hara et al., *Evidence for* $B^- \to \tau^- \bar{\nu}$ *with a Semileptonic Tagging Method*, *Phys. Rev.* **D82** (2010) 071101, [arXiv:1006.4201].

[250] **Belle** Collaboration, I. Adachi et al., *Evidence for* $B^- \to \tau^- \bar{\nu}_\tau$ *with a Hadronic Tagging Method Using the Full Data Sample of Belle*, *Phys. Rev. Lett.* **110** (2013), no. 13 131801, [arXiv:1208.4678].

[251] **BaBar** Collaboration, J. P. Lees et al., *Evidence of* $B^+ \to \tau^+ \nu$ *decays with hadronic B tags*, *Phys. Rev.* **D88** (2013), no. 3 031102, [arXiv:1207.0698].

[252] **CKMfitter Group** Collaboration, J. Charles, A. Hocker, H. Lacker, S. Laplace, F. R. Le Diberder, J. Malcles, J. Ocariz, M. Pivk, and L. Roos, *CP violation and the CKM matrix: Assessing the impact of the asymmetric B factories*, *Eur. Phys. J.* **C41** (2005) 1–131, [hep-ph/0406184].

[253] **LUX** Collaboration, D. S. Akerib et al., *First results from the LUX dark matter experiment at the Sanford Underground Research Facility*, *Phys. Rev. Lett.* **112** (2014) 091303, [arXiv:1310.8214].

[254] **COUPP** Collaboration, E. Behnke et al., *First Dark Matter Search Results from a 4-kg* CF_3I *Bubble Chamber Operated in a Deep Underground Site*, *Phys. Rev.* **D86** (2012), no. 5 052001, [arXiv:1204.3094]. [Erratum: Phys. Rev.D90,no.7,079902(2014)].

[255] **XENON100** Collaboration, E. Aprile et al., *Limits on spin-dependent WIMP-nucleon cross sections from 225 live days of XENON100 data*, *Phys. Rev. Lett.* **111** (2013), no. 2 021301, [arXiv:1301.6620].

[256] J. Alwall, M. Herquet, F. Maltoni, O. Mattelaer, and T. Stelzer, *MadGraph 5 : Going Beyond*, *JHEP* **06** (2011) 128, [arXiv:1106.0522].

[257] J. Alwall, R. Frederix, S. Frixione, V. Hirschi, F. Maltoni, O. Mattelaer, H. S. Shao, T. Stelzer, P. Torrielli, and M. Zaro, *The automated computation of tree-level and next-to-leading order differential cross sections, and their matching to parton shower simulations*, *JHEP* **07** (2014) 079, [arXiv:1405.0301].

[258] T. Sjöstrand, and S. Mrenna, and P. Z. Skands, *PYTHIA 6.4 Physics and Manual*, *JHEP* **05** (2006) 026, [hep-ph/0603175].

[259] J. Pumplin et al., *New generation of parton distributions with uncertainties from global QCD analysis*, *JHEP* **07** (2002) 012, [hep-ph/0201195].

[260] M. L. Mangano, M. Moretti, F. Piccinini, and M. Treccani, *Matching matrix elements and shower evolution for top-quark production in hadronic collisions*, *JHEP* **01** (2007) 013, [hep-ph/0611129].

[261] **DELPHES 3** Collaboration, J. de Favereau, C. Delaere, P. Demin, A. Giammanco, V. LemaÃőtre, A. Mertens, and M. Selvaggi, *DELPHES 3, A modular framework for fast simulation of a generic collider experiment*, *JHEP* **02** (2014) 057, [arXiv:1307.6346].

[262] M. Cacciari, G. P. Salam, and G. Soyez, *The anti-k_t jet clustering algorithm*, *JHEP* **04** (2008) 063, [arXiv:0802.1189].

[263] M. Cacciari, G. P. Salam, and G. Soyez, *FastJet User Manual*, *Eur. Phys. J. C* **72** (2012) 1896, [arXiv:1111.6097].

[264] E. Conte, B. Fuks, and G. Serret, *MadAnalysis 5, A User-Friendly Framework for Collider Phenomenology*, *Comput. Phys. Commun.* **184** (2013) 222–256, [arXiv:1206.1599].

[265] E. Conte, B. Dumont, B. Fuks, and C. Wymant, *Designing and recasting LHC analyses with MadAnalysis 5*, *Eur. Phys. J.* **C74** (2014), no. 10 3103, [arXiv:1405.3982].

[266] B. Dumont, B. Fuks, S. Kraml, S. Bein, G. Chalons, E. Conte, S. Kulkarni, D. Sengupta, and C. Wymant, *Toward a public analysis database for LHC new physics searches using MADANALYSIS 5*, *Eur. Phys. J.* **C75** (2015), no. 2 56, [arXiv:1407.3278].

[267] G. Chalons and D. Sengupta, *Madanalysis 5 implementation of the ATLAS multi jet analysis documented in arXiv:1405.7875, JHEP 1409 (2014) 176*, tech. rep., 2015.

[268] B. Fuks, M. Blanke, and I. Galon, *MadAnalysis5 implementation of ATLAS-SUSY-2013-04*, tech. rep., 2015.

[269] A. L. Read, *Presentation of search results: The CL_s technique*, *J. Phys. G* **28** (2002) 2693–2704.

[270] P. Jackson, C. Rogan, and M. Santoni, *Sparticles in Motion - getting to the line in compressed scenarios with the Recursive Jigsaw Reconstruction*, *Phys. Rev.* **D95** (2016), no. 3 035031, [arXiv:1607.08307].

[271] A. Buckley, *PySLHA: a Pythonic interface to SUSY Les Houches Accord data*, *Eur. Phys. J.* **C75** (2015), no. 10 467, [arXiv:1305.4194].

[272] **CTA Consortium** Collaboration, M. Doro et al., *Dark Matter and Fundamental Physics with the Cherenkov Telescope Array*, *Astropart. Phys.* **43** (2013) 189–214, [arXiv:1208.5356].

[273] **LZ** Collaboration, D. S. Akerib et al., *LUX-ZEPLIN (LZ) Conceptual Design Report*, arXiv:1509.02910.

[274] G. Jungman, M. Kamionkowski, and K. Griest, *Supersymmetric dark matter*, *Phys. Rept.* **267** (1996) 195–373, [hep-ph/9506380].

[275] A. Djouadi, M. Drees, P. Fileviez Perez, and M. Muhlleitner, *Loop induced Higgs and Z boson couplings to neutralinos and implications for collider and dark matter searches*, *Phys. Rev.* **D65** (2002) 075016, [hep-ph/0109283].

[276] **LUX** Collaboration, D. S. Akerib et al., *Improved Limits on Scattering of Weakly Interacting Massive Particles from Reanalysis of 2013 LUX Data*, *Phys. Rev. Lett.* **116** (2016), no. 16 161301, [arXiv:1512.03506].

[277] ATLAS Collaboration, *Search for direct production of charginos, neutralinos and sleptons in final states with two leptons and missing transverse momentum in pp collisions at $\sqrt{s} = 8$ TeV with the ATLAS detector*, *JHEP* **05** (2014) 071, [arXiv:1403.5294].

[278] ATLAS Collaboration, *Search for direct production of charginos and neutralinos in events with three leptons and missing transverse momentum in $\sqrt{s} = 8$ TeV pp collisions with the ATLAS detector*, *JHEP* **04** (2014) 169, [arXiv:1402.7029].

[279] ATLAS Collaboration, *Search for electroweak production of supersymmetric particles in final states with two or three leptons at $\sqrt{s} = 13$ TeV with the ATLAS detector*, arXiv:1803.02762.

[280] ALEPH Collaboration, *Search for scalar leptons in e^+e^- collisions at center-of-mass energies up to 209 GeV*, *Phys. Lett. B* **526** (2002) 206–220, [hep-ex/0112011].

[281] ALEPH Collaboration, *Search for charginos nearly mass degenerate with the lightest neutralino in e^+e^- collisions at center-of-mass energies up to 209 GeV*, *Phys. Lett. B* **533** (2002) 223–236, [hep-ex/0203020].

[282] ALEPH Collaboration, *Absolute lower limits on the masses of selectrons and sneutrinos in the MSSM*, *Phys. Lett. B* **544** (2002) 73–88, [hep-ex/0207056].

[283] ALEPH Collaboration, *Absolute mass lower limit for the lightest neutralino of the MSSM from e^+e^- data at $\sqrt{s}$ up to 209 GeV*, *Phys. Lett. B* **583** (2004) 247–263.

[284] DELPHI Collaboration, *Searches for supersymmetric particles in e^+e^- collisions up to 208 GeV and interpretation of the results within the MSSM*, *Eur. Phys. J. C* **31** (2003) 421–479, [hep-ex/0311019].

[285] L3 Collaboration, *Search for charginos with a small mass difference with the lightest supersymmetric particle at $\sqrt{s} = 189$ GeV*, *Phys. Lett. B* **482** (2000) 31–42, [hep-ex/0002043].

[286] L3 Collaboration, *Search for scalar leptons and scalar quarks at LEP*, *Phys. Lett. B* **580** (2004) 37–49, [hep-ex/0310007].

[287] OPAL Collaboration, *Search for anomalous production of dilepton events with missing transverse momentum in e^+e^- collisions at $\sqrt{s} = 183$ GeV to 209 GeV*, *Eur. Phys. J. C* **32** (2004) 453–473, [hep-ex/0309014].

[288] OPAL Collaboration, *Search for nearly mass degenerate charginos and neutralinos at LEP*, *Eur. Phys. J. C* **29** (2003) 479–489, [hep-ex/0210043].

[289] S. D. Thomas and J. D. Wells, *Phenomenology of Massive Vectorlike Doublet Leptons*, *Phys. Rev. Lett.* **81** (1998) 34–37, [hep-ph/9804359].

[290] Z. Han, G. D. Kribs, A. Martin, and A. Menon, *Hunting quasidegenerate Higgsinos*, *Phys. Rev. D* **89** (2014), no. 7 075007, [arXiv:1401.1235].

[291] M. Baryakhtar, J. Bramante, S. W. Li, T. Linden, and N. Raj, *Dark Kinetic Heating of Neutron Stars and An Infrared Window On WIMPs, SIMPs, and Pure Higgsinos*, *Phys. Rev. Lett.* **119** (2017), no. 13 131801, [arXiv:1704.01577].

[292] M. Ibe, S. Matsumoto, and R. Sato, *Mass splitting between charged and neutral winos at two-loop level*, *Phys. Lett. B* **721** (2013) 252–260, [arXiv:1212.5989].

[293] A. Achterberg, S. Amoroso, S. Caron, L. Hendriks, R. Ruiz de Austri, and C. Weniger, *A description of the Galactic Center excess in the Minimal Supersymmetric Standard Model*, *JCAP* **1508** (2015), no. 08 006, [arXiv:1502.05703].

[294] M. van Beekveld, W. Beenakker, S. Caron, and R. Ruiz de Austri, *The case for 100 GeV bino dark matter: A dedicated LHC tri-lepton search*, *JHEP* **04** (2016) 154, [arXiv:1602.00590].

[295] M. Endo, K. Hamaguchi, S. Iwamoto, and T. Yoshinaga, *Muon g-2 vs LHC in Supersymmetric Models*, *JHEP* **01** (2014) 123, [arXiv:1303.4256].

[296] M. A. Ajaib, B. Dutta, T. Ghosh, I. Gogoladze, and Q. Shafi, *Neutralinos and sleptons at the LHC in light of muon $(g-2)_\mu$*, *Phys. Rev. D* **92** (2015), no. 7 075033, [arXiv:1505.05896].

[297] **MEG** Collaboration, A. M. Baldini et al., *Search for the lepton flavour violating decay $\mu^+ \to e^+\gamma$ with the full dataset of the MEG experiment*, *Eur. Phys. J. C* **76** (2016), no. 8 434, [arXiv:1605.05081].

[298] ATLAS Collaboration, *Search for the direct production of charginos, neutralinos and staus in final states with at least two hadronically decaying taus and missing transverse momentum in pp collisions at $\sqrt{s} = 8$ TeV with the ATLAS detector*, *JHEP* **10** (2014) 096, [arXiv:1407.0350].

[299] "ATLAS SUSY Working Group Summary Plots." https://atlas.web.cern.ch/Atlas/GROUPS/PHYSICS/CombinedSummaryPlots/SUSY/ATLAS_SUSY_EWSummary_WH/history.html.

[300] ATLAS Collaboration, *Search for supersymmetry in events with four or more leptons in $\sqrt{s} = 8$ TeV pp collisions with the ATLAS detector*, *Phys. Rev. D* **90** (2014) 052001, [arXiv:1405.5086].

[301] CMS Collaboration, *Searches for electroweak production of charginos, neutralinos, and sleptons decaying to leptons and W, Z, and Higgs bosons in pp collisions at 8 TeV*, *Eur. Phys. J. C* **74** (2014) 3036, [arXiv:1405.7570].

[302] CMS Collaboration, *Search for supersymmetry in events with soft leptons, low jet multiplicity, and missing transverse energy in proton–proton collisions at $\sqrt{s} = 8$ TeV*, *Phys. Lett. B* **759** (2016) 9, [arXiv:1512.08002].

[303] CMS Collaboration, *Search for electroweak production of charginos and neutralinos in multilepton final states in proton–proton collisions at $\sqrt{s} = 13$ TeV*, *JHEP* **03** (2018) 166, [arXiv:1709.05406].

[304] CMS Collaboration, *Search for new physics in events with two soft oppositely charged leptons and missing transverse momentum in proton-proton collisions at $\sqrt{s} = 13$ TeV*, *Phys. Lett.* **B782** (2018) 440–467, [arXiv:1801.01846].

[305] CMS Collaboration, *Search for supersymmetric partners of electrons and muons in proton–proton collisions at $\sqrt{s} = 13$ TeV*, *Phys. Lett.* **B790** (2019) 140–166, [arXiv:1806.05264].

[306] H. Baer, A. Mustafayev, and X. Tata, *Monojet plus soft dilepton signal from light higgsino pair production at LHC14*, *Phys. Rev. D* **90** (2014), no. 11 115007, [arXiv:1409.7058].

[307] G. F. Giudice, T. Han, K. Wang, and L.-T. Wang, *Nearly degenerate gauginos and dark matter at the LHC*, *Phys. Rev. D* **81** (2010) 115011, [arXiv:1004.4902].

[308] P. Schwaller and J. Zurita, *Compressed electroweakino spectra at the LHC*, *JHEP* **03** (2014) 060, [arXiv:1312.7350].

[309] S. Gori, S. Jung, and L.-T. Wang, *Cornering electroweakinos at the LHC*, *JHEP* **10** (2013) 191, [arXiv:1307.5952].

[310] B. Dutta, T. Ghosh, A. Gurrola, W. Johns, T. Kamon, P. Sheldon, K. Sinha, K. Wang, and S. Wu, *Probing compressed sleptons at the LHC using vector boson fusion processes*, *Phys. Rev. D* **91** (2015), no. 5 055025, [arXiv:1411.6043].

[311] Z. Han and Y. Liu, *MT2 to the Rescue – Searching for Sleptons in Compressed Spectra at the LHC*, *Phys. Rev. D* **92** (2015), no. 1 015010, [arXiv:1412.0618].

[312] A. Barr and J. Scoville, *A boost for the EW SUSY hunt: monojet-like search for compressed sleptons at LHC14 with 100 fb^{-1}*, *JHEP* **04** (2015) 147, [arXiv:1501.02511].

[313] ATLAS Collaboration, *Luminosity determination in pp collisions at $\sqrt{s} = 8$ TeV using the ATLAS detector at the LHC*, *Eur. Phys. J. C* **76** (2016) 653, [arXiv:1608.03953].

[314] J. Alwall, M.-P. Le, M. Lisanti, and J. G. Wacker, *Searching for Directly Decaying Gluinos at the Tevatron*, *Phys. Lett. B* **666** (2008) 34–37, [arXiv:0803.0019].

[315] U. De Sanctis, T. Lari, S. Montesano, and C. Troncon, *Perspectives for the detection and measurement of supersymmetry in the focus point region of mSUGRA models with the ATLAS detector at LHC*, *Eur. Phys. J. C* **52** (2007) 743–758, [arXiv:0704.2515].

[316] A. Djouadi, M. M. Muhlleitner, and M. Spira, *Decays of supersymmetric particles: The Program SUSY-HIT (SUspect-SdecaY-Hdecay-InTerface)*, *Acta Phys. Polon. B* **38** (2007) 635–644, [hep-ph/0609292].

[317] P. Artoisenet, R. Frederix, O. Mattelaer, and R. Rietkerk, *Automatic spin-entangled decays of heavy resonances in Monte Carlo simulations*, *JHEP* **03** (2013) 015, [arXiv:1212.3460].

[318] T. Sjöstrand, S. Mrenna, and P. Z. Skands, *A brief introduction to PYTHIA 8.1*, *Comput. Phys. Commun.* **178** (2008) 852–867, [arXiv:0710.3820].

[319] ATLAS Collaboration, "ATLAS Pythia 8 tunes to 7 TeV data." ATL-PHYS-PUB-2014-021, 2014.

[320] L. Lönnblad and S. Prestel, *Matching tree-level matrix elements with interleaved showers*, *JHEP* **03** (2012) 019, [arXiv:1109.4829].

[321] R. D. Ball et al., *Parton distributions with LHC data*, *Nucl. Phys. B* **867** (2013) 244, [arXiv:1207.1303].

[322] ATLAS Collaboration, "Simulation of top-quark production for the ATLAS experiment at $\sqrt{s} = 13$ TeV." ATL-PHYS-PUB-2016-004, 2016.

[323] ATLAS Collaboration, "Multi-Boson Simulation for 13 TeV ATLAS Analyses." ATL-PHYS-PUB-2017-005, 2017.

[324] ATLAS Collaboration, "ATLAS simulation of boson plus jets processes in Run 2." ATL-PHYS-PUB-2017-006, 2017.

[325] ATLAS Collaboration, "Modelling of the $t\bar{t}H$ and $t\bar{t}V(V = W, Z)$ processes for $\sqrt{s} = 13$ TeV ATLAS analyses." ATL-PHYS-PUB-2016-005, 2016.

[326] T. Gleisberg, S. Höche, F. Krauss, M. Schönherr, S. Schumann, F. Siegert, and J. Winter, *Event generation with SHERPA 1.1*, *JHEP* **02** (2009) 007, [arXiv:0811.4622].

[327] T. Gleisberg and S. Höche, *Comix, a new matrix element generator*, *JHEP* **12** (2008) 039, [arXiv:0808.3674].

[328] F. Cascioli, P. Maierhofer, and S. Pozzorini, *Scattering Amplitudes with Open Loops*, *Phys. Rev. Lett.* **108** (2012) 111601, [arXiv:1111.5206].

[329] S. Schumann and F. Krauss, *A Parton shower algorithm based on Catani-Seymour dipole factorisation*, *JHEP* **03** (2008) 038, [arXiv:0709.1027].

[330] S. Höche, F. Krauss, M. Schönherr, and F. Siegert, *QCD matrix elements + parton showers: The NLO case*, *JHEP* **04** (2013) 027, [arXiv:1207.5030].

[331] S. Alioli, P. Nason, C. Oleari, and E. Re, *A general framework for implementing NLO calculations in shower Monte Carlo programs: the POWHEG BOX*, *JHEP* **06** (2010) 043, [arXiv:1002.2581].

[332] S. Alioli, P. Nason, C. Oleari, and E. Re, *NLO Higgs boson production via gluon fusion matched with shower in POWHEG*, *JHEP* **04** (2009) 002, [arXiv:0812.0578].

[333] P. Nason and C. Oleari, *NLO Higgs boson production via vector-boson fusion matched with shower in POWHEG*, *JHEP* **02** (2010) 037, [arXiv:0911.5299].

[334] P. Z. Skands, *Tuning Monte Carlo generators: The Perugia tunes*, *Phys. Rev. D* **82** (2010) 074018, [arXiv:1005.3457].

[335] **NNPDF** Collaboration, R. D. Ball et al., *Parton distributions for the LHC Run II*, *JHEP* **04** (2015) 040, [arXiv:1410.8849].

[336] S. Catani, L. Cieri, G. Ferrera, D. de Florian, and M. Grazzini, *Vector boson production at hadron colliders: a fully exclusive QCD calculation at NNLO*, *Phys. Rev. Lett.* **103** (2009) 082001, [arXiv:0903.2120].

[337] H.-L. Lai, M. Guzzi, J. Huston, Z. Li, P. M. Nadolsky, J. Pumplin, and C. P. Yuan, *New parton distributions for collider physics*, *Phys. Rev. D* **82** (2010) 074024, [arXiv:1007.2241].

[338] M. Cacciari, M. Czakon, M. Mangano, A. Mitov, and P. Nason, *Top-pair production at hadron colliders with next-to-next-to-leading logarithmic soft-gluon resummation*, *Phys. Lett. B* **710** (2012) 612–622, [arXiv:1111.5869].

[339] M. Czakon and A. Mitov, *NNLO corrections to top pair production at hadron colliders: the quark-gluon reaction*, *JHEP* **01** (2013) 080, [arXiv:1210.6832].

[340] M. Czakon and A. Mitov, *NNLO corrections to top-pair production at hadron colliders: the all-fermionic scattering channels*, *JHEP* **12** (2012) 054, [arXiv:1207.0236].

[341] M. Czakon, P. Fiedler, and A. Mitov, *Total Top-Quark Pair-Production Cross Section at Hadron Colliders Through $O(\alpha_S^4)$*, *Phys. Rev. Lett.* **110** (2013) 252004, [arXiv:1303.6254].

[342] N. Kidonakis, *NNLL resummation for s-channel single top quark production*, *Phys. Rev. D* **81** (2010) 054028, [arXiv:1001.5034].

[343] N. Kidonakis, *Next-to-next-to-leading-order collinear and soft gluon corrections for t-channel single top quark production*, *Phys. Rev. D* **83** (2011) 091503, [arXiv:1103.2792].

[344] R. Frederix, E. Re, and P. Torrielli, *Single-top t-channel hadroproduction in the four-flavour scheme with POWHEG and aMC@NLO*, *JHEP* **09** (2012) 130, [arXiv:1207.5391].

[345] N. Kidonakis, *Two-loop soft anomalous dimensions for single top quark associated production with a W^- or H^-*, *Phys. Rev. D* **82** (2010) 054018, [arXiv:1005.4451].

[346] S. Dittmaier et al., "Handbook of LHC Higgs Cross Sections: 2. Differential Distributions." CERN-2012-002, 2012.

[347] ATLAS Collaboration, "Summary of ATLAS Pythia 8 tunes." ATL-PHYS-PUB-2012-003, 2012.

[348] A. D. Martin, W. J. Stirling, R. S. Thorne, and G. Watt, *Parton distributions for the LHC*, *Eur. Phys. J. C* **63** (2009) 189–285, [arXiv:0901.0002].

[349] ATLAS Collaboration, *The ATLAS Simulation Infrastructure*, *Eur. Phys. J. C* **70** (2010) 823, [arXiv:1005.4568].

[350] **GEANT4** Collaboration, S. Agostinelli et al., *GEANT4—a simulation toolkit*, *Nucl. Instrum. Meth. A* **506** (2003) 250.

[351] ATLAS Collaboration, "The simulation principle and performance of the ATLAS fast calorimeter simulation FastCaloSim." ATL-PHYS-PUB-2010-013, 2010.

[352] D. J. Lange, *The EvtGen particle decay simulation package*, *Nucl. Instrum. Meth. A* **462** (2001) 152.

[353] ATLAS Collaboration, *Topological cell clustering in the ATLAS calorimeters and its performance in LHC Run 1*, *Eur. Phys. J. C* **77** (2017) 490, [arXiv:1603.02934].

[354] ATLAS Collaboration, *Jet energy scale measurements and their systematic uncertainties in proton–proton collisions at $\sqrt{s} = 13$ TeV with the ATLAS detector*, *Phys. Rev. D* **96** (2017) 072002, [arXiv:1703.09665].

[355] ATLAS Collaboration, *Performance of pile-up mitigation techniques for jets in pp collisions at $\sqrt{s} = 8$ TeV using the ATLAS detector*, *Eur. Phys. J. C* **76** (2016) 581, [arXiv:1510.03823].

[356] ATLAS Collaboration, *Characterisation and mitigation of beam-induced backgrounds observed in the ATLAS detector during the 2011 proton–proton run*, *JINST* **8** (2013) P07004, [arXiv:1303.0223].

[357] ATLAS Collaboration, *Performance of b-jet identification in the ATLAS experiment*, *JINST* **11** (2016) P04008, [arXiv:1512.01094].

[358] ATLAS Collaboration, "Optimisation of the ATLAS b-tagging performance for the 2016 LHC Run." ATL-PHYS-PUB-2016-012, 2016.

[359] ATLAS Collaboration, *Electron reconstruction and identification in the ATLAS experiment using the 2015 and 2016 LHC proton-proton collision data at* $\sqrt{s} = 13$ *TeV*, arXiv:1902.04655.

[360] ATLAS Collaboration, *Muon reconstruction performance of the ATLAS detector in proton–proton collision data at* $\sqrt{s} = 13$ *TeV*, *Eur. Phys. J. C* **76** (2016) 292, [arXiv:1603.05598].

[361] M. Zgubič, Miha and J. J. Junggeburth, and N. M. Köhler, and S. Rosati, and F. Sforza, "Isolation selection efficiency on 2016 data: Preliminary Public Plots." ATL-COM-PHYS-2017-1685, Nov, 2017.

[362] ATLAS Collaboration, *Search for supersymmetry in events with four or more leptons in* $\sqrt{s} = 13$ *TeV pp collisions with ATLAS*, arXiv:1804.03602.

[363] ATLAS Collaboration, "Performance of missing transverse momentum reconstruction with the ATLAS detector in the first proton–proton collisions at $\sqrt{s} = 13$ TeV." ATL-PHYS-PUB-2015-027, 2015.

[364] ATLAS Collaboration, *Observation and measurement of Higgs boson decays to* WW^* *with the ATLAS detector*, *Phys. Rev. D* **92** (2015) 012006, [arXiv:1412.2641].

[365] J. Butterworth et al., *PDF4LHC recommendations for LHC Run II*, *J. Phys.* **G43** (2016) 023001, [arXiv:1510.03865].

[366] M. Baak, G. J. Besjes, D. Cote, A. Koutsman, J. Lorenz, and D. Short, *HistFitter software framework for statistical data analysis*, *Eur. Phys. J. C* **75** (2015) 153, [arXiv:1410.1280].

[367] G. Cowan, K. Cranmer, E. Gross, and O. Vitells, *Asymptotic formulae for likelihood-based tests of new physics*, *Eur. Phys. J. C* **71** (2011) 1554, [arXiv:1007.1727].

[368] ATLAS Collaboration, *Search for long-lived charginos based on a disappearing-track signature in pp collisions at* $\sqrt{s} = 13$ *TeV with the ATLAS detector*, *JHEP* **06** (2018) 022, [arXiv:1712.02118].

[369] ATLAS Collaboration, "Search for direct pair production of higgsinos by reinterpretation of the disappearing track analysis with 36.1 fb^{-1} of $\sqrt{s} = 13$ TeV data collected with the ATLAS experiment." ATL-PHYS-PUB-2017-019, 2017.

[370] H. Fukuda, N. Nagata, H. Otono, and S. Shirai, *Higgsino Dark Matter or Not: Role of Disappearing Track Searches at the LHC and Future Colliders*, *Phys. Lett.* **B781** (2018) 306–311, [arXiv:1703.09675].

[371] ATLAS Collaboration, *Search for direct pair production of a chargino and a neutralino decaying to the* 125 *GeV Higgs boson in* $\sqrt{s} = 8$ *TeV pp collisions with the ATLAS detector*, *Eur. Phys. J. C* **75** (2015) 208, [arXiv:1501.07110].